AFRL-RY-HS-TR-2010-0001

PROCEEDINGS OF THE 2009 ANTENNA APPLICATIONS SYMPOSIUM, VOLUME II

Dr. Daniel Schaubert
University of Massachusetts Amherst
Electrical and Computer Engineering
100 Natural Resources Road
Amherst MA 01003

12 December 2009

Final Report

AIR FORCE RESEARCH LABORATORY
Sensors Directorate
Electromagnetics Technology Division
80 Scott Drive
Hanscom AFB MA 01731-2909

NOTICE AND SIGNATURE PAGE

DAVID D. CURTIS
Chief, Antenna Technology Branch

MICHAEL N. ALEXANDER
Technical Advisor
Electromagnetic Technology Division

REPORT DOCUMENTATION PAGE

1. REPORT DATE *(DD-MM-YYYY)*	2. REPORT TYPE	3. DATES COVERED *(From - To)*
20-12-2009	FINAL REPORT	22 Sep 2009 - 24 Sep 2009

4. TITLE AND SUBTITLE

Proceedings of the 2009 Antenna Applications Symposium, Volume II

5a. CONTRACT NUMBER
F33615-02-D-1283

5b. GRANT NUMBER

5c. PROGRAM ELEMENT NUMBER

6. AUTHOR(S)

Daniel Schaubert et al.

5d. PROJECT NUMBER
4916

5e. TASK NUMBER
HA

5f. WORK UNIT NUMBER
01

7. PERFORMING ORGANIZATION NAME(S) AND ADDRESS(ES)

University of Massachusetts Amherst
Electrical and Computer Engineering
100 Natural Resources Road
Amherst, MA 01003

8. PERFORMING ORGANIZATION REPORT

9. SPONSORING / MONITORING AGENCY NAME(S) AND ADDRESS(ES)

Electromagnetics Technology Division
Sensors Directorate
Air Force Research Laboratory
80 Scott Drive
Hanscom AFB MA 01731-2909

10. SPONSOR/MONITOR'S ACRONYM(S)
AFRL-RY-HS

11. SPONSOR/MONITOR'S REPORT NUMBER(S)
AFRL-RY-HS-TR-2010-0001

12. DISTRIBUTION / AVAILABILITY STATEMENT
APPROVED FOR PUBLIC RELEASE; DISTRIBUTION UNLIMITED

13. SUPPLEMENTARY NOTES
Volume I contains pages 1 – 257   Public Affairs release Number 66ABW-2010-0005
Volume II contains pages 258-509

14. ABSTRACT

The Proceedings of the 2009 Antenna Applications Symposium is a collection of state-of-the art papers relating to antenna arrays and elements, millimeter wave antennas, simulation and measurement of antennas, integrated antennas, and antenna bandwidth and radiation improvements.

15. SUBJECT TERMS
Antennas, phased arrays, digital beamforming, millimeter waves, metamaterials, antenna measurements, airborne antenna applications, Vivaldi antennas, waveguide antenna arrays, broadband arrays, electrically small antennas

16. SECURITY CLASSIFICATION OF:			17. LIMITATION OF ABSTRACT	18. NUMBER OF PAGES	19a. NAME OF RESPONSIBLE PERSON David D. Curtis
a. REPORT	b. ABSTRACT	c. THIS PAGE	UU	520	19b. TELEPHONE NUMBER *(include area code)*
Unclassified	Unclassified	Unclassified			N/A

2009 ANTENNA APPLICATIONS SYMPOSIUM Volume II

22 - 24 September 2009
Monticello, Illinois

Identifiers for Proceedings of Symposia

The USAF Antenna Research and Development Program

Year	Symp. No.	Identifier
1951	First	
1952	Second	ADB870006
1953	Third	ADB283180
1954	Fourth	AD63139
1955	Fifth	AD90397
1956	Sixth	AD114702
1957	Seventh	AD138500
1958	Eighth	AD301151
1959	Ninth	AD314721
1960	Tenth	AD244388 (Vol. 1)
		AD319613 (Vol. 2)
1961	Eleventh	AD669109 (Vol. 1)
		AD326549 (Vol. 2)
1962	Twelfth	AD287185 (Vol. 1)
		AD334484 (Vol. 2)
1963	Thirteenth	AD421483
1964	Fourteenth	AD609104
1965	Fifteenth	AD474238L
1966	Sixteenth	AD800524L
1967	Seventeenth	AD822894L
1968	Eighteenth	AD846427L
1969	Nineteenth	AD860812L
1970	Twentieth	AD875973L
1971	Twenty-First	AD888641L
1972	Twenty-Second	AD904360L
1973	Twenty-Third	AD914238L

Antenna Applications Symposium

Year	Symposium	Technical Report #	Identifier
1977	First	None	ADA 955413
1978	Second	None	ADA 955416
1979	Third	_____	ADA 077167
1980	Fourth	_____	ADA 205907
1981	Fifth	_____	ADA 205816
1982	Sixth	_____	ADA 129356
1983	Seventh	_____	ADA 142003; 142754
1984	Eighth	85-14	ADA 153257; 153258
1985	Ninth	85-242	ADA 166754; 165535
1986	Tenth	87-10	ADA 181537; 181536
1987	Eleventh	88-160	ADA 206705; 206704
1988	Twelfth	89-121	ADA 213815; 211396
1989	Thirteenth	90-42	ADA 26022; 226021
1990	Fourteenth	91-156	ADA 37056; 237057
1991	Fifteenth	92-42	ADA 253681; 253682
1992	Sixteenth	93-119	ADA 268167; 266916
1993	Seventeenth	94-20	ADA 277202; 277203
1994	Eighteenth	95-47	ADA 293258; 293259
1995	Nineteenth	96-100	ADA 309715; 309723
1996	Twentieth	97-189	ADA 341737
1997	Twenty First	1998-143	ADA 355120
1998	Twenty Second	1999-86	ADA 364798
1999	Twenty Third	2000-008 (I) (II)	ADA 386476; 386477
2000	Twenty Fourth	2002-001 Vol I & II	ADA 405537; 405538
2001	Twenty Fifth	2002-002 Vol I & II	ADA 405328; 405327
2002	Twenty Sixth	2005-001 Vol I & II	ADA 427799; 427800
2003	Twenty Seventh	2005-005 Vol I & II	ADA 429122
2004	Twenty Eighth	2005-016 Vol I & II	ADA431338; 431339
2005	Twenty Ninth	2005-039 Vol I & II	ADM001873
2006	Thirtieth	2006-0047 Vol I & II	ADA464059
2007	Thirty First	2007-0037 Vol I & II	ADA475327, 475333
2008	Thirty Second	2008-0026 Vol I & II	ADA494632, 494633

2009 Author Index

Leaky-Wave Antenna Supporting 2.5 Gb/s on a 92 GHz Carrier

Richard W. Ridgway, Stephen Yen, and David W. Nippa
Battelle Memorial Institute
505 King Avenue
Columbus, OH 43201
ridgway@battelle.org

Abstract – **Periodic structures placed near a dielectric waveguide create a leaky-wave antenna that radiates in directions dependent on the periodicity of the structure. While leaky-wave antennas have been studied for several decades, it is only recently that their high data rate performance can be evaluated. This paper describes what is believed to be the first demonstration of a leaky-wave antenna operating at a data rate of 2.5 Gb/s. The W-band antenna is comprised of polystyrene dielectric waveguide and a conductive periodic structure. Photonic components, including a laser diode and electrooptic modulators, are used to generate and modulate the millimeter waves in an on-off keying modulation scheme. A high-speed photodiode converts the doubly modulated optical signal to a millimeter-wave signal. The 92 GHz modulated signal is transmitted by the leaky-wave antenna and received using a W-band horn. A Schottky-diode detector demodulates the on-off keyed signal. Successful transmission of data rates up to 2.5 Gb/s is verified using a bit error rate oscilloscope. The leaky-wave antenna supports data transmission over a scan angle ranging from 75° to 125° as the periodicity is varied from 3.3 mm to 1.7 mm.**

1   INTRODUCTION

Modern unmanned aerial vehicles (UAVs) used for surveillance and reconnaissance often collect and store large amounts of data from cameras. Real-time transmission of high definition video is often desirable between a UAV and a ground station. Millimeter waves are of interest for these links because they can support high data rates as well as propagate through clouds, fog, and dust. To date, most millimeter-wave links are stationary and use fixed high gain antennas (e.g. 2 foot Cassegrain) between ground stations. These antennas are large and not aerodynamic. Furthermore, the gimbals needed for beam tracking would be large and onerous. As a result, an alternative antenna design is needed that operates at millimeter-wave frequencies and has the form-factor and functionality suitable for UAVs.

When a periodic structure is placed near a dielectric waveguide, as shown in Figure 1, a leaky-wave antenna is formed. Energy emerges from the dielectric waveguide at an

angle dependent on the period of the periodic structure [1]. Leaky-wave antennas are attractive for the UAV application because they can be flush mounted to the UAV's exterior surface, provide beam steering and operate at millimeter-wave frequencies. Although they have been studied for decades, literature that reports their millimeter-wave performance when transmitting high-speed data could not be found. High data performance is of particular interest because the aperture of the leaky-wave antenna is equal to the length of the dielectric waveguide. When the data rate increases to the point that the physical length of the bit approaches the length of the waveguide, inter-symbol interference will degrade system performance and increase the bit error rate. This inter-symbol interference at high data rates will be particularly severe as the radiated pattern moves from normal incidence.

This paper reports experimental results for a leaky-wave antenna operating at 2.5 Gb/s on a 92 GHz carrier signal. The leaky-wave antenna explored in this work is a periodic dielectric consisting of a uniform dielectric waveguide with an air cladding and a perturbing metallic grating. Dielectric materials, such as polystyrene, provide compact (0.05" × 0.1") cross-sectional geometries at millimeter-wave frequencies and are easily fabricated. By changing the characteristics of the metallic grating the directionality of the antenna can be changed. This high-bandwidth, ultra low-profile and beam-steerable antenna can be flush-mounted to the bottom of a UAV to provide a variable field of vision directly below the vehicle. This paper begins with a description of Battelle's photonic approach for generating and modulating millimeter waves. This modulated signal is used to investigate the performance of the leaky-wave antenna. The antenna structure, experimental setup, and results are reported.
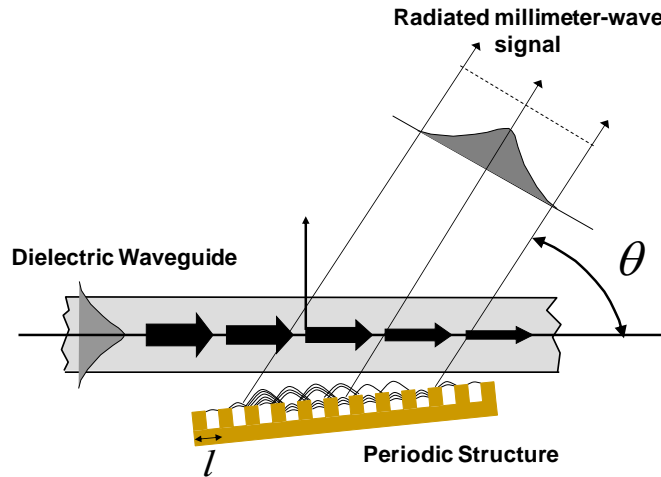
Figure 1: Schematic Representation of a Leaky-wave Antenna Employing a Dielectric Waveguide and a Periodic Grating.

2   MILLIMETER-WAVE COMMUNICATIONS LINK

Communications links operating at millimeter-wave frequencies can enable data rates currently unattainable. As rule of thumb, a carrier can support data to occupy up to about 10% of the carrier bandwidth. In other words, as illustrated in Figure 2, a microwave carrier at 10 GHz can support 1 Gb/s of data and a millimeter-wave carrier at 100 GHz can support 10 Gb/s of data using on-off keying (OOK). If spectral efficient techniques are employed, such as quadrature phase-shift keying (QPSK) and quadrature amplitude modulation (QAM), then these carrier frequencies can support larger amounts of data. A carrier can support a data rate approximately equal to the 10% bandwidth times the spectral efficiency. A QPSK modulation scheme (with a spectral efficiency of 2 bits-per-symbol) operating at 2.5 Gsymbols/sec would have a data rate of 5 Gb/s. A millimeter-wave carrier at 100 GHz, using 16-QAM (with a spectral efficiency of 4 bits/symbol) can support data rates up to 40 Gb/s. The bandwidth required for this data rate would be about 10 GHz centered around 100 GHz. It is anticipated that a data capacity of 100 Gb/s can be achieved with a millimeter-wave carrier at 250 GHz operating with a 16-QAM modulation scheme.
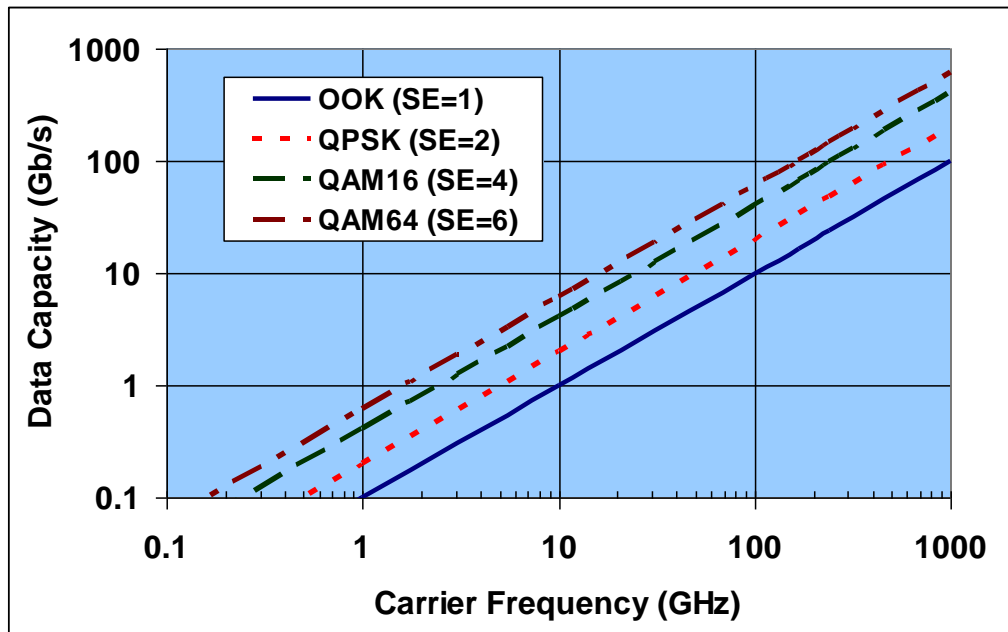
Figure 2: Millimeter-wave Frequencies Can Support Large Data Capacities with Spectrally-efficient (SE) Modulation Schemes.

While techniques for generating millimeter-wave carriers have been around for many years, modulating these carriers with data has been difficult because there are only a few components that operate at the high frequencies and no components that can directly modulate these high frequency carriers. To enable high data rates on millimeter-wave carriers, components are needed to amplitude and phase modulate the carrier with high

fidelity. However, at present there are limits to the carrier frequencies that can be directly modulated using RF electronics. The traditional RF approach is to start with a intermediate frequency (IF) that can be modulated, operating around 15 GHz, and then mix the IF up to the millimeter-wave carrier, such as 85 GHz. Using this technique it is not possible to encode data in excess of about 1.5 Gb/s because the bandwidth of the IF is too low.

Researchers at Battelle have been working for several years developing solutions to improve high-speed communications using millimeter waves. Battelle's approach is to use optical components to generate the millimeter waves and to modulate these signals with data while still in the optical domain. This work has included the design and fabrication of photonic-based systems incorporating high-speed optical modulators, variable optical attenuators optical amplifiers, optical filters and photodetectors in novel configurations [2-6]. Millimeter-wave carrier frequencies from 30 GHz to 300 GHz have been generated using this approach. In addition, these signals have been modulated at data rates between 2.5 Gb/s and 20 Gb/s, depending on the carrier frequency. The following paragraphs describe the amplitude modulation of millimeter waves using this photonic approach.

Battelle researchers have developed a millimeter-wave communications link that uses standard communications-grade optical components operating at 15.4 GHz to generate a 92 GHz millimeter-wave carrier and to encode OOK data onto the carrier at a rate up to 10 Gb/s. All of the modulation and data encoding is carried out in the optical domain with a continuous-wave laser diode (CW-LD) source operating near 1550 nm. The signal is converted to the millimeter-wave domain using an ultra-high frequency photodiode (PD). The PD enables the generation of the millimeter-wave signals at frequencies greater than 100 GHz and at power levels near 1 mW without electronic amplification.

The millimeter-wave signal is formed in the optical domain by generating sidebands on the optical carrier that are separated by the desired millimeter-wave frequency. These sidebands are generated by overdriving an electrooptic modulator using a microwave signal with a peak-to-peak amplitude two to three times larger than the modulator's V_π (i.e. voltage corresponding to a π phase shift). Both phase modulators and Mach-Zehnder interferometer modulators can be used to generate these optical sidebands. A Mach-Zehnder interferometer is used in this system since it can be driven in a push-pull configuration, which reduces the drive voltages needed to achieve the sidebands. Also, the bandwidth constraints are reduced on the optical filter used to eliminate the unwanted sideband since biasing can emphasize or deemphasize the even or odd harmonics.

The transmitter of the photonic-based millimeter-wave communications link is shown in Figure 3. A standard telecommunications-grade laser diode operating near 1550 nm provides the optical carrier at a power of 17 dBm. A standard dual-drive lithium niobate modulator (LNM) (Fujitsu FT7912ER) with a low drive voltage is overdriven at 15.4 GHz and configured to generate sidebands on the optical carrier. The +/– third sidebands

are positioned at +/– 46 GHz from the optical carrier, or 92 GHz apart. The phase and amplitude of the two microwave signals that drive the modulator, as well as the DC bias of the LNM, are set to maximize the power in the +/– third sidebands. In general, the two sinusoidal signals that drive the LNM are 180° out of phase and each have a peak-to-peak amplitude equal to 1.5 V_π to maximize the power in the +/– third sidebands of the laser carrier. Figure 4(a) shows the optical spectrum after the sideband LNM.

A 40-channel AWG from ANDevices with 25-GHz bandwidth ports is used to filter the sidebands. Two output ports, separated by 100 GHz, are summed together with an integrated Y-combiner waveguide to coherently combine the two desired optical sidebands. The AWG is adjusted so that the center port is set to the optical carrier wavelength and the center wavelength of the desired ports (+/– 2) are positioned +50 and −50 GHz, respectively, from the optical carrier wavelength. The peaks of the wavelength response are separated by 0.8 nm, or 100 GHz in frequency.   Figure 4(b) shows the sidebands after being filtered by the AWG. All of the undesired sidebands are now at least 20 dB below the +/– third sidebands. If this optical signal could be observed in the time domain, it would show an optical carrier that is modulated at 92 GHz with a high modulation depth.

A second LNM (Lucent 2623NA) is then used to encode data onto the 92-GHz modulated optical signal while still in the optical domain. Data from a pseudo-random-binary sequence generator (PRBS) (Synthesys, BSA12500A) is used to drive the data encoder resulting in OOK data at 10.6 Gb/s. This optical signal is amplified using an erbium-doped fiber amplifier (EDFA) (Nuphoton NP2000RS).
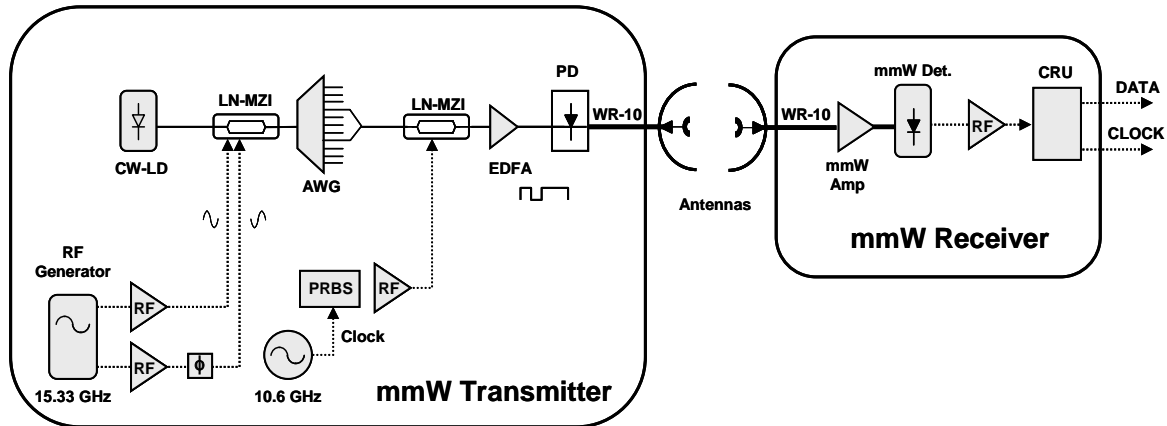
Figure 3: Schematic Drawing of the Photonic-based Millimeter-wave (mmW) Transmitter.
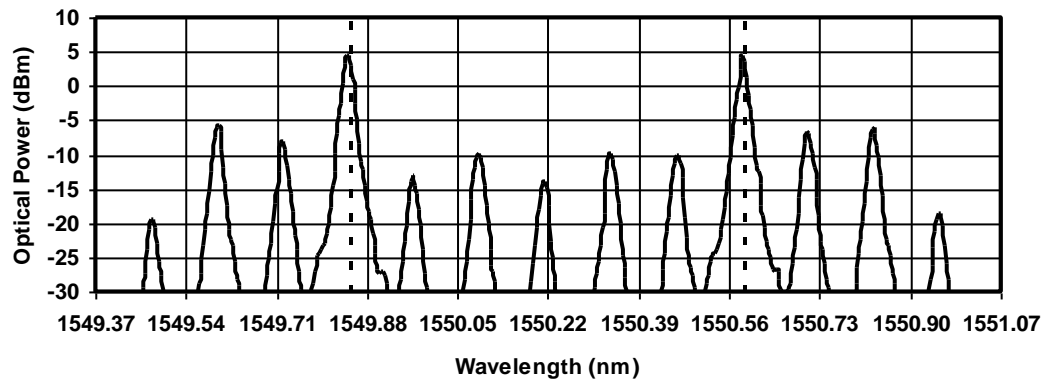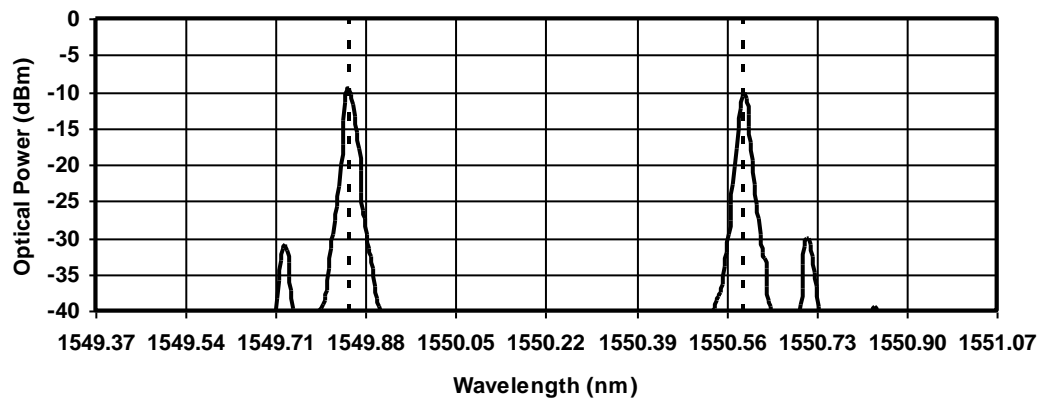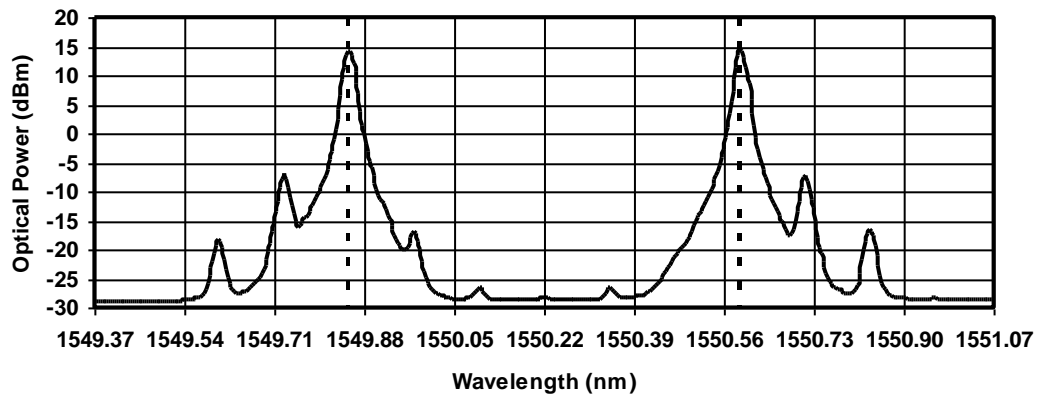
Figure 4: Optical Spectrum Analyzer Output Showing the (a) Spectrum of Sidebands After the First Modulator, (b) Spectrum Of Sidebands After The AWG, (c) Spectrum of the Filtered Sidebands With Data After the EDFA.

Two high speed photodetectors have been used to convert the doubly modulated optical signal to a modulated millimeter-wave signal. First, a p-i-n photodiode (PIN-PD) from HHI-Fraunhofer [7] and second, a uni-traveling carrier photodiode (UTC-PD) from Nippon Telegraph & Telephone Corp. (NTT) [8]. The PIN-PD, shown in Figure 5(a), is packaged with a 1-mm connector as its RF interface. It has a response to 100 GHz. The output power reaches a maximum of –2 dBm with an input optical power of 10 dBm. The bias current increases to about 12 mA for this output power when the bias voltage is set to provide a reverse bias on the PDs of 2 volts. The UTC-PD, shown in Figure 5(b), has a PD positioned in an F-band (90 GHz to 140 GHz) waveguide. With the input optical power of 11 dBm, the output millimeter-wave power is about 2 dBm. The bias current was about 9 mA when the PD is reverse biased by 1 volt.

A schematic of the receiver for the millimeter-wave communications link is shown in Figure 3. On the back of the receive antenna is a millimeter-wave preamplifier (Millitech, LNA-10-031052N) with 15 dB gain followed by a Schottky-diode-based millimeter-wave detector (Millitech DXP-10). The clock is recovered and the data successfully received using a clock and data recovery circuit.

Field tests of this system were conducted at Battelle's West Jefferson, Ohio facility on a 1 km range. Data rates at 2.5 Gb/s and 10 Gb/s were transmitted and received using 2-foot Cassegrain antennas without errors using a bit error rate test (BERT) scope (SyntheSys Research Inc., BSA12500A).

(a)   (b)
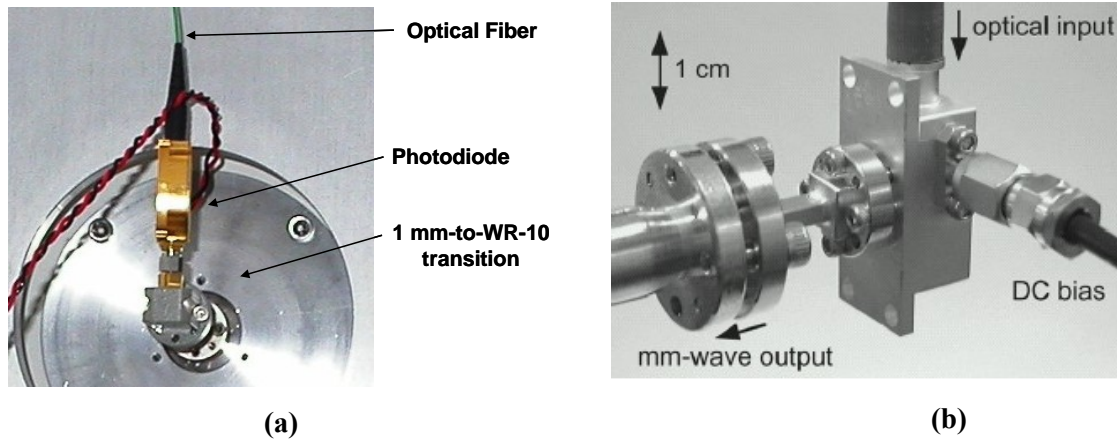
Figure 5: Photo of (a) HHI-Fraunhofer's PIN-PD and (b) NTT's UTC-PD [7].

3   LEAKY-WAVE ANTENNA

The periodic dielectric waveguide studied in this research is comprised of a dielectric waveguide with a metallic periodic grating near the surface. Interaction between the two structures causes leakage of the signal traveling through the dielectric waveguide over a specific frequency range governed by the waveguide's dielectric constant [9]. The design of the leaky-wave antenna is described in the following subsection followed by experimental results.

3.1   ANTENNA DESIGN

In the 1980s Battelle researchers reported the design and operation of a leaky-wave antenna operating at millimeter-wave frequencies [10]. While the operation of the antenna was verified, signal modulation techniques were not available to evaluate the data transmission characteristics of the antenna. The waveguide's dielectric constant and the air cladding govern the cross-sectional dimensions necessary for single-mode propagation at millimeter-wave frequencies. Polystyrene, with a relative dielectric constant of 2.54, was chosen due to its low attenuation at W-band frequencies. The first order-mode cutoff frequency for a dielectric slab is given by

$$f_c = \frac{c}{2a\sqrt{\mu_d \varepsilon_d - 1}}$$

(1)

where c is the speed of light, a is the dielectric thickness, μ_d is the dielectric's permeability, and ε_d is the relative dielectric constant [11]. The millimeter-wave signal is coupled to the dielectric waveguide by inserting the ends into WR-10 metallic waveguides with interior channel dimensions of 0.05" × 0.1". If a is 0.1", then f_c is 95.2 GHz and above the 92 GHz operating frequency. Therefore the cross-sectional dimension of the polystyrene is 0.05" × 0.1". As shown in Figure 6(a), the polystyrene was fabricated with the last 4 mm of both ends tapered to minimize coupling loss. Figure 6(b) shows the dielectric waveguide and brass grating in close proximity to form the leaky-wave antenna.

The beam angle and beam width of this leaky-wave antenna is governed by the periodicity of the metallic grating structure. The beam angle θ is determined by

$$\cos \theta = \frac{c}{v_g} - n\frac{\lambda}{l}$$

(2)

where v_g is the propagation velocity in the waveguide, n is the mode number, λ is the free space wavelength, and l is the period of the grating. The relative dielectric constant of the material (ε_d=2.54 for polystyrene) and the waveguide dimensions (0.05" x 0.1") determine the effective dielectric constant and thus the velocity of the millimeter-wave
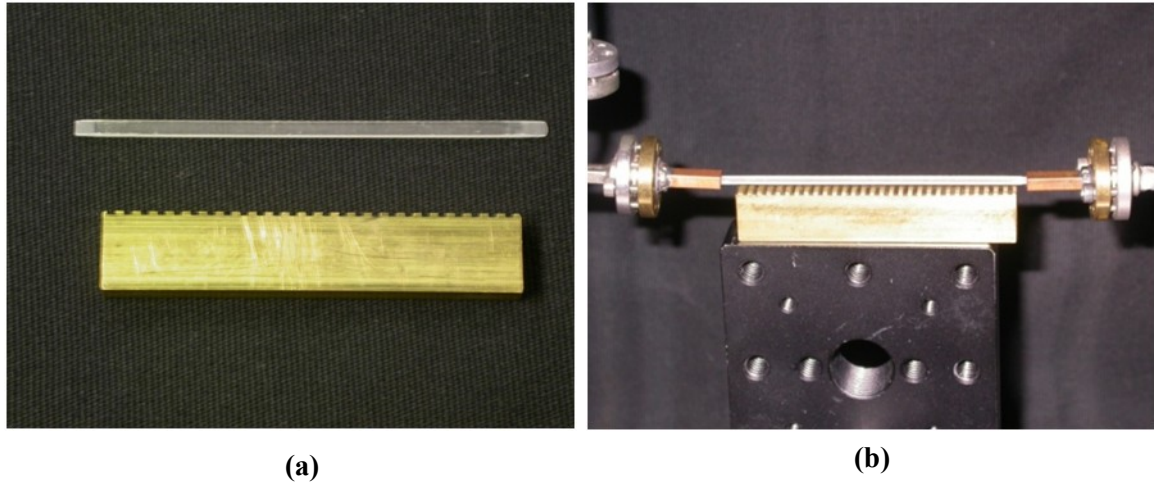
Figure 6: (a) Antenna Components -- Polystyrene Waveguide Above, Brass Grating Below and (b) Leaky-Wave Antenna Configuration.

Table 1. Periods of Experimental Gratings

Grating Period (mm)	Predicted Beam Angle (Degrees)
1.62	138.6
1.68	132.8
2.26	101.1
2.6	90.4
2.9	83.1
3.3	75.4

signal in the waveguide. For the polystyrene waveguide described in this paper, c/v_g is equal to 1.218 [10]. Six periodic structures, summarized in Table 1, were designed and fabricated in brass to provide a wide range of beam angles. The beam width is controlled by the length of the grating structure. As the aperture of the antenna increases the beam width decreases. In this work, 3"- long gratings were fabricated to provide a leaky-wave antenna with a 3" aperture-length. These components were used to experimentally verify the output from the leaky-wave antenna at different beam angles.

3.2   EXPERIMENTAL SETUP

A BERTScope 12500A generated PRBS-11 data encoded at 2.5 Gb/s. As described in Section 2, this RF signal was used to generate a modulated millimeter-wave signal operating at 92 GHz. Figure 7 shows the experimental setup for the transmitter and receiver antennas. The millimeter-wave signal was launched into a 0.5" WR-10 metallic stub and coupled to the polystyrene waveguide. Any power not diffracted out of the

waveguide or attenuated was delivered to a Millitech DXP-10 Schottky-diode-based detector. The signal transmitted by the leaky-wave antenna was directed vertically. A Baytron W-Band horn antenna with 25 dBi gain was used to capture the transmitted signal. A Millitech DXP-10 was used to detect the transmitted signal. The detected signal was routed to a 2.5 Gb/s ADN2812 Clock and Data Recovery Board (CDRB). A BERTScope provided a measure of the Bit-Error-Rate (BER).

A support structure was created to suspend the receive antenna 1.7' above the leaky-wave antenna. It is desirable to conduct these measurements in the far field to simulate real-world applications. However, the far field region for this leaky-wave antenna operating at 92 GHz is beyond 9.5'. As a result, all measurements were taken in the near field.

3.3 RESULTS

Figure 8 shows the theoretical and measured beam angles as a function of grating period. These results show that Eq. 2 accurately predicts the beam angle to within a 5% absolute relative error.

The W-band transmission loss through the dielectric waveguide suspended in air was evaluated by measuring the S_{21} parameter using an Agilent E8363B PNA and OML V10VNA2-T/R. Results indicate that the average transmission loss of the waveguide is 3.7 dB. Although this did not hinder the main results of the research, a loss of less than 1 dB could have been achieved with other dielectric waveguide materials. For example, alumina and high-resistive silicon could provide lower waveguide loss [11].

(a)   (b)
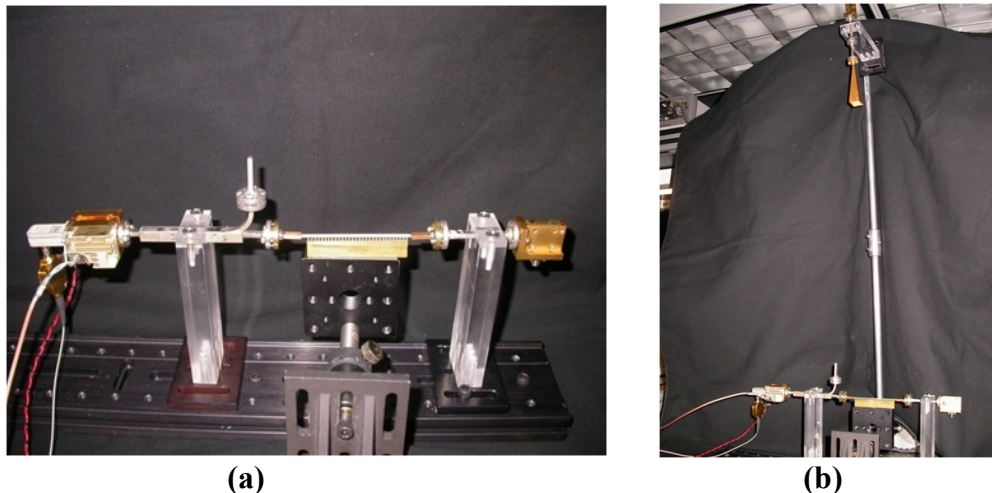
Figure 7: Wireless Link with the (a) Leaky-Wave Antenna as a Transmitter and a (b) Baytron WR-10 Horn as a Receiver.
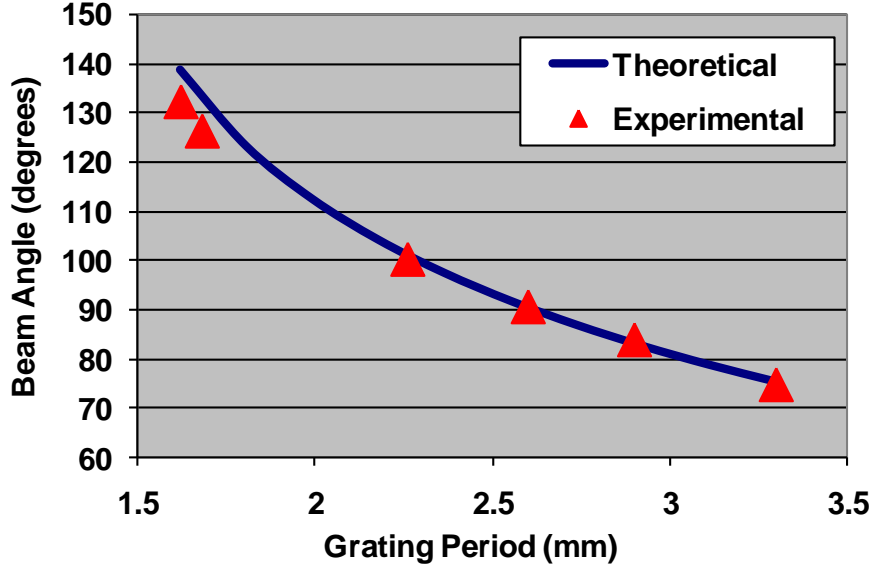
Figure 8: Beam Angle vs. Grating Period for the Leaky-Wave Antenna.

The successful transmission from the leaky-wave antenna of PRBS-11 encoded data at 1.0 Gb/s and 2.5 Gb/s is shown in Figure 9. A grating period of 2.6 mm was used to steer the signal to the receive antenna. Although the received signal power was the same for both data rates, the 1.0 Gb/s signal is visually cleaner and has a higher SNR than the 2.5 Gb/s signal. The CDRB was able to clean up the 2.5 Gb/s signal prior to BER testing. The BERTScope showed that the recovered data had a BER of zero and resulted in the excellent eye pattern shown in Figure 9(c). These results show that the leaky-wave antenna is capable of transmitting at data rates of at least 2.5 Gb/s.

This leaky-wave antenna has been described as a self-excited array where each element of the periodic structure is driven in series [1]. When the antenna is fed with a continuous wave signal, the half-power beamwidth is given by [1]:

$$\Delta\theta \cong \frac{\lambda}{L \cdot sin\theta} \tag{3}$$

where L is the length of the grating. However, as the data rate of the signal increases, and the physical length of a bit approaches the length of the grating, the beam width of the antenna can actually vary during the bit period.

(a)

(b)

(c)
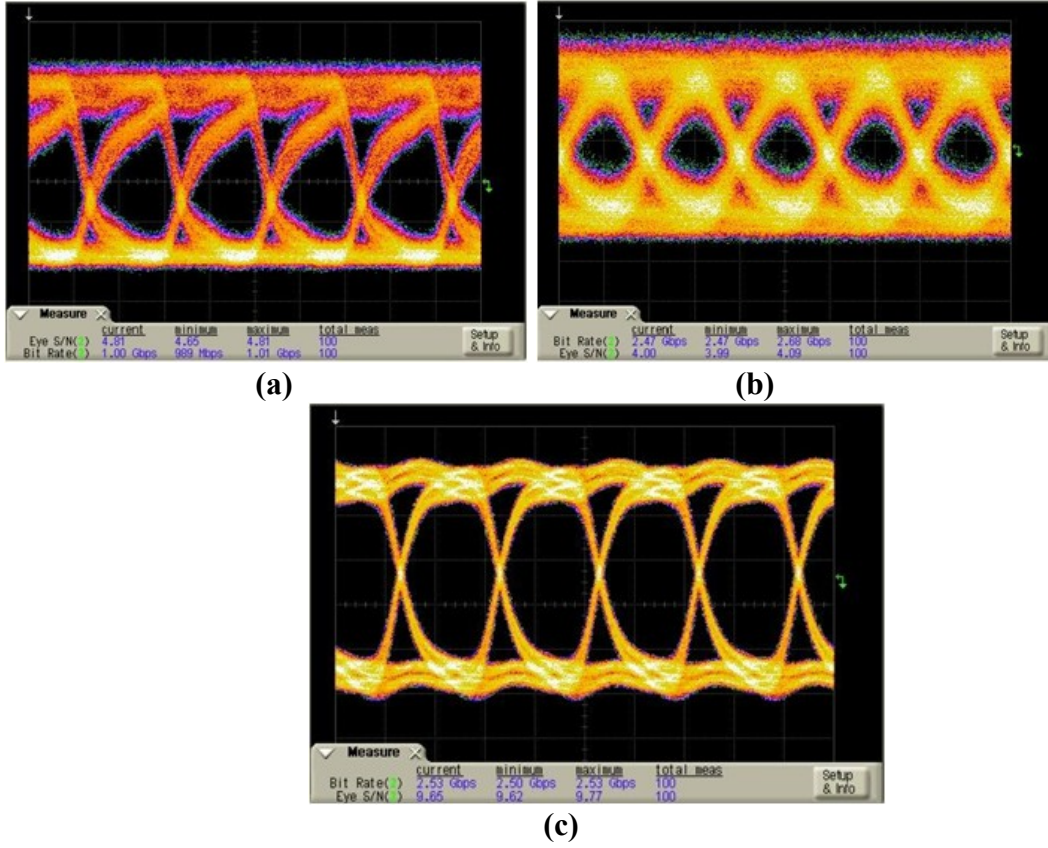
Figure 9: Results From the Oscilloscope Showing (a) the 1.0 Gb/s Received Signal Pre-CDRB, (b) 2.5 Gb/s Received Signal Pre-CDRB, and (c) 2.5 Gb/s CDRB Output.

Essentially, the traveling-wave nature of the signal in the waveguide and the physical length of the grating will cause inter-symbol interference as the data rate increases. One can consider three steps as a bit enters the leaky-wave antenna:

1. The initial portion, as the bit transition moves across the antenna (L/v_g seconds)
2. The middle portion, as the bit fully illuminates the antenna, ($T–L/v_g$ seconds), and
3. The final portion, as the next bit transition moves across the antenna (L/v_g seconds)

where T is the bit period. These steps are illustrated in Figure 10. The period of the radiated bit, T_{rad} is the sum of the three portions and is given by

$$T_{rad} = T + L/v_g \; . \tag{4}$$
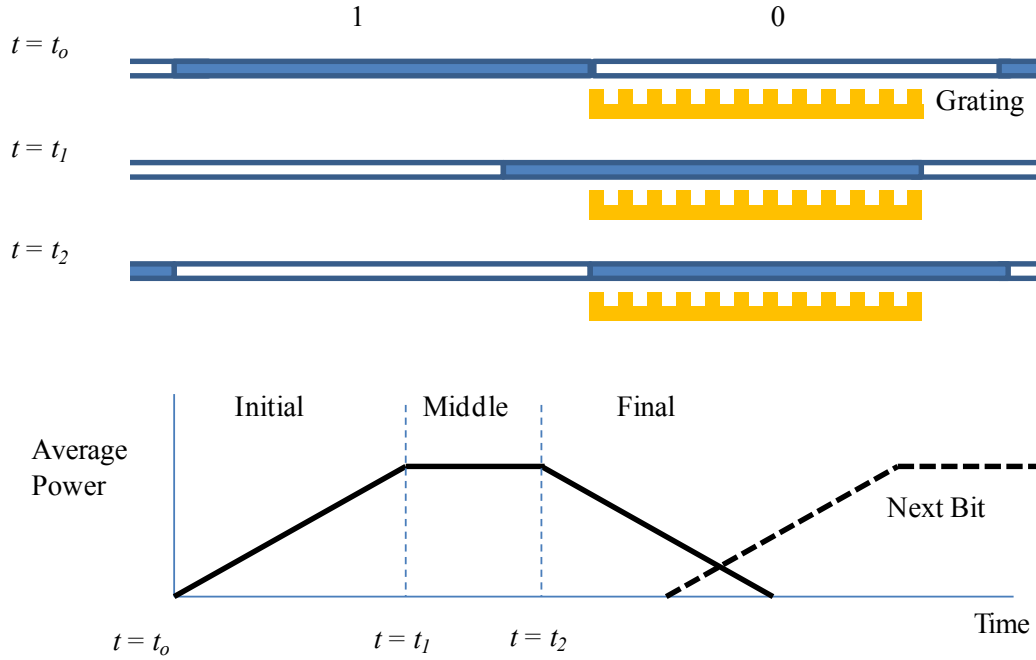
Figure 10: Schematic Showing the Progression of a 1010 Bit Pattern Propagating through the Grating Region of the Leaky-wave Antenna.

As the data rate increases and T approaches L/v_g the bit transition will overlap the adjacent bit resulting in inter-symbol interference and an increase in the bit error rate.

The physical length of a bit in the waveguide is dependent on the velocity of the signal in the waveguide and the data rate. Figure 11 graphically shows this relationship for the dielectric waveguide described in this paper. It is interesting to note that the physical length of the on-off keyed bit at 2.5 Gb/s in the polystyrene dielectric waveguide is 4". The grating, on the other hand, is 3" in length. From Equation (3), the duration of the transmitted bit is about 0.7 ns, or 70% larger than the original bit period.

The bit error rate measurements were made for several data rates between 1 Gb/s and 2.5 Gb/s using the six brass grating periods and a receive antenna located at the appropriate angle. At 1 Gb/s, the BERTscope recorded no errors at the receive angle positions for the six grating periods. Similarly, at 1.7 Gb/s, no errors were recorded for the six positions. However, at 2.5 Gb/s, successful transmissions with no errors were only recorded for periods greater than 1.62 mm. The leaky-wave antenna employing a 3" periodic element was only able to successfully transmit 2.5 Gb/s over angles between 80 degrees and 100 degrees (i.e. near normal to the plane of the antenna).
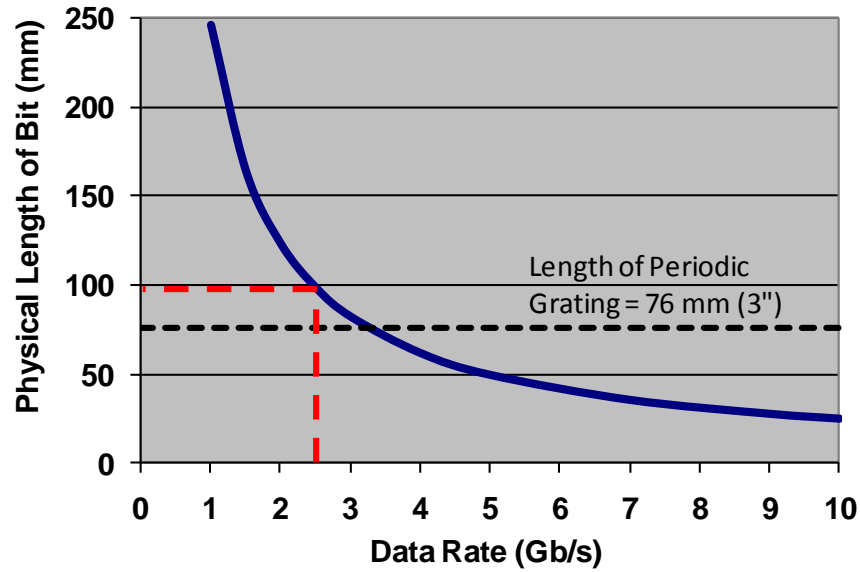
Figure 11. Physical Length of Bit in Dielectric Waveguide (ε_{eff} = 1.48) as a Function of Data Rate.

4   CONCLUSIONS

This work shows that leaky-wave antennas can be used for high data rate transmissions. However, the data rate should be low enough that the physical length of the bit in the waveguide is larger than the length of the periodic grating element. For a 3 inch grating element, data rates of 1 Gb/s were successfully transmitted at angles from 75 degrees to 138 degrees by varying the period of the grating from 3.3 mm to 1.62 mm. However, at 2.5 Gb/s, successful transmissions were only able to operate between 80 degrees and 100 degrees. It is contemplated that the inter-symbol interference, caused by the lengthening of the bits in the leaky-wave antenna, degrades the bit error rate and limits the angular performance.

5   REFERENCES

[1] M.R. Seiler & B.M. Mathena, "Millimeter-wave Beam Steering Using Diffraction Electronics", IEEE Trans. Ant. and Propagat., vol. AP-32, no. 9, pp. 987-990, Sept. 1984.

[2] R. W. Ridgway *et al.*, "Modulation of Light Using Kerr-Clad Silica Waveguide," Proceedings of the SPIE, vol. 5351, pp. 87-95, 2004.

[3] R. W. Ridgway & D. W. Nippa, "The Integration of Modulators and Multiplexers on Silica Planar Lightwave Circuits," Proceedings of the SPIE, vol. 5595, pp. 420-427, 2004.

[4] R. W. Ridgway *et al.*, "Fast VOA employing Electrooptically-Clad Silica Waveguide," Proceedings of the SPIE, vol. 5724, pp. 72-79, 2005.

[5] D. W. Nippa *et al.*, "Four-waveguide variable optical attenuator," in Integrated Photonics Research and Applications/Nanophotonics for Information Systems, Technical Digest (Optical Society of America, 2006), paper IMF2.

[6] R. W. Ridgway and D. W. Nippa, "Generation and Modulation of a 94-GHz signal using electrooptic modulators," *IEEE Photonics Tech. Lett*., vol. 20, no. 8, 2008.

[7] H.G. Bach *et al.*, "InP-based Narrow Band Photodetector Modules for 40 to 100 GHz Linear High Power Applications," IEEE LEOS Conference, 2006.

[8] H. Ito *et al.*, "High-Speed and High-Output InP-InGaAs Unitraveling Carrier Photodiodes," *IEEE J. Sel. Topics Quantum Electron.*, vol. 10, no. 4, pp. 709-727, Jul/Aug 2004.

[9] R. C. Johnson, Ed., *Antenna Engineering Handbook*, 3rd ed., Ch. 10, New York: McGraw-Hill, 1993.

[10] M. R. Seiler and R. W. Ridgway, "Studies of Millimeter-Wave Diffraction Devices and Materials," Defense Technical Information Center OAI-PMH Repository (USA), 28 Dec., 1984.

[11] Ramo *et al.*, *Fields and Waves in Modern Radio,* Second Edition, pp.388-390, John Wiley and Sons, New York, 1953.

[12] D. Saeedkia e*t al.*, "A Low-Loss Dielectric Waveguide Structure for Terahertz Applications," *18th International Symposium on Space-Terahertz Technology*, California Institute of Technology, Pasadena, USA, 21-23 March, 2007.

COLLINEAR ARRAYS FOR JTRS

James McDonald*[1,2], Farzin Lalezari[2], Dejan Filipović[1]

[1]Department of Electrical and Computer Engineering
University of Colorado at Boulder, UCB 425, Boulder, CO, USA 80309
[2]FIRST RF Corporation
4865 Sterling Dr., Boulder, CO, USA 80301

Abstract: Joint Tactical Radio System (JTRS) requires simple, robust, and multifunctional antennas that provide high gain from 200-2000 MHz. In this paper a collinear array topology is investigated as a candidate for JTRS. Conical dipoles and monopoles are integrated in a collinear fashion to provide a broadband high gain response. Radiation pattern instability caused by element pattern stability, and array factor is evaluated computationally. Radiation pattern of an array of resonant half-wave dipoles is used as a benchmark for computation of bandwidth. The performance of a classical monocone is improved by merging a cone with a circular cylinder at the position referred to as the junction location. The cone angle and junction location are optimized using efficient global optimization to determine the best embodiment for a modified monocone-bicone collinear array. It is shown that the monocone-bicone collinear array arrangement can provide a stable radiation pattern over several octaves.

1. Introduction

Modern military communications systems, such as the Joint Tactical Radio System (JTRS) require high-gain antennas with stable radiation patterns over large bandwidths. Current JTRS systems use up to 8 antennas to cover the 2-2000 MHz band, thus presenting a significant challenge for both individual antenna design and their placement on the host platform [1]. Wideband solutions covering any subset of the JTRS band are currently sought [2]. It is anticipated that an antenna operating over 200-2000 MHz bandwidth would replace up to 5 antennas and allow a radio to maintain legacy functionality as well as the ability to use newly defined JTRS waveforms.

A biconical antenna is inherently broadband and could be used to cover this bandwidth. This paper will explore an alternate framework for defining the bandwidth; both for a single bicone and for a monocone-bicone collinear array. The bandwidth of a modified monocone is explored. The classical monocone is improved by adding a circular cylinder to a cone at a position called the junction location. The geometry of this modified monocone is parametrically studied for both its cone angle and its junction location. The full-wave data are then used to optimize a monocone-bicone array for its cone angle and junction location. An ideally fed numerical model of this collinear array is also examined.

1.1. Conical Antennas

A biconical antenna is one of the oldest antennas that has been studied for over a century. Early works include a patent by Lodge in 1898 [3], Marconi's implementation of a conical wire monopole (wire monocone) in Trans-Atlantic experiments [4], and Carter's version for wideband short wave radio [5]. An excellent survey of various topics in conical antenna engineering including the history of developments is given by Bevensee [6]. A bicone is a canonical antenna and was used by many researchers to develop and test numerical methods as discussed by Bevensee. These methods include conical transmission line model, boundary value problem, and the variational method [7]-[9]. Brown and Woodward noted that many of the theoretical methods utilize some simplifying assumptions and approximations to reduce the mathematical difficulty of solving for the impedance and radiation patterns of a conical antenna [10]. Thus, they performed a series of measurements on both the impedance and radiation patterns for different cone angles and antenna heights. With the advent of modern computing, focus shifted to numerical methods to compute input impedance and radiation pattern of a conical antenna. Mautz and Harrington applied the method of moments to characterize the radiation from several surface-of-revolution antennas [11]. The versatility of this method allows for easy analysis of a conical antenna, including the addition or removal of a spherical cap or a broadband monocone design.

1.1.1. Conical Antenna Bandwidth Framework

There are many ways that can be used to determine bandwidth. The IEEE bandwidth definition states "The range of frequencies within which the performance of the antenna, with respect to some characteristic, conforms to a specified standard." [12] The bandwidth of antennas is most commonly determined on the basis of its impedance response [13]. If the far-field pattern is considered it is typically limited to a few radiation patterns [14] or the gain at horizon [15]. An alternate method was proposed [16] that takes into account the bandwidth of monocone antennas in terms of the minimum system or realized gain over a 39° elevation field of view.

This field of view was chosen based on the 3 dB beamwidth of a resonant quarter-wave monopole. Thus the optimized 2 dBi bandwidth antennas will have up to 0.14 dB minimum gain dropout when compared to an ideal quarter wave monopole within its 3 dB beamwidth. Consequently the 2 dBi bandwidth monocone will have a radiation pattern similar to that of a quarter wave monopole throughout its operating bandwidth.

The far-field pattern of a resonant quarter-wave monopole and the field of view used to compute the bandwidth are shown in Figure 1. The realized gain, G_r, is defined as,

$$G_r = G_A 10 \log_{10}(1 - |\Gamma|^2),\qquad(1)$$

where G_A is the antenna gain, and Γ is the reflection coefficient computed (here) based on the nominal line impedance of 50Ω. In this work the monocone bandwidth is defined as the ratio of the highest (f_2) and lowest (f_1) frequency of operation where G_r is greater than G_{min} over the desired field of view, $51° \leq \theta \leq 90°$. Thus, the bandwidth is

$$BW = \frac{f_2}{f_1},\qquad(2)$$

where these two frequencies are determined as,

$$\begin{aligned}f_s &\triangleq f|_{G_r(f,\theta)\geq G_{min}} \text{ where } 51° \leq \theta \leq 90° \\ f_2 &= \max(f_s) \\ f_1 &= \min(f_s).\end{aligned}\qquad(3)$$
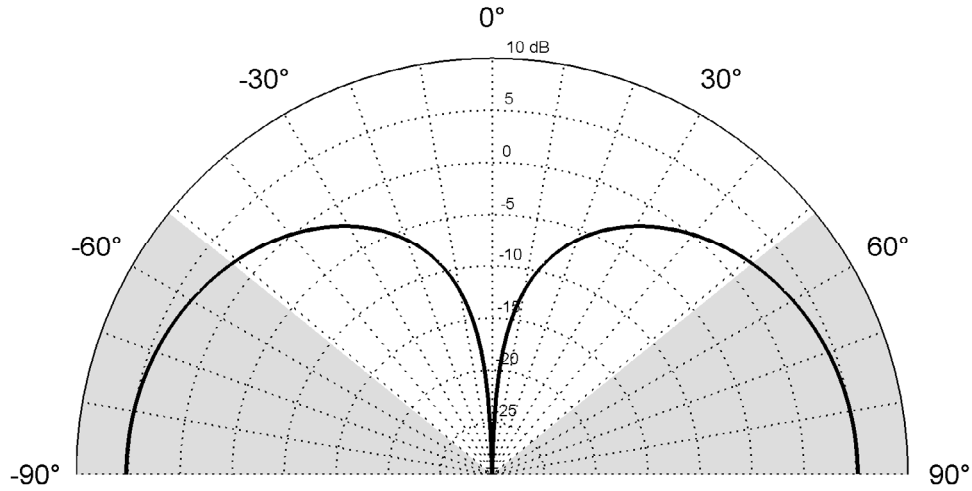
Figure 1: An elevation radiation pattern of a quarter-wave monopole at its resonance. The highlighted elevation field of view corresponding to the 3 dB beamwidth is used for bandwidth determination. For all antennas studied in this paper the azimuthal pattern is omni-directional, at a specified elevation angle.

Equations (2) and (3) can be illustrated by the example of the resonant quarter-wave monopole over an infinite ground plane (see Figure 2). Frequency is normalized with

respect to the nominal resonant frequency of a quarter-wave monopole, f_0. In this figure f_2 and f_1 are illustrated for $G_{min} = 2$ dBi; and they are equal to 0.998 and 0.944 respectively. Thus the 2 dBi bandwidth of this antenna as defined in equation (2) is 1.057. In [16] a simple modification of a monocone, shown in Figure 3, was proposed, and the bandwidth optimization for the cone angle α and junction location ρ is conducted. Results have shown that this modification reduces the weight and bulk of a monocone, and increases the 2 dBi bandwidth by about 37% compared to the classical monocone.
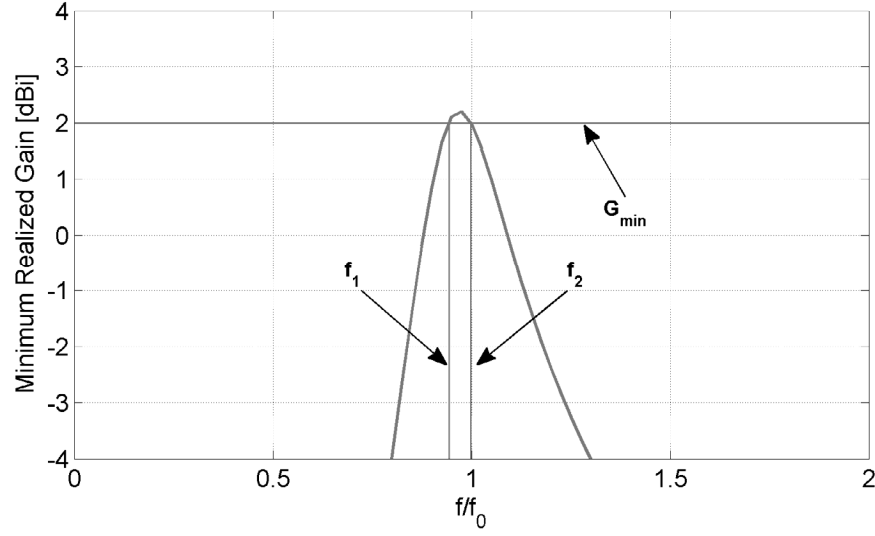
Figure 2: A minimum system gain of a thin monopole with a 39° elevation field of view. Important values for determining the bandwidth are denoted. Note that the bandwidth criterion for minimum gain in this case is $G_{min} = 2$ dBi. The realized gain bandwidth of a thin monopole is 1.057 as defined in equation (2).
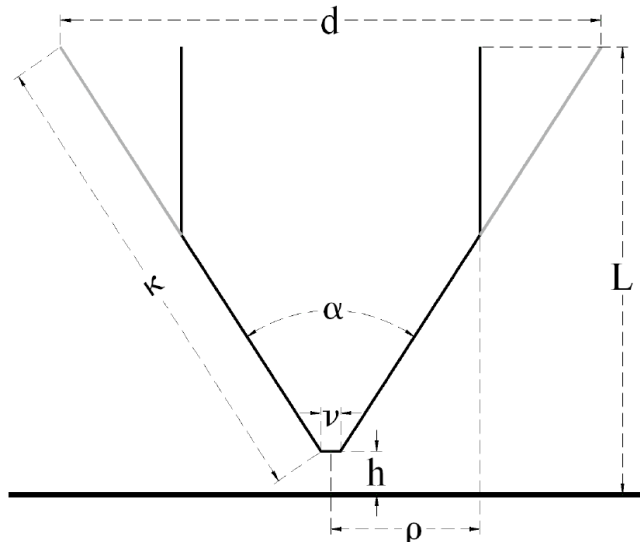
Figure 3: 2-D cross-section of studied monocones. Illustrated are the antenna structural parameters: the cone height L, the cone diameter d, the cone angle α, the base diameter v, the base height h, and the junction location ρ.

1.2. Collinear Dipole Arrays

Collinear arrays of dipoles have long been used to increase the gain of a single element. One of the major advantages of this array configuration is that it has much lower coupling between elements than other types of planar arrays, such as row-echelon [20]. There is a secondary coupling effect that is caused by the current induced on the feed line of the upper dipoles. This can typically be compensated over a narrow bandwidth by using current chokes [21]. Bach [22] discusses the directivity of a set of short collinear dipoles. Some contour plots are given that plot directivity as a function of spacing and phase progression constants. An expression is given for the array factor of this array. Kiang examines coaxial collinear antennas [23], which have remained the most common embodiment since they can be configured to radiate like an array of dipoles. Miyashita et. al. have developed an electromagnetically coupled collinear dipole array as a variant of the popular coaxial collinear (COCO) antenna [24]. This array is band-limited because of the narrow-band nature of the dipole elements. Because of the inherent difficulty in reducing the currents on feed cables and the narrowband nature of dipole antenna elements, collinear arrays are typically not used over a large bandwidth. There are a few examples of conical arrays which are capable of sustaining a much broader bandwidth because of the broadband stability of the radiation pattern. Litchford discloses a stack of three biconical antennas in which the biconical sections are supported by metallic members [25]. Button et. al. attempt to overcome the secondary coupling of the transmission line by winding a bundle of transmission lines helically around the cylindrical periphery of the biconical antennas [26]. This feed system causes interference on the outgoing signal, which distorts the radiation pattern. Honda et. al. overcome the feed cable coupling by using a distributed slot feed system [27]. However, using this feed network it is not possible to feed the elements with uniform phase over a large bandwidth. In order to have broadband radiation pattern stability it is necessary to feed the elements with uniform amplitude and phase.

1.2.1. Collinear Array Bandwidth Framework

A similar method for defining a framework for bandwidth as was discussed in Section 1.1.1 is proposed for a collinear monocone-bicone array. For a collinear array this is based on an array of resonant dipoles. In the open literature collinear array bandwidth has been defined in various ways. For example, Bregains et. al. use the half power beamwidth, sidelobe level, ripple, and maximum element active impedance to determine the bandwidth of a collinear array of dipoles [28]. The maximum bandwidth they report is 1.17:1 for beamwidth and 1.10:1 for active impedance stability. Kragalott et. al. uses an active VSWR for several different scan angles to achieve a 5:1 bandwidth notch array [29]. In this paper, we follow a similar approach in determining array bandwidth as in [16] (discussed in section 1.1.1) where the bandwidth is defined as the frequency range in which the realized or system gain is greater than some minimum level inside a 39° field of view. This angular dependence is determined based on the half-power beamwidth of a resonant quarter-wave monopole. Here a monocone-bicone collinear array bandwidth is based on the baseline collinear array composed of; a quarter-wave resonant monopole and a resonant half-wave dipole (see Figure 4). The patterns for this array are computed

based solely on the array factor and the element pattern [19]. These are ideal patterns in that no mutual coupling and practical effect of feeding are considered. For this configuration the half-power beamwidth is dependent on the electrical separation of the two phase centers as shown in Figure 5. Also shown in this figure is the minimum gain computed by subtracting 3 dB from the maximum gain value within the array's half-power beamwidth.
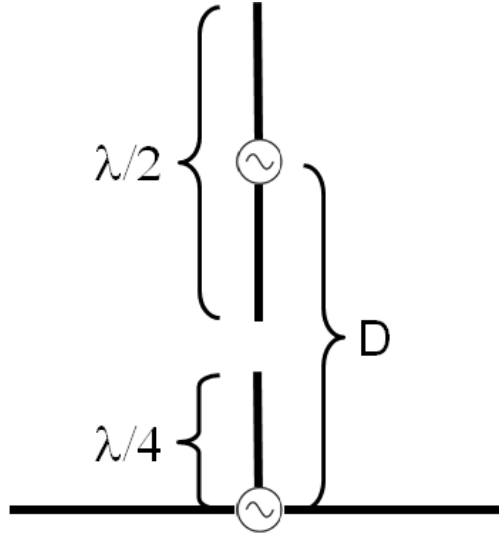
Figure 4: A resonant monopole dipole collinear array is used as a baseline for determining the array bandwidth.
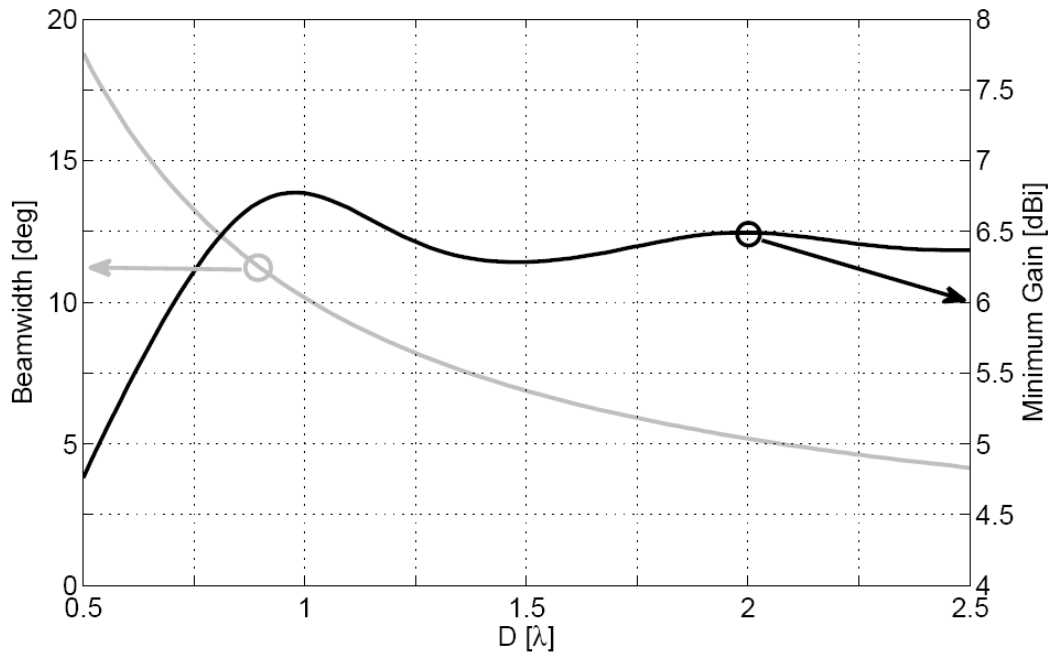
Figure 5: The half-power beamwidth of a monopole dipole collinear array varies with the electrical separation, *D*. This beamwidth is used to define the bandwidth. The minimum gain, or half-power of the directivity, is also used to define the bandwidth.

2. Modified Monocone

A common method for improving the bandwidth of a conical antenna is to make the antenna have a bulbous or spherical surface [18]. In [16], another approach for increasing the monocone bandwidth was investigated. Specifically, the monocone was modified by merging a cone with a circular cylinder at the position referred to as the junction location. A 2-D cross section of this structure is shown in Figure 3, and as was shown, a significant bandwidth improvement was obtained without added fabrication complexity.

2.1. Bandwidth Optimization

To determine the bandwidth improvement a complete parametric study was conducted for the variables α and ρ. The antenna height above the infinite ground plane L, was kept constant. The values for h and v are fixed at $0.007\lambda_0$ and $0.013\lambda_0$ as was determined in [16] to be the optimum values for the monocone ($\lambda_0 = 4L$). For $G_{min} = 2$ dBi the optimal cone angle, $\alpha = 80°$, and the junction location, $2\rho/d = 52\%$.

The minimum system gain over the desired field of view is shown in Figure 6. As can be seen this simple modification in monocone shape improved the monocone antenna bandwidth by 37%. The lowest and highest frequencies of operation for the 2 dBi antenna were $f_1 = 0.793\,f_0$ and $f_2 = 3.672\,f_0$ respectively. Note that the volume of the sphere that encloses this antenna was decreased by 76% when compared to the volume of the optimized 2 dBi classical monocone.
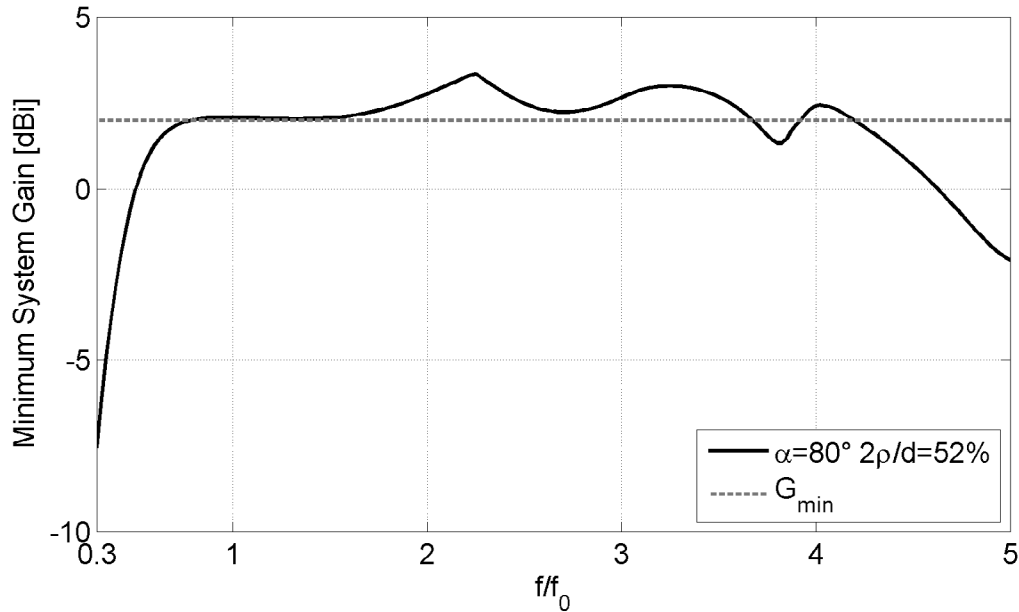
Figure 6: The minimum system gain over $51° \leq \theta \leq 90°$ for optimum the 2 dBi modified monocone.

2.2. Bandwidth Contour

The bandwidth of a modified monocone for various cone angles, α, and junction locations $2\rho/d$ is shown in Figure 7 for G_{min} equal to 2 dBi. The numbers on the contour

lines are constant bandwidth values for the entire search space in α and $2\rho/d$. This plot can be easily used in a design to determine the best dimensions for a specified bandwidth, allowing one to make appropriate tradeoff between desired bandwidth and antenna size, volume, and/or weight.
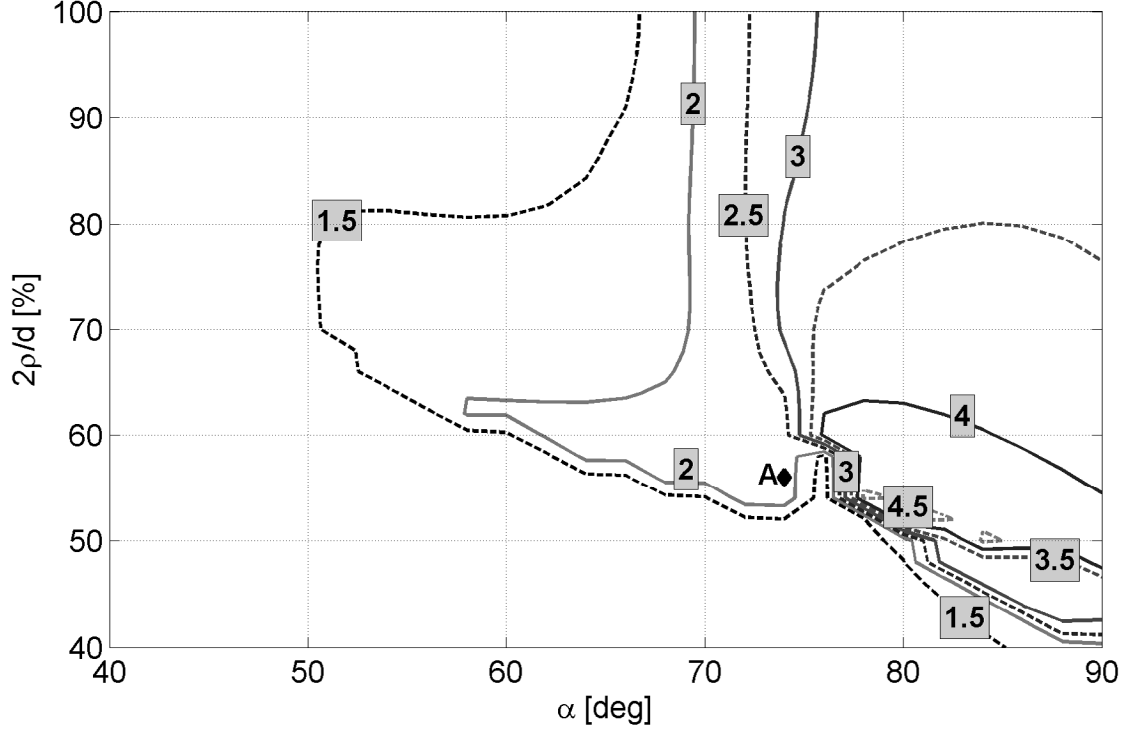
Figure 7: Contour plot of a constant $G_{min} = 2$ dBi bandwidth of a modified monocone versus α and $2\rho/d$. The point A denotes the bandwidth of the fabricated monocone. It is located at $\alpha = 74°$ and $2\rho/d = 56\%$ and has a bandwidth of 2.28:1.

2.3. Model Validation

The validity of the results is demonstrated by building and measuring a modified monocone with parameters $\alpha = 74°$, $2\rho/d = 56\%$, $v = 0.013\lambda_0$, and $h = 0.007\lambda_0$ ($f_0 = 1$ GHz). A photo of the fabricated antenna is shown in Figure 8, and its 2 dBi bandwidth is denoted as point A in Figure 7. For measurements the antenna was mounted on a $2\lambda_0$ diameter ground plane. The impedance was measured with an Agilent E8363B network analyzer, and comparison with the simulation is given in Figure 9. As seen, excellent agreement with computed results is obtained throughout the measured frequency range. Radiation patterns were also taken and Figure 10 shows the measured and simulated results at 4 discrete frequencies. Along with excellent agreement with the model, the pattern stability remains good even though the antenna is mounted on an untreated finite size ground plane. The finite size of the ground plane allows reradiation in the lower half-space effectively reducing the gain at horizon [19].

Figure 8: A photograph of the fabricated monocone mounted on a 60 cm diameter circular ground plane.
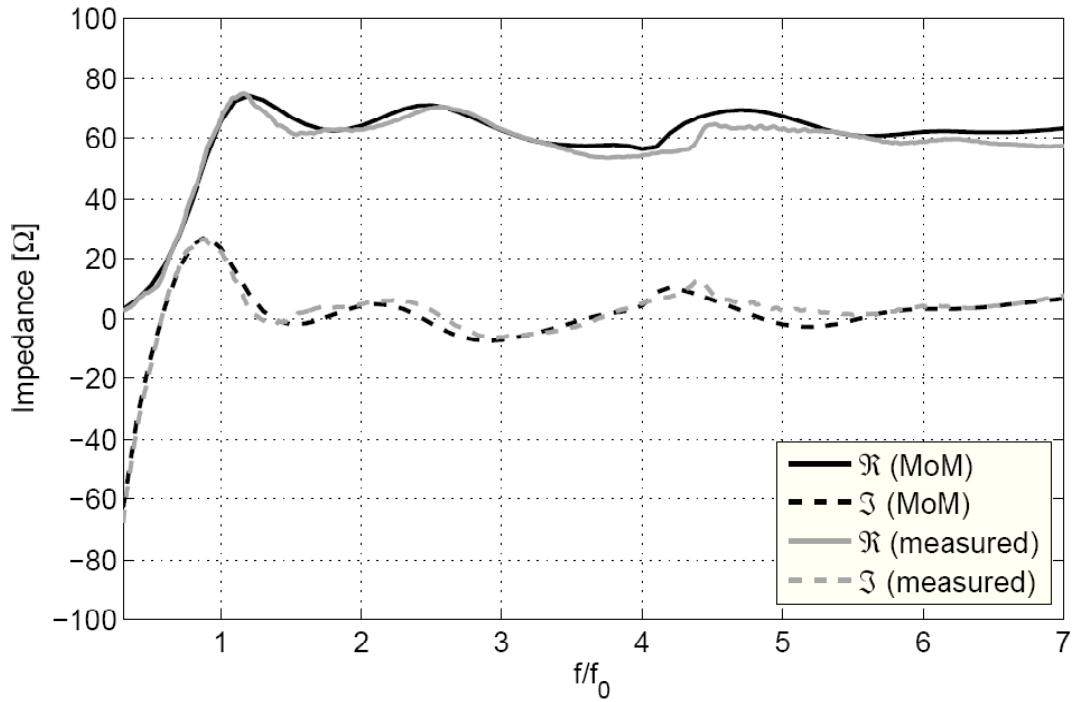
Figure 9: Simulated and measured input impedance of the fabricated modified monocone on a circular 60 cm diameter ground plane.
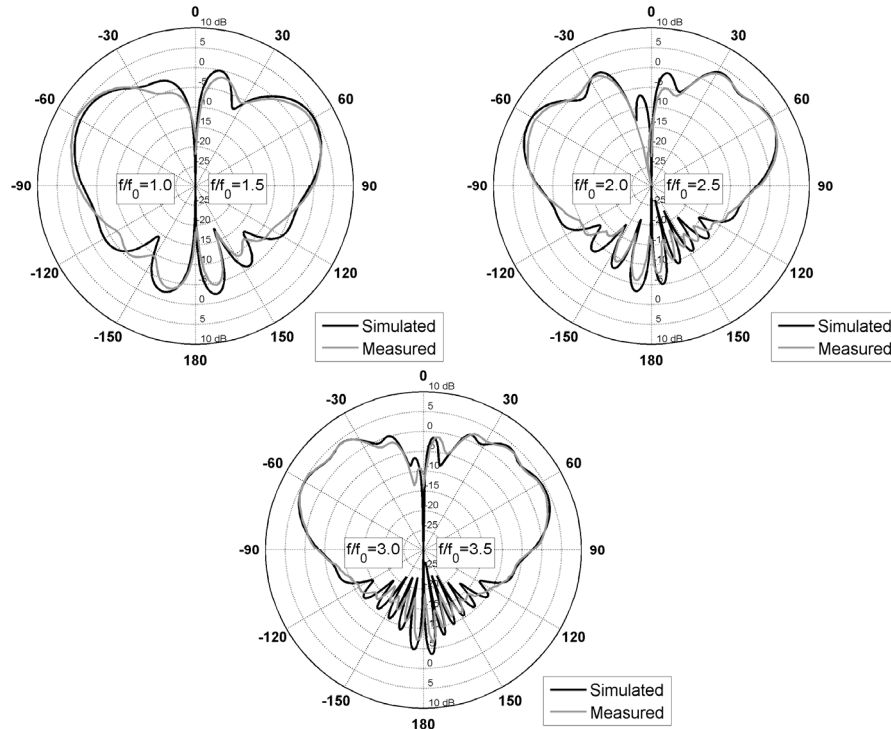
Figure 10: A comparison between computed and measured radiation patterns at four discrete frequencies within 3.5:1 bandwidth. The polar plots are split in two half spaces each corresponding to a pattern at specific normalized frequencies shown in the legend. The modified monocone was placed in a $2\lambda_0$ finite circular ground plane.

2.4. Modified Monocone Summary

A method of computing the bandwidth that takes into account the impedance and pattern stability was used to study the wideband properties of several antennas. The lowest and highest frequencies of operation are determined based on the reference values for the minimum system gain over a 39° elevation beamwidth from horizon. This angle is chosen as it corresponds to the 3 dB beamwidth of a thin resonant quarter-wave monopole placed in an infinite ground plane. A simple modification of a monocone was also proposed. For the same height above the ground plane and base diameter, the optimum modified monocone has a bandwidth of 4.6:1. The overall volume of a sphere that completely encloses the antenna is reduced by 76% compared to a classical monocone. Various designer plots are also provided. A test article is fabricated and measurements are used to not only demonstrate the wideband performance of a modified monocone, but also validate our results.

3. Monocone-Bicone Array

The full-wave data presented in the contour plot in Figure 7 were obtained using a commercial method of moments solver EMSS's FEKO [30]. These full-wave data are used in an array simulator to find the optimal monocone-bicone geometry seen in Figure 11. The monocone and bicone cone angles α_m and α_b and the monocone and bicone

junction locations ρ_m and ρ_b are optimized using Efficient Global Optimization (EGO) [31].
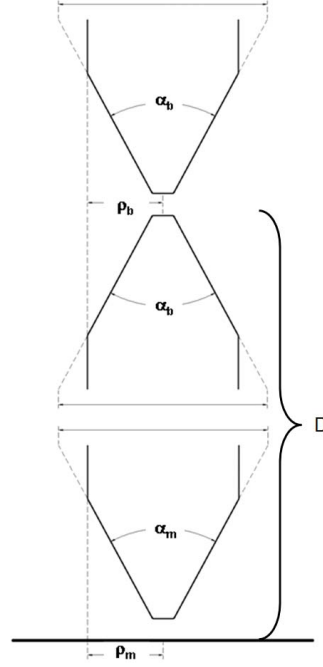
Figure 11: The monocone-bicone geometry is optimized for the structural parameters: the monocone and bicone cone angles α_m and α_b, and the monocone and bicone junction location ρ_m and ρ_b.

3.1. Cost functions

The monocone-bicone collinear array bandwidth is evaluated using three different criteria or cost functions: bandwidth above 6.2 dBi, percent bandwidth above baseline, and area above baseline.

3.1.1. Bandwidth Above 6.2 dBi

The cost function for the bandwidth above 6.2 dBi is defined as the ratio of frequencies over which the minimum matched antenna gain, G^a_{min} inside the defined field of view is greater than 6.2 dBi. The field of view is a function of the electrical separation between the monocone and the bicone, D that varies as the half-power beamwidth of the baseline array (see Figure 4 and Figure 5). The value 6.2 dBi is chosen as this is the value of the dip shown in Figure 5 of the baseline array at $D \approx 1.5\lambda$. This is similar to the definition of bandwidth (2) that was used for a single monocone.

3.1.2. Percent Bandwidth Above Baseline

The cost function for the bandwidth above the baseline is defined as the percentage of frequency points in which the matched antenna gain, G^a_{min} is greater than the baseline antenna gain, G^b over a fixed frequency band. In the JTRS application for example this band would be from 200-2000 MHz.

3.1.3. Area Above Baseline

The cost function for the area above the baseline attempts to minimize the area below the baseline collinear array. It does this by finding the difference between the matched antenna gain of the antenna, G_{min}^a and the baseline antenna gain G^b at all frequency points. There is no reward for the antenna gain being greater than the baseline antenna, being greater and at this frequency point the delta is set to zero. The optimal cost function would be zero, as that would mean that at all frequencies the antenna performs better than the baseline.

3.2. Bandwidth Optimization

The full-wave data from [16] are used in an array simulator to find the optimal monocone-bicone geometry of the collinear array in Figure 11. This simulator takes the individual element patterns and multiplies them by the array factor thus; it neglects coupling between the monocone and bicone. The monocone and bicone cone angles α_m and α_b and the monocone and bicone junction locations ρ_m and ρ_b are optimized using Efficient Global Optimization (EGO) [31]. The EGO algorithm is a global optimizer that generates a statistical model of the cost function using the Design and Analysis of Computer Experiments (DACE) predictor [32]. This statistical model is often called a response surface. One advantage of this type of model is that the response of the cost function is predicted as well as the error of the prediction. This allows the surface response to be refined throughout the optimization process by predicting areas that need further refinement, either because they are near the optimal point or are in an area of high error because the area has not been examined [33]. Compared to other global optimization methods the number of cost function evaluations needed to find an optimal solution is greatly reduced. In this optimization the distance D is fixed while α_m, α_b, ρ_m, and ρ_b are optimized for the three cost functions summarized above. The directivity of arrays can be computed from the individual element pattern, which is obtained from the full-wave modeled data, and the array factor, which is a function of the geometry of the array [19]. MATLAB code has been written to optimize the geometry of the array. As was discussed earlier this code does not include the effect of coupling between the monocone and bicone. Thus the optimization is performed for an ideal array geometry. The results of the optimization are given in Table 1. As can be seen in this table the monocone and bicone have similar geometries; a cone angle of about 90° and a junction location of approximately 90%.

Table 1: An optimal geometric solution for each of the three cost functions.

Cost Functions	α_m	α_b	ρ_m	ρ_b	Value
BW above 6.2 dBi	90°	80°	92%	90%	3.3:1
Percent BW above baseline	90°	90°	90%	86%	82.9%
Normalized area above baseline	90°	90°	92%	90%	0.524

The geometry and minimum directivity inside the field of view, θ_b, as defined in (4) for each of the three cost functions is shown in Figure 12, Figure 13, and Figure 14.
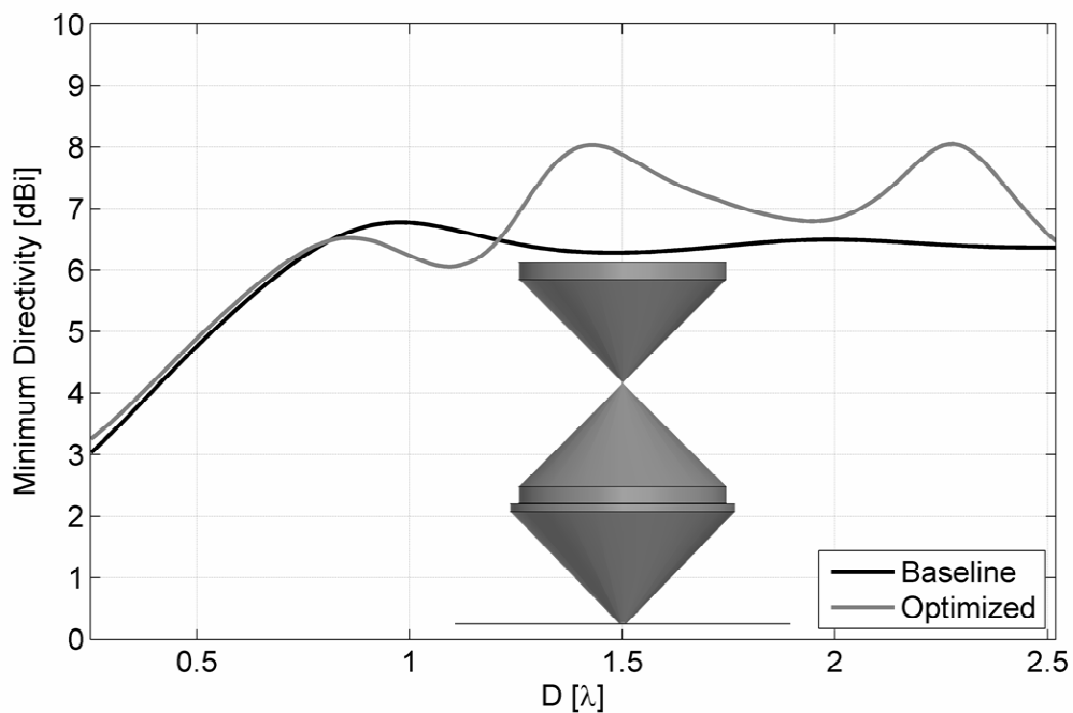
Figure 12: The minimum directivity of the geometry optimized for the cost function bandwidth above 6.2 dBi. Bandwidth is 3.3:1.
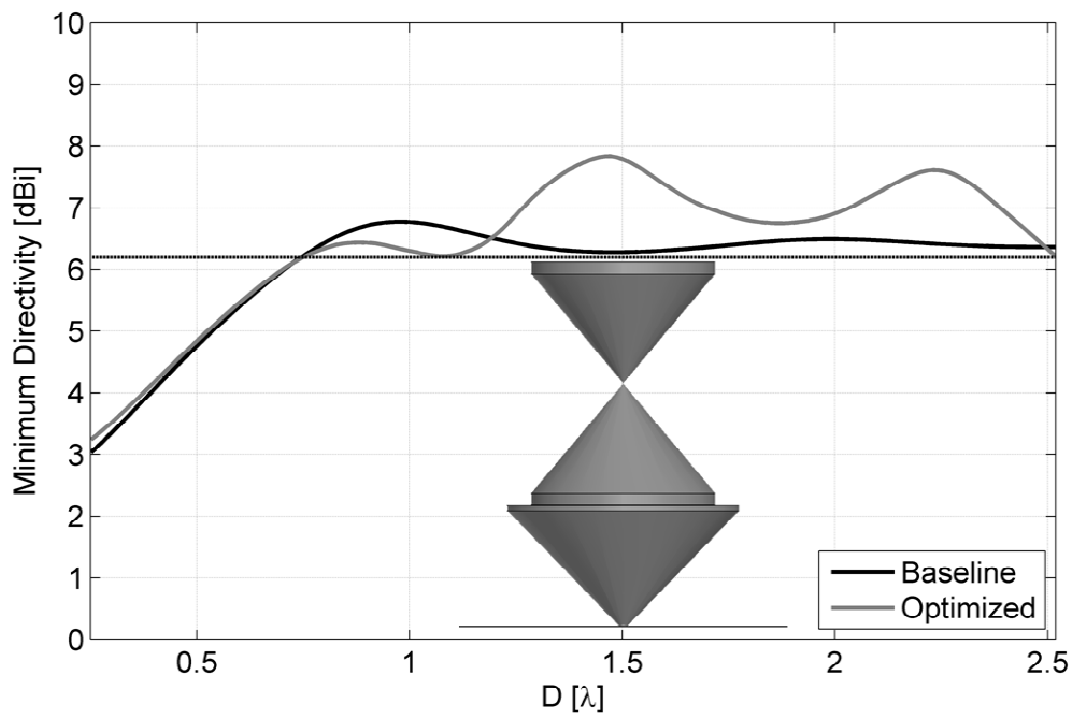
Figure 13: The minimum directivity of the geometry optimized for the cost function 'percent bandwidth above baseline'.
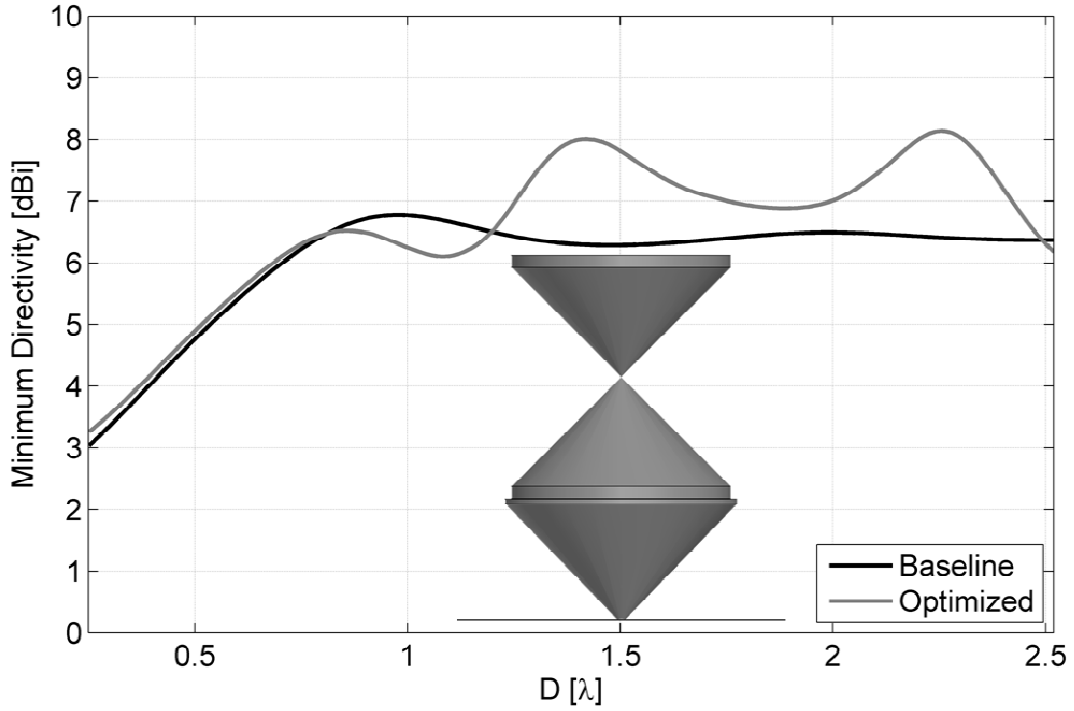
Figure 14: The minimum directivity of the geometry optimized for the cost function 'area above baseline'.

As is seen in these figures the baseline and the optimized geometry are nearly the same until the phase center separation, D is 0.8λ. This is because the element pattern of all of the monocones and bicones are nearly the same as a resonant monopole and dipole up to this frequency. Thus the result is nearly completely dependent on the array factor, and not the element patterns. After 0.8λ the geometry of the cones affects the element patterns, thus for these geometries we begin to see a deviation from the baseline case.

Because the geometries of these optimized solutions are similar we also see similar trends in the minimum directivity; peaks at about 0.85λ, 1.40λ, and 2.25λ and troughs at about 1.1λ and 1.9λ.

3.3.   Numerical Results

The design illustrated in Figure 13, which was optimized for the percent bandwidth above baseline cost function, is modeled using two different commercially available electromagnetic solvers; Ansoft's HFSS [33] which uses the Finite Element Method and CST's Microwave Studio Transient Solver [34] which uses the a time-domain solution of the Finite Integration Technique. As can be seen in Figure 15 and Figure 16 the agreement between the two methods is excellent. In both models the bicone and monocone are excited using a simple delta gap excitation.

The directivity of the monocone-bicone is also computed using the Finite Element Method. As seen in Figure 17 the minimum directivity of the modeled monocone-bicone array has different performance than that of the coupling free array simulation (see

Section 3.2). This is difference attributed to the feed of the elements and the coupling between the monocone and the bicone. While the performance of the full-wave model and the coupling free array is different the peaks and troughs occur at similar frequencies in both models.
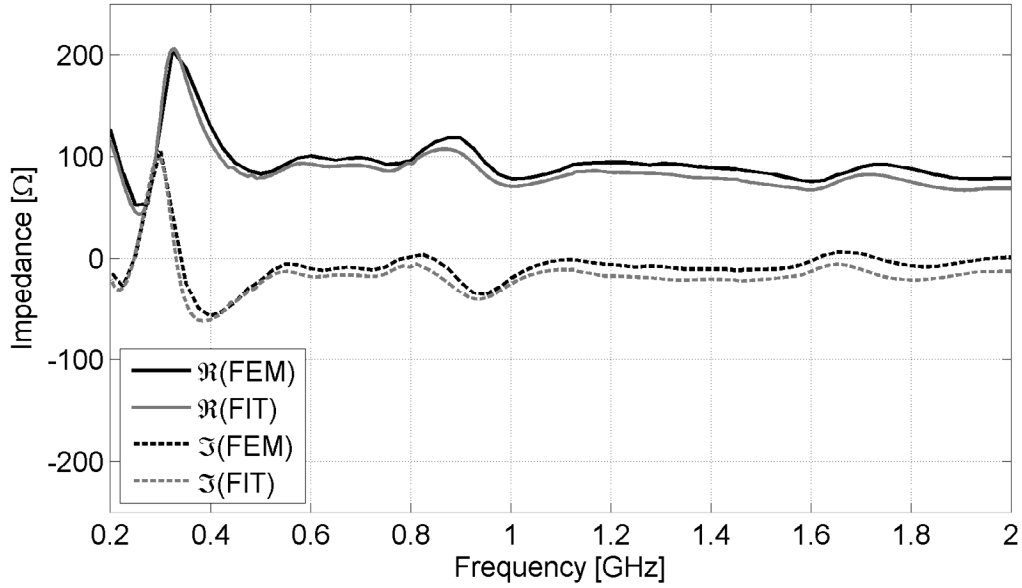
Figure 15: The bicone impedance computed using two different numerical techniques based on the finite element and finite integration methods.
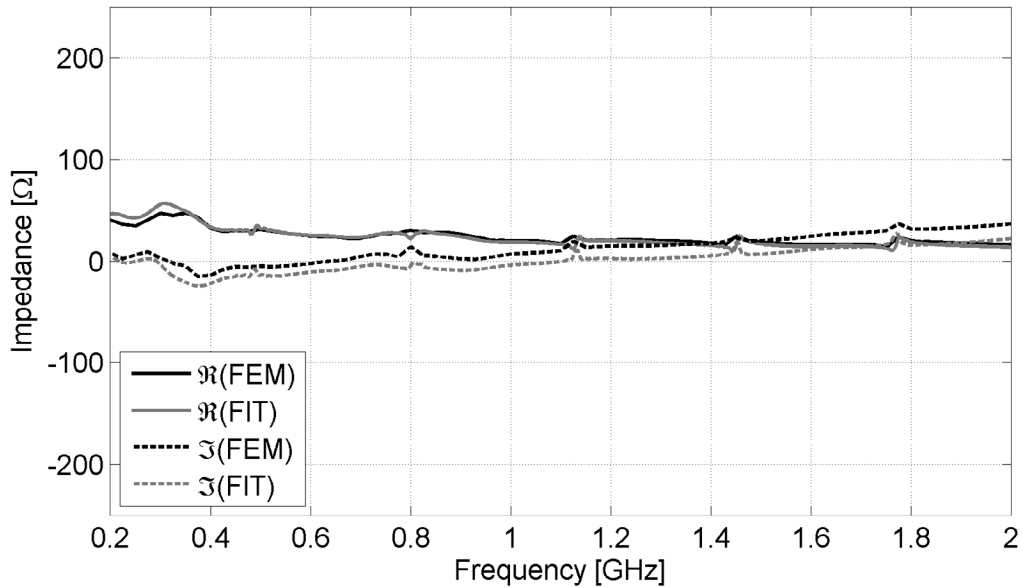
Figure 16: The monocone impedance computed using two different numerical techniques based on the finite element and finite integration methods.
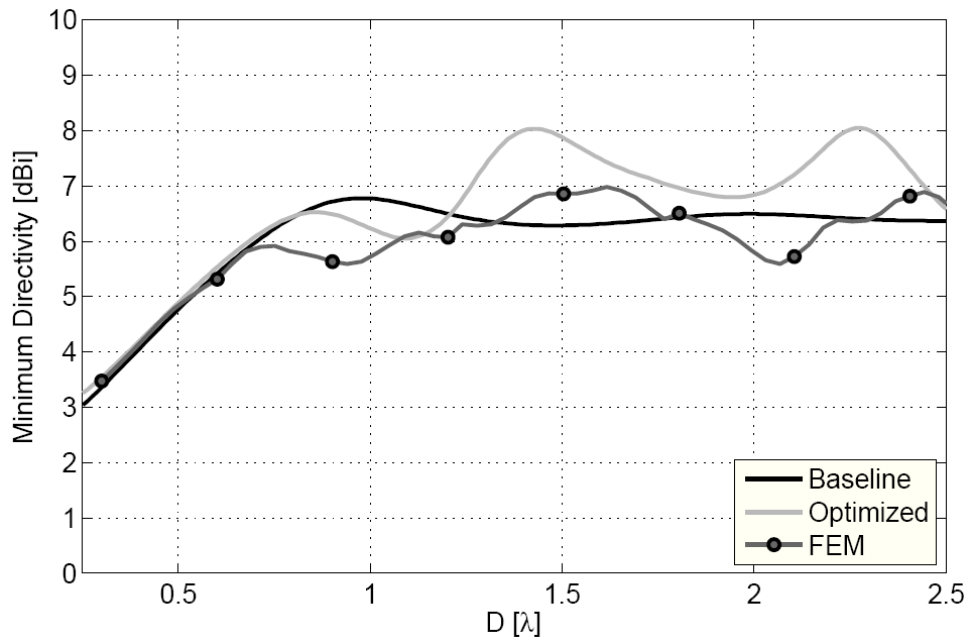
Figure 17: The FEM computed minimum directivity of the monocone-bicone array has different performance compared to the array optimized simulations.

Radiation patterns of the FEM modeled collinear array are shown in Figure 18. As can be seen the agreement between the optimized data and the modeled data is pretty good over the majority of the band. This is especially true near horizon. Additionally these patterns illustrate the broadband nature of the radiation patterns, for the baseline, optimized, and the numerically modeled designs.
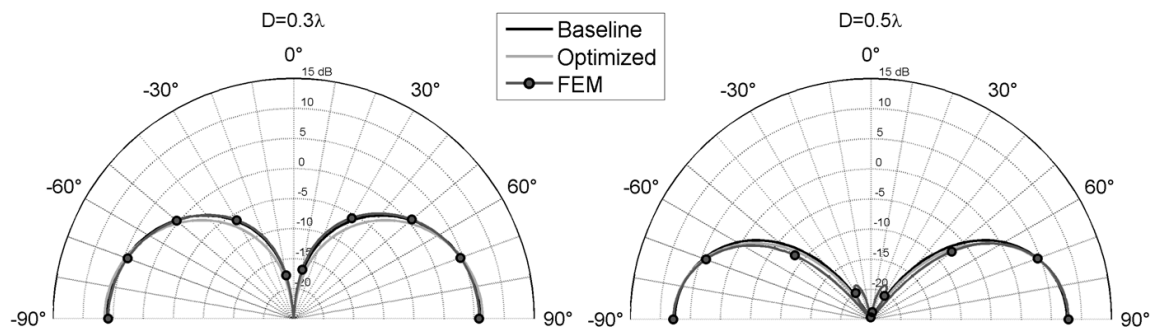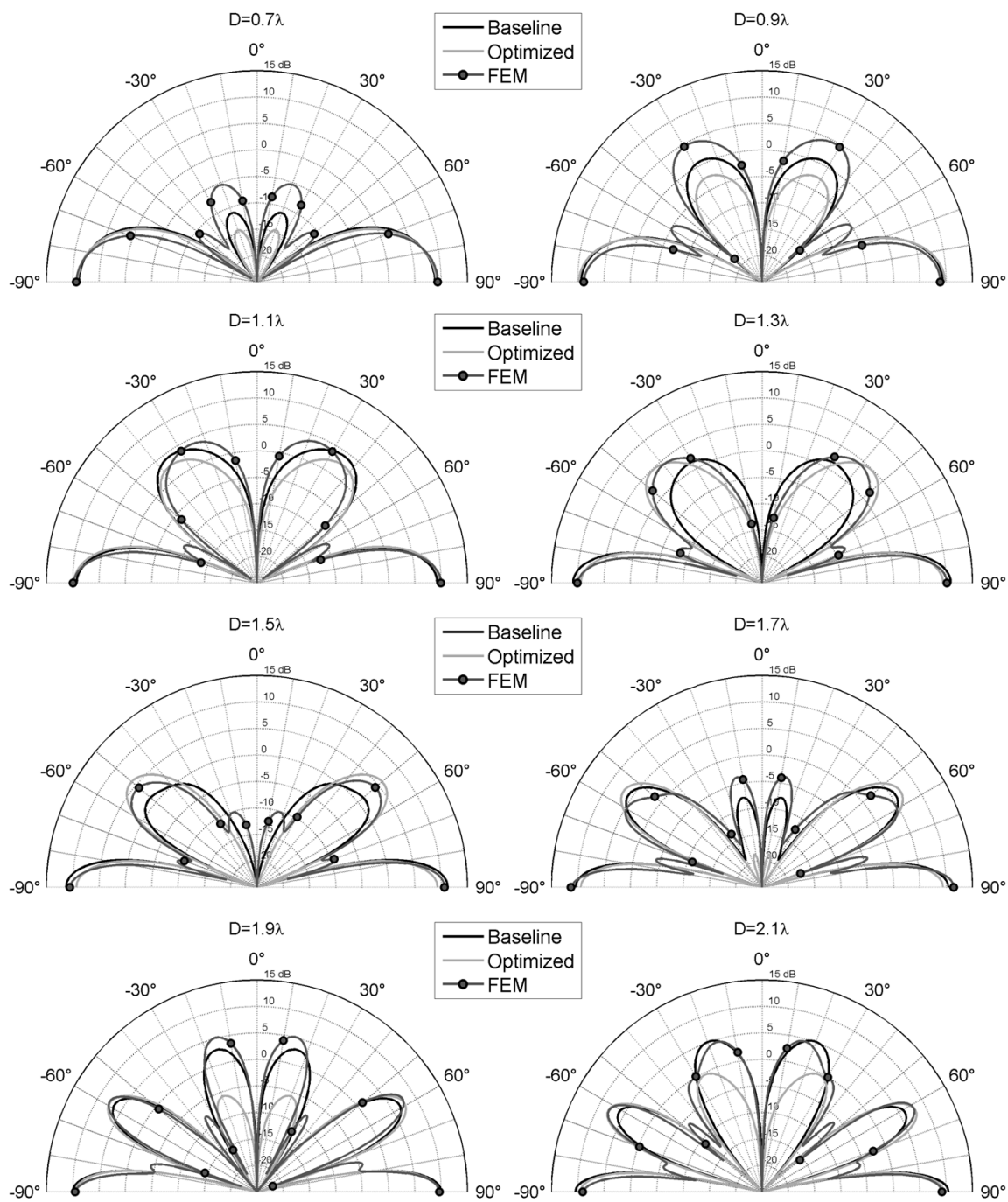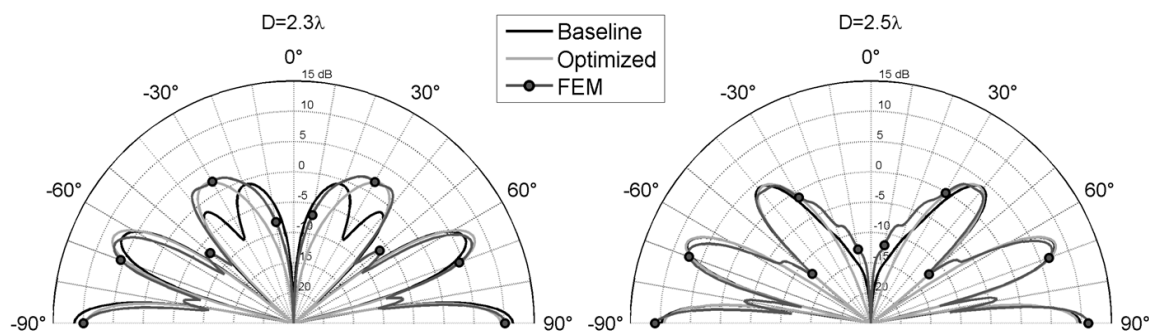
Figure 18: Radiation patterns at 12 different electrical separations illustrate broadband nature of the optimized radiation patterns.

4. Summary

A framework for determining the bandwidth has been established for a single monocone and for a monocone-bicone collinear array. This bandwidth framework utilizes a resonant monopole and a resonant monopole-dipole pair. Three separate cost functions or bandwidth definitions are proposed and computed. Bandwidth performances of over a 3.3:1 and 10:1 bands are demonstrated.

5. References

[1] R. Mangra, "Advancements in Traditional Broadband Antennas," in *4th Annual Military Antennas*. Washington, D.C.: IDGA, May 6-8, 2008.

[2] S. R. Best, "Performance Limits and Advances in the Design of Small Wideband Antennas," in *4th Annual Military Antennas*. Washington, D.C.: IDGA, May 6-8, 2008.

[3] O. J. Lodge, "Electric Telegraphy," U.S. Patent 609,154, August 16, 1898.

[4] J. S. Belrose, "A Radioscientist's Reaction to Marconi's First Transatlantic Wireless Experiment – Revisited," in *IEEE Antennas and Propagation Society International Symposium,* vol. 1, Boston, MA, July 8-13, 2001, pp. 22–25.

[5] P. S. Carter, "Wide band, short wave antenna and transmission line system," U.S. Patent 2,181,870, December 5, 1939.

[6] R. M. Bevensee, *Handbook of Conical Antennas and Scatterers*. New York: Gordon and Breach, Science Publishers, Inc., 1973, ch. 1.

[7] S. A. Schelkunoff, "Theory of Antennas of Arbitrary Size and Shape," *Proc. IRE*, vol. 29, pp. 493–521, September 1941.

[8] C. T. Tai, "Application of a Variational Principle to Biconical Antennas," *Journal of Applied Physics*, vol. 20, pp. 1076–1084, November 1949.

[9] C. H. Papas and R. W. P. King, "Input Impedance of Wide Angle Conical Antennas Fed by a Coaxial Line," *Proc. IRE*, vol. 37, pp. 1269–1271, November 1949.

[10] G. H. Brown and O. M. Woodward, Jr., "Experimentally Determined Radiation Characteristics of Conical and Triangular Antennas," *RCA Rev.*, vol. 13, no. 4, pp. 425–452, December 1952.

[11] J. R. Mautz and R. F. Harrington, "Radiation and Scattering from Bodies of Revolution," *Appl. Sci. Res.*, vol. 20, no. 1, pp. 405–435, January 1969.

[12] "IEEE Standard Definitions of Terms for Antennas," *IEEE Std. 145-1993*, pp. 6, 21 Jun 1993.

[13] Youngwook Kim; Keely, S.; Ghosh, J.; Hao Ling, "Application of Artificial Neural Networks to Broadband Antenna Design Based on a Parametric Frequency Model," *IEEE Transactions on Antennas and Propagation*, vol.55, no.3, pp. 669-674, March 2007.

[14] A. A. Eldek, "Ultrawideband Double Rhombus Antenna with Stable Radiation Patterns for Phased Array Applications," *IEEE Transactions on Antennas and Propagation*, vol.55, no.1, pp.84-91, January 2007.

[15] S.D. Rogers, C.M. Butler, A.Q. Martin, "Design and realization of GA-optimized wire monopole and matching network with 20:1 bandwidth," *IEEE Transactions on Antennas and Propagation*, vol.51, no.3, pp. 493-502, March 2003.

[16] J. L. McDonald and D. S. Filipovic, "On the Bandwidth of Monocone Antennas," *IEEE Transactions on Antennas and Propagation*, vol. 56, no. 4, pp. 1196–1201, April 2008.

[17] S. A. Schelkunoff and H. Friis, *Antennas: Theory and Practice*. New York: John Wiley and Sons, 1952.

[18] C. A. Balanis, *Antenna Theory: Analysis and Design*, 2nd edition New York: John Wiley and Sons, 1997.

[19] J. D. Kraus and R. J. Marhefka, *Antennas: for all Applications*, 3rd edition New York, NY: McGraw-Hill, 2002.

[20] D. Campbell, S. Fich, and F. Schwering, "Suppression of Parasitic Currents on Feed Lines of Colinear Dual Antenna Systems," *IEEE Transactions on Antennas and Propagation*, vol. 28, no. 5, pp. 658–662, September 1980.

[21] H. Bach, "Directivity of Basic Linear Arrays," *IEEE Transactions on Antennas and Propagation*, vol. 18, no. 1, pp. 107–110, January 1970.

[22] J.-F. Kiang, "Analysis of Linear Coaxial Antennas," *IEEE Transactions on Antennas and Propagation*, vol. 46, no. 5, pp. 636–642, May 1998.

[23] H. Miyashita, H. Ohmine, K. Nishizawa, S. Makino, and S. Urasaki, "Electromagnetically Coupled Coaxial Dipole Array Antenna," *IEEE Transactions on Antennas and Propagation*, vol. 47, no. 11, pp. 1716–1726, November 1999.

[24] G. B. Litchford, "Multi-lobe Omnidirectional Radio Navigation System," U.S. Patent 2,711,533, June, 1955.

[25] D. D. Button, W. D. Wyatt, and J. F. McGrath, "Stacked Biconical Omnidirectional Antenna," U.S. Patent 5,534,880, July 9, 1996.

[26] R. M. Honda and C. E. Rossman, "Collinear Coaxial Slot-Fed-Biconical Array Antenna," U.S. Patent 6,593,892, July 15, 2003.

[27] J. C. Bregains, F. Ares, and E. Moreno, "Variation in the Bandwidths of Pattern-Quality Parameters and Maximum Embedded Impedance Among the Solutions to Shaped-Beam Synthesis Problems for Collinear Dipole Arrays," *IEEE Antennas and Wireless Propagation Letters*, vol. 2, pp. 267–268, 2003.

[28] M. Kragalott, W. R. Pickles, and M. S. Kluskens, "Design of a 5:1 Bandwidth Stripline Notch Array from FDTD Analysis," *IEEE Transactions on Antennas and Propagation*, vol. 48, no. 11, pp. 1733–1741, November 2000.

[29] "FEKO Suite 5.3," EM Software and Systems (www.feko.info), 2007.

[30] D. R. Jones, M. Schonlau, and W. J. Welch, "Efficient Global Optimization of Expensive Black-Box Functions," *Journal of Global Optimization*, vol. 13, no. 4, pp. 455–492, Dec. 1998.

[31] J. Sacks, W. J. Welch, T. J. Mitchell, and H. P. Wynn, "Design and Analysis of Computer Experiments," *Statistical Science*, vol. 4, no. 4, pp. 409–423, Nov. 1989.

[32] H. L. Southall, T. H. O'Donnell, and B. Kaanta, "Efficient Global Optimization for Antenna Design," in *Proceedings of the 32nd Annual Antenna Applications Symposium*, Monticello, IL, Sep. 16-18, 2008, pp. 250–269.

[33] "HFSS version 11.1," Ansoft (www.ansoft.com), 2008.

[34] "Microwave Studio version 2009," Computer Simulation Technology (www.cst.com), 2009.

ON THE DESIGN OF A COMPACT AND LOW COST RADIATING ELEMENT FOR SATELLITE BROADCASTING AUTOMOTIVE RECEIVING ARRAYS

R. Torres-Sánchez[1], Juan R. Mosig[1], S. Vaccaro[2] and D. Llorens del Río[2]
[1] Laboratory of Electromagnetics and Acoustics (LEMA), Ecole Polytechnique Fédérale de Lausanne (EPFL), Switzerland, roberto.torres@epfl.ch
[2] JAST SA, PSE-EPFL Bat. C, CH-1015 Lausanne Switzerland, stefano.vaccaro@jast.ch

Abstract: In the domain of low profile phased arrays, printed circuit technology remains a very appealing solution for many consumer applications. In particular, vehicular antennas can take advantage of such streamlined geometries but at the expense of a high level of integration of the required functionalities into a complex multilayered structure. As a result, the array antenna elements must fulfill very stringent mechanical and dimensional constraints in addition to the already very demanding electromagnetic performance requirements. The present contribution is devoted to illustrate a novel approach to tackle such a challenging trade-off between available real state and required electromagnetic performance from the point of view of a radiating element conceived for a compact Ku band phased array with fully electronic beam steering and polarization pointing capabilities. The design procedure for this radiating element, the major constraints related to this design and a comparison between its theoretical electromagnetic performances and measurement results are included in this paper.

1. Introduction

The European Space Agency (ESA) is planning to re-allocate several of its satellites to broadcast telecom services (radio, TV, internet) in Ku-band to cars and other mobile targets. An adequate reception of satellite signals in cars imposes   stringent requirements in terms of performance, cost and aesthetics of the receiving antenna system. As a part of a huge coordinated effort, ESA has launched its project NATALIA (New Automotive Tracking Antenna for Low-cost Innovative Applications [1]) which aims to develop a low profile electronically steerable Ku-band phased antenna array with polarization tracking capabilities and with a size close to that of a Compact Disc. A typical application scenario is depicted in Fig. 1. A promising strategy to fulfill the array specifications is to consider a compact multilayered slot-fed patch antenna. Every patch antenna includes a dual-port access to provide polarization agility and constitutes the basic radiating element for the full array, which may include several hundreds of these elements.

293

This paper reviews the most recent improvements introduced in the basic brick of our array, the multilayer patch antenna. After sketching the current design procedure, some preliminary results are provided, fully characterizing the array element.
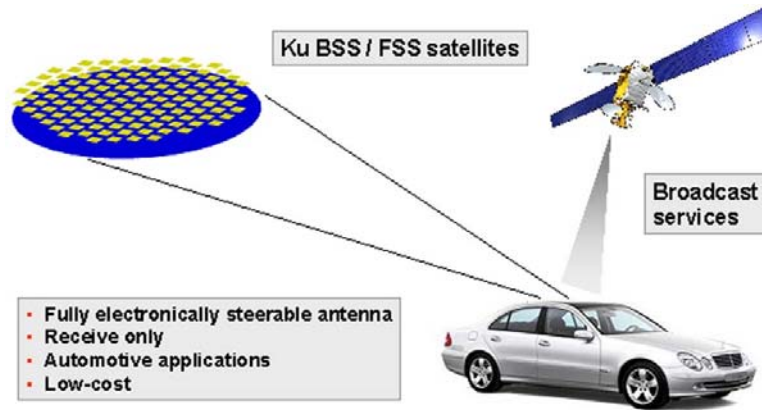
Fig. 1. NATALIA application scenario
(image courtesy of the NATALIA project team, after [2]).

2. Initial considerations

A preliminary design of the NATALIA radiating element, through which the proposed multilayer concept was conveniently assessed, has been already outlined in a previous paper [2]. Here, we upgrade the design with additional technical requirements, achieving a more mature implementation of a radiating element which is ready to be integrated in the first breadboard of the complete NATALIA array[1].

The foremost of these requirements is the size of the multilayered 'basic cell,' in which each radiating element must be integrated. The space assigned to this basic cell (roughly 8 x 12 mm^2) is mainly determined by the array grid design, but also by the existence in the levels below every radiating element of several beam-forming, active and logic circuits that might be needed for every application. In particular, one must look at the interconnections between the cells of the array that must frequently provide the adequate phase-shift characteristics. All this, together with some technological restrictions from the manufacturing processes, lead to a tight competition for real estate that must be addressed in all the three dimensions of the multilayer stack-up.

As expected, such competition has an impact on the electromagnetic performance of the radiating element and a trade-off must be reached. The new elements are more compact,

---

[1] More information is available online, through the following link:
https://documents.epfl.ch/users/t/to/torres/public/Allerton_AAS_Sep_2009_RJSD_draft_paper.pdf

but their performances should still match or improve those of the preliminary version [2]. In particular, a further reduction in the inter-element mutual coupling is strongly sought-after, to guarantee the global performances of the array. The radiating element presented in the following section is the result of these compromises.

3. New element design

The proposed radiating element is based in the patch antenna presented in [2] and depicted in Fig. 2. Let us start with a reminder of the initial architecture followed by some key design considerations.
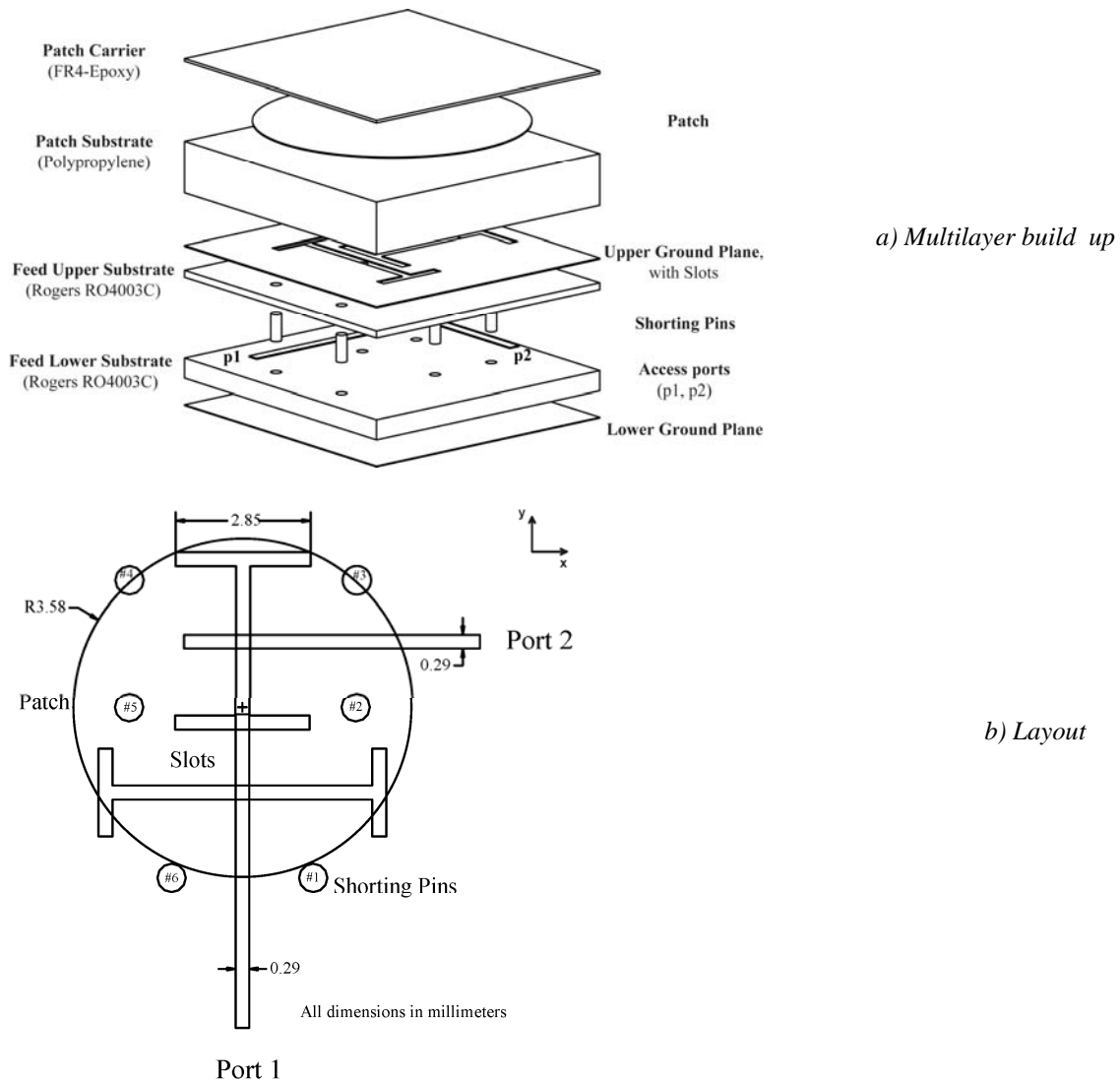

a) Multilayer build up

b) Layout

Fig. 2. Preliminary radiating element structure (from [2]).

The radiating element is an inverted microstrip patch antenna with dual linear polarization. The patch is fed by two striplines through a couple of narrow orthogonal apertures in the ground plane that lies between the lines and the patch [3-7]. The stripline technology has been selected to minimize the spurious radiation from the beam-forming network and additional elements electronics.

Fig. 2(a) shows a exploded view of the radiating element's basic multilayer structure. This build-up is composed by four metallization layers (the patch, the slotted ground plane, the feeding lines and a lower ground plane), three kinds of dielectric materials (epoxy, polypropylene and Rogers RO4003C™) and six metallic posts (shorting pins), which vertically cross part of the stack to connect both ground planes. The distribution of these shorting pins around the slots, together with the port assignment and some representative dimensions, are displayed in Fig. 2(b).

From these illustrations, it becomes evident that the role of the upper ground plane is to provide a convenient isolation between the radiation and the feeding sections of the radiating element, while the lower one prevents possible undesired interactions of the element with the phased array logic, which will be embedded in the lower part of the shared multilayer build-up.

However, the stripline-like feeding structure defined between these two ground planes requires special precautions. On the one hand, a proper coupling between the feeding lines and the patch through the slot must be ensured. On the other hand, the unavoidable power leakage due to parasitic modes propagating in the parallel plate waveguide associated to the stripline configuration must be mitigated as much as possible.

These two issues are addressed in the present design by the use of an asymmetric stripline, which improves the coupling between the feeding lines and the slots, and by carefully placing six metallic posts around the slots, which will short-circuit the most dangerous parallel plate waveguide mode [6].

On the basis of the above considerations, a new more refined design has been realized, exhibiting certain modifications of the layout of the radiating element, which were prompted by a more detailed definition of the antenna manufacturing processes, together with the fixation of some key parameters of the array logic to be integrated in the basic cell. This additional information, translated in terms of competition for real estate within the basic cell, allowed us to precise the nature and the magnitude of the adjustments to be performed in the radiating element design.

Basically, the real estate competition affects the distribution of the shorting pins around the slots, which are shifted closer to the slots and towards the center of the patch, and the slots themselves (especially those associated to port #1 in Fig. 2(b)), which had to be shifted and length-reduced.

These layout adjustments resulted in a significant degradation of the performance of the preliminary radiating element (mainly with regard to port #1) which can be attributed to a reduction of signal coupling between the corresponding feeding line and the patch.

Two ways for increasing the signal transferred to the patch were considered: either to increase the patch's substrate permittivity of the preliminary radiating element or to use a thinner substrate for the patch, bringing the patch closer to the slot [7,8,9].

The first option was discarded since it can lead to a potential increase of surface wave leakage and the subsequent lowering of radiation efficiency. The second option is, a priory, compatible with reduced levels of surface wave leakage, but it may result in a considerable bandwidth reduction, due to the overall volume reduction of the radiating element. Finally the second option was retained, but to compensate the bandwidth reduction a second resonator was stacked over that of the thinned radiating element. The final design is the stacked patches architecture illustrated in Fig. 3 [9,10].
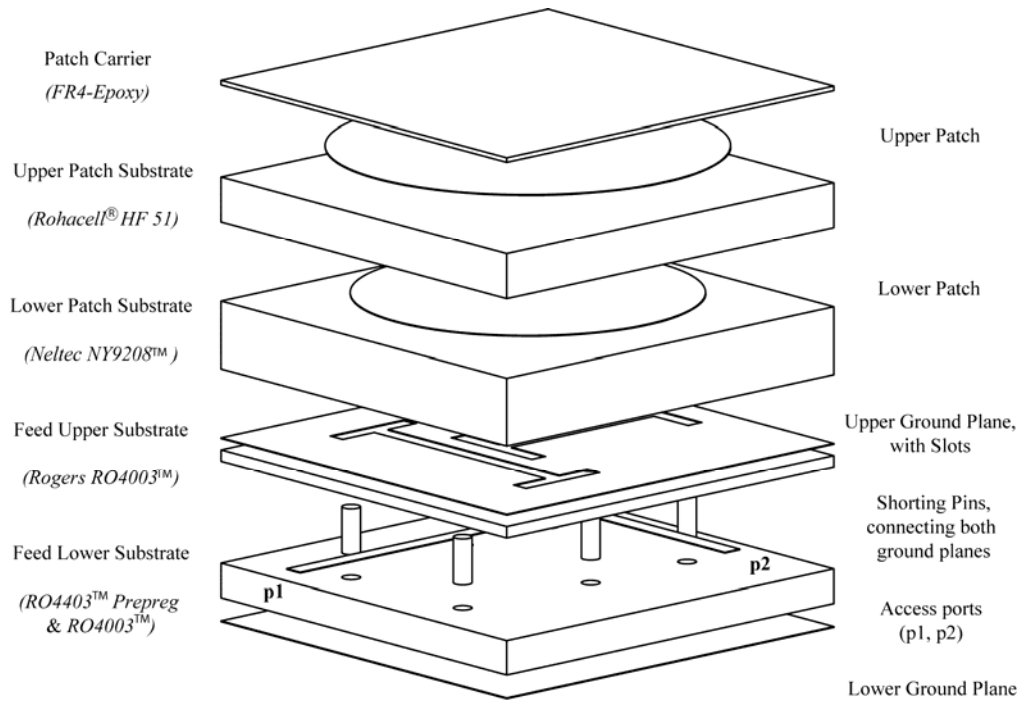
Fig. 3. Radiating element multilayer structure.

Thanks to the additional degrees of freedom provided by this stacked structure, the original performances achieved with the original radiating element [2] were maintained or even improved, while meeting the new real estate restrictions.

Finally, the patches were miniaturized by slitting their perimeter (see Fig. 4). This strategy was applied to both patches (as shown in the optimized layout of Fig. 5) in order to reach the desired reduction of the inter-element mutual coupling, without noticeably degrading the remaining performance parameters. These facts will be clearly quantified in the next section.
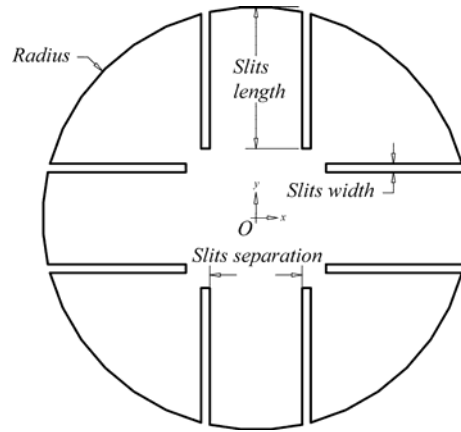
Fig. 4. Slitted patch layout.
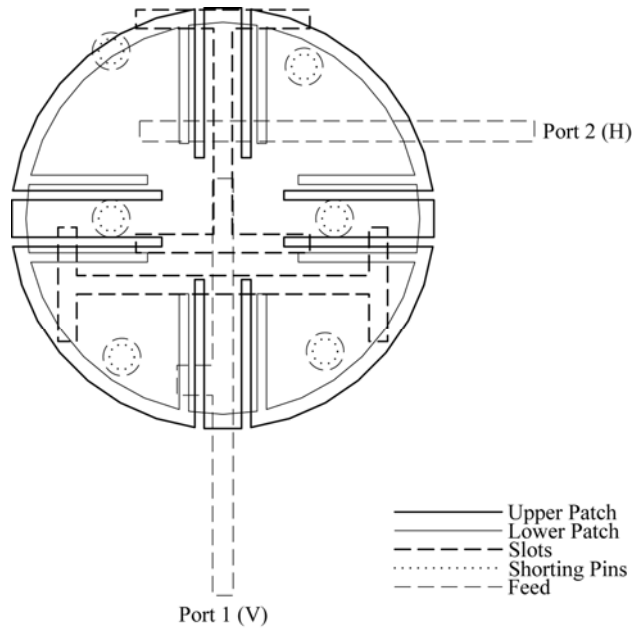
Fig. 5.   Radiating element final layout.

4. Preliminary results

The electromagnetic modeling of the new radiating element has been performed with two different full wave commercial simulation tools (Ansoft's Designer and HFSS). A very good agreement between their predictions was observed and this provided us with a strong confidence on the expected performances of the element. With proper impedance matching ($|S_{ii}| \leq$ -11.6 dB between 10.7 GHz and 12.75 GHz, $|S_{ii}| \leq$ -10 dB over a relative bandwidth of 21%), and with port decoupling better than 30 dB, the performance of the new radiating element matches or improves that of the preliminary one.

Moreover, the simulations also show good levels of radiation efficiency (over 66%), symmetry of the radiation diagrams, good polarization purity (with a crosspolar component 18 dB below the broadside copolar level) and convenient directivity values (between 7.5 dB and 8.2 dB) over the whole frequency band of interest (10.7-12.7 GHz).

In addition, this design shows a clear improvement in terms of inter-element mutual coupling, with a reduction of almost 1 dB (-16.9 dB versus -17.8 dB, maximum levels in the frequency band for an unchanged spacing of 0.54λ).

Another fundamental issue is the sensitivity to the manufacturing tolerances of the radiating element's performances, evaluated in terms of scattering parameters and radiation patterns.

In this study, we have included the tolerances which refer to the alignment between the different metallization layers that compose the stack-up of the radiating element ($\pm 37.5\mu m$), their etching ($\pm 10\mu m$) and the permittivity and the thickness of the dielectric materials. The later are summarized in Tables 1 and 2.

	ε_r	$\Delta\varepsilon_r$	Source
FR4-Epoxy	4.4	$\pm 10\%$	Estimation
Rohacell® HF51	1.07	$\pm 10\%$ *	Estimation
Neltec NY9208(IM)™	2.08	$\pm 0.96\%$	Catalog
3M™ 300LSE	2.8	$\pm 10\%$	Estimation
Rogers Prepreg RO4403™	3.17	$\pm 10\%$	Bibliography
RO4003™	3.55	$\pm 1.5\%$	Catalog

*with $\varepsilon_r \geq 1$

Table 1.   Dielectric permittivity tolerances.

	Δt	Source
FR4-Epoxy	±10%	Estimation
Rohacell® HF51	±10%	Estimation
Neltec NY9208(IM)™	±10%	Estimation
3M™ 300LSE	±10%	Estimation
Rogers Prepreg RO4403™	±10%	Estimation
RO4003™ (*Upper Feed Substrate*)	±12.5%	Catalog
RO4003™ (*Lower Feed Substrate*)	±6.25%	Catalog

Table 2.   Dielectric layer thickness tolerances.

From the evaluation of the impact of these tolerances on the scattering parameters of the radiating element, it has been found that, as expected, the most critical parameters are the permittivity and thickness of the dielectric substrates, especially of those holding the patches. Although this study did not reveal any abnormally high sensitivity, our estimations on the dielectric thickness tolerances in Table 2 are probably too pessimistic.

A study of the effect of permittivity tolerances on port input matching and port coupling is displayed in Figs. 5 and 6, respectively. These figures show only small deviations from the nominal design. Hence, our design is proven to be robust, the performance of the element not suffering any significant degradation.

(a) Impedance matching. *Port #1*

(b) Impedance matching. *Port #2*

(c) Input impedance. *Port #1*

(d) Input impedance. *Port #2*
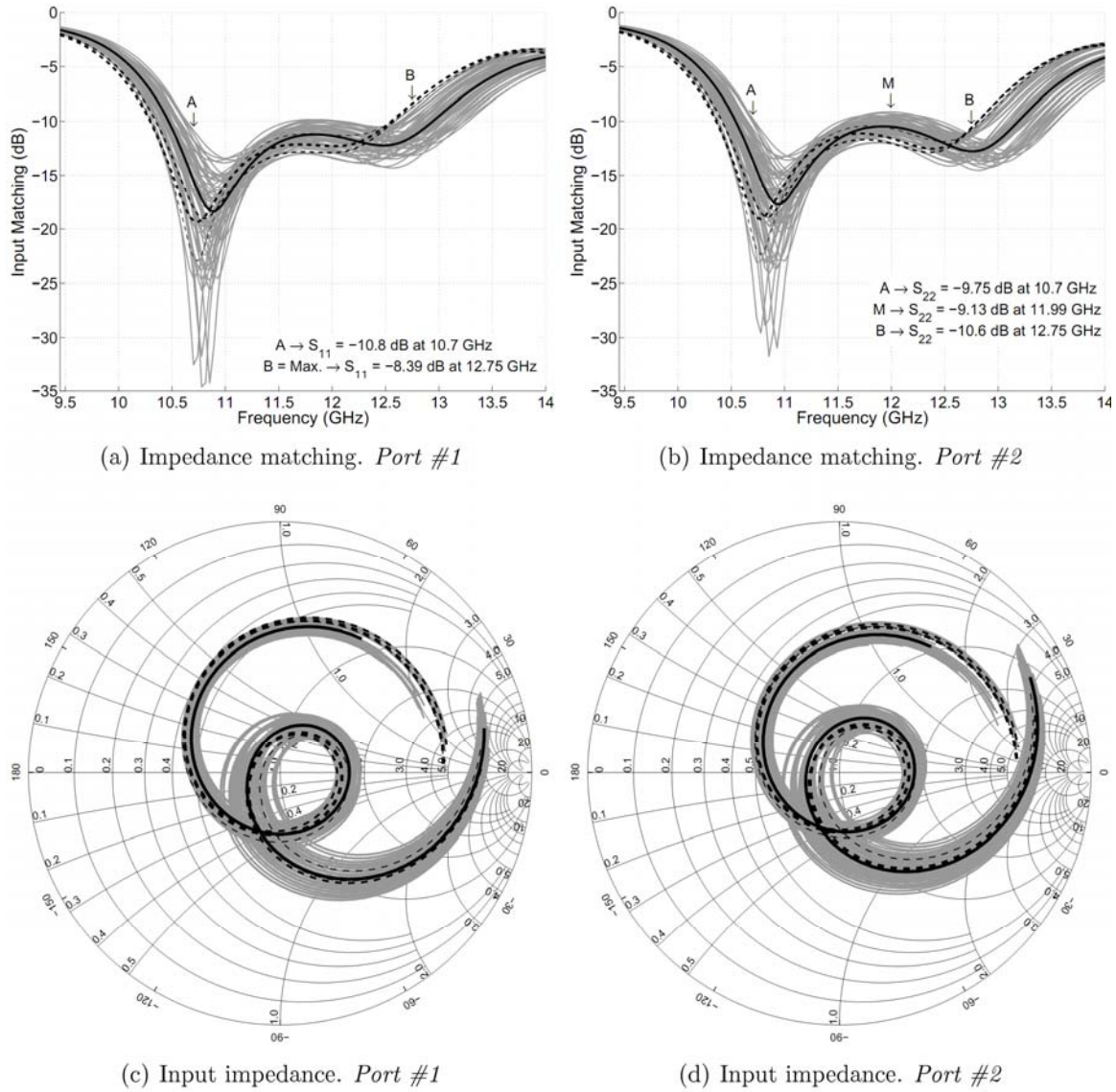
Fig. 5.   Calculated reflection coefficients in the two ports of the radiating element (Z_0=50Ω). The nominal curves (in continuous black line), those obtained for different values of the parameters subject to manufacturing tolerances (in continuous grey line) and the three cases with worst impedance matching levels (in dashed black line) are displayed superimposed. Here, only the substrate permittivity is considered subject to tolerance.
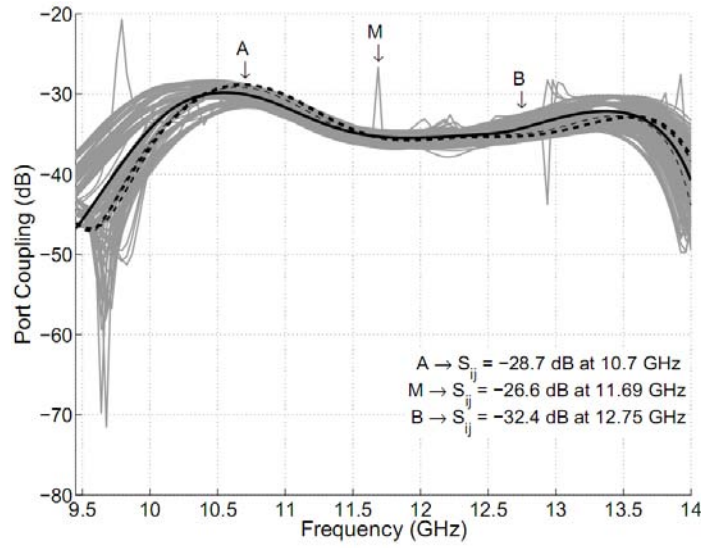
Fig. 6. *Calculated coupling between the two ports of the radiating element. The nominal curves (in continuous black line), those obtained for different values of the parameters subject to manufacturing tolerances (in continuous grey line) and the three cases with worst impedance matching levels (in dashed black line) are displayed superimposed. Here, only the substrate permittivity is considered subject to tolerance.*

With regard to the radiation diagram of the element and even though this study is carried out considering simultaneously all the manufacturing tolerances described above (dielectric thickness tolerances included), the impact of the manufacturing tolerances is found to be small and it is observable, mainly, in the level of the cross-polar component, while the variations in the shape and level of the copolar components are very limited. This behavior is illustrated in Figs. 7 and 8, which confirm that it is only in the crosspolar component that relatively significant variations may take place. However, in all cases, the maximum crosspolar level within the scan domain of the projected array (360° in azimut and from 20° to 70° in elevation) remains below -15 dB.

Fig. 8 reveals a shift of the optimum polarization purity levels towards the upper side of the operating frequency band. A similar shift is also observable in the impedance matching plots of Figs. 5(a-b), as well as in other antenna parameters. These shifts reveal the performance compromise made during the design of the patches of the radiating element, since the inter-element mutual coupling reduction was achieved through a miniaturization of the patches, which makes the element prone to operate better at higher frequencies.
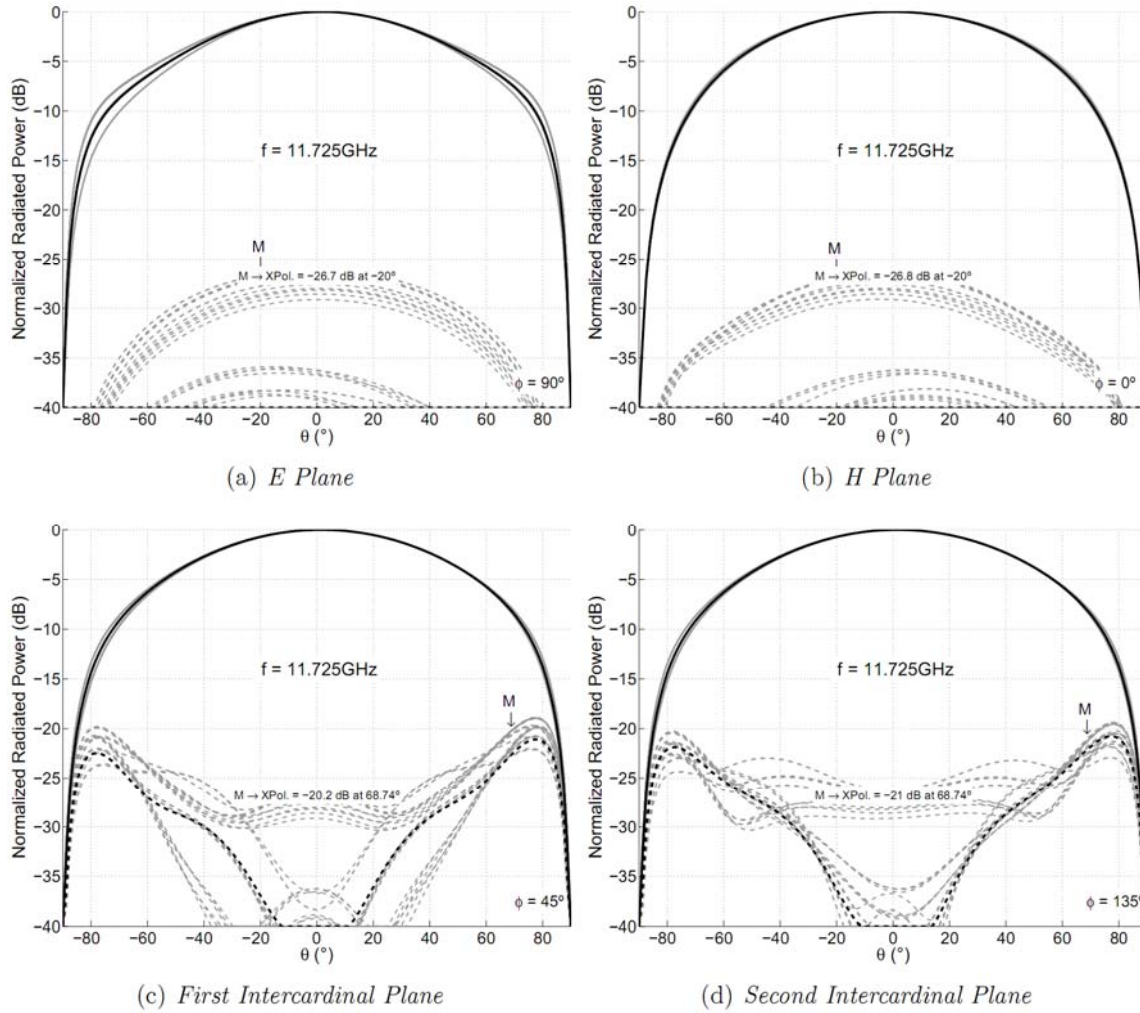
Fig. 7. *Calculated elevation cuts of the radiation diagram corresponding to Port #1 at the central frequency of the band (for the others frequencies within the band as well as for Port #2, the results are very similar). The copolar and crosspolar components correspond to Ludwig's third definition [11] and are plotted in continuous and dashed line, respectively. The nominal radiation diagram (in black) and those obtained for different values of the parameters subject to manufacturing tolerances (in grey) are displayed superimposed. Here, all the parameters are considered subject to tolerance.*

(a) Port 1   (b) Port 2
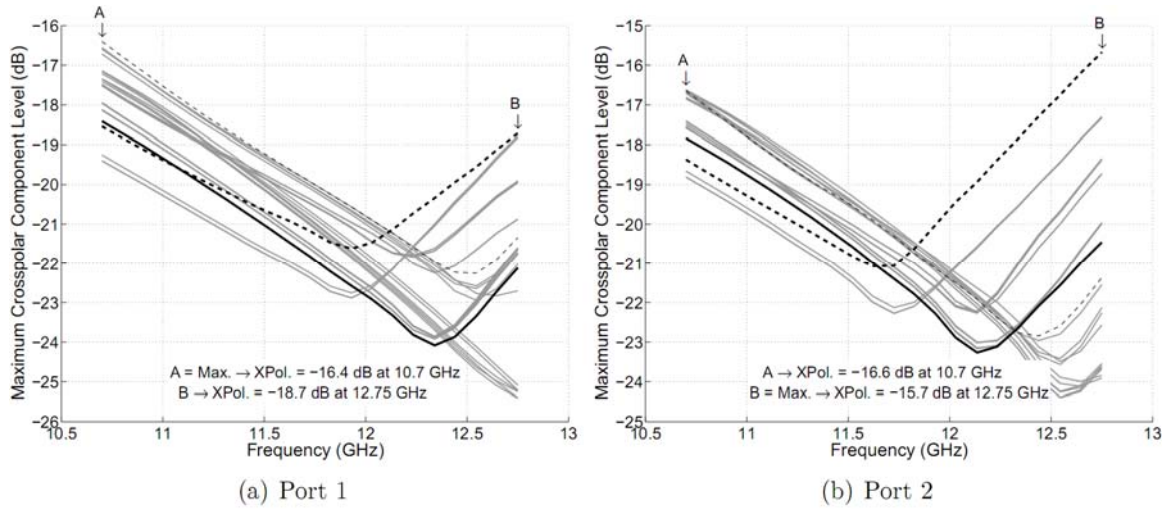
Fig. 8. *Calculated maximum levels of the crosspolar components (Ludwig's third definition [11]) in the scan domain corresponding to Ports #1 and #2 over the frequency band of interest. The nominal levels (in continuous black line), those obtained for different values of the parameters subject to manufacturing tolerances (in continuous grey line) and the cases with worst cross-polarization levels (in dashed black line) are displayed superimposed. Here, all the parameters are considered subject to tolerance.*

Finally, Fig. 9 gives an illustration of one of the manufactured prototypes. In these prototypes, special connectors and microwave transitions are employed to access the stripline ports of the radiating element, which are embedded in the final multilayer stack-up of the active array antenna. It is worth noticing the very narrow slits, present although barely visible in the picture.
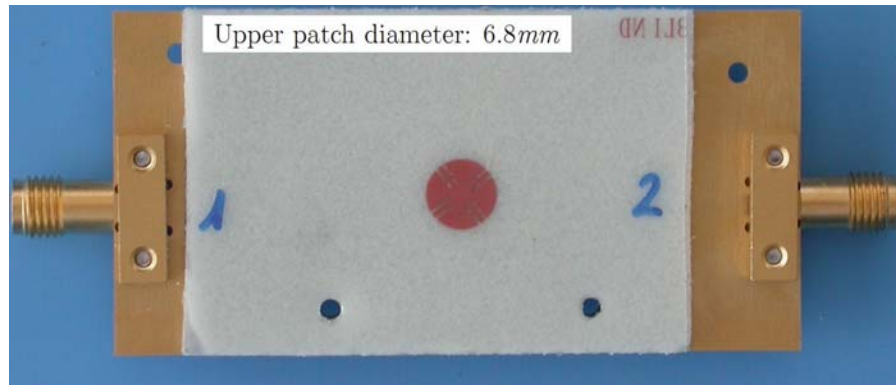
Fig. 9. *Photograph of a manufactured sample.*

5. Conclusion

In this paper, an improved and mature design of a basic radiating element for low cost automotive planar antenna arrays receiving satellite broadcasting in the Ku-band has been presented. With respect to previously existing designs, this element represents a significant evolution in terms of predicted performances while matching new more stringent real estate requirements and being fully compatible for integration within to foreseen active phased arrays.
The presented results validate the introduced improvements and in particular the concept of asymmetric stripline feeding. Definitive measurements of the radiating element and additional information about the planar array will be presented at the symposium.

6. Acknowledgements

7. References

[1]   R. Baggen, S. Vaccaro, D. Llorens del Río, "Design Considerations for Compact Mobile Ku-Band Satellite Terminals", presented at II European Conference on Antennas and Propagation, EuCAP 2007. Edinburgh, UK, November 2007.
[2]   R. Torres-Sánchez, S. Vaccaro, and J. R. Mosig, "A compact and low cost radiating element for automotive satellite broadcasting reception arrays" presented at 30th ESA Antenna Workshop for Earth Observation, Science, Telecommunication and Navigation Space Missions, ESA/ESTEC, Noordwijk, The Netherlands, May 2008. [Online]. Available:
https://documents.epfl.ch/users/t/to/torres/public/ESA_Workshop_Paper_May_08.pdf
[3]   D. M. Pozar, "Microstrip antenna aperture-coupled to a microstripline", Electron. Lett., vol. 21, no. 2, pp. 49–50, January 1985.
[4]   J.-F. Zürcher, "The SSFIP: A global concept for high performance broadband planar antennas", Electron. Lett., vol. 24, no. 23, pp. 1433–1435, November 1988.
[5]   D. M. Pozar and S. D. Targonski, "Improved coupling for aperture-coupled microstrip antennas", Electron. Lett., vol. 27, no. 13, pp. 1129–1131, June 1991.

[6] P. Brachat and J. M. Baracco, "Dual-polarization slot-coupled printed antennas fed by stripline", IEEE Trans. Antennas Propagat., vol. 43, no. 7, pp. 738–742, July 1995.

[7] P. L. Sullivan and D. H. Schaubert, "Analysis of an aperture coupled microstrip antenna", IEEE Trans. Antennas Propagat., vol. AP-34, no. 8, pp. 977–984, August 1986.

[8] R. Torres-Sánchez, " Two beam printed antenna array for satellite reception", Master Thesis (in Spanish), Escuela Técnica Superior de Ingenieros de Telecomunicación. University of Málaga. Spain, March 2006. [Online]. Available: https://documents.epfl.ch/users/t/to/torres/public/PFC_Roberto_Torres_2006.pdf

[9] J.-F. Zürcher and F. E. Gardiol, Broadband patch antennas. Boston: Artech House, 1995.

[10] S. D. Targonski, R. Waterhouse, and D. M. Pozar, "Design of wide-band aperture-stacked patch microstrip antennas", IEEE Trans. Antennas Propagat., vol. 46, no. 5, pp. 1245–1251, September 1998.

[11] A. C. Ludwig, "The definition of cross polarization", IEEE Trans. Antennas Propagat., vol. AP-21, pp. 116–119, Jan. 1973.

Army SATCOM On-The-Move Initiatives

Herald Beljour, Louis Coryell, Tat Fung, Jim Gallagher,
Rich Hoffmann, Gerald Michael and Joseph Shields

US Army CERDEC S&TCD, Fort Monmouth, NJ and Aberdeen Proving Ground, MD

Abstract

The Army is increasingly reliant on Beyond Line of Sight (BLOS) communications due to a non-contiguous battlefield. The Warfighter also requires mobility and network connectivity to provide the needed level of near real-time, tactically-relevant information. On-the-move (OTM) space based communications forms a critical layer in supporting these essential networking capabilities.

There are a significant number of inter-related technical hurdles involved in developing satellite communications (SATCOM) OTM systems. Size, weight, and power (SWaP) are limited on tactical vehicles. There are many tactical vehicles in the Army inventory, used differently by different units, representing diverse integration issues and challenges. Required data rates need to be supported within size and power restrictions, driving higher antenna and radio frequency (RF) performance. Ground communications are required in a high velocity, high acceleration, high blockage, cross country environment, driving rigorous pointing requirements. Systems need to be designed to work with current and planned military satellites in their respective frequency bands, which typically drives state-of-the-art. Electronic jamming protection and extremely low profile need to be considered in order to maintain communications and avoid visual targeting of the host tactical vehicle.

Space and Terrestrial Communications Directorate (STCD) Space Systems Division has been analyzing and addressing the technology to support required satellite communications (SATCOM) OTM system performance. Successful research and develop initiatives will be discussed, as well as planned initiatives to support future efforts addressing advanced requirements and future Military SATCOM systems at Extremely High Frequency (EHF). Specific component technologies and how they fit into meeting overall system objectives will be included. Lastly, the transition of these technologies to the tactical Army will be addressed.

1. Technical Hurdles

There are a significant number of inter-related technical hurdles involved in developing satellite communications (SATCOM) OTM systems.

Ground communications are required in a harsh, high velocity, high acceleration, high blockage, cross country environment, driving rigorous pointing requirements. The currently applicable standard for the Army cross country environment is the Churchville B course located at the Aberdeen Proving Ground, MD. This requires accommodating angular accelerations typically on the order of 500 deg/sec^2. Table 1 shows maximum angular accelerations and velocities measured around three axes (z down, x forward, y right). This data represents one test series for different courses at APG [1].

Vehicle	Course	Maximum |Angular Velocity| (deg/s)			Maximum |Angular Accel| (deg/s^2)		
		x	y	z	x	y	z
M1113 HMMWV	Churchville B	14.8	76.6	32.6	209.4	568.7	76.3
	Perryman 3	27.5	57.5	23.7	237.5	397.1	96.5
	Belgian Block	30.0	30.6	22.1	441.2	414.5	115.8
M1152 HMMWV	Churchville B	14.5	37.9	31.8	182.3	301.6	100.0
	Perryman 3	46.8	58.2	22.5	504.1	407.3	131.0
	Belgian Block	39.9	31.4	20.9	598.4	394.1	135.5
	Imbedded Rock	16.2	19.8	11.8	301.8	353.0	166.6

Table 1. Maximum Angular Velocities and Accelerations.

Antenna beamwidth, driven by performance requirements, also impacts pointing requirements. Tactical Army systems typically require SATCOM OTM data rates of 512 kbps. As antenna gain is increased to support required rates, beamwidth decreases and pointing requirements become more demanding. Vehicle characteristics also contribute to pointing requirements because accelerations experienced by the SATCOM OTM system are dependent on the location on the vehicle and vehicle characteristics such as suspension stiffness. Pointing requirements drive system components, such as Inertial Navigation System (INS) accuracy and azimuth/elevation motor size for mechanical SATCOM OTM systems. This creates a performance vs. size, weight, and power (SWaP) challenge on tactical vehicles. This issue is compounded if unique military frequency bands or multiple frequency bands need to be supported. The Wideband Global System (WGS) satellite constellation, which operates at X and K/Ka bands, is a current focus for SATCOM OTM systems, as is the K/Q band to support protected OTM operation on the Advanced Extremely High Frequency (AEHF) constellation.

Maximizing antenna performance within available SWaP makes cooling a significant issue. SATCOM OTM systems are required to be covered in a radome, restricting air flow. One potential or partial solution is increasing the power added efficiency of the

power amplifier, typically the major heat contributor. Increasing efficiency decreases heat required to be dissipated. This drives state of the art, especially at military frequency bands, and can increase cost. Additionally, novel cooling approaches such as liquid cooled systems are being explored to minimize complexity and cost.

The high blockage cross country environment also drives the type of tracking required for SATCOM OTM systems. Closed loop tracking in at-the-halt (ATH) SATCOM systems is generally implemented when the beamwidth is small compared to satellite motion. Closed loop allows the use of continual updates from a receive signal or beacon to modify the positioning of the ground antenna boresight. However, blockages encountered while OTM disrupt and skew the closed loop process. Approaches such as open loop pointing with periodic closed loop updates and carefully designed algorithms to deal with the contingencies of an OTM system have been investigated. Specific solutions and selection of closed/open/hybrid approaches require trading performance versus cost for a given system. In the case of specialized SATCOM systems, such as frequency hopping systems, feedback from the modem may be required in order to provide closed loop updates. All of this contributes to the complexity of SATCOM OTM systems. Figure 1 shows the interactions of some of the relevant SATCOM OTM trade characteristics and requirements. For example, severity of pointing requirements will drive SWaP and cost by affecting the accuracy of the Inertial Navigation System (INS) required and motor sizes for mechanical antenna implementations.
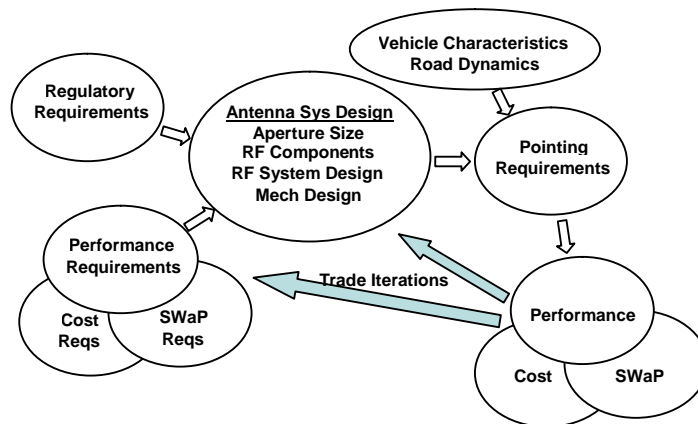
Figure 1. SATCOM OTM Characteristics/Requirements Interaction

All of these issues and complexities driven by OTM requirements can drive cost. Particular cost drivers include pointing, frequency bands, and reduced SWaP requirements. Cost needs to be considered as a trade parameter during design.

2. Early Phased Array Efforts

2.1. Nomad/Bronco.

Efforts in on-the-move satellite communications began in the mid 1990s when two Harris phased array antenna systems were inherited from another Government agency. The first system, named Nomad, was a C and S band (1.75 to 6.5 GHz) system of 5ea ~40 inch square phased array panels arranged in a cube on a trailer. They used coherent combining to achieve a constant G/T and EIRP over their hemispherical coverage. The system had three independent receive beams and a single transmit beam. A $5M effort ensued to develop a VME based on-the-move controller for this system. The resulting system was renamed Bronco with the panels separated and mounted on the sides and top of a HMMWV (Figure 2). This was the first Army SATCOM On-The-Move antenna system, first demonstrated in February of 1995 at the Harris facility.

Figure 2. Bronco Phased Array Antenna System

2.2. Juniper.

The second system, Juniper, was a 7-11 GHz dual beam transmit and receive phased array antenna system (figure 3). Juniper was demonstrated at the Joint Warfighter Interoperability Demonstration (JWID) at Ft. Gordon, GA in September of 1995. A 128 Kb/s compressed video signal was received from a simulated UAV, sent to Fort Monmouth via a DSCS satellite, looped and received on the second beam via the same DSCS satellite.

Figure 3. Juniper X-Band Phased Arrays

2.3. Radio Access Point.

With the success of the Bronco and Juniper efforts it was decided to develop a complete On-The-Move X-Band antenna system. The Radio Access Point (RAP) utilized the on-the-move controller from Bronco and the X-Band arrays from Juniper. Two sets of transmit and receive phased array panels were fabricated, each utilizing half of the elements from the cannibalized Juniper system (figure 4

Figure 4. Radio Access Point Antenna System.

The RAP antenna system had two problems: (1) it cost over $500K per system and (2) it was based on obsolete technology developed for Juniper during the early 1990s. Transmit and receive modules were failing and the controller parts were no longer available.

2.4. Dual Use Antenna Program (DUAP).

A new effort was planned to make affordable arrays with the performance of the RAP arrays, a seemingly impossible task at the time. The Harris corporation won this effort for a Dual Use Antenna Program on a 50/50 cost sharing basis. The idea was to use

discrete devices (no costly transmitter and receiver modules or MMIC amplifiers) on a printed wiring board. The entire Government and Contractor design team took a week long course in Integrated Product and Process Development to learn how to do the trade studies required to design affordability into the design. The effort, started in October 1998 ended in success in October of 2002. Not only did the team develop affordable planar transmit and receive arrays (figure 5), but they also developed a low cost PC-104 controller to replace the costly VME controller. The effort did have its challenges. The receive printed wiring board took almost a year to layout and check all 15 layers manually. With the advent of CAD software, the transmit board subsequently only took a month for layout and checking. Board assembly using automated pick and place took only 20 minutes. The estimated production system cost was <$50K in 100 ea quantities [3].
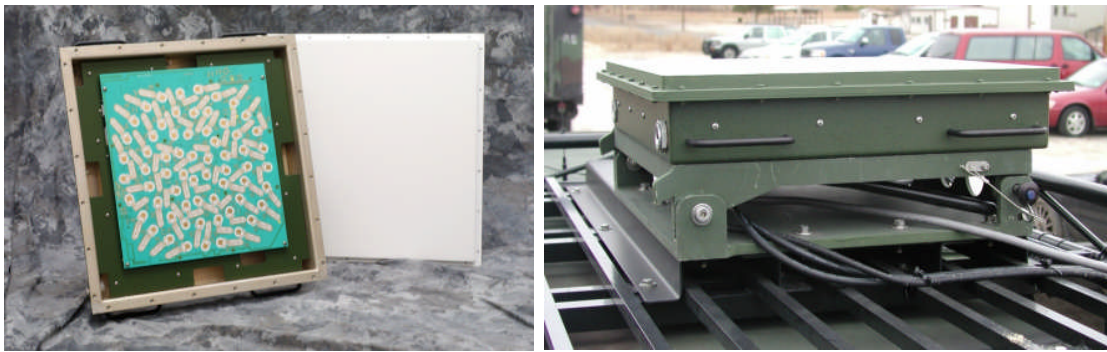
Figure 5. Harris Dual Use Antenna Program X-Band Phased Array.

A major problem presented itself when it became apparent that the use of current X-Band DSCS satellites would not be possible due to their constant use. We were informed by Program Manager Warfighter Information Networks – Tactical (PM WIN-T) that all on-the-move SATCOM initiatives would need to be conducted in K/Ka bands of the planned Wideband Gapfiller Satellites. Could we replicate our X-Band success at K/Ka bands?

2.5. Dual Use Science & Technology Program (DUST).

Buoyed by our success at X-Band we embarked on a new 50/50 cost sharing program with Harris for K/Ka-Band arrays. The initial problem was that the arrays would need substantially higher EIRP (48 dBW vs 34 dBW) and G/T (12 dB/K vs 4 dB/K) than any arrays we had fabricated previously. This would lead to higher size, weight and power consumption (SWaP). The size of each array ballooned to a nominal 40 inches on a side and 11-13 inches high. The height was required by the air-air heat exchangers (the arrays themselves were only 4 inches high). Power consumption was over 2 KW due to the dissipation of the power amplifiers and the >1350 low noise amplifiers, each drawing 0.3 watts. The arrays weighed 160 to 210 pounds, largely due to the heat exchangers [4].

Finally, there were phase shifter issues. There were no production 30 GHz MMIC phase shifters at the time. The decision was made to utilize ferroelectric phase shifters for both the receive and transmit arrays. These phase shifters were the subject of a new manufacturing technology program. Their loss was only 6 dB while the switching speed was less than 1 microsecond. The completed arrays were delivered in June of 2005 (figure 6). The estimated production cost for the arrays was almost $400K, far from our goal of less than $200K. The cost was driven primarily by the power amplifiers low noise amplifiers and associated packaging. At $10 each, the ferroelectric phase shifters did not substantially drive the cost of the arrays.

Figure 6. K/Ka-Band Phased Arrays

The determination was made to suspend all phased array work until we could address the aspects of array design that led to the problems with the K/Ka arrays. The first area to be addressed would be high efficiency power amplifiers, the second high efficiency low noise amplifiers, the third additional development and testing of the ferroelectric phase shifters and MEMS phase shifters under our manufacturing technology program and lastly advanced cooling techniques. The resulting development programs in these areas will be discussed in Section 7. PM WIN-T indicated that any antenna to be transitioned to their office would need to be 30 inches on a side, maximum due to vehicle constraints. Power consumption would need to be less than 1200 watts, also due to vehicle constraints. This pushed us to look for a new solution to providing communications on-the-move for the tactical Warfighter.

3. The Move to Dish Antennas

3.1. EHF/MILSTAR On-the-Move.

An initial effort to develop and demonstrate an on-the-move terminal based on the Milstar Low Data Rate (LDR) waveform met all of the technical hurdles described in Section 1. The 44 GHz uplink frequency and a 12" antenna gave a tight pointing accuracy requirement while avoiding potential regulatory issues. Initial analysis of the baseband issues was examined in detail by MIT Lincoln Laboratory (MIT-LL) [5]. The Extremely High Frequency (EHF) OTM antenna was built by Harris Corporation, with

some radio frequency components from MIT-LL. This was a three-axis antenna, out of concern for the "keyhole" problem, where OTM pointing for a two axis antenna at zenith requires impossibly high angular accelerations. The Milstar OTM terminal (shown in Figure 7) was used in a number of experiments to investigate timing, protocol and blockage issues in a number of environments [6,7,8,9]. A demonstration of the terminal at Fort Monmouth, NJ in June 2002 proved to the community that EHF SATCOM OTM was technically feasible.

Figure 7. Milstar On-the-Move Vehicle

3.2. Ka On The Move Antenna System.

Based on this success, STCD and PM Warfighter Information Network – Tactical (WIN-T) partnered to develop a Ka-band OTM antenna for use on the Wideband Global SATCOM (WGS) constellation to provide an OTM capability for PM WIN-T's Ka-Band SATCOM Augmentation Terminal (KaSAT) terminal.   The initial concept was to develop a very low-profile antenna, but in dialog with vehicle programs, PM WIN-T discovered that area is at a great premium on tactical vehicles. This discussion changed the antenna specifications by significantly reducing the available antenna base area. The resulting contract with Titan/Datron (now part of L3 Communications) was to develop a three-axis Ka-band OTM antenna with a 12" aperture. Though the antenna development was successful, there was a several year delay in the launch of the first WGS satellite. On their own, L3/Datron developed this Ka-band antenna into a very successful Ku-band product line. Figure 8 shows the Titan/Datron Ka-band OTM antenna.

Figure 8. Ka-OTM antenna

In parallel with the OTM terminal efforts, STCD also contracted with Boeing Phantom Works to investigate the issues, performance and mitigations of transmitting Internet Protocol (IP) traffic over a SATCOM OTM link [10,11,12]. This effort leveraged significant investment Boeing had made in their planned Connexion airborne IP service, as well as some other IR&D projects. Recognizing that a small number of cooperating OTM terminals with high-band terrestrial could significantly reduce the re-transmit delay for missed packets, we entered into a Small Business Innovative Research (SBIR) contract with Fantastic Data. Fantastic Data was able to develop and demonstrate a protocol that takes advantage of a common satellite footprint to enable cooperating OTM terminals to fill in missed packets at any one OTM terminal in terrestrial transmission times, rather than in satellite round trip delays, while greatly increasing overall end-to end performance and reliability [13].

4. Affordable Directional Antenna and Pointing Technology (ADAPT) Army Technology Objective (ATO)

Following the proof of concept work in EHF, and as a consequence of guidance from the Army Science Board, STCD initiated the ADAPT ATO to further develop SATCOM OTM antenna technology. During the approval process ADAPT was merged into the Tactical Network and Communication Antennas (TNCA) ATO.

The ADAPT ATO was geared to respond to Army program needs for affordable SATCOM antennas. Specifically, ADAPT developed solutions that would meet size, weight, and power (SWAP) constraints for PM WIN-T and reduce SATCOM OTM positioner costs. The ADAPT products were as follows:

4.1. Low-cost Ku/Ka OTM antenna.

This low profile dish based antenna system significantly reduced the SWaP as well as cost required to support SATCOM OTM in two baseline frequency bands. Technology advances allowed required tracking performance to be achieved with an internal MEMS inertial reference system, eliminating the need for an external TALIN Attitude Heading Reference System (AHRS). Figure 9 shows the resultant antenna.
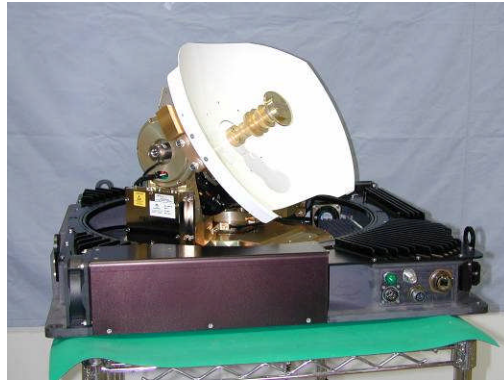
Figure 9. ADAPT Low-cost Ku/Ka OTM Antenna System

4.2. Low-profile, single-beam antenna.

The low-profile, single-beam antenna was an effort to reduce the antenna height of reflector-based solutions. The antenna design employed a single-line array and a rexolite lens material to achieve necessary beam forming in a package under 8 inches high and 38 inches in diameter. This antenna also had the advantage of carrying both Ku and Ka transceiver chains and allowing the user to select the operating band electronically. This is a cooperative effort with the Office of Naval Research (ONR) and was contracted to Millitech in FY2007 and would produce three prototypes in late FY2009.

4.3. X-band point of presence (PoP).

This antenna was contracted to DRS Codem in FY2006. The goal was to create affordable X-band OTM antennas with the same SWaP and cost constraints as the low-cost Ku/Ka OTM antenna. The intent of this development was to examine OTM performance on the emerging X-band satellites such as XTAR and WGS. Figure 10 shows the X-band OTM antenna developed under this effort.

Figure 10. DRS X-Band Point of Presence

4.4. Ku- and Ka-band power amplifiers.

Higher power added efficiency (PAE) power amplifiers would provide greater output power while also reducing heat burden on an antenna system. The power amplifiers will use innovative technologies such as spatial combining or high power pseudomorphic high electron mobility transistor carriers to increase output power. Both Ku- and Ka-band power amplifiers will be developed and be compatible with the low cost PoP.

ADAPT had a very successful conclusion. The low-cost Ku/Ka OTM performance and unit production cost made it an attractive antenna. It was subsequently selected by PM WIN-T for the Increment 2 OTM Soldier Network Extension (SNE) requirements for lower echelons.

5. Affordable Low Profile Satellite (ALPS) Comms OTM Army Technology Objective (ATO)

The ALPS ATO continues the development efforts described before. ALPS is a four year program, FY09 to FY12, to develop low profile and affordable antenna systems for Directional and Satellite Communications (SATCOM) on-the-move (OTM) to meet current and future force cost, SWaP, and performance requirements. Antennas for SATCOM OTM applications will be developed utilizing the widest bandwidths possible while maintaining adequate antenna gain, low visual signature, disciplined side-lobes, directivity, and pointing accuracy. Technologies will be developed for use in current and future military frequency bands (X, Ku, Ka and Q bands). There are five SATCOM projects in the ALPS ATO.

5.1. Low-Profile, Single-Beam Antenna.

This is a continuation of the ADAPT Low-Profile, Single-Beam Antenna described above.

5.2. Low Profile, Multi Band, K/Ka/Q Antenna System.

The K/Ka/Q antenna system is a very low profile (6 inch objective) high performance system with a single transmit beam, a single receive beam and an optional second, fully independent receive beam. This system supports Ka and Q bands for transmit and K band for receive. All required equipment to support all bands will be included in the basic terminal design. Band changing will be fully electronic.

5.3. Low Profile, Multi Band, X/K/Ka Antenna System.

The X/K/Ka antenna system, shown in Figure 11, is a low profile system, with single transmit and receive beams. This antenna system would support communications over both frequency bands supported by the Wideband Global System (WGS) satellite.
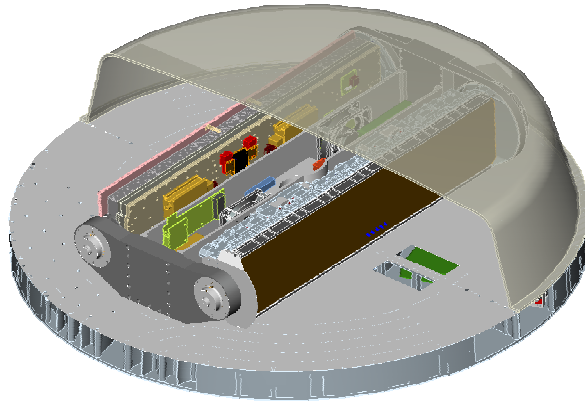
Figure 11. ThinKom X/K/Ka Antenna System

5.4. Integrated Ka/Q Band Power Amplifier.

The integrated Ka/Q band power amplifier will be developed as a form, fit, and function replacement component for the appropriate antenna. This power amplifier will provide operation in both frequency bands and at a high power added efficiency.

5.5. Small Aperture BFT Antenna.

The small BFT antenna provides a potential migration path for the FBCB2/BFT system into frequency bands supported by military satellites (i.e., X). This antenna provides a small form factor and price point for high density fielding.

Table 2 lists a few key performance metrics of the 6 projects.

\

ALPS Project	Performance Metrics	Current	ALPS Project Objectives	Army Objectives
Low-profile, single-beam (Ku/Ka) antenna	Unit cost Form Factor Throughput G/T	$135k (gimbal) 17"x26"x 26" 256/1544 kbps 11/12 dB-K	$125k (hybrid) 8in x 38 in dia 512/1544 kbps >12/12 dB-K	$75k 6in x 30 in dia 512/1544 kbps >12/12 dB-K
Low-profile, multi-band K/Ka/Q antenna	Unit cost Form Factor Throughput	$400k 12"x40"x40" 512/1544 kbps	$150k 6"x24"x36" 1544kpbs	$150k 6"x24"x36" 1544kpbs
Integrated Ka/Q power amp	Unit cost Power eff Form Factor	$25k 24%(Ka)/15%(Q) 70cu in/20lbs	$12k >25% 30 cu. In/8.5 lb	$10k >25% 30 cu. In/8.5 lb
Low-profile multi-band X/K/Ka antenna	Unit cost Form Factor Throughput	>$250k 20" diameter 256kbps (single band)	$125k 12" diameter 1544kbps (dual band)	$100k 12" diameter 1544kbps (dual band)
Small aperture BFT	Unit cost Form Factor Throughput	$5k (L-band) 8"x8"x6" 2.4kpbs	$5-10k (Ka or X) 8"x8"x6" 32kbps	$5k (Ka or X) 8"x8"x6" 64kbps

Table 2. Key Performance Metrics of ALPS SATCOM Projects

The ALPS ATO has put forth a number of challenging objectives. Some of the areas of investigation which could potentially provide solutions for the ALPS projects to meet their objectives:

- Develop low-profile technologies such as hybrid scan, slotted arrays, continuous transverse stub, and phased array apertures to reduce SWaP.
- Develop technologies for phased array elements, multiple beam pointing and steering, and smaller RF components to achieve simultaneous transmission capability in a very small form factor.
- Explore higher power and wider band gap amplifier technologies including Gallium Nitride, Metamorphic High Electron Mobility Transistor (mHEMT) to create a dual-band and high efficiency power amplifier.
- Develop lower cost antenna pointing technologies such as micro electro mechanical systems (MEMS) gyros/sensors and leverage AMRDEC MTO (R.LE.2002.01) for lower cost MEMS technology.

- Leverage antenna technologies: Small Aperture X-Band SBIR Phase II, and DARPA 3-D Micro Electromagnetic Radio Frequency Systems (3D MERFS) Program to develop Blue Force Tracking (BFT) antennas in military bands.

The technologies developed by the ALPS ATO are expected to be transition to various Army Program of Records in order to reduce some of their technology risks and to facilitate meeting future requirements.

- Low-profile, single beam (Ku/Ka) antenna to PM WIN-T, FY11
- Integrated Ka/Q-band power amplifier to PM WIN-T HC3, FY13
- Low-profile, multi-band K/Ka/Q antenna to PM WIN-T, FY13
- Low-profile, multi-band X/K/Ka antenna to PM WIN-T, FY 12
- Small aperture BFT antenna to PM FBCB2, FY12

6. Next Generation SOTM ATO

The next generation ATO addressing SOTM technology gaps is envisioned to take SOTM to the next level. Objective requirements will be supported such as supporting more integration into future vehicles resulting in very little space utilized and very low observable profile, the ultimate solution being a conformal antenna utilizing the infrastructure of the vehicle. Scalable and separable apertures will be developed in order to ease integration and provide the best performance in the space available using standardized building blocks. Efforts are envisioned to be multi-beam, multi-band antenna systems with excellent performance. DTUPC will continue to be a focus.

7. Supporting Technology Initiatives

Early on it became apparent that there were many technical hurdles to be addressed if low cost tactical on-the-move SATCOM was to become a reality. The earliest problem areas included the controller, phased shifter and attitude and heading reference system cost and performance. Later problem areas included the high power dissipation of power amplifiers and low noise amplifiers as well as the need for advanced cooling systems.

7.1. Controller and AHRS.

The initial controller for on-the-move systems utilized a VME chassis and cost over $50K. This was accompanied by a $>50K Honeywell Tactical Advanced Land Inertial Navigator (TALIN). A dual use application program for low cost X-Band phased arrays (Harris Corp) developed a low cost PC-104 controller, which cut controller costs to $5K and resulted in a considerable SWaP savings. The TALIN replacement has been an ongoing effort with Enpoint, LLC, which started as a SBIR and has continued thru Phase II+ and additional development. The result is Pinpoint, which in its final form will

provide a heading accuracy of 0.1 degree and is estimated to cost <$5K thanks to the use of MEMS sensors and coherent GPS.

7.2. Phase Shifters.

Phase shifters are a problem area all to themselves. They are the single most costly element ($50-150 ea) in the phased arrays we have developed to date. The solution was a Manufacturing Technology Program for both Ferroelectric (Agile RF) and MEMS phase shifters (Raytheon). Phase shifters from both efforts are shown in Figure 12. The ferroelectric phase shifters have sub-microsecond switching times and moderate loss, while the true time delay MEMS phase shifters have modest switching speeds and very low loss. The low loss of the MEMS phase shifters makes the development of passive or semi-passive transmit phased arrays practical. These three year programs have resulted in the development of volume production facilities that can produce phase shifters at frequencies from X-Band through Q-Band at a cost of <$10 each in production quantities.
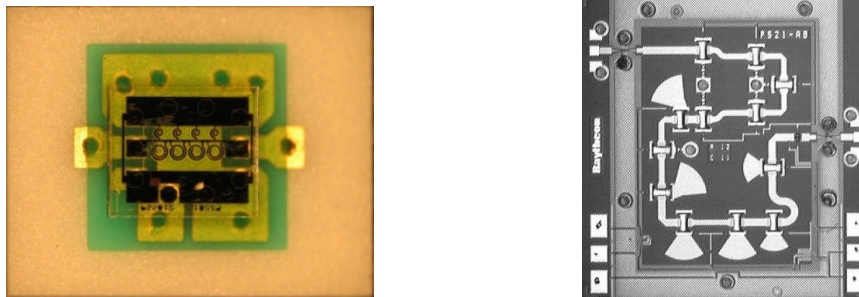

Figure 12. Agile RF Ferroelectric and Raytheon MEMS Phase Shifters

7.3. Power Amplifiers.

The power added efficiency of commercial power amplifiers at Ku and Ka bands was found to be inadequate for on-the-move systems, where the systems require a sealed radome to protect the antenna system against the harsh tactical military environment. A contract was let to Wavestream to develop high efficiency power amplifiers at both Ku and Ka Bands. These amplifiers (shown in Figure 13) were to be form, fit and function equivalent to the commercial amplifiers initially utilized in our Ku/Ka on-the-move antenna system concurrently developed by L-3 Datron. Wavestream doubled the power output at Ku band while reducing the amplifier power consumption. The Ka band amplifier is still under development.
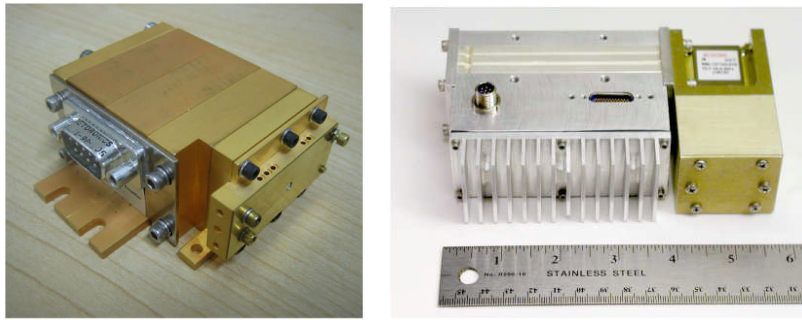
Figure 13. Wavestream High Efficiency Ka and Ku Band Power Amplifiers

We have recently begun development of a 30 GHz, 10 watt GaN power amplifier with Hittite under a SBIR program. This amplifier is expected to have a PAE >30% utilizing a developmental GaN process. In addition to this program we have partnered with the Army Research Laboratory in the advancement of GaN device and amplifier design using multiple domestic foundries to produce linear 10 watt amplifiers at 30 GHz and saturated power amplifiers at 44 GHz. The objective here is to hasten the development of released foundry processes for GaN amplifiers at 30 GHz and 44 GHz.

7.4. Low Noise Amplifiers.

When one considers that current low noise amplifiers draw only ~250 milliwatts, it is hard to realize that they can lead to a phased array with excessive power dissipation. Such was the case with the 512 element dual beam K Band array developed by Harris. It required a 1 kW heat exchanger to cool the >1350 low noise amplifiers. We now have low noise amplifiers with power dissipations of 25 to 50 milliwatts with state-of-the-art noise figures under development by Custom MMIC Design Services under an SBIR program. The low dissipation and high performance of these amplifiers will allow the design and fabrication of receive arrays with >4000 elements with modest cooling systems.

7.5. Cooling Systems.

Cooling systems are an important aspect of system design and reliability, but are often an afterthought in antenna system design. We have three new SBIR programs which offer the promise of much higher cooling efficiencies than we have achieved in present systems. Creare is developing a high efficiency phased array cooling system with advanced cross flow blowers and a heat pipe cold plate. Aspen systems is developing a high efficiency refrigeration based cooling system for cooling dish antenna systems. Lastly, Technology Applications, Inc is developing a similar high efficiency refrigeration based cooling system for phased arrays.

All of these component technology efforts have been carefully selected and pursued for their contributions to performance and cost reduction for required antenna systems.

8. Collaboration and System Efforts

A persistent theme from the discussions above is the emphasis on affordability. There is a constant drive to create technical solutions that are not only better, but cheaper. This is due to the reality of a cost-constrained Army. Programs of record cannot accept a technological development when the unit cost is prohibitive; their budgets are fixed.

So too the Army science and technology budget is cost constrained and fixed. The EHF proof of concept, the ADAPT ATO, and the ALPS ATO must work within limited funding while facing significant challenges. One mitigation to the funds limitations has been successful partnering with other organizations. An example is the low-profile, single-beam antenna.

The ADAPT/ALPS low-profile, single-beam antenna has been a cooperative effort between CERDEC S&TCD and the Office of Naval Research (ONR). ONR Code 30 supports USMC expeditionary forces that have OTM challenges similar to the Army. This common cause led CERDEC S&TCD and ONR to enact a memorandum of agreement in May 2007 to jointly fund this development. Under the MOA both organizations participate in the formulation of requirements, monitor performance (with Army leading and having contracting responsibility), and will cooperatively test the prototypes upon delivery.

The single-beam antenna also gives example to collaborate with a transition partner. PM WIN-T has shown interest in the low-profile, single-beam antenna and attends technical reviews. The interest also has extended to adding funding to the contract.

Collaboration has not been solely a fiduciary activity. The similarities of requirements discovered while establishing the MOA above had lead to CERDEC S&TCD and ONR collaborating by knowledge sharing and in lending expertise to each other's efforts. Another example is CERDEC S&TCD monitoring ONR development of two separate X-band OTM antennas for USMC situational awareness and communications.

9. MIL-STD-188-164B Initiatives

Since the X-band payload on the Wideband Global SATCOM (WGS) satellites are significantly more powerful than the Defense Satellite Communications System (DSCS) satellites they are replacing, we started investigating the potential of using X-band for SOTM. There are significant potential advantages for X-band SOTM, including higher capacity than commercial L-band, and a greater weather robustness than Ku or Ka-band

given the same satellite resources. The interference issue is potentially less than in the commercial Ku-band due to a greater average angular separation between geo-stationary satellites, and the use of military satellites represents a great potential recurring cost savings over commercial satellites.

However, before a terminal is permitted to operate on the WGS constellation, it has to go through a terminal certification process to show that it complies with MIL-STD 188-164, "Interoperability of SHF Satellite Communications Earth Terminals." The current version of MIL-STD 188-164 does not have a terrestrial OTM terminal class, so in parallel with the development of the ADAPT X-band OTM antenna, we started analysis in support of developing the necessary changes to the MIL-STD so that these changes could be inserted during the current revision cycle [14]. Our analysis efforts are continuing, and have expanded to include examination of the issues and implications of moving the Blue Force Tracking (BFT) function from commercial L-band to X-band.

10. Transition of Technologies to the Tactical Army

Our technology development efforts typically result in a prototype that is then available for testing and demonstration. Because a transition partner is identified early, a successful technology will typically be turned over to a program of record for production. Any final system changes and logistics efforts would be accomplished under the program of record. Programs of record like WIN-T and MBCOTM are providing the SATCOM OTM solutions for the tactical Army, and our technology efforts will continue to target their requirements and identified technology gaps.

11. Summary

SATCOM OTM technology initiatives were outlined in this paper. CERDEC S&TCD has provided and will continue to provide successful SATCOM OTM solutions for the tactical Army, supporting a non-contiguous battlefield OTM. Inter-related technical hurdles are analyzed and specific technologies are targeted to support system performance requirements and attain production cost goals. Current efforts are supporting technical challenges within known constraints and future efforts will target upcoming objectives to include a more integrated approach within the infrastructure of new vehicles. CERDEC S&TCD will continue to partner with our Joint Services as well as other technical agencies to leverage resources to achieve the most technical advances possible and continue to successfully transition developed technology to programs of record for fielding.

REFERENCES

[1] Choi, John, J.T. Delisle, J.J. Hilger, "MIT Lincoln Labs memorandum 63L-06-20, Response to inquiry on vehicle dynamics measurement campaign", 11 July 2006

[2] Harris Corporation, Government Communication Systems Division, "Radio Access Point Antenna (RAPA)" proposal, 16 January 1996

[3] Harris Corporation, Government Communication Systems Division, "Final Report for the Low Cost Phased Array Dual Use Application Program", 7 October 2002

[4] Harris Corporation, Government Communications Systems Division, "Final Report for the Low Cost Dual Use Science and Technologies Program", 17 June 2005.

[5] Schodorf, Jeffrey B., "EHF Satellite Communications on the Move: Baseband Considerations," Tech Report 1055, MIT Lincoln Laboratory, February 2000.

[6] Schodorf, J.B.; Gouker, M.A.; "EHF SATCOM on-the-move testbed description," MILCOM 2000 Proceedings Volume 2, Page(s):1235 – 1238.

[7] Schodorf, Jeffrey B., "EHF Satellite Communications on the Move: Experimental Results," Tech Report 1087, MIT Lincoln Laboratory, August 2003.

[8] Schodorf, J.B.; Gouker, M.A., "Performance evaluation of a hybrid ARQ protocol implementation for EHF SATCOM on the move systems," MILCOM 2001 Proceedings, Volume 1, Page(s):311 – 315.

[9] Faulkner, E.A.; Worthen, A.P.; Schodorf, J.B.; Choi, J.D., "Interactions between TCP and link layer protocols on mobile satellite links," MILCOM 2004 Proceedings, Volume 1, Page(s):535 – 541.

[10] Spagnolo, P.A.; Henderson, T.R.; Kim, J.H.; Michael, G.T., "TCP gateway design considerations for satellite link blockage mitigation," IEEE International Conference on Communications, Volume 1, Page(s):433 – 437.

[11] Duke, M.H.; Henderson, T.R.; Spagnolo, P.A.; Kim, J.H.; Michael, G.T., "Stream control transmission protocol (SCTP) performance over the land mobile satellite channel," MILCOM 2003, Volume 2, Page(s):1325 – 1331

[12] Zhang, Y.; Henderson, T.R., "An implementation and experimental study of the explicit control protocol (XCP)," 24th Annual Joint Conference of the IEEE Computer and Communications Societies. Proceedings Volume 2, Page(s):1037 – 1048.

[13] Thomas Hammel, Mark Rich, Steven P. Lescrinier, and Gerald T. Michael, "Multi-Vehicle Blockage Mitigation Techniques For On-The-Move Satellite Communication," MILCOM 2005

[14] Lino Gonzalez, Gerald Michael, Joseph Shields and Carl Swenson, "Capacity and Regulatory Study On The Potential Use Of
Satellite On the Move Terminals At X-Band," Milcom 2008.

LOW-COST LOW-PROFILE DUAL CIRCULARLY POLARIZED KU-BAND ANTENNAS FOR MOBILE SATELLITE PLATFORMS

Songnan Yang[1], Mohamed H. Awida[1], Shady Suleiman[2] and Aly E. Fathy[1]

[1]EECS Dept., University of Tennessee at Knoxville, TN 37996

[2]Winegard Company, Burlington, IA, 52601

Abstract: Two structures for low-cost low-profile DBS antennas on the move have been investigated. The first structure is based on slotted waveguide structure and the second one is cavity backed patches. To reduce fabrication cost, substrate integrated waveguide (SIW) technology has been used to develop both structures. Meanwhile, to keep a low profile, the antenna aperture was splitted into two or more and the outputs of the splitted structures were combined. The slotted waveguide structure has inherent radiation beam tilt angle that can significantly lead to reduced heights; but it suffers from frequency beam squint and is limited to reception of one polarization at a time. On the other hand, the cavity backed patches has relatively larger profiles as the antenna boards need to be initially inclined at 45° degrees but still need to be mechanically steered by ±25° degrees off their initial position. Preliminary results are very encouraging and will be presented here.

1. INTRODUCTION

Mobile communications is becoming an essential part of our daily life. We love the flexibility of wireless cell phones and even accept their lower quality of service when compared to wired links. Similarly, we are looking forward to the day that we can continue watching our favorite TV programs while travelling anywhere and everywhere including satellite channels and the wish list goes on. Mobility, flexibility, and portability are the themes of the next generation communication. Motivated and fascinated by such technology breakthroughs, this effort is geared towards enhancing the quality of wireless services and bringing mobile satellite reception one step closer to the market.

For satellite reception on the move, the question was not: can we do it or not? It was the possibility of a low profile implementation. Add to that: was the proposed solution within the customer's anticipated budget?. People now can receive satellite signals on the move but they are using bulky reflector antennas (see Fig. 1), which could explain the limited use/spread of such products. Other proposed solutions include sophisticated phased arrays, which is quite expensive solution for such consumer type product and has extremely limited market. Typical required specification for mobile DBS in USA are given in Table 1 and could explain the difficulties/challenges in developing such a product.

Fig. 1. Conventional reflector antenna

TABLE 1
Required Specifications for Mobile DBS in USA

Antenna Gain > 32 dB
Antenna Physical Area approx. 240 in² @ 12.45GHz
G/T >12 dB/K
Azimuth Coverage φ=360º
Elevation Coverage 20º<θ<70º from Horizon
Dual Circular Polarization
Low Profile for SUV/VAN/RV for Customers' Satisfaction

*Assuming 60% efficiency

In this paper, we report on two different approaches to build such low-profile low-cost satellite receivers on the move designed especially for RVs or Mini-Vans. The first approach is a low profile mobile satellite antenna design based on a slotted antenna array implementation. It uses a low loss, low cost, light weight, and relatively efficient multi-layer printed circuit technology to emulate stacked waveguide structures for both feeding and radiating elements based on substrate integrated waveguide technology (SIW). The slotted antenna array has been successfully demonstrated, however, it only provides one polarization at a time [1]. The second approach is based on cavity backed patches fed by waveguide feed networks but with a larger profile compared to the slotted array approach. The cavity-backed patches approach, however, is capable of receiving the two circular polarizations simultaneously [2]. In this paper, we will first discuss a full metallic waveguide realization, followed by our results for low cost implementation using the SIW technology for both approaches.

2. SLOTTED ARRAY DEVELOPMENT

Planar antennas are the best low profile choice, yet electrically steering up to 70° would lead to significant gain drop and performance deterioration. Hence, we developed a low-profile planar slotted array antenna structure of circular polarization for the US market that has an inherent tilt angle. We utilized slotted waveguide radiating structures to radiate at an off-broadside angle to reduce the elevation steering volume. The theory of travelling wave slot array antennas is well-known and can be found for instance in [3-4]. In this section, we will briefly describe the development of a single radiating slotted rectangular waveguide, followed by a full array implementation of a 32 guide radiators to summarize our efforts along these lines.

a) Single Element Design:

The single element is designed on WR62, a standard waveguide size for Ku band. As can be seen in Fig. 2, thirteen "X" shaped slots are cut on the top wall, with an offset from the center line S_1 = 3mm and cross angle δ = 80°. The travelling wave slotted waveguide radiates at an angle off-broadside that can be primarily controlled by the choice of the radiating waveguide's wide dimension "a". Additionally, the leakage angle is a function of the coupling strength of the slots (e.g. the slot length), the spacing between the "X" shaped slots, and the operating frequency. This leaky waveguide radiates a circular polarization at the main beam, which already has a tilt angle θ. In order to minimize the mechanical steering requirement in the elevation, θ is selected to be 45°. As a result of this inherent tilt, a maximum of only ± 25° mechanical tracking/steering in elevation is required to cover the 20º to 70º DBS elevation observation range required as shown in Fig. 3.
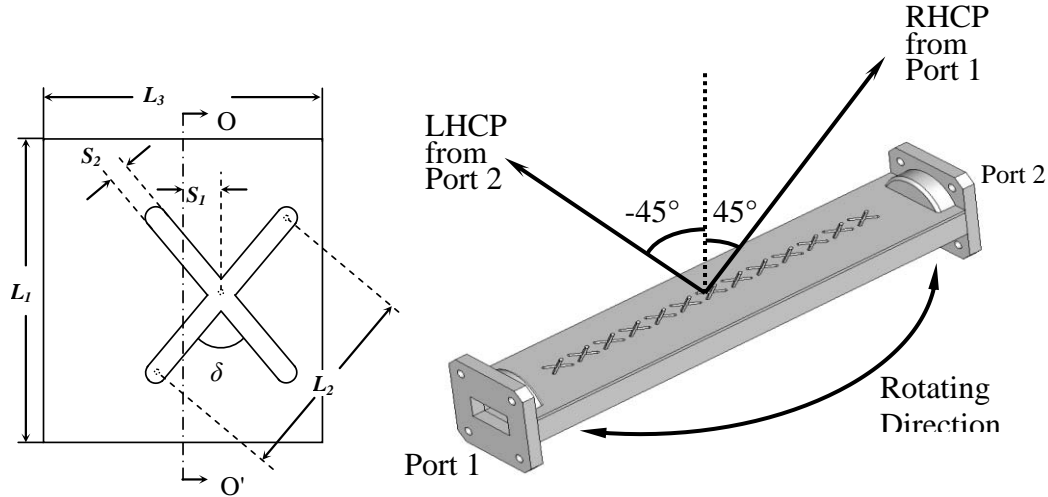

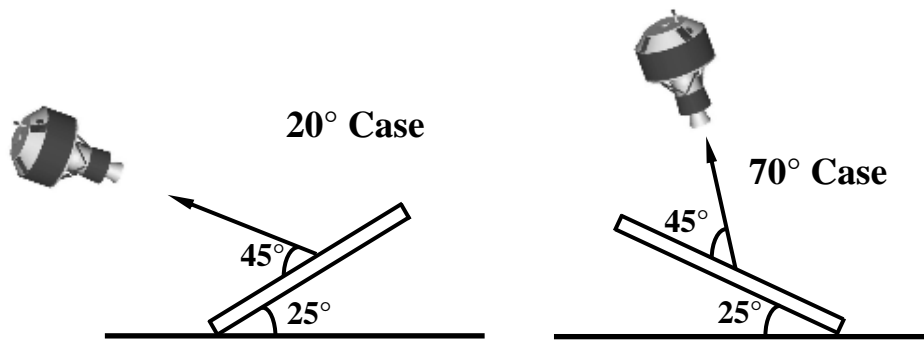Fig. 2. A single "X" shaped slot and realization of dual circular polarization

Fig. 3. Elevation tracking coverage of leaky wave slot array antenna

Meanwhile, the efficiency of a symmetric travelling wave slot array is analyzed in [8], where the gain hits a maxima at particular predetermined coupling factors. So the length and spacing of slots in our design need to be carefully selected to simultaneously achieve both the 45° beam tilt angle and the maximum antenna gain. In our implementation shown in Fig. 2, the slot length L_2 is the same for all slots, and is designed to be 9.6mm with a slot width $S_2 = 1$mm. Meanwhile, the spacing between the two radiating elements is $L_1 = 9.3$mm. These design values are chosen to maximize the gain, and maintain a good axial ratio for the tilted beam.

b) Single Element Performance:

Fig. 4 shows a prototype built using CNC machining. Thirteen "X" shaped slots were selected to assure better than −10 dB termination loss; while adding more slots would increase the overall height of the roof mounted antenna. Also, utilizing less than ten elements would reduce the amount of radiated power and thus the overall antenna efficiency. This slot array antenna is measured in the far field and the predicted and measured results are shown in Fig. 5 indicating more than 15dB gain and its side-lobe levels are at least 13dB down. The main beam is strategically located around 45° off broadside in the elevation direction. It is imperative here to recognize that there is a significant beam squint with frequency that should be accounted for when designing the beam steering satellite tracking mechanism.
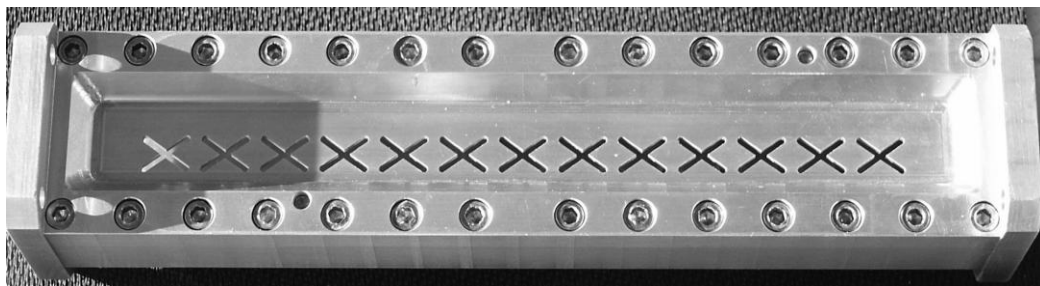

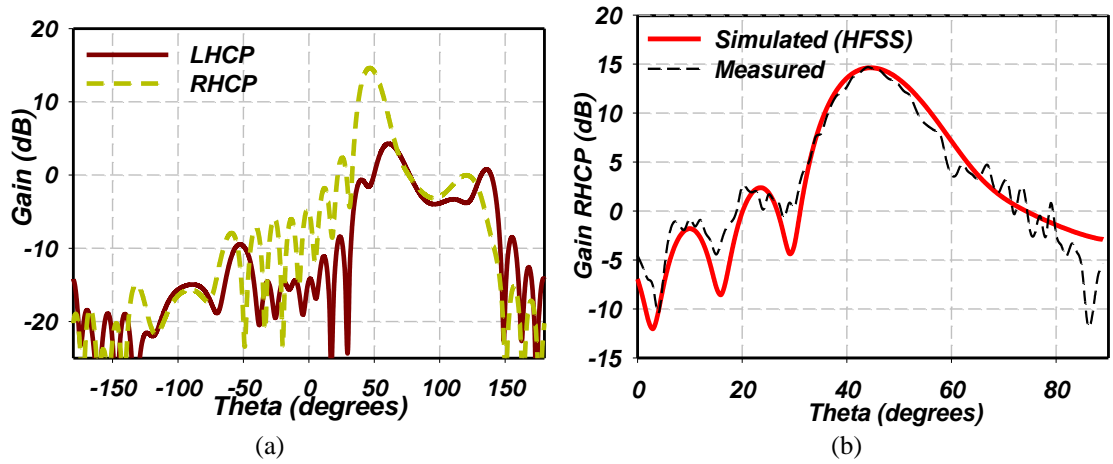Fig. 4. Fabricated single radiating slotted waveguide element prototype

Fig. 5. Simulated (a) and comparison (b) of results of a single element.

c) Slotted Waveguide Array Development:

First, the above single waveguide element with cross-slots was utilized as an element in a 6x13 sub-array antenna [5]. Subsequently, the design was implemented in both metallic guides and SIW [6]. Table 2 compares the results/advantages of both implementations schemes. Based on pure cost analysis, it was decided to adapt the SIW technology to develop the DBS antenna as clearly noticed from Table 2. Designs for 16, 32, and 64 elements were pursued [7] and here we will present only our final optimized design for the 32 element array but for further design details refer to [8].

TABLE 2
Comparison between Metallic Waveguide and SIW Slot Sub-arrays

	Metallic Waveguide Slot Array	**SIW Slot Array**
Cost	Very high, requires CNC machining, and high precision manufacturing	Low, slots are 1 mil accurate using conventional PCB technology
Loss	<0.025 dB/in for WR62 with a 0.280 in reduced height waveguide	<0.07 dB/in, for a 0.125in thick Duroid 5880 substrate
Beam Tilt	Metallic waveguide travelling wave slot array radiates forward	SIW slot array radiates backward
Feed Network	Requires wider "a" dimensions, less area efficiency. Need multi-layer feed network for large arrays.	Feeds could be easily integrated with coplanar circuits. Less than 0.25 inch for two layer feeding networks.
Weight	Bulky, heavy	Light, and low profile
Assembly	Many pieces, complicated to assemble	Standard PCB, no need to assemble

d) 32-Element Array Development:

A five stage binary feed network has been implemented comprised of compact SIW junctions for the development of the 32 radiating SIWs folded feed array design. The fabricated combining network is shown in Fig. 6. Where the insertion loss of the feed network has been minimized using an optimized feed tapering scheme. The widths of the SIWs at each combining stage has been carefully selected such that the stage with the longest transmission line has the widest SIW "a" dimension, which in turn gives the lowest insertion loss per unit length according to [8].

The developed combining network is connected back to back as shown in Fig. 6, and its measured results are shown in Fig. 7, where a good return loss has been achieved and the measured back to back insertion loss is less than 1.5 dB across the DBS band. The feed network is folded to the back of the radiating elements to provide significant size reduction (about 50%). At the end of each output SIW, a transition between the two SIW layers is used to couple the feed network to the radiating waveguides [8].
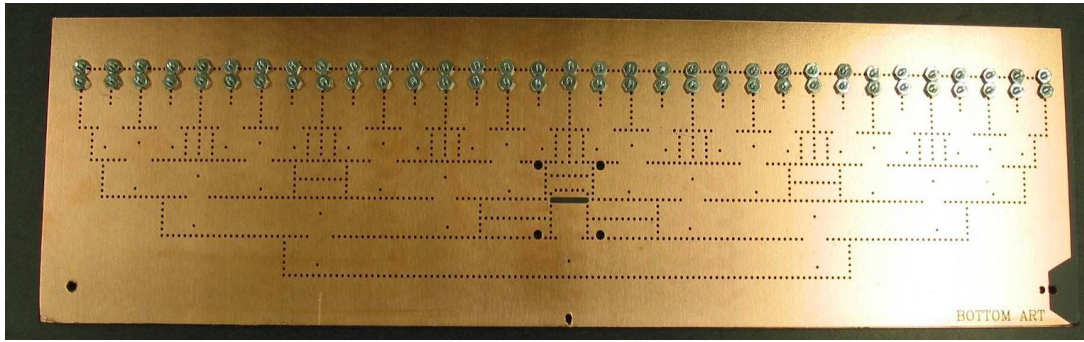

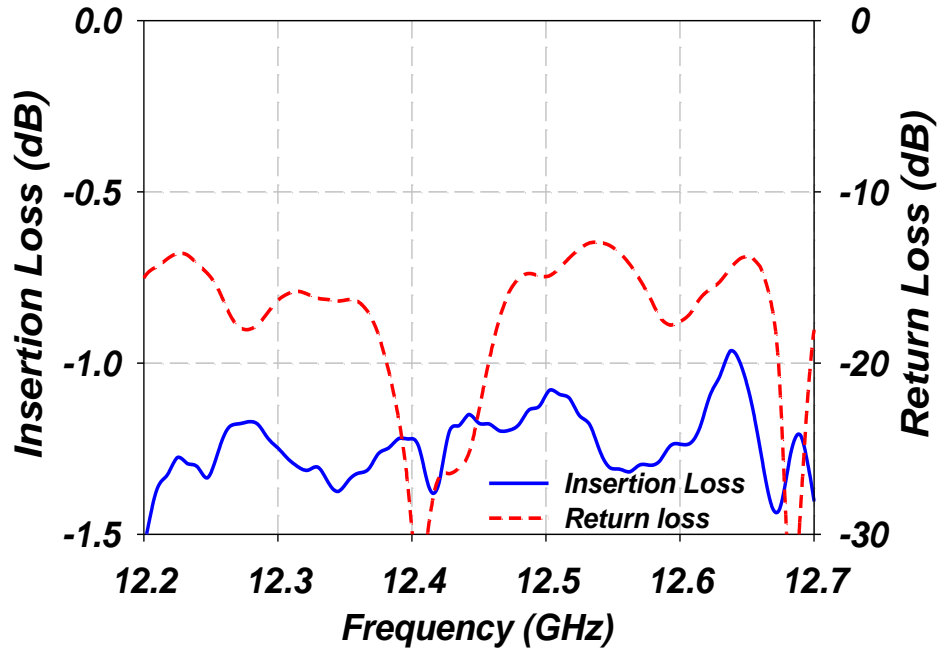Fig. 6. Back to back connected feed network of SIW 1 to 32 feed networks.

Fig. 7. Measured return & insertion loss of back to back 1 to 32 feed networks.

e) Measurement Results:

The fabricated array with the folded feed network is shown in Fig. 8, and its measured return and termination losses are shown in Fig. 9. The radiation patterns of the fabricated arrays have been evaluated over the 12.2 GHz to 12.7 GHz frequency range using near-field measurements, an example of these measurements at the central frequency is shown in Fig. 10 and 11 for the LHCP and RHCP, respectively. A summary of the measured radiation characteristics are listed in Table 3. The sidelobe levels in the elevation cuts have been maintained at levels better than 17dB down from the peak radiation which is a result of the slot length tapering. Due to the relatively highly efficient feed network, the average gain of the LHCP radiation is more than 26.3 dBi and the RHCP gains are slightly lower, which is most likely caused by misalignment between the radiating SIWs and the feed network during assembly.
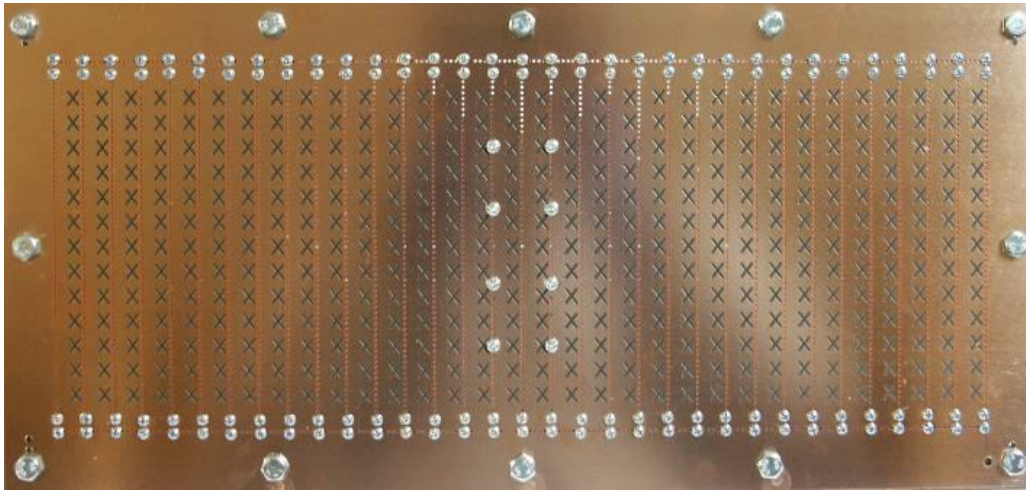

Fig. 8. Fabricated 32 radiating SIWs slot array with folded feed networks.
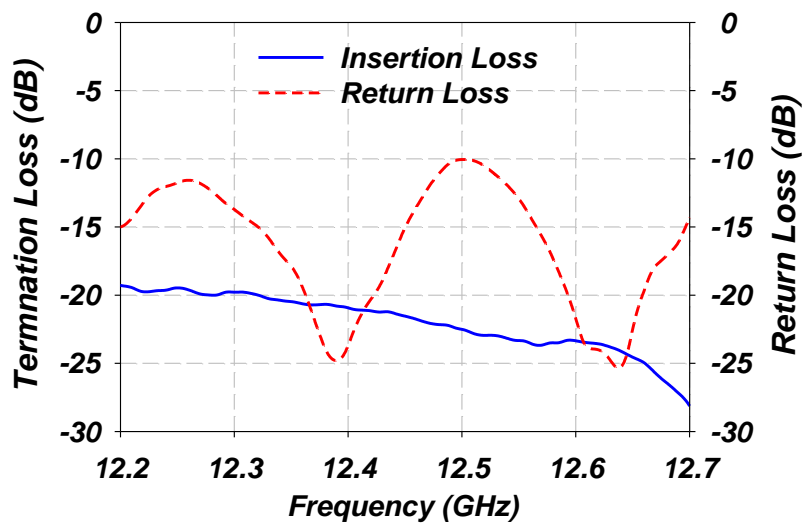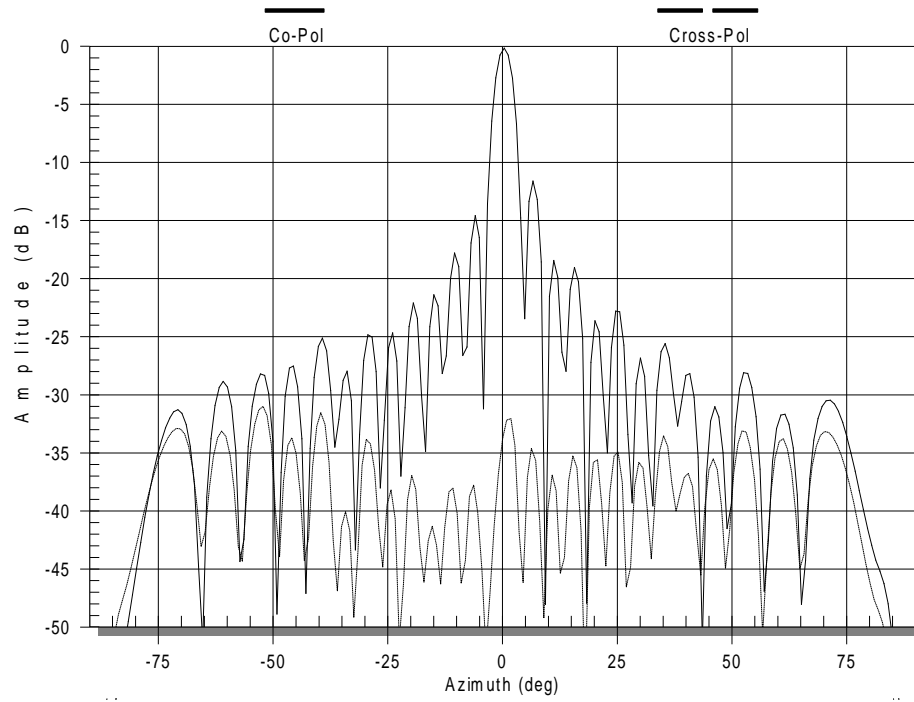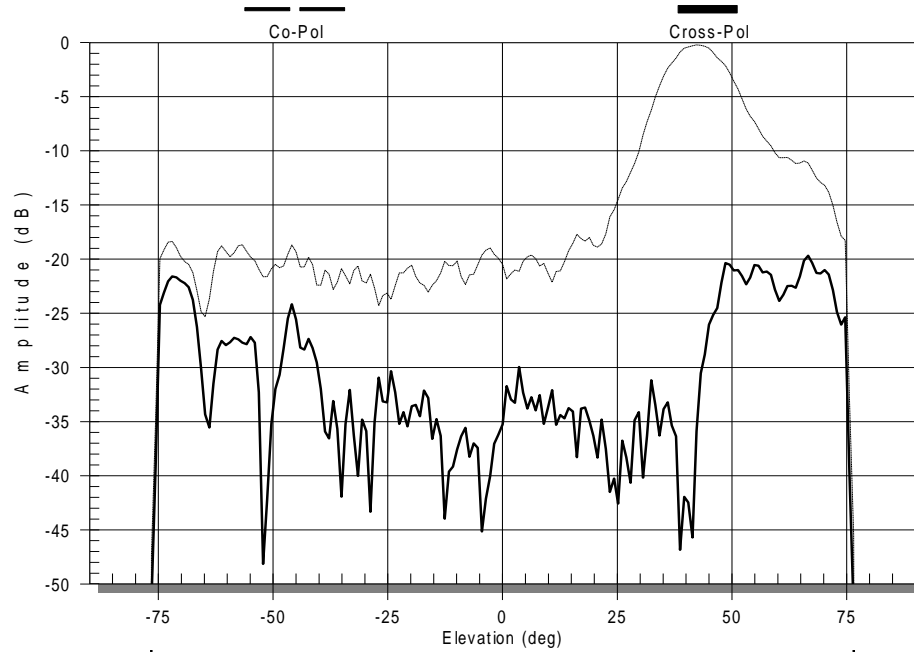

Fig. 9. Measured results of the slot array with folded feed networks.

Fig. 10. LHCP Radiation patterns of the 32 radiating SIWs slot array with folded feed networks at 12.45GHz. (a) Azimuth cut. (b) Elevation cut.
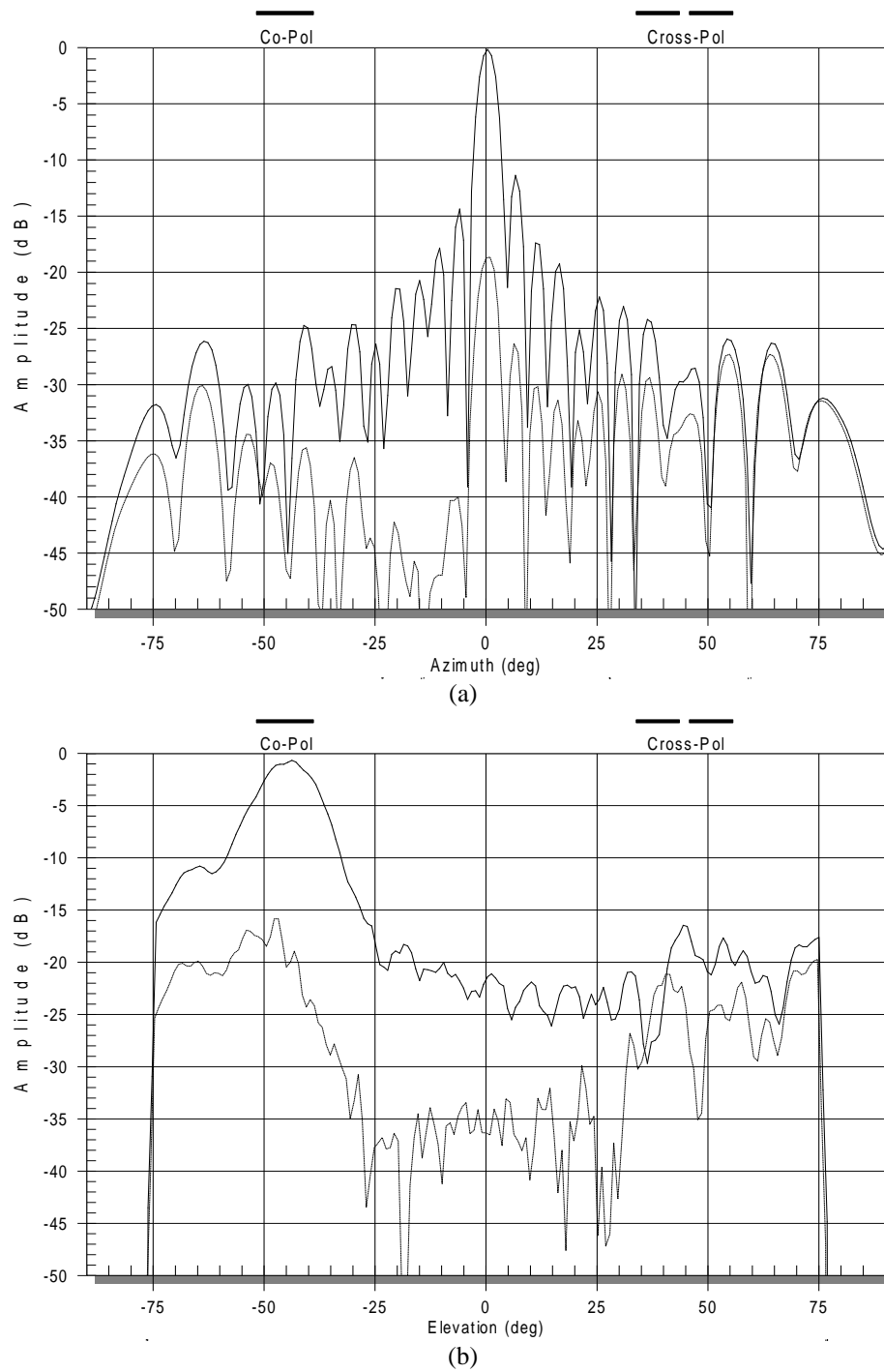
Fig. 11. RHCP Radiation patterns of the 32 radiating SIWs slot array with folded feed networks at 12.45GHz. (a) Azimuth cut. (b) Elevation cut.

335

TABLE 3
Measured results for the 32 radiating SIWs array with folded feed network

Frequency	Polarization	Peak Gain (dBi)	Elevation Peak (deg)	Sidelobe level (dB)	Cross Pol level (dB)
12.2GHz	LHCP	26.07	49.9	-17	-18
12.45GHz	LHCP	26.52	42.3	-18	-33
12.7GHz	LHCP	26.43	34.7	-18	-27
12.2GHz	RHCP	25.87	-50.2	-17	-14
12.45GHz	RHCP	26.17	-43.9	-18	-19
12.7GHz	RHCP	26.14	-36.5	-19	-20

In summary, this 32 element array has the best compromise between optimum gain and efficiency among the developed prototypes. The 32 radiating SIW folded feed array has been used to receive DBS TV broadcasting in Knoxville area, however, with low gain margin. The DBS antenna reliability can be improved by combining two or more parallel apertures and embed LNAs after each sub-array to assure high S/C levels. Hence, this slotted SIW array design could lead to a low profile antenna (≈3in height) upon folding the feed structure, and will surmount to over 30 dB gain when combining parallel apertures as discussed in [7]. However, it only receives one polarization at a time.

3. Cavity-Backed Patch Antenna Development

In general, conventional planar microstrip antennas have narrow bandwidth and low efficiency performance. Factors that cause performance degradation include feed line losses, complicated feed networks to provide dual CP operation, and the patches' inherent narrow bandwidth, but the microstrip patch arrays (having a broadside beam) have been proposed either with suspended substrate [9] or with cavity backed patches [2] to enhance the microstrip patch inherent limited bandwidth. Suspended substrate designs are more common, for ease of their manufacturability while the fabrication of cavity backed patches is not common as it would require the integration of metal cavities in the back, requiring two fabrication processes; the first is the conventional PCB process to print the microstrip patch layer and the other is probably a CNC machining or metal casting process to fabricate the waveguide metalized cavities. The previously prescribed fabrication scenario potentially increases the total fabrication cost and complicates the structure assemblage.

Nevertheless, cavity-backed patches exhibit superior performance rather than the suspended substrate structures due to their salient features of surface waves suppression, isolation from the surroundings, reduced coupling in an array configuration, better matching, wider scan performance in infinite arrays, and reduced backward radiation [10]. In this section, we will present our efforts in developing cavity backed patch structures based on solid metal implementation first, then its subsequent realization using SIW technology.

a) Printed Circuit Development-- Preliminary Experiment

We have designed rectangular patch antenna printed on top of RO4003C substrate material with ε_r=3.38, and a thickness of 0.008 inch. The patch was suspended (backed) above a circular cavity with a diameter of 0.6 inch and a depth of 0.04 inch, an air gap of 0.032 inch is sustained between the patch and the metal ground plane. The previously defined cavity was imprinted on the metal ground plane, i.e. solid cavities. The structure and the simulated return loss of a single cavity-backed patch are shown in Fig. 12. As can be seen, the cavity backed patches provides over 10% bandwidth [2] as compared to the 1-2% bandwidth of the conventional microstrip radiator.

The developed single cavity design has been extended to improve the performance of the microstrip patch antenna. It utilizes a waveguide feed network to reduce the feed losses, and the cavities to widen the bandwidth. This feed network is comprised of reduced height WR62 solid metallic waveguides and utilizes H-plane T-junction splitters. A full synthesis of these equal or arbitrary two-way power splitters was developed in [11], and utilized to develop a 1 to 8 power splitter as shown in Fig. 13. Also, a tapered amplitude distribution is utilized to get a -25dB side lobe level. The simulated return loss and transmission at each output is shown in Fig. 14. It is noticeable that an excellent input match, and a constant tapered-amplitude over the operating frequency range can be achieved.
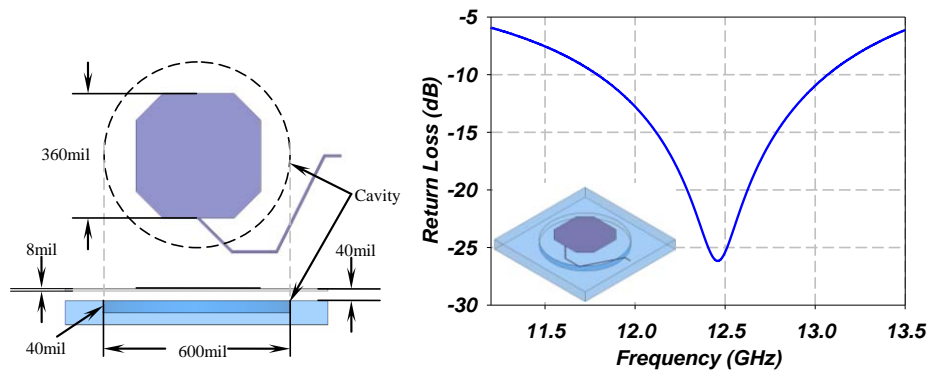
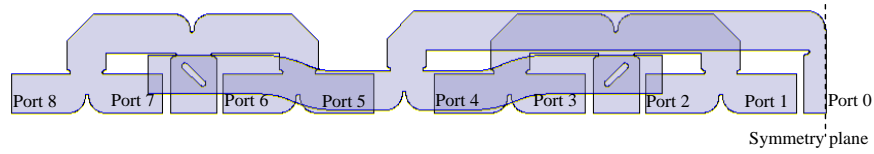Fig. 12. Structure of a Single cavity backed patch and its performance.
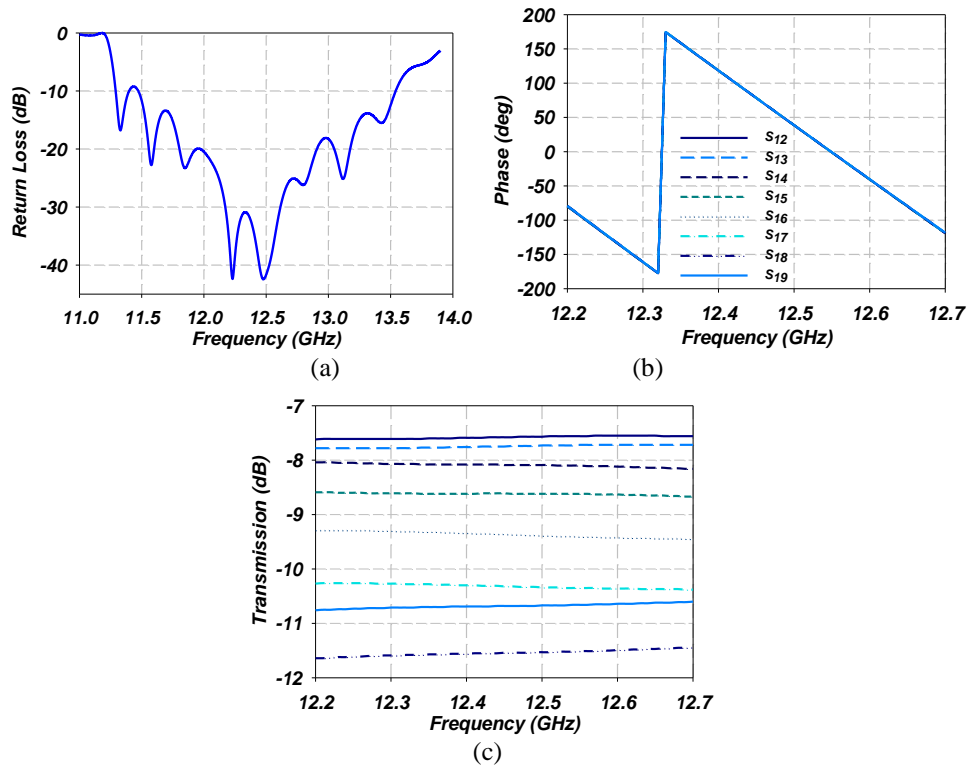

Fig. 13. 1 to16 power divider with tapered amplitude.

(a)

(b)

(c)

Fig. 14. a) Input return loss of the feed network, b) the linear phase performance c) the tapered amplitude distribution.

338

b) Dual Microstrip Feed:

To provide dual polarization, we have used rectangular patches that are fed using dual microstrip line feed networks. The two feeds excite two orthogonal linear modes as shown in Fig. 15. Here, it is essential to minimize the length of these feeding microstrip lines as much as possible and go directly to waveguides using feed through probes. Two independent waveguide feed networks are used to provide dual linear operation as shown in Fig. 15. Then, a quadrature-hybrid circuit is used to combine the two orthogonal linearly polarized signals at the output of an LNA in order to provide the polarization transformation from dual linear to dual circular polarization.
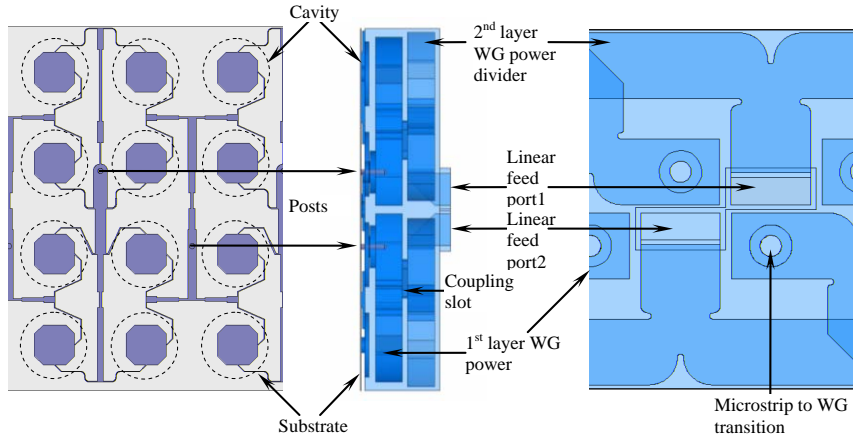

Fig. 15. Unit cell of circular polarization patch array and feeding network.

c) SIW Implementation:

Recently, SIW technology was elegantly suggested as an alternative technique to facilitate the low cost implementation of waveguide-like components using the standard PCB technology [12]. In principal, using via holes properly spaced at about $\lambda g/20$, the waveguide metal walls could be emulated. Substrate integrated waveguide (SIW) was utilized in [1, 13] to achieve a low cost, yet relatively low loss feed network. We extend the use of the SIW cavities to back microstrip patches instead of the conventional metalized ones presenting here a dual linearly polarized 3x4 sub-array. This proposed sub-array is easy to fabricate and should lead to a significant cost reduction in attaining large DBS antenna arrays as it will be combined with a SIW waveguide feed network for large arrays.

The developed SIW cavity-backed patch 3x4 sub-array basically consists of a stack of two substrates namely; microstrip substrate of dielectric constant ε_{r1} and a cavity substrate of dielectric constant ε_{r2} as shown in Fig. 16(b). Trimmed square patches of side length "a" were printed on microstrip substrate while being fed through a staggered dual probe-fed microstrip dividers; one provides the horizontal polarization (1st divider) while the other one provides the vertical polarization (2nd divider), as shown in Fig. 16(a). The ground of the microstrip substrate and the top layer of the cavity substrate have circular openings of radius "R" underneath the patches. Many via holes spaced along the circular openings were drilled in the cavity substrate and were platted through constituting the SIW circular cavities backing the patch as shown in Fig. 16.
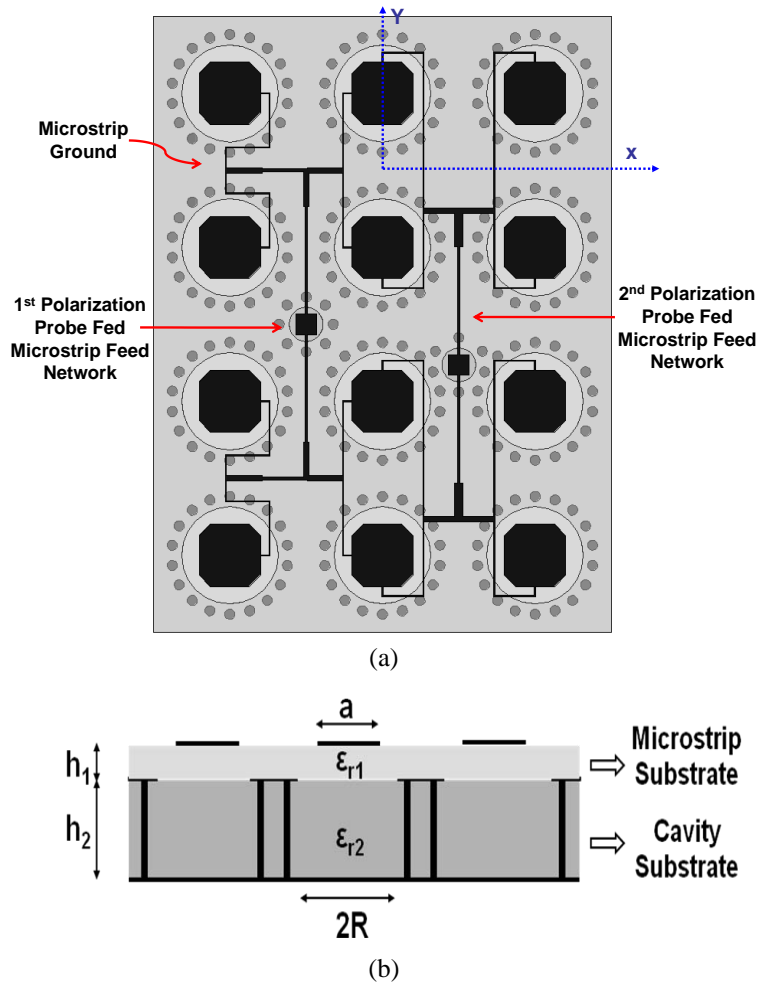
(a)

(b)

Fig. 16.   Proposed substrate-integrated cavity-backed microstrip patch 3x4 subarray with dual linear/circular polarization.

An integrated 50Ω coaxial probe feed topology similar to that proposed by [14] , was adopted to excite the antenna sub-array as shown in Fig. 16(a), where many via holes were implemented to emulate a coaxial probe excitation thus minimizing feed losses. A simple microstrip feed divider with quarter wave transformers was used to guide the wave from the probe feed to the patches as shown in Fig. 16(a). It is worth noting that the patches are being fed from opposite sides to be able to stagger both polarization feed networks in the available space. Therefore, 180 ° electrical length differences between the opposite feed arms are maintained in both networks to compensate for that opposite feed topology.

To that end the design of the SIW cavity-backed patch antenna involves the selection of the substrates properties (thickness and dielectric constant) and the determination of the patch and cavity dimensions. Following the design guidelines in [15], we have used a 0.381 mm thin Rogers 5880, a quite thin substrate ~ 0.02 λ_0 , for the microstrip feed and patch printing to minimize the feed network losses. As far as the cavity substrate, we have used the same material, Rogers 5880, to avoid any thermal expansion mismatch between the different layers, however of 1.575 mm ~ 0.066 λ_0 in thickness to achieve a minimum fractional BW of 9%.

In fact, the cavity and patch dimensions will basically determine the input impedance and resonant frequency of the SIW cavity-backed patch antenna. Using the

design graphs presented in [15] the patch size is determined to be 7.65 mm while the cavity size is 6 mm.

The proposed dual-polarized 3x4 sub-array was fabricated as shown in Fig. 17 (a). A standard SMA with a solder cup contact was utilized in launching the signal to the structure. The measured reflection response of the both feed ports is shown in Fig. 17(b). The sub-array covers the required DBS frequency range at both ports while the isolation between the ports is better than 35 dB along the band of operation.

Measurements of the far field antenna radiation patterns at 12.5 GHz of both polarizations are shown in Fig. 18 for the YZ cut. The side lobe level is better than -14 dB while the cross-pol is better than -19 dB in both cases as shown in Fig. 18(a) and (b) for the horizontal and vertical polarization excitation respectively.
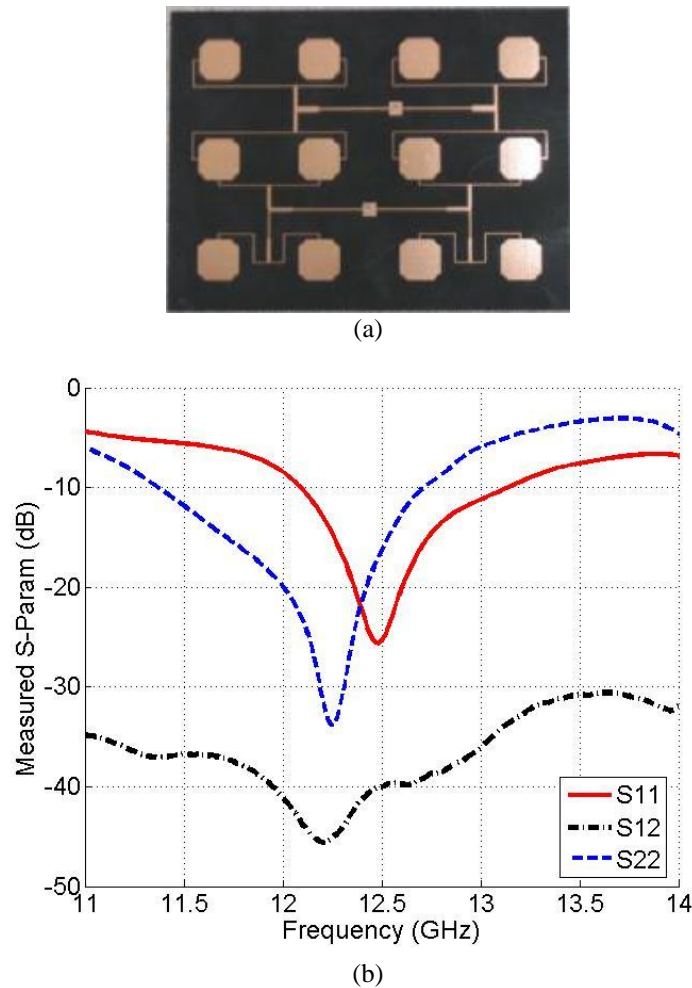

(a)

(b)

Fig. 17. Dual linearly-polarized 3x4 sub-array. (a) Picture of the fabricated structure. (b) Measured S-parameters showing the reflection response of the two feeding ports and the mutual coupling between them.
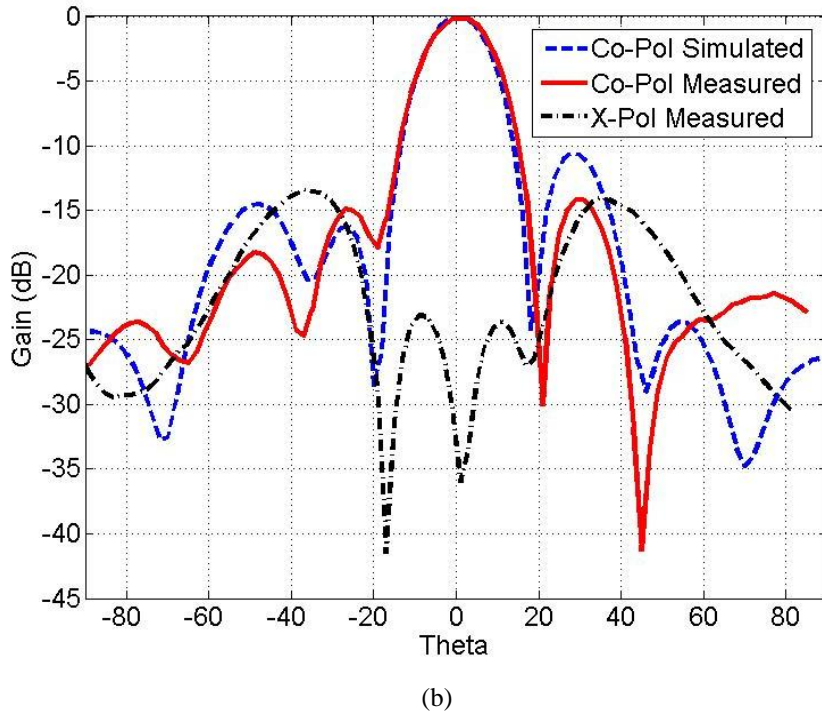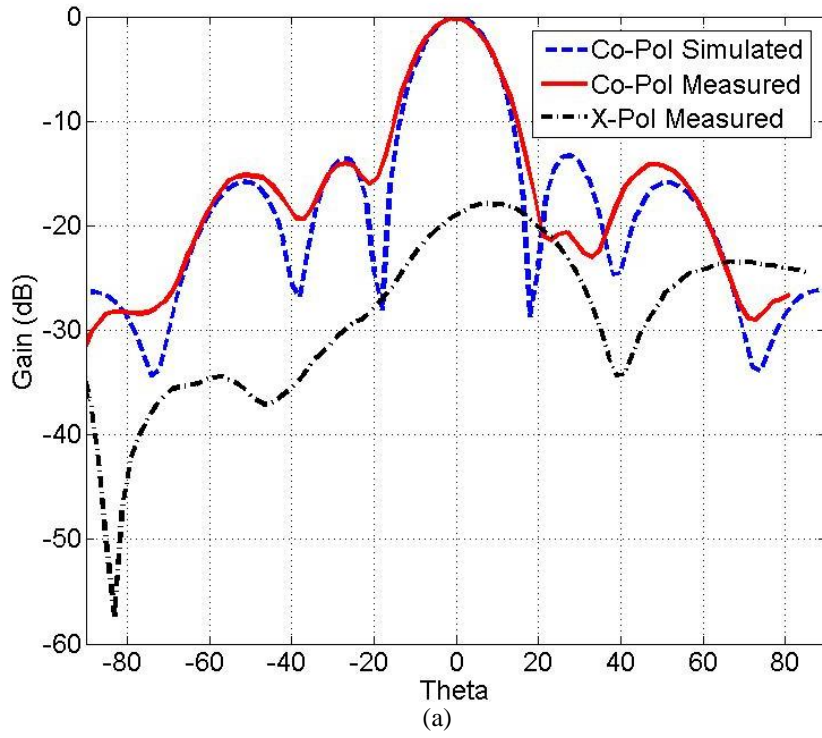
Fig. 18. Measured radiation pattern (solid) vs. the simulated one (dotted) of the cavity backed microstrip patch 3x4 sub-array. (a) YZ-cut while port1 is excited and port 2 is matched. (b) YZ-cut while port2 is excited and port1 is matched.

4. Split Aperture Concept

To achieve a certain gain as required for DBS antennas reception, we must use a minimum antenna size. This could lead to an unacceptable high profile antenna structure. But, relatively low profile antennas still can be implemented by splitting the antenna into more than one board. However, the combined overall radiation pattern of these splitted apertures could have unacceptable side-lobe levels. In the case of mobile DBS antennas which require wide-angle steering capability as well, splitting the aperture could degrade the overall performance unless the system is carefully designed. The number of splitted apertures is typically limited by the amount of insertion loss caused by the interconnecting feed structures, and its mechanical flexibility, as required in the case of mechanical steering. Splitting the antenna approach will be adapted for both the slotted array and the cavity-backed patch antenna approach. Hence, the overall system performance and interconnecting hardware details need to be optimized to minimize such degradation while achieving the greatest practical height reduction, here for illustration we will discuss only the cavity backed patch antenna splitting.

In the United States, for example, the requirements of a high gain (greater than 32 dB) and a wide scanning range (20º to 70º from the horizon) is very challenging. If we assume an overall antenna efficiency of 60%, then an area greater than 200 inch^2 is necessary to obtain such high gain at Ku-band. For illustration, if we use a 25 inch long single board we would require a board width of about 8 inch. Such a scenario would lead to a height of at least 8 inch when maximally steered (20º from horizon), an unacceptable height. However, the market is driving these height requirements to less than 3 inch. In section, we are investigating the splitting of the aperture to circumvent such physical constraints. Utilization of n sub-apertures can significantly reduce the overall height by almost a factor of n where n is the number of utilized apertures. Our proof of concept experiment and its associated predicted results will be presented here.

a) Experimental Evaluation:

In this investigation, we have utilized one feed network for one polarization to simplify the structure and prove our proposed concepts. However, results of split/shared apertures experiments can be generalized for the general case of dual polarization. In this feasibility study we have fabricated two 4*16 element-arrays that use the 1:8 tapered waveguide power divider shown in Fig. 19 (a). The radiation pattern for each sub-array is shown in Fig. 19(b) and an individual gain of 26.5 dB for each aperture has been demonstrated, which translates to 70% aperture efficiency.
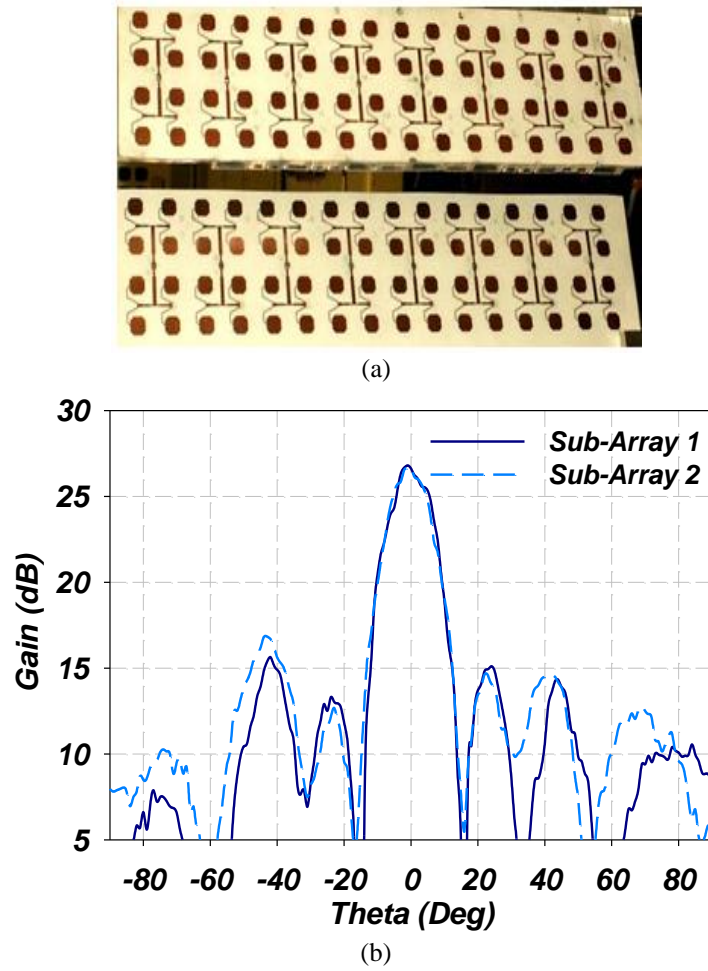
(a)

(b)

Fig. 19. Linear polarization sub-array (a) Fabricated structure (b) Measured radiation pattern.

To achieve a full steering volume in both planes, the 360º azimuthal steering is achieved using a rotating table (Lazy Susan), meanwhile for the cavity backed patches azimuthal steering--we initially mounted the structure inclined by a 45º degrees. Subsequently, it is only required to steer within a range of ±25º in the elevation plane. The two inclined antennas are spaced at a distance of 3.4 inch, and their outputs are combined using a 2 to 1 power combiner. One phase shifter is utilized to compensate for the difference between the two-phase fronts in order to bring the two received signals in phase. The required phase shift as a function of inclination angle is given by

$$d = L \cos (\theta_{sat})$$

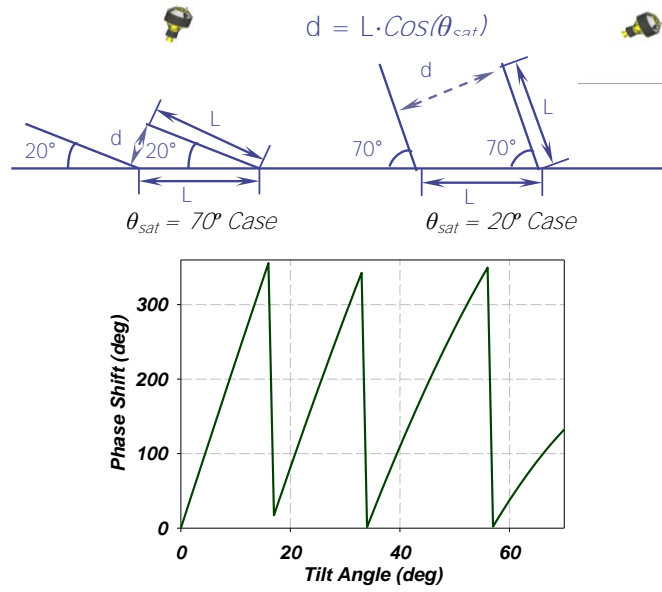Fig. 20. Steering mechanism and phase shift needed for each tilt angle in elevation.

b) **Wave Front adjustment:**

The overall radiation patterns of two groups of extreme inclination angles are shown in Fig. 21. When no phase shifter is used and the inclination angle is 0°, 17°, 34°, or 57°, the spacing between the sub-arrays is a multiple of λ. So as expected, the overall radiation pattern is similar to the pattern of an array with twice the area of each sub-array, i.e. placing the two sub-arrays next to each other. The overall gain reaches 29.2dB which is almost twice the gain of a single sub-array structure. Similarly, as the inclination angle increases and according to Fig. 21, at 26° and 44° degrees the distance between the two plates should be multiples of half wavelengths. Thus the signal from the two sub-arrays should be out of phase, and a complete cancellation can be seen as demonstrated in Fig. 21 which validates our predictions.
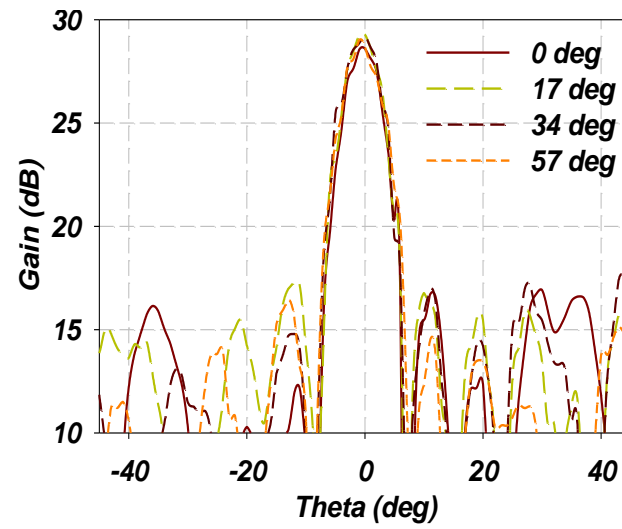
(a)
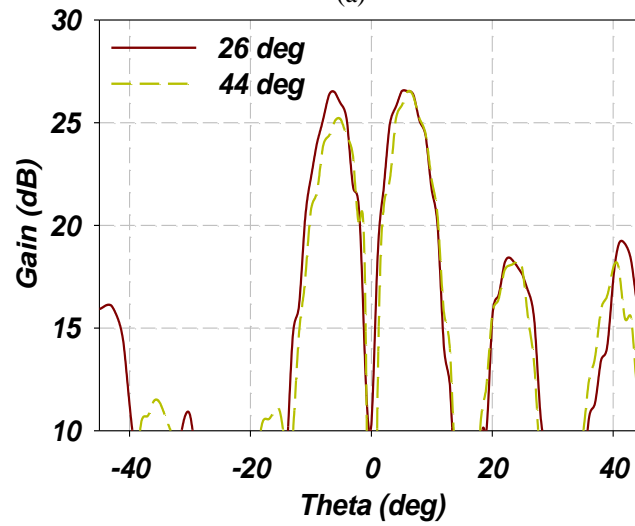
(b)

Fig. 21.   Measured radiation pattern at inclination angles where the spacing between sub-arrays are multiples of half wavelengths

c) **Practical Limitations of Shared Apertures :**

In principle, the shared aperture concept can be extended to utilize n apertures and reduce the overall height to provide significantly lower profile antennas. Obviously, the limit would be the use of single row antenna platforms. However, increasing the number of boards would require the use of a multitude of combining networks. These combining networks would be required to have minimal insertion loss. However, it is not practical to use waveguide structures, and flexible cables would be most likely used. Meanwhile, using an LNA at the output of each single platform could improve the overall performance but could lead to higher DC power consumption and appreciable errors due to amplifier imbalances. Hence, it is essential to compromise the overall structure and its performance.

5. CONCLUSION

Splitting/sharing n-apertures rather than utilizing a single large size aperture can help in developing low profile antennas. It is essential to use highly efficient radiating apertures in order to minimize the overall aperture to achieve a given gain as well as use phase shifters and LNAs to adjust the phases and set-up the noise figure. In our application, a cavity backed patch fed by waveguide network is essential to achieve over 70% aperture efficiency. Meanwhile, for manufacturing purposes, the use of MMIC LNAs and phase shifters could reduce the need for unnecessary calibration steps.

The proposed alternative structures for low-cost low-profile DBS antennas on the move are very promising. Both of them can be manufactured using substrate integrated waveguide (SIW) technology. To reduce the steering volume to ±25 degrees rather than 20-70 degrees, the slotted array has an inherent tilt angle that can help in reducing the height requirement. However, the cavity backed board needs to be mounted at 45 degrees initially to get to the ±25 degrees steering angle. A comparison between the two approaches is given in Table 4.

TABLE 4
Slotted waveguide array vs. the cavity-backed microstrip patch array

	Slotted waveguide array	**Cavity backed patch array**
Mounting position	Flat	Inclined at 45 degrees
Required area	Reduced gain by the cosine of the beam squint angle	The beam is always broadside
Beam squint	Serious problem and should be accounted for	No beam squint
Profile	Low	Larger
SIW implementation	Two layers	Three layers
Polarization	Single polarization; one at a time	Simultaneous operation

REFERENCES

[1] S. Yang*, et al.*, "Development of a slotted substrate integrated waveguide (SIW) array antennas for mobile DBS application," in *Antenna Application Symposium*, 2006, pp. 103-131.

[2] S. Yang and A. E. Fathy, "Cavity-backed patch shared aperture antenna array approach for mobile DBS applications," in *Antennas and Propagation Society International Symposium* 2006, pp. 3959-3962.

[3] W. Gestinger, "Elliptically polarized leaky-wave array," *IRE Transactions on Antennas and Propagation,* vol. 10, pp. 165-171, 1962.

[4] A. Simmons, "Circularly polarized slot radiators," *IRE Transactions on Antennas and Propagation,* vol. 5, pp. 31-36, 1957.

[5] S. Yang*, et al.*, "Slotted arrays for low profile mobile DBS antennas," in *Antenna Application Symposium*, 2005, pp. 3137-3140.

[6] S. Yang*, et al.*, "Ku-Band Slot Array Antennas for Low Profile Mobile DBS Applications: Printed vs. Machined," in *Antenna Application Symposium*, 2006, pp. 3137-3140.

[7] S. Yang*, et al.*, "Low-profile multi-layer slotted substrate integrated waveguide (SIW) array antenna with folded feed network for mobile DBS applications," in *Antenna Application Symposium*, 2007, pp. 3137-3140.

[8] S. Yang, "Antenna and arrays for mobile platforms," in *Phd dissertation, UTK*, 2008.

[9] M. Shahabadi*, et al.*, "Low-cost, high-efficiency quasi-planar array of waveguide-fed circularly polarized microstrip antennas," *IEEE Transactions on Antennas and Propagation,* vol. 53, pp. 2036-2043, Jun 2005.

[10] N. C. Karmakar, "Investigations into a cavity-backed circular-patch antenna," *IEEE Transactions on Antennas and Propagation,* vol. 50, pp. 1706-1715, Dec 2002.

[11] S. Yang and A. E. Fathy, "Design Equations of Arbitrary Power Split Ratio Waveguide T-Junctions Using a Curve Fitting Approach," *International Journal of Rf and Microwave Computer-Aided Engineering,* vol. 19, pp. 91-98, 2009.

[12] F. Xu and K. Wu, "Guided-wave and leakage characteristics of substrate integrated waveguide," *IEEE Transactions on Microwave Theory and Techniques,* vol. 53, pp. 66-73, Jan 2005.

[13] D. Busuioc*, et al.*, "High frequency integrated feed for front end circuitry and antenna arrays," *International Journal of RF and Microwave Computer-Aided Engineering,* vol. 19, pp. 380-388, May 2009.

[14] H. Pawlak*, et al.*, "High isolation substrate integrated coaxial feed for Ka-band antenna arrays," in *European Microwave Conference*, 2007, pp. 1507-1510.

[15] M. H. Awida and A. E. Fathy, "Substrate-Integrated Waveguide Ku-Band Cavity-Backed 2x2 Microstrip Patch Array Antenna," *IEEE Antennas and Wireless Propagation Letters*.

Measured Results of an X-Band Edge Slot Waveguide 1D Electronically Scanned Array (ESA)

Brian Herting, Wajih Elsallal, James West, John Mather and Daniel Woodell

400 Collins Rd. NE. M/S: 108-102
Advanced Technology Center
Rockwell Collins
Cedar Rapids, IA 52498

Abstract: In this paper, the authors present the measured results and lessons learned from the fabrication of a flight-worthy 1D electronically scanned array (ESA) at X band. The 1D ESA consists of a 24″ diameter edge slot waveguide aperture, a 1:36 compact ridge waveguide corporate feed, and a series of 36 dual mode ferrite phase shifters. Previously developed mathematical models and EM simulation tools [1-3] were used to design the edge slot waveguide aperture, which was center fed from the back by a flush mounted, compact ridge waveguide corporate feed. Excellent agreement between simulated and measured results was obtained as the fabricated 1D ESA met all design requirements over the desired band (9.3 – 9.4 GHz) and scan volume (-40° to +40°).

1. Introduction

Most of today's Radar Systems operate with a mechanical positioner for both azimuth and elevation scanning. As more functionality is added, e.g. radar terrain awareness warning system (RTAWS) and runway incursion, faster scan rates are required to alleviate the "busy" radar issue. In general, an electronic scanning array (ESA) in both azimuth and elevation would benefit such system. For our specific needs, it was determined that the benefits of an electronic scanning in the azimuth axis to be minimal. Therefore, the decision was made to investigate electronic scanning for the elevation axis only to alleviate the "busy" radar problem and offers improved pointing accuracy.

In less than seven months of development, the Rockwell Collins Advanced Technology Center (ATC) built a flight worthy 24″ diameter 1D ESA prototype consisting of an edge slot waveguide aperture, a ridge waveguide corporate feed, a set of 36 dual-mode ferrite phase shifters, and a beam steering computer (BSC).

2. Development 1D ESA Prototype Design

The 1D ESA prototype involved detailed electrical and mechanical design. In this section, an overview is given of the design for the 4 major sub-components: the aperture, the feed, and the excitation control.

a. Aperture

The 1D ESA prototype aperture design consisted of 36 resonant edge slot waveguide stick radiators of differing lengths similar to that shown in Figure 1. Each edge slot waveguide stick is fed at its center by a single ridge waveguide through a coupling slot. The entire electrical design was accomplished using method described in references [1-3] that can be summarized as following:
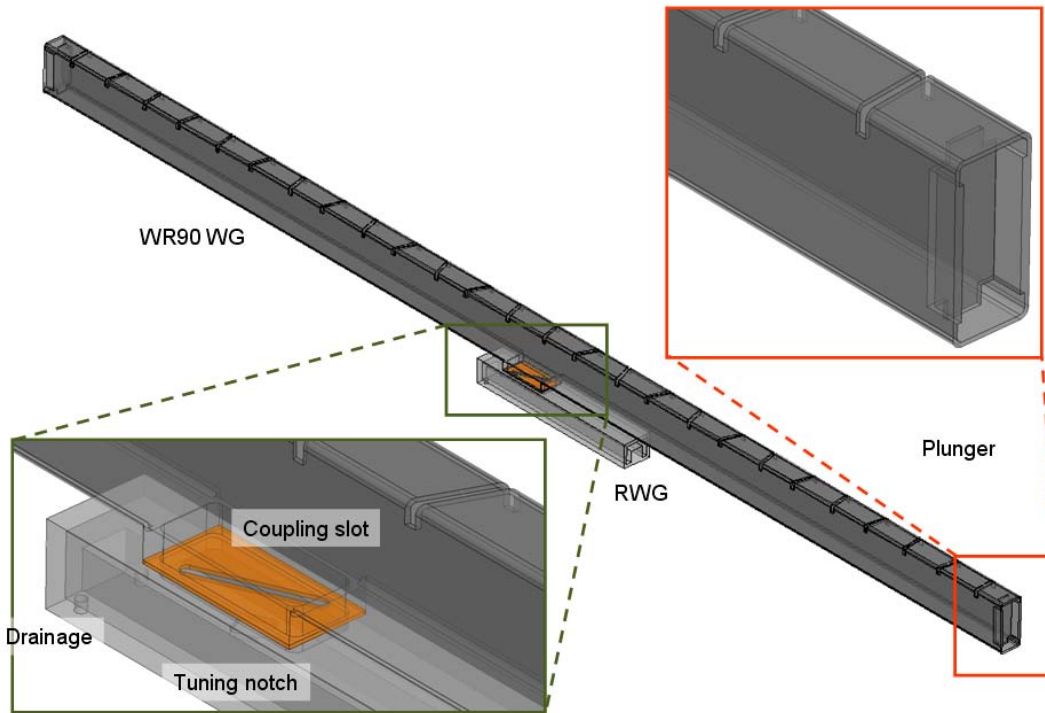

Figure 1. Edge slot waveguide stick radiator for 1D ESA prototype aperture.

I. **Determine slot impedance and design parameters in waveguide (see reference [1]).**
   a. Generate the expressions for slot tilt angle as a function of slot conductance and slot depth as a function of tilt angle using the incremental conductance method in Ansoft HFSS™.
   b. Determine each slot's required tilt angle and depth to generate the appropriate amplitude taper for the desired array side lobe level (SLL).

II. **Control amplitude and phase distribution in the array (see reference [2]).**
   a. Simulate each edge slot waveguide stick in a finite × infinite array setting using master/slave boundaries in HFSS, and correct anomalies in the amplitude distribution due to higher order mode coupling from the neighboring radiating elements and the waveguide feed.
   b. Determine the active element pattern of each edge slot waveguide stick by simulating a finite × finite "window" of the entire array. This allows more

accurate analysis of the array. The aperture shown in Figure 2 shows the "windows" used for this analysis. The approach is especially helpful when the whole aperture size is large.

  c. Post process data from step II-b using standard array theory to predict array performance as a function of scan.

III. Determine the dimensional tolerance of the final slot parameters (see reference [3]).

  a. Perform a Monte Carlo analysis utilizing a standard shunt admittance transmission line model for the edge slot waveguide in a circuit simulator. The shunt admittances are derived by interpolating between a three dimensional dataset generated in Ansoft HFSS™ from step I-a.
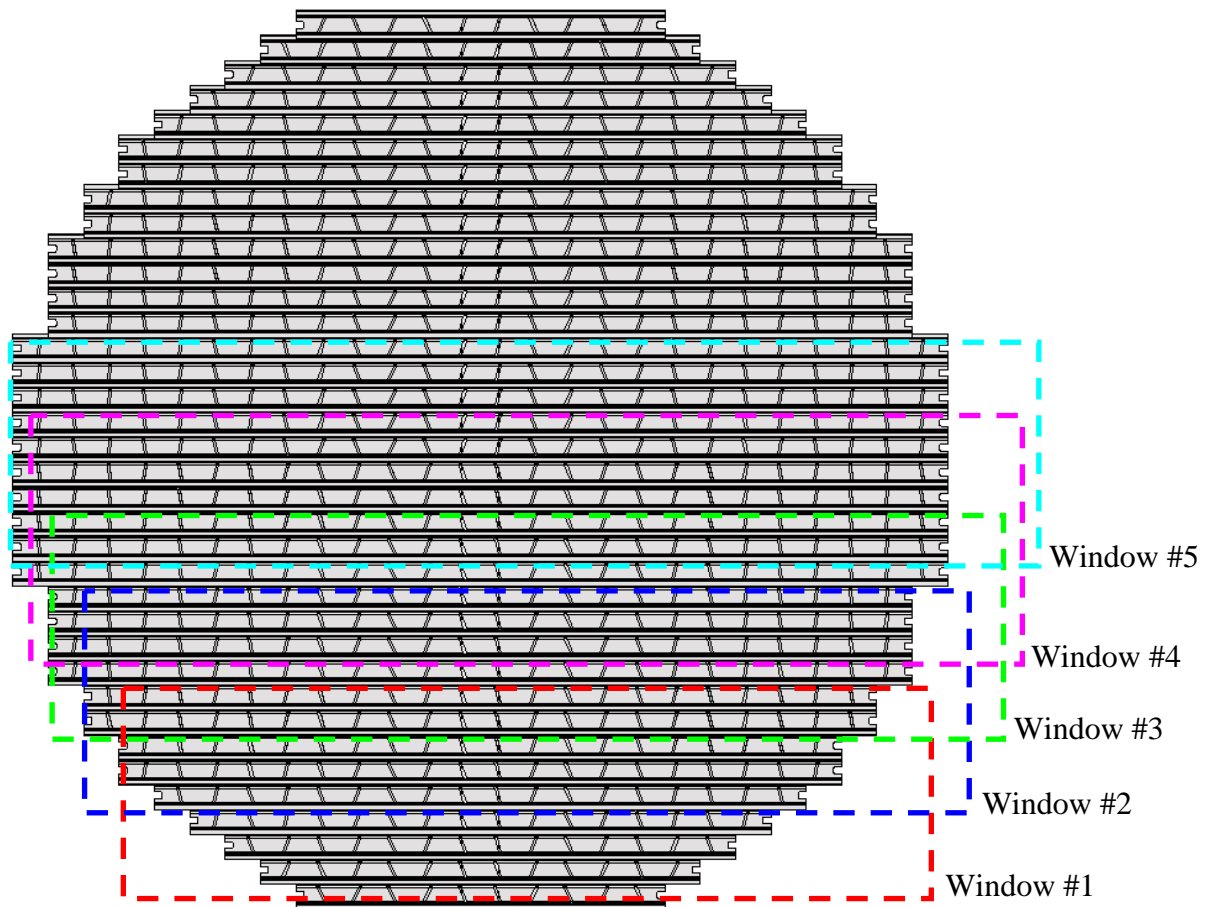

Figure 2. Simulation of a large finite array using overlapped windows of sticks. This reduces the complexity of the computational domain to include edge effect.

b. Feed

The 1:36 corporate feed was designed and fabricated in ridge waveguide using quadrature hybrid couplers. Ridge waveguide was selected for its low loss and quadrature hybrids

were used to provide high isolation between the 36 feed outputs. The RF input to the feed includes both a sum and delta port for advanced radar operation.

The design of the 1:36 Ridge Waveguide Corporate Feed was accomplished by combining accurate Ansoft HFSS 3D electromagnetic (EM) models of the ridge waveguide feed subcomponents in Ansoft Designer (see Figure 3) utilizing the following procedure:

I. Construct and optimize half, or 18 outputs, of the feed by varying the
   a) Hybrid Coupler coupling ratio via the common wall slot length and width to achieve the desired amplitude taper, and
   b) electrical lengths of connecting waveguide to achieve near modulo 90° phase at all outputs.
II. Copy the optimized half of the feed to construct the other half of the feed and connect both halves using a Magic Tee.

The advantage of this approach of combining Ansoft HFSS models in Ansoft Designer is that (1) the effective mesh density can be much greater leading to improved accuracy and (2) the efficiency of only having to perform a 3D full wave simulation on the component being varied rather than on the entire feed.

Simulation results of the optimized and integrated 1:36 Ridge Waveguide Corporate Feed predict an insertion loss of approximately 0.2 dB with a maximum RMS amplitude and phase errors of 0.064 dB and 1.275° respectively. Figure 4 shows the simulated amplitude taper as it compares with the desired taper. Measurements showed RMS amplitude and phase errors of only 0.296 dB and 3.365° respectively. This level of error is more than adequate to provide the required SLL performance of the final ESA. The input return loss and insertion loss were also quite good at better than -23 dB and typically 0.5 dB respectively.

The feed was fabricated in a combination of manufacturing steps that involved detailed machining and dip brazing. The assembly is shown in Figure 5.
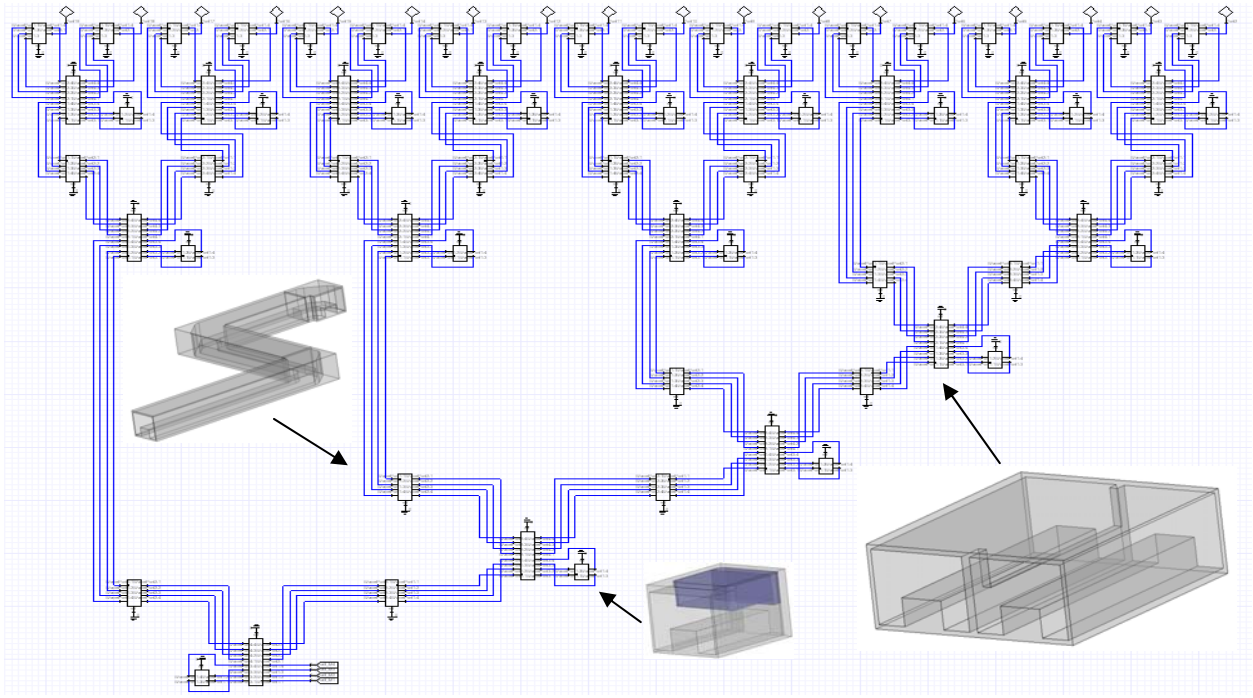
(a)
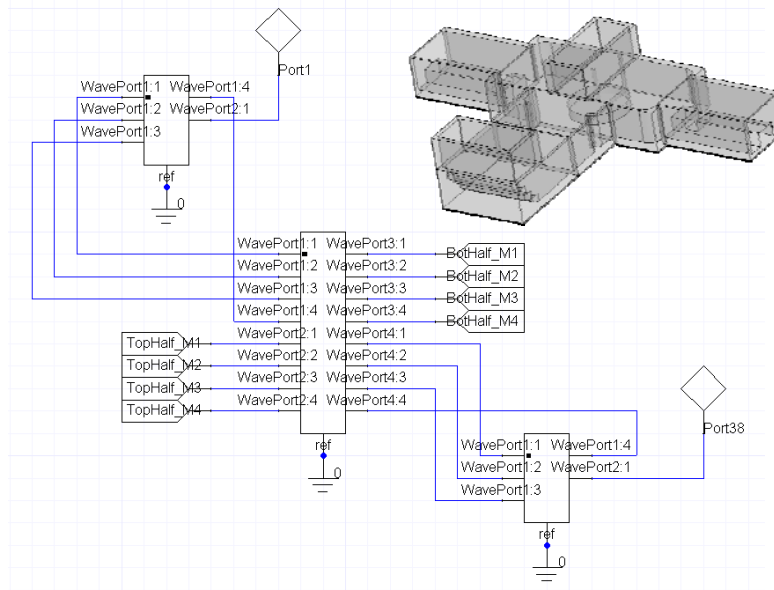
(b)

Figure 3. Ansoft Designer Integrated Feed Schematic. (a) Half of the ridge waveguide feed of the 1D edge slot waveguide ESA aperture. The subcomponents shown are narrow-wall coupler, waveguide load and bends. (b) Combing the feeds in part (a) with the Magic-Tee at the RF system input.
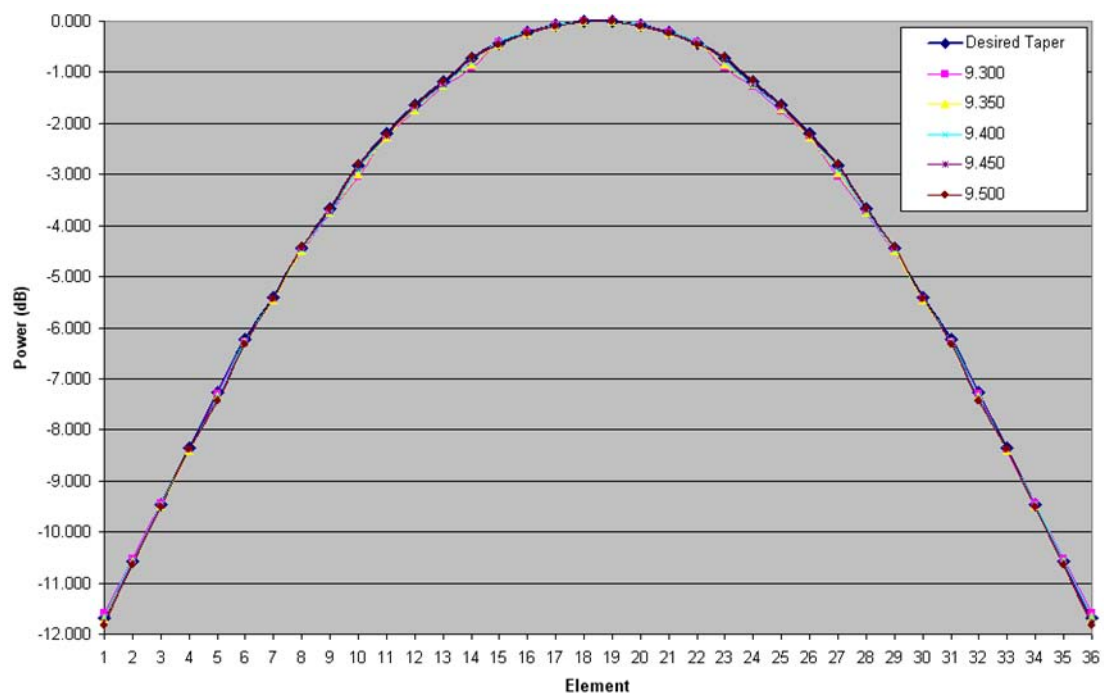
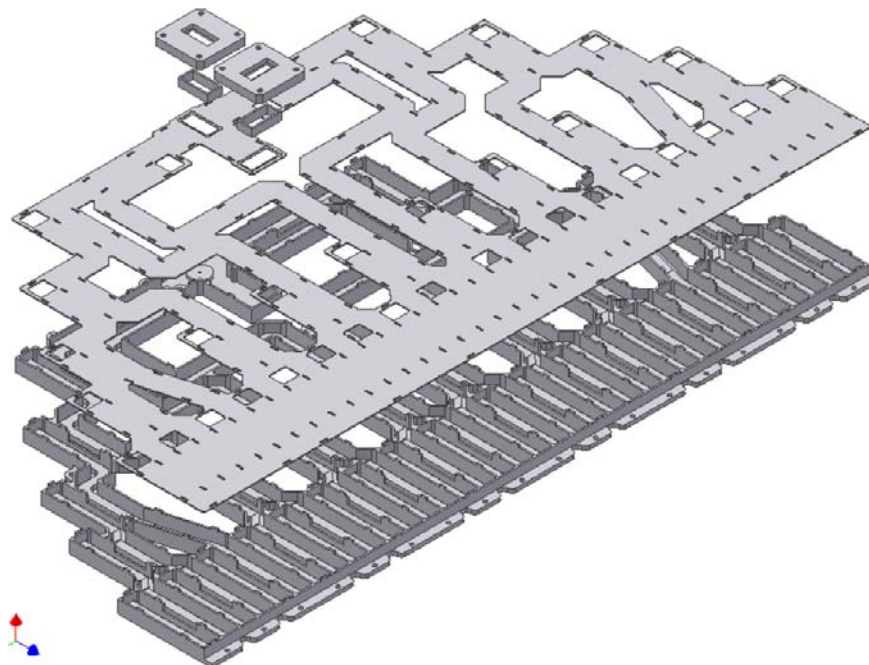Figure 4. Ansoft Designer Integrated Feed Simulated Amplitude Taper.

Figure 5. Waveguide feed corporate splitter dip braze assembly.

c. Excitation Control

Dual mode ferrite phase shifters were chosen as the excitation control for the 1D ESA prototype due to their rugged nature and proven performance. These devices and their accompanying drivers were procured from MAG Corporation. The insertion loss, return loss and switching speed of the devices were measured to be 0.7 dB typical, -17 dB minimum, and 30 μs respectively.

3. 1D ESA Prototype Measured Performance

A planar near field scan of the 1D ESA was taken between 9.30 and 9.40 GHz for scan angles from -60° to +60° in 10° increments. The equipment setup is shown in Figure 6.
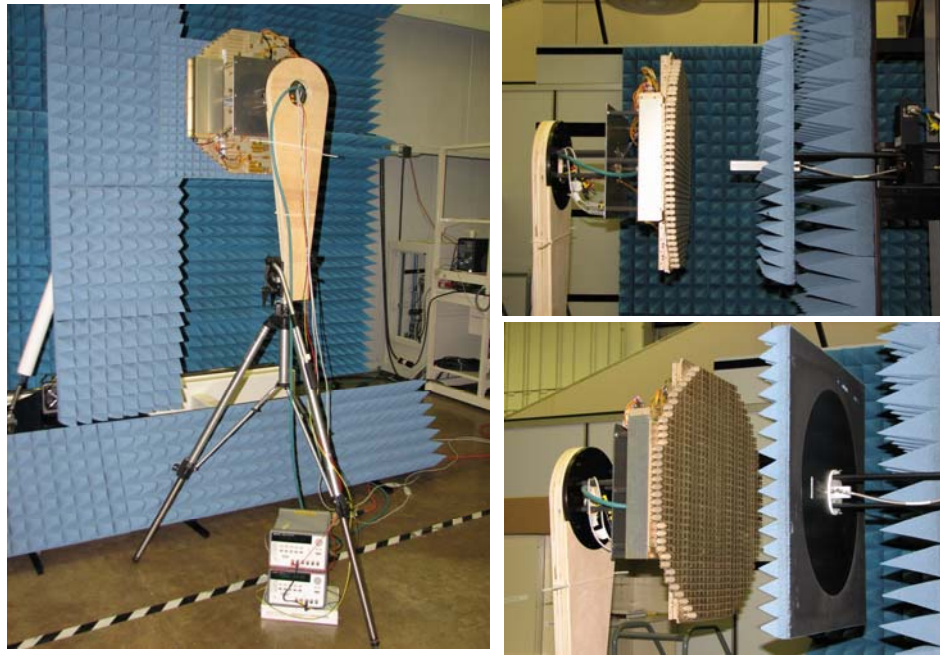

Figure 6. Near field measurement setup

Comparision between a sample of measured and simulated data at 9.35 GHz at two scan angles are shown in Figure 7 and 8. The figures confirm that the window simulation results, which were briefed in section 2 of this paper, has a better agreement with the measured data than that predicted from the finite x infinite array simulation analysis. Although the desired design goal was to achieve a -30 dB sidelobe, simulation and measured data suggest that due to the inherent nature of tilted slots [1], the sidelobe will not exceed -22.5dB between broadside and 40° scan angle, see Figure 9. The measured aperture's gain suggests that the aperture will follow a $\cos^{1.3}\theta$ scan loss (see Figure 10) with a maximum gain of 32.5dB at broadside. By utilizing the mirroring technique discussed in reference [2], the cross polarization will always stay lower than -25dB at all scan angles, see Figure 11. Due to the dimensional tolerance in the fabricated feed and aperture, the results of scanning at both azimuth planes are not completely symmetric but they do stay within acceptable limits.
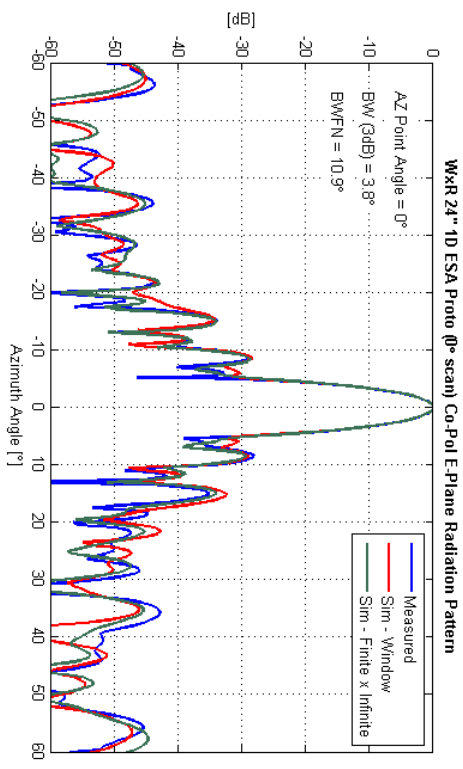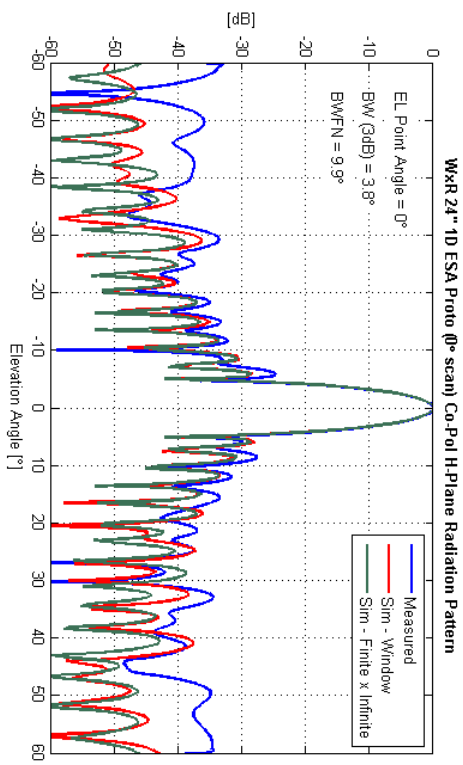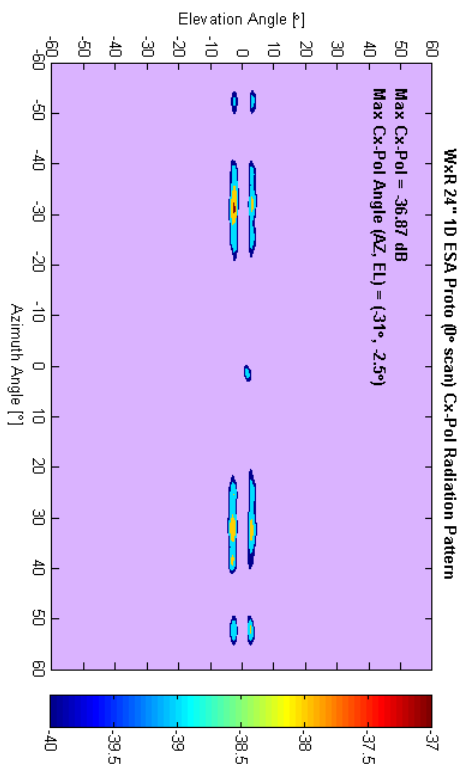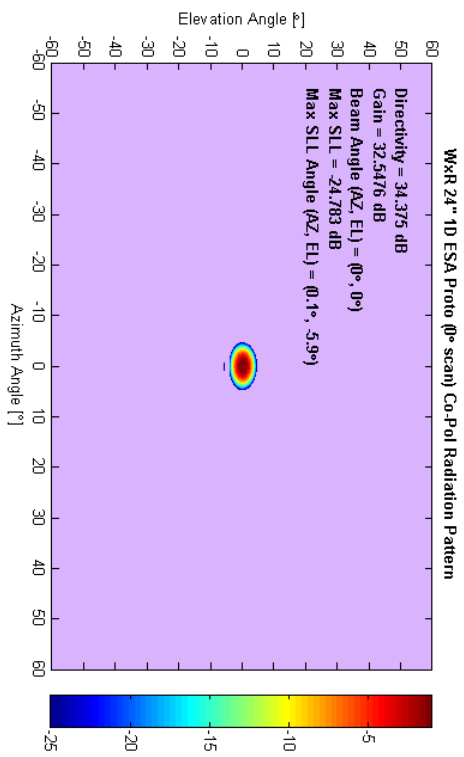
Figure 7. Measured and simulated performance of the 1D ESA prototype at broadside (θ=0°, Φ=0°).

356

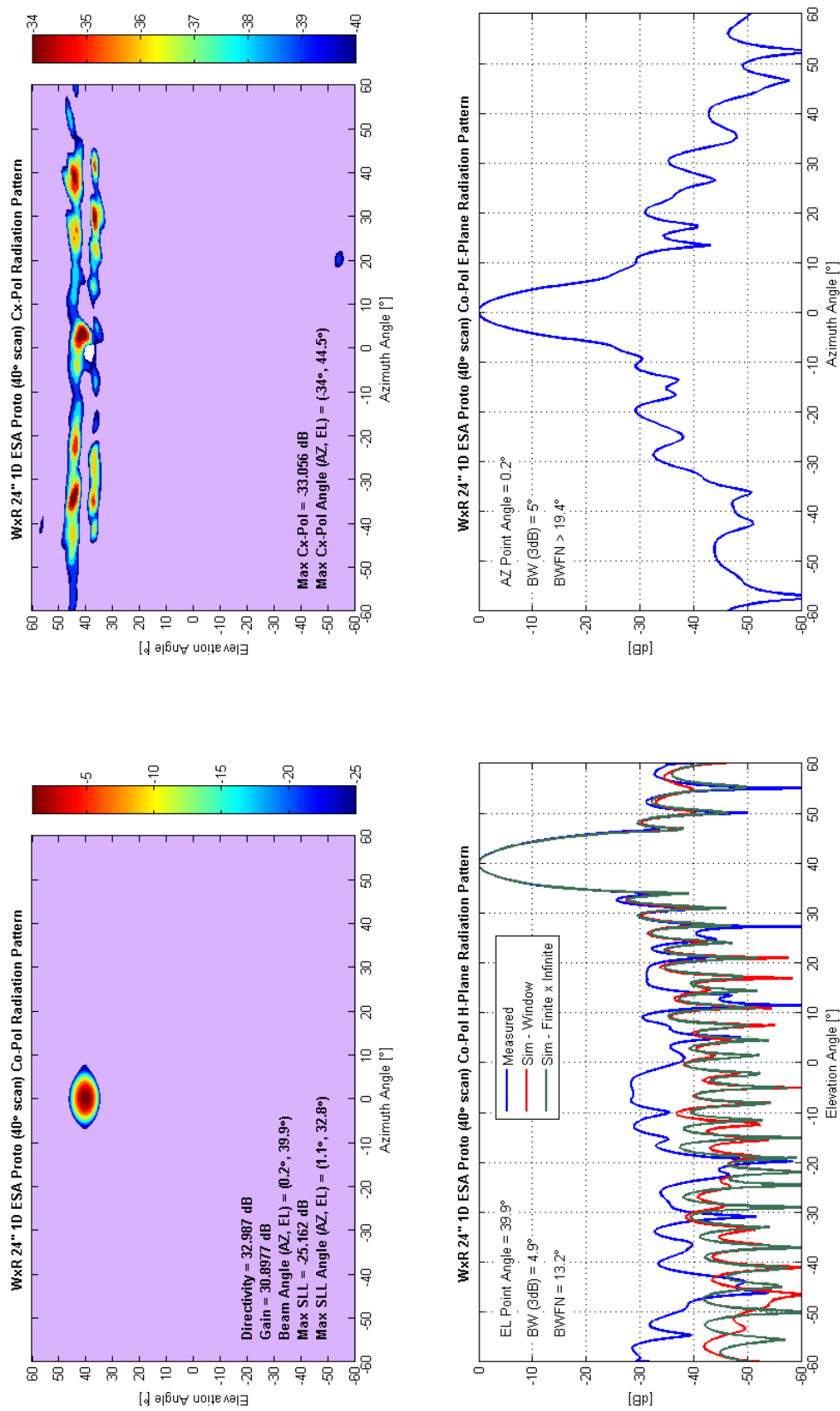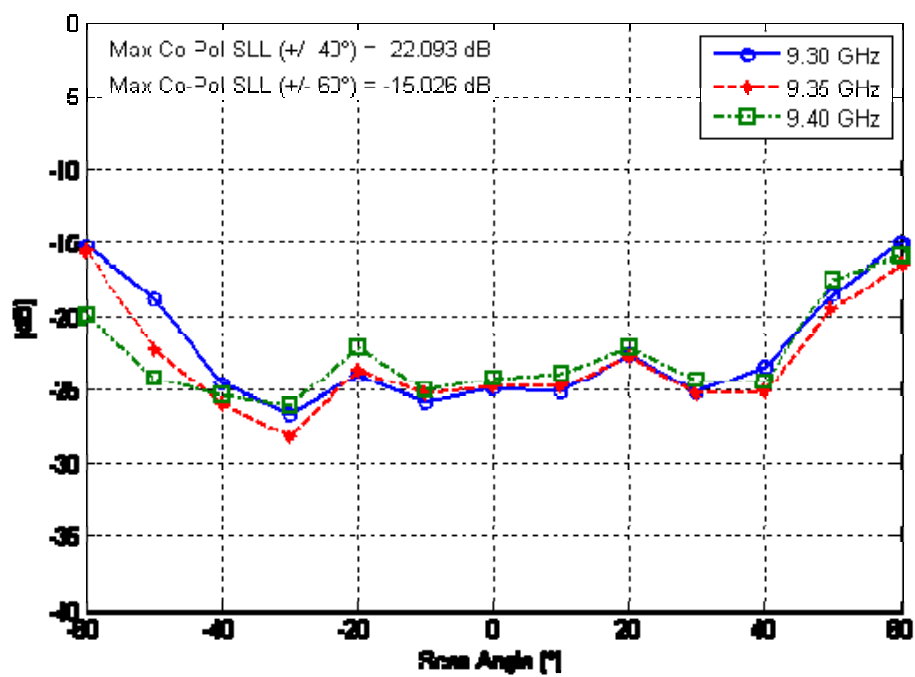Figure 8. Measured and simulated performance of the 1D ESA prototype at (θ=40°, Φ=0°).

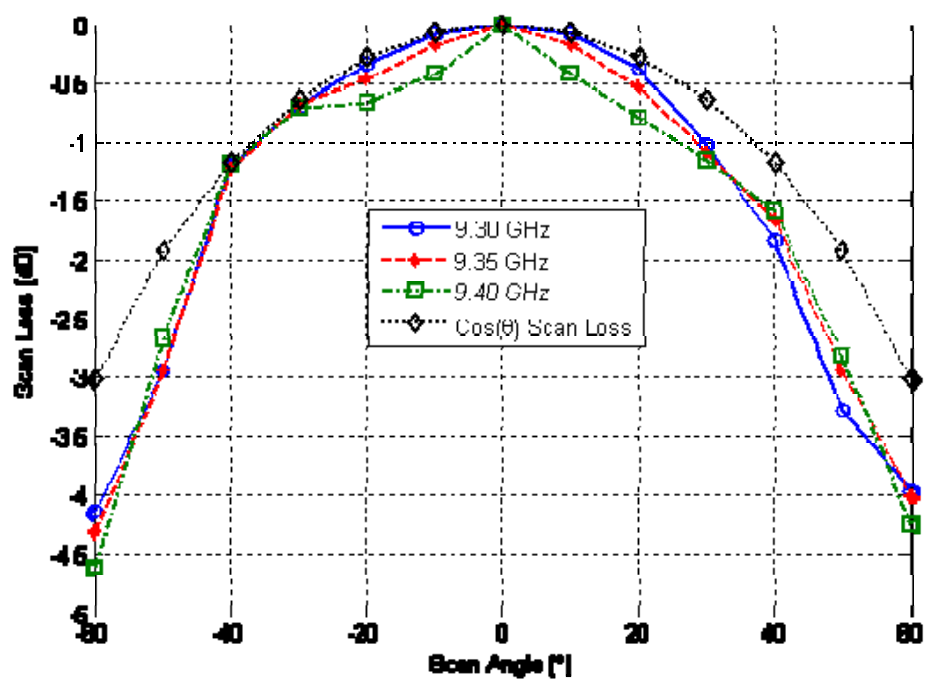Figure 9. 1D ESA prototype max SLL vs. scan

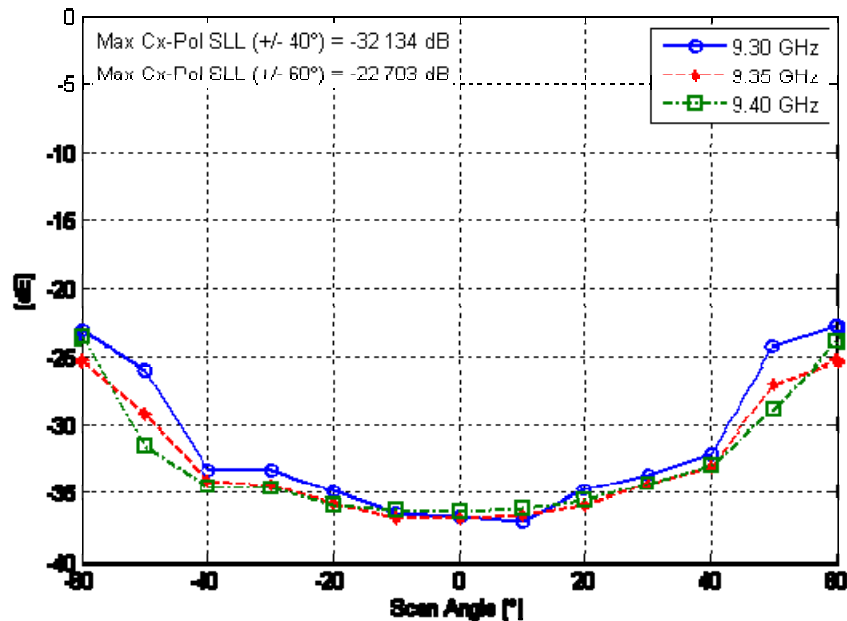Figure 10. 1D ESA prototype active scan loss vs. scan

Figure 11. 1D ESA prototype max Cx-Pol vs. scan

4. CONCLUSION

The 1D ESA prototype developed by the Rockwell Collins Advanced Technology Center is flight worthy and successfully met most of design requirements set forth at the beginning of the program. During the course of development, robust computational electromagnetic (EM) models were utilized that allowed a first time successful build of this complex ESA system in less than seven months. Excellent agreement between simulated and measured results was obtained over the desired band (9.3 – 9.4 GHz) and scan volume (-40° to +40°).

References:

1. M.W. Elsallal, B. J. Herting and J. B. West, "Planar Edge Slot Waveguide Array Design Using COTS EM Simulation Tools," *Antenna Applications Symposium*, September, 2007. Monticello, IL

2. B. J. Herting, M.W. Elsallal and J. B. West, "Sub-Array Mirroring for the Mediation of Second-Order Beams in Planar Edge Slot Waveguide Arrays," *Antenna Applications Symposium*, September, 2007. Monticello, IL

3. B. J. Herting, M.W. Elsallal, J. C. Mather and J. B. West, "Novel Hybrid Tolerance Analysis Method with Application to the Low Cost Manufacture of Edge Slot Waveguide Arrays," *Antenna Applications Symposium*, September, 2008. Monticello, IL

DUAL-BAND, DUAL-POLARIZED ANTENNA ELEMENT AND ARRAY

W. Mark Dorsey[1,2], Amir I. Zaghloul[2,3], John Valenzi[1]

[1]US Naval Research Laboratory, Washington, DC, USA
[2]Virginia Polytechnic Institute and State University, Virginia, USA
[3]US Army Research Laboratory, Adelphi, MD, USA

Abstract: Dual-band antenna elements that support dual-polarization provide ideal performance for applications including space-based platforms, multifunction radar, wireless communications, and personal electronic devices. In many communications and radar applications, a dual-band, dual-polarization antenna array becomes a requirement in order to produce an electronically steerable, directional beam capable of supporting multiple functions. The multiple polarizations and frequency bands allow the array to generate multiple simultaneous beams to support true multifunction radar.

The element described in this paper achieves a low-profile from its printed circuit board realization. The high band square ring slot is realized in stripline, and the low band element is a shorted square ring element. Both elements can be operated with either dual-linear or dual-circular polarization. The size of the low band radiator can be reduced by the introduction of a capacitive loading structure. This size reduction reduces the element's footprint and facilitates array placement. Array analysis reveals good axial ratio and cross-polarization discrimination over a wide grating lobe-free scanning region in both frequency bands. The operation of this element is verified with simulated and measured results.

1   Introduction

As the field of wireless communications grows, electronic devices are required to support multiple functions that require communications within distinct frequency bands. As the requirements for personal wireless devices increases, the desired footprint for the device seemingly decreases. These size restraints make dual-band antenna elements virtually a necessity in order to minimize the number of antenna elements required within the device. Moreover, personal communications devices operate within restricted frequency bands of the electromagnetic spectrum. An antenna element capable of simultaneously operating with two orthogonal senses of polarization can efficiently use the allotted frequency spectrum by reusing frequencies. This increases the capacity of the system without requiring additional frequency coverage. A dual-band antenna element capable of operating with dual-orthogonal polarization in each frequency band provides invaluable flexibility to a system. Additionally, if this element could be realized in printed circuit board technology, it could be made low profile and lightweight while allowing for easy integration with the accompanying electronics in the system and providing affordable manufacturing costs.

Antenna arrays are used to provide highly directional beams that can be scanned electronically. Applications requiring large arrays range from communication, to radar, to electronic warfare (EW). As the number of required functions increases, the number of required potentially large arrays increases as

well. Significant research has been completed to minimize the number of arrays on various platforms. For example, the U.S. Naval Research Laboratory (NRL) carried out the Advanced Multifunction RF System (AMRFS) program to develop a broadband array capable of performing multiple communications, radar, and EW functions in an effort to reduce the number of topside antenna arrays on a U.S. Navy ship [1, 2]. The AMRFS effort was chosen to have broadband coverage in order to provide adequate performance for multiple functions. A dual-band, dual-polarized antenna array would also permit one array to carry out a number of functions, thus reducing the number of large arrays required in a system. If the frequency bands were chosen to satisfy multiple needs aboard the ship, a large array of dual-band, dual-polarized antenna elements would reduce the number of expensive – both in cost and real estate – on the ship.

The research described in this document is aimed at designing a dual-band, dual-polarized antenna element that can operate both as an isolated element as well as a part of an array environment. The element achieves a low profile from its printed circuit board realization and contains two concentric, dual-polarized radiators. The low frequency band radiator is a shorted square ring antenna, and the high frequency band radiator is a square ring slot. A novel size reduction technique was developed that allows for significant reduction of the element's footprint. This size reduction facilitates the placement of the element within an array environment. The design discussed in this document operates at frequencies contained in separate industrial, scientific, and medical (ISM) bands. These frequency bands are increasingly popular in low power communication devices because unlicensed operation is permitted. These bands were chosen due to their popularity, but this antenna is not restricted to these bands or frequency ratio.

The exploration into the design of this element dates back to the late 1980s when Sorbello and Zaghloul completed research on introducing perturbations to the corners of square ring slot antennas to produce single-feed circular polarization [3]. Their work discussed the addition of orthogonal feed lines to generate dual-linear or dual-circular polarization from a square ring slot in an array environment, and it received a patent in 1996 [4]. Ravipati and Zaghloul discussed a dual-band antenna element in 1994 that was suitable for wide-angle scanning in a phase array environment[5]. This element was a hybrid of microstrip and waveguide radiators that involved the placement of an open-ended waveguide inside of the shorted region of a shorted annular ring antenna. Their element was capable of operating with dual-linear polarization in each of the two frequency bands, but was unable to use dual-circular polarization.

In 2007, Dorsey and Zaghloul combined the two previously mentioned elements by placing a square ring slot in the center of a shorted square ring antenna element [6]. This element used a size reduction technique designed by Dorsey and Zaghloul [7, 8] to reduce the size of the element and allow for wide frequency ratios than the design presented in [5]. In order to accurately analyze the performance of this complex element in an array environment, Dorsey derived an array analysis approach that uses multiple active element patterns to approximate the exact active element pattern for elements in given geometrical regions within the array [9].

The remaining sections of this document detail the design and analysis of dual-band, dual-polarized antenna elements and arrays. The analysis begins with a detailed look at the constituent antenna elements that serve as the building blocks for the dual-band, dual-polarized antenna element. After a thorough understanding of the constituent elements is established, the elements are combined to form a dual-band

element capable of simultaneous operation with orthogonal polarizations. A dual-band dual-CP antenna element was designed, built, and measured to illustrate the performance. The performance of this element is compared to existing elements in the literature. The element performance is also analyzed in an array environment. A hybrid technique is developed that uses multiple active element patterns in the analysis. This technique is applied to the dual-band dual-polarized antenna array to show that the array maintains excellent polarization characteristics at wide scan angles in both frequency bands.

2 Constituent Element Analysis

The basic building blocks for the coplanar, dual-band, dual-polarized antenna element are the shorted square ring antenna and the square ring slot antenna. The former will be used as the low band radiator, while the latter has been selected as the high band radiator.

Printed slot antennas have the advantage of wider impedance bandwidth than the traditional microstrip antennas. The resonant frequency of the square annular ring antenna can be derived by utilizing a transmission line analysis following from [10]. The square annular ring antenna can be divided into two transmission line sections of lengths l_1 and l_2, where the total length of the ring is $l=l_1+l_2$ as shown in Figure 2-1. Each of these sections is viewed as a length of transmission line, and $z_{1,2}$ measures the distance along the corresponding line as measured from the $z_{1,2}=0$ point. If the transmission line is taken to be lossless, the voltage and current on the line can be defined by (1) and (2). In these equations, Z_0 is the characteristic impedance of the line, and $\beta_{1,2}$ is the propagation constant of the specified line.
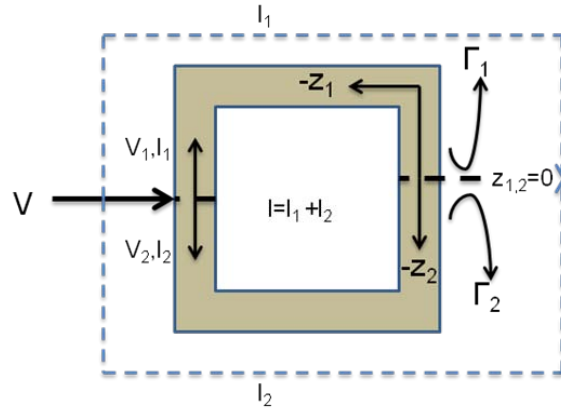

Figure 2-1: Transmission line model of the square annular ring antenna element

$$V_{1,2}(z_{1,2}) = V_0^+\left(e^{-j\beta z_{1,2}} + \Gamma_{1,2}(0)e^{j\beta z_{1,2}}\right) \tag{1}$$

$$I_{1,2}(z_{1,2}) = \frac{V_0^+}{Z_0}\left(e^{-j\beta z_{1,2}} - \Gamma_{1,2}(0)e^{j\beta z_{1,2}}\right) \tag{2}$$

The resonant frequency of the square ring slot structure corresponds to the frequency where a standing wave exists on the transmission lines. The standing wave on each section of the transmission line repeats for multiples of the half-wavelength in the guide. As a result, the shortest length of the ring that can support the standing wave is one guided wavelength. The expression for the resonant frequency is shown

in (3). This expression contains a factor – R – that accounts for the presence of a dielectric material in the slot. Multiple expressions exist for R including those shown in [11] and [12].

$$f_0 \approx \frac{c}{2(l_1 + l_2)} R \tag{3}$$

Opposing corners of the square ring slot antenna can be perturbed to generate circular polarization (CP) with a single feed point. The introduction of these triangular perturbations excites two, near-degenerate modes. If these modes are excited in phase quadrature, CP performance is obtained. If a single feed line is present, either RHCP or LHCP is radiated, with the sense of CP being determined by the location of the feed with respect to the truncations. However, if orthogonal feed lines are present, both senses of CP can be excited simultaneously as described in [3]. The geometry of the microstrip realization for a square ring slot with single-feed CP is shown in Figure 2-2.
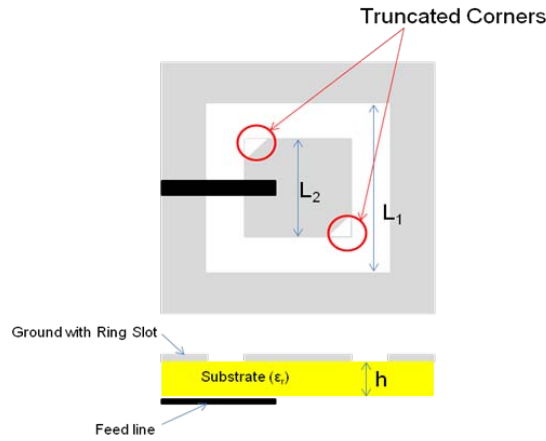

Figure 2-2: Illustration of a square ring slot antenna using perturbations to excite CP with a single feed line (microstrip realization)

The shorted annular ring antenna serves as the basic element for the low band operation of the proposed dual-band element. This element consists of an annular aperture printed on a microwave substrate shorted at the inside of the annulus to the ground plane. This type of element is commonly realized with a circular aperture shape, but it can also be realized with the square aperture. The modes in the circular shorted ring antenna are governed by the transcendental equation shown in (4), where a and b are the outer and inner radii of the radiating annular ring respectively. In (4), k_{n1} is the wavenumber of the dominant TM_{11} mode. The geometry of the square shorted ring antenna does not lend itself to a convenient closed-form expression, but the performance of the element is analogous to the circular design. In both cases, the TM_{11} mode is typically preferred owing to its broadside radiation pattern similar to that of a traditional microstrip antenna.

$$Y_n(k_{n1}b)J_n'(k_{n1}a) = J_n(k_{n1}b)Y_n'(k_{n1}a) \tag{4}$$

If perturbations are present at opposing corners of this design as shown in Figure 2-3, CP performance can be obtained with a single feed point. The area of the truncations in this design can be calculated from the quality factor of the unperturbed antenna using (5) [13]. An orthogonal feed can be added for dual-CP performance.
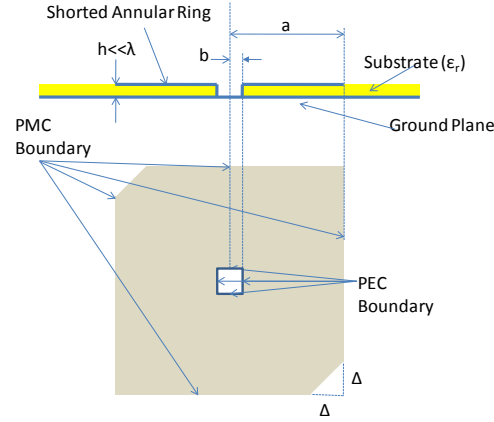
363

$$\Delta_{AREA} = \frac{1}{2Q} \tag{5}$$

Figure 2-3: Illustration of a shorted square ring antenna using perturbations to excite CP with a single feed point

3 Dual-Band, Dual-Polarized Antenna Element

The dual-band, dual-CP element is illustrated in Figure 3-1. The topology of this element has been discussed in [14]. An isometric view of the element is shown in Figure 3-1(a). The shorted square ring and square ring slot elements used for the low and high band operation respectively are indicated. The top view shown in Figure 3-1(b) indicates the pertinent parameters for the design. The shorted square ring has an outer side length of L_0 and an inner side length of L_1. The high band square ring slot has outer and inner side lengths of L_1 and L_2 respectively. The element consists of a microwave substrate with a ground plane on the bottom side and conductor on the top. The square ring slot acts as a slotted stripline circuit that forms the high band radiator. The portion of the conductor outside of the slot is treated as the low band shorted square ring. The low band radiator is shorted to the ground plane with plated through holes located at the inner perimeter of the shorted square ring. The top view of Figure 3-1(b) also shows the isosceles triangle shaped perturbations at opposing corners of both the high and low band radiator. The triangular perturbations have side lengths of Δ_{LB} and Δ_{HB} for the low and high band respectively. The use of these perturbations creates two, near-degenerate modes that provides CP polarization with a single feed point. The location of the feed point with respect to the truncated corners determines the sense of CP. Therefore, by having two orthogonal feed points for each band, this dual-band element is capable of generating simultaneous dual-CP operation for each frequency range.

The high band square ring slot element is fed with orthogonal feed lines. These stripline transmission line feeds pass underneath of the square ring slot, and they are terminated in open circuited stubs. In many instances, the ideal stub length for achieving the best axial ratio and impedance match results in the feed extending beyond the center of the element. If the orthogonal feed lines were present in the same vertical plane, they would physically intersect as they passed this center point. In order to eliminate this problem, a thin substrate (referred to as the feed substrate) is placed at the center of the dielectric profile. The two feed lines are printed on opposing sides of the feed substrate. The feed substrate is then sandwiched between two other substrate layers and conductors are present on the top and bottom of the sandwiched dielectric profile.
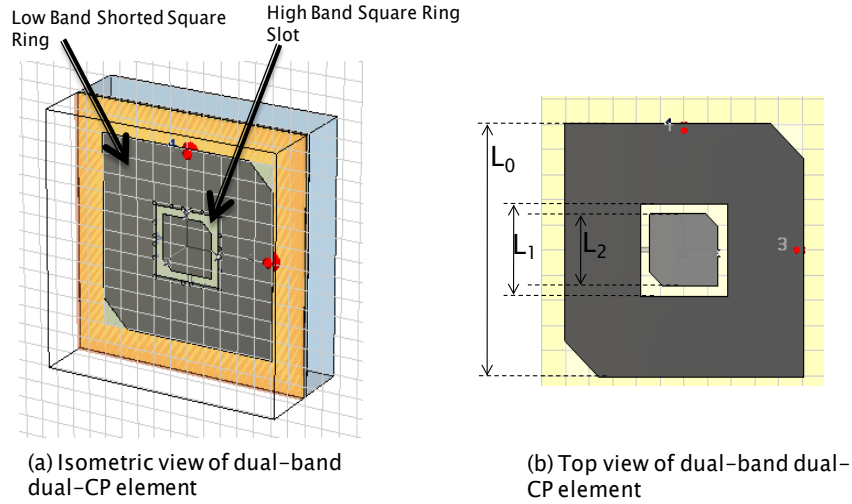
Figure 3-1: Dual-band, dual-polarized antenna element topology

The stripline feeds for exciting the high band element must pass through the plated through holes that provide the shorting mechanism for the low band element. These plated through holes serve multiple purposes. As previously mentioned, they are used as the shorting mechanism for the low band element. Additionally, they act as mode suppressors for the parallel plate mode that can be generated from the slotted stripline element used for the high band radiator. Slotted stripline designs can be subject to power loss, low efficiency, and degraded pattern shape as a result of the parallel plate mode [15]. Work by Bhattacharyya, Fordham, and Liu [16] has shown that vias can be used to suppress the parallel plate mode in slot-coupled patch antennas fed by stripline feed networks. Their design contains vias surrounding the slot. They show that the presence of the vias improves the gain by increasing the available power for radiation. In this element design, the shorting vias for the low band element will also assist the efficiency of the high band element by working to eliminate the propagation of the parallel plate mode.

3.1 Simulated and Measured Results

An element using this topology was designed to cover the 2.45 GHz and 5.8 GHz ISM bands with dual-CP operation in each band. The element used a feed substrate of thickness 0.004" with a dielectric constant of 2.33 (Rogers RT5880 material). The feed substrate was sandwiched between 0.060" thick dielectric layers with the same properties as the feed substrate. The stripline feeds that excite the orthogonal polarizations in the high band are transitioned to a microstrip layer beneath the antenna ground plane. This layer has a 0.030" thick layer of the same dielectric material used on for the remaining layers. The high band feed transition is present for two reasons. Firstly, the presence of the high band feeds under the low band radiator was seen to degrade the polarization purity of the low band CP states. Secondly, the presence of the microstrip layer beneath the antenna ground plane facilitates antenna installation.

This antenna element was simulated, built, and measured. The simulations were performed using CST Microwave Studio, a computational electromagnetic software package employing the finite integration technique (FIT) [17]. The assembly of the element involves a complex process due to the multilayered

365

design of the antenna element. Each of the layers must be etched, and selected layers must be bonded together with precise alignment. The layers were bonded together with a dielectric-matched epoxy having an overall thickness of approximately 0.001". The location, thickness, and material properties of the epoxy were included in the simulations. A photograph of the constructed element is provided in Figure 3-2. The photograph shows the top view of the antenna element on the left and the bottom view on the right. The bottom view shows the location where the four connectors are installed.
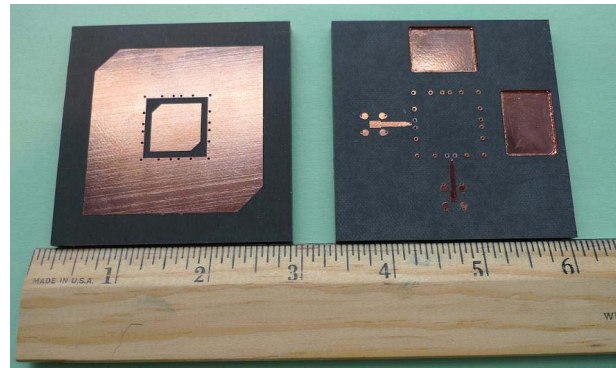

Figure 3-2: Photograph of the dual-band, dual-CP antenna element operating at the 2.45 and 5.8GHz ISM Bands

The dual-band, dual-CP antenna element can be viewed as a four port microwave network. The high band RHCP and LHCP are defined as ports 1 and 2 respectively, while the low band LHCP and RHCP are ports 3 and 4 respectively. The measured s-parameters are compared to the simulated s-parameters in Figures 3-3 for the high band and 3-4 for the low band. Each of these figures shows the magnitude of the s_{ij} parameter for a fixed 'j' value.

The results show good agreement between the measurements and simulations. For the high band RHCP state, all four s-parameters match very well with the simulated results. The return loss (s_{11}) shows a value exceeding 10dB across the band of operation. The biggest discrepancy between measurements and simulations for the high band RHCP is seen in the s_{21} parameter. This parameter defines the coupling between the high band LHCP and RHCP ports. The simulations showed a null with minimum value of -42dB located at 5.75 GHz, while the measurements showed a slightly shallower null (minimum value of -29dB located at 5.675 GHz. Comparison of the frequency location of the s_{21} null indicates a 1.3% discrepancy between measurements and simulations. The coupling between the high band RHCP port and the two low band ports (s_{31}, s_{41}) show good agreement. Similar results are seen for the high band LHCP port shown in Figure 3-3b.

The only discrepancies between the measured and simulated s-parameters for the low band ports are seen in the two return loss curves (s_{33} and s_{44}) shown in Figure 3-4. These differences are partially attributed to the loss present in the integration of the coaxial connector. The simulation models utilized a discrete port to excite the low band polarizations. A discrete port is a simplified, ideal version of a coaxial probe that negates the circuit parameters and physical size of the connector. All remaining s-parameters are in excellent agreement with the simulations.
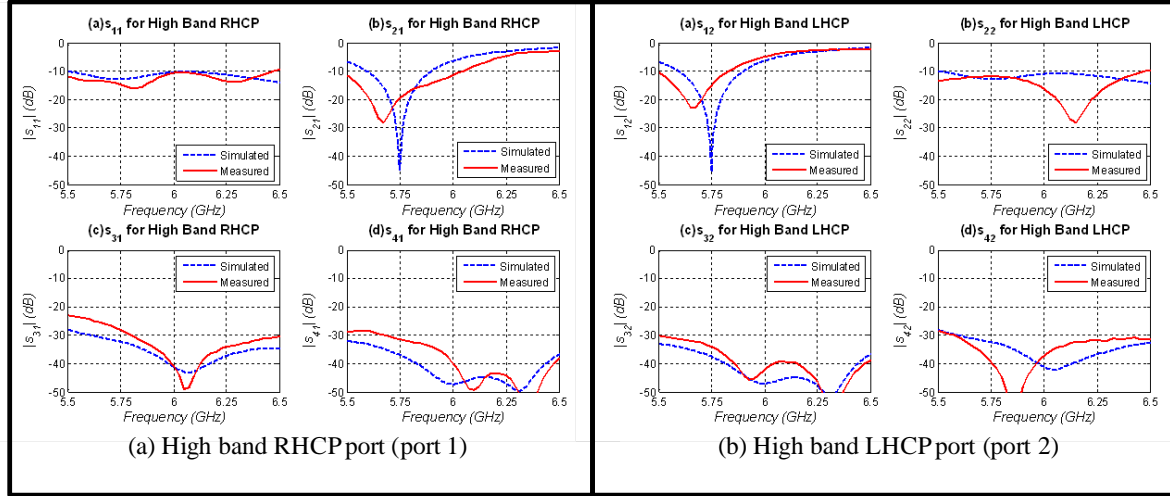
(a) High band RHCP port (port 1) (b) High band LHCP port (port 2)

Figure 3-3: Measured and simulated s-parameters for the high band ports of the dual-band, dual-CP antenna element

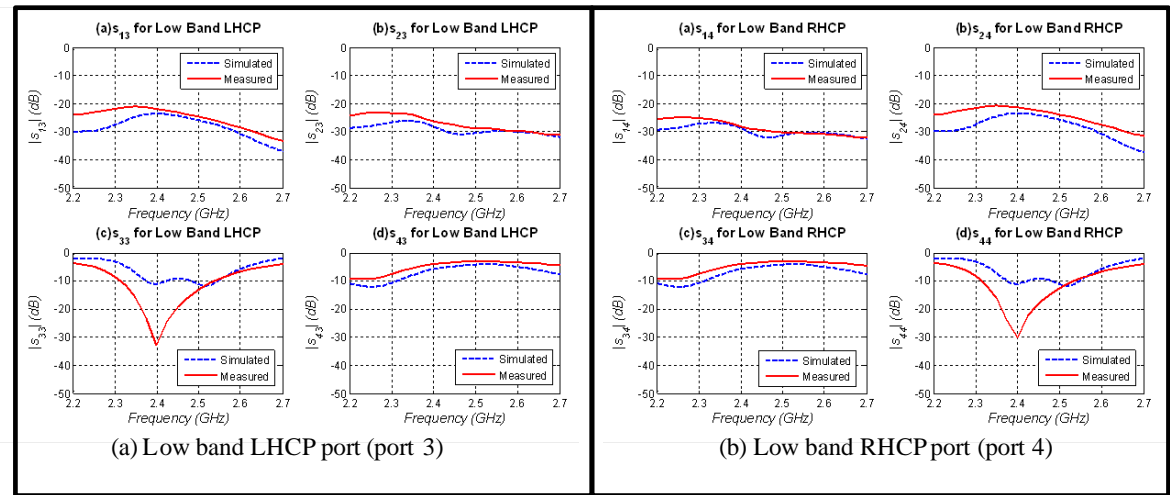(a) Low band LHCP port (port 3) (b) Low band RHCP port (port 4)

Figure 3-4: Measured and simulated s-parameters for the low band ports of the dual-band, dual-CP antenna element

In addition to showing good impedance match and isolation performance, this element also shows excellent circular polarization purity (axial ratio) for all polarization states. The axial ratio for the low and high band ports is plotted in Figure 3-5. The low band has a minimum axial ratio of 0.33dB occurring at 2.44 GHz, and the axial ratio is below 3dB over the majority of the 2.45 GHz ISM band. The high band element has a much broader CP bandwidth, which is typical of slot elements compared to microstrip radiators. The high band element has a minimum axial ratio of 0.32dB for RHCP and 0.89dB for LHCP. In both cases, the minimum axial ratio occurs at 5.9 GHz. The high band element has an axial ratio better than 3dB from 5.6 – 6.1 GHz, a bandwidth of 8.5%.
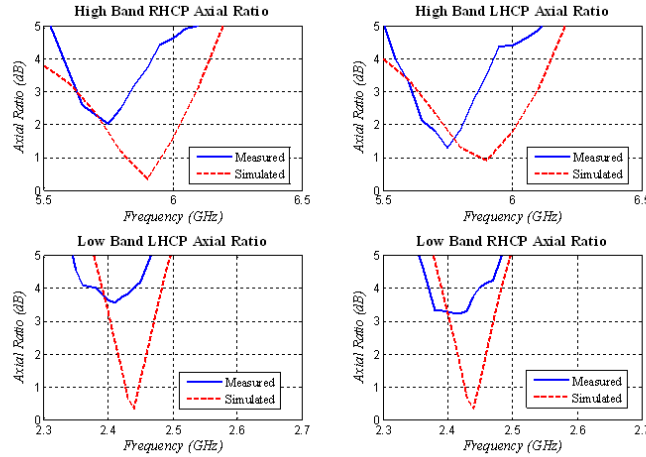
Figure 3-5: Measured and simulated broadside axial ratio for the four ports of a dual-band, dual-CP antenna element

If the element will be used in an antenna array or in an application requiring a broad beamwidth, it is important that the axial ratio remains near unity over a wide range of angles. The contour plots in figure 3-6 provide a look at the axial ratio vs. frequency vs. theta for the high band RHCP and low band LHCP. In these plots, theta represents the angle measured from broadside. The high band plot shows that the axial ratio is less than 3dB over a theta region of ±60° within the 5.8GHz ISM frequency band. At 5.85GHz, the axial ratio is below 1dB over for $|\theta|$<30°. The axial ratio holds up well for frequencies outside of the 5.8GHz ISM band. The contour plot of Figure 3-6a shows that the axial ratio is less than 3dB over $|\theta|$<30° for frequencies ranging from 5.65 – 6.05 GHz, a fractional bandwidth of 6.8%. The low band plot shown in Figure 3-6b indicates excellent axial ratio over the 2.45GHz ISM frequency band. The axial ratio stays below 1dB for $|\theta|$<40° between the frequencies of 2.43 and 2.45GHz. Over the remainder of the 2.45GHz ISM band, the axial ratio is less than 3dB for $|\theta|$<60°.

(a) Axial ratio vs. theta for the high band RHCP port of a dual-band, dual-CP antenna element

(b) Axial ratio vs. frequency vs. theta for the low band LHCP port of a dual-band, dual-CP antenna element
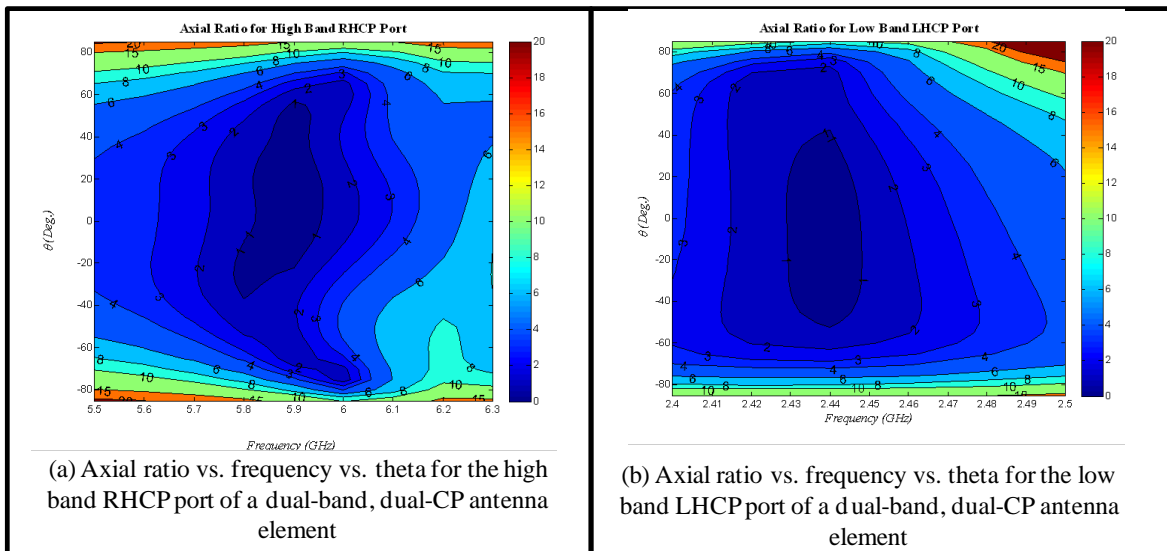
Figure 3-6: Simulated axial ratio vs. frequency vs. theta for the dual-band, dual-CP antenna element

368

The *Cross-Polarization Discrimination* (XPD) defines the ratio of the signal level at the output of a receiving antenna that is nominally co-polarized to the transmitting antenna to the output of a receiving antenna that is the same gain but nominally orthogonally polarized to the transmitter. If the incoming wave is perfect CP, XPD becomes independent of the tilt angle. In this case, the XPD is related to the axial ratio (AR) as defined in (6). [18].

$$XPD = \left[\frac{AR+1}{AR-1}\right]^2 \qquad\qquad (6)$$

The volumetric radiation pattern of the dual-band, dual-polarized antenna element was measured using a near field scanning facility. The resulting XPD and AR are plotted in Figure 3-7 for the high band LHCP polarization at 5.75GHz as a function of elevation and azimuth. The results show a minimum axial ratio of 0.82dB. This value is slightly lower than the minimum value from the compact range measurements shown in Figure 11 due to the finer frequency sampling in the near field scans. The AR remains below 3dB over a wide azimuth and elevation coverage.
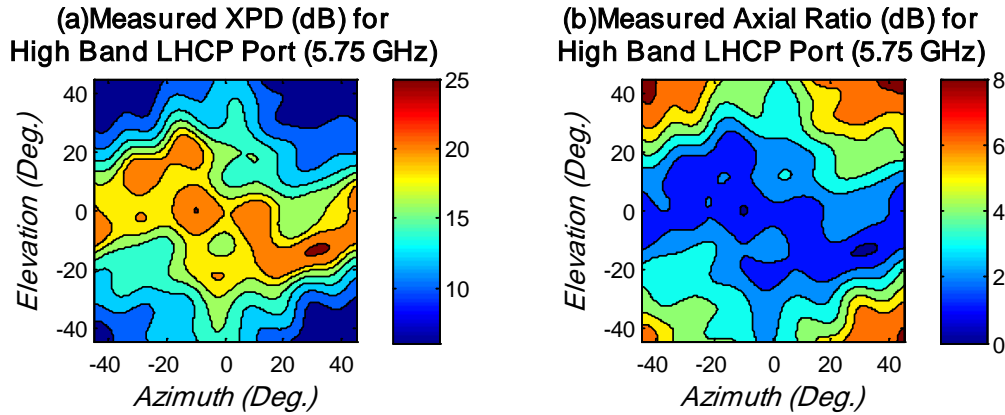

Figure 3-7: Measured (a) cross-polarization discrimination and (b) axial ratio as a function of azimuth and elevation for the High Band LHCP port at 5.75GHz

The measured results for the dual-band, dual-CP antenna element show good agreement with the simulated results. The s-parameters for all four ports of the antenna are in excellent agreement with the simulations. The assembly process of this element involves a complex series of steps involving etching of copper layers, alignment and bonding of multiple layers, and drilling and plating a series of holes to maintain electrical continuity between several layers. The tolerances of the alignment and bonding process are essential to the overall performance of the element, and careful attention must be placed on the locations and depths of the plated through holes.

3.2 Capacitive Loading for Size Reduction of the Dual-Band, Dual-Polarized Antenna Element

The size of the low band radiating element is the limiting factor in the array lattice spacing for this dual-band, dual-polarized antenna element. In cases with large separation between the two operational

frequency bands, the low band element will force a large element spacing that will lead to poor scanning performance and the early introduction of grating lobes at the high frequency. The dual-substrate capacitive loading technique described in [14, 19-20] can be used to reduce the size of the low band element, and thus reduce the overall footprint of the dual-band element. In [14], the dual-substrate capacitive loading technique was applied to a linearly polarized antenna element. In order to maintain the dual-CP performance of this element, the capacitive loading technique was modified.

A section view of the dual-band, dual-polarized antenna element is provided in Figure 3-8. The low band radiating element is a shorted square ring with outer side length L_0 and inner side length L_1. The high band radiating element is a square ring slot with outer side length L_1 and inner side length L_2. The radiating apertures use isosceles triangle perturbations at opposing corners to achieve single feed CP operation. The equal sides of the isosceles triangles are of length Δ_{LB} and Δ_{HB} for the low and high band elements respectively. In order to allow the CP operation, the outer perimeter of the capacitive patch is modified to follow the outer perimeter of the low band shorted square ring radiator. The truncated corner is illustrated in the bottom of Figure 3-8. The capacitive patch width (w_{cap}) and height (h_{cap}) can be changed to control the capacitance of the loading structure. Additionally, the dielectric properties (ε_{cap}) can be varied to control the capacitive effect of the load structure. The width and shape of the capacitive substrate are identical to that of the capacitive patch.

The location of the vias is also shown in Figure 3-8. The shorting vias provide electrical continuity between the low band radiator and the ground plane. These vias provide the shorting mechanism for the low band shorted square ring while also suppressing the parallel plate mode that can propagate in the slotted stripline structure of the high band radiator. The capacitive vias are located at the outer perimeter of the low band radiator, and they provide electrical continuity between the low band radiating structure and the capacitive patch.

A dual-band, dual-CP element incorporating the dual-substrate capacitive loading technique for size reduction was designed and simulated. The element covers two distinct ISM frequency bands centered at 2.45 GHz and 5.85 GHz. Each frequency band supports simultaneous dual-CP operation. Table 1 provides the dimensions for the capacitively loaded element. The performance parameters of the capacitively loaded are compared to those for the dual-band, dual-CP element described in the previous section in Table 2.

The addition of the loading structure has reduced the outer side length L_0 to 56% of its unloaded value. The outer side length for the loaded element is 2.921cm (1.150"), which is 0.56λ at the high frequency band for this dual-band element. That spacing will allow close element spacing in an array environment to allow for wide scanning capabilities. The unloaded element had a value for L_0 that was equal to 0.99λ at the high frequency. That element size would not lead to adequate scanning performance in a phased array environment.

The values for L_1 and L_2 remained unchanged, as did the substrate thickness h_1, h_2, and h_3. The increased element capacitance resulted in a decreased value for Δ_{LB}, while leaving Δ_{HB} unchanged. The capacitive loading structure uses a capacitive patch of width 0.102cm (0.040"). The separation between the capacitive patch and the ground plane is 0.056cm (0.022"), and the capacitive substrate has a dielectric constant of 10.

Table 1: Comparison of parameters for dual-band, dual-polarization antenna elements with and without the inclusion of capacitive loading

Parameter	L_0	L_1	L_2	Δ_{HB}	Δ_{LB}	w_{CAP}	ε_{CAP}	h_{CAP}	h_1	h_2	h_3
Loaded Element	1.150"	0.735"	0.575"	0.105"	0.058"	0.040"	10	0.022"	0.060"	0.060"	0.004"
Unloaded Element	2.020"	0.735"	0.575"	0.105"	0.285"	N/A	N/A	N/A	0.060"	0.060"	0.004"

Table 2: Performance comparison between dual-band, dual-CP antenna elements with and without capacitive loading

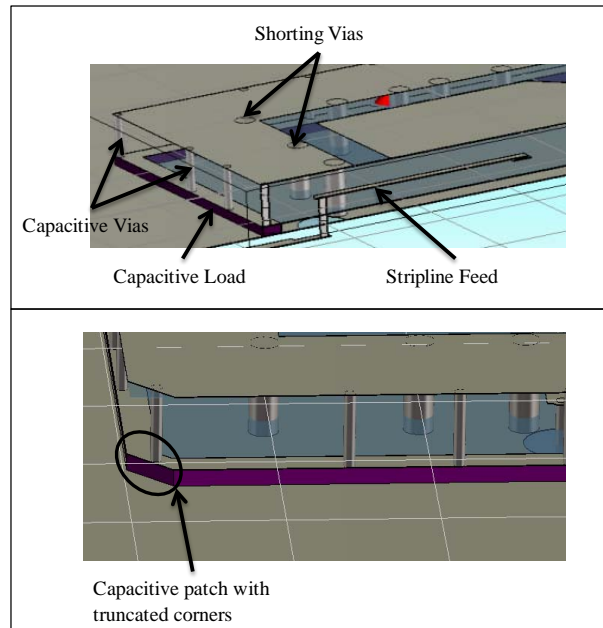| Parameter	Loaded Element	Unloaded Element
Impedance Match Fractional Bandwidth	2.65%	7.02%
Axial Ratio Fractional Bandwidth	1.01%	2.78%
2.45 GHz Realized Gain	2.673 dBi	5.638 dBi
Total Efficiency	43%	52%
2.45 GHz 3dB Beamwidth ($\varphi=0°$)	94.9°	71.0°
2.45 GHz 3dB Beamwidth ($\varphi=0°$)	95.1°	71.7°
L_0	1.150"	2.020"

Figure 3-8: (Top) Section view highlighting the integration of the dual-substrate capacitive load structure into the dual-band, dual-CP antenna element (Bottom) Illustration showing the truncated corner of the capacitive load structure to support single-feed circular polarization

The VSWR plots of Figure 3-9 (a)-(b) show that the addition of the capacitive loading structure leaves the impedance match of the high band ports unchanged. Figures 3-9(c) and (d) show a decreased bandwidth at the low frequency bands as a result of the capacitive loading structure. The increased capacitance resulting from the loading structure has increased the quality factor of the antenna; subsequently, the bandwidth of the antenna has been reduced. The unloaded element shows a fractional impedance bandwidth of 7.02% compared to the 2.65% fractional bandwidth for the capacitively loaded element.
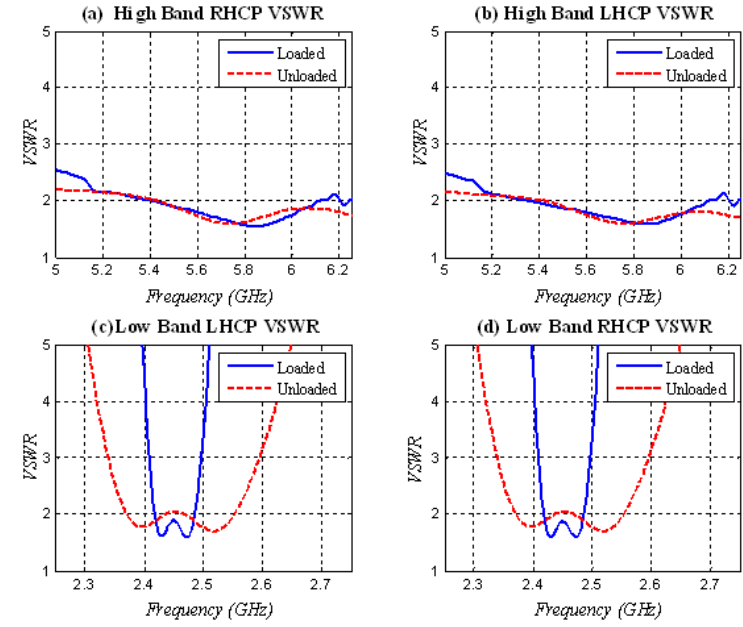
Figure 3-9: Comparison of the VSWR for a dual-band, dual-CP antenna elements with and without the introduction of a dual-substrate capacitive loading technique for size reduction of the low band element

The axial ratio for the loaded element is compared to that of the unloaded element in Figure 3-10(a)-(d) for the four ports of the dual-band dual-CP antenna element. The high band performance is left relatively unchanged when the capacitive loading structure is added. The slight differences are attributed to the reduction of the low band shorted square ring, which corresponds to a reduction in the ground plane size for the square ring slot. In the unloaded element, L_0 is almost three times larger than L_1, resulting in a ground plane that appears near "infinite" to the slot. When the loading structure is added, the size of L_0 is cut almost in half. However, it should be reiterated that any differences in performance at the high frequency band are virtually negligible.

The usable axial ratio region serves as the limiting factor for the overall usable bandwidth of the dual-band, dual-CP element with capacitive loading in the low frequency bands. Figures 3-10(c) and (d) show that the loaded element has a 3dB axial ratio bandwidth of 1.01% compared to the 2.78% bandwidth for the unloaded element. This shows that – while the impedance match bandwidth of the loaded element covers the 2.45 GHz ISM band – the axial ratio performance of the element is limited to a narrow portion at the center of the frequency band. This finding is evident in the axial ratio vs. frequency vs. theta contour plot of Figure 3-11. In this figure, the horizontal axis is frequency (GHz), and the vertical axis represents theta (Deg.). The axial ratio contours in this plot are elliptical in nature with a major axis parallel to the theta axis and a minor axis parallel to the frequency axis. This indicates that the frequency

bandwidth is the limiting factor in the axial ratio coverage. The major axis of the elliptical contours shows that the axial ratio remains below 3dB for $|\theta| < 45°$ over the narrow frequency band. This result suggests that the element can be used in an array environment requiring broad scanning, as long as the frequency limitations are acceptable.
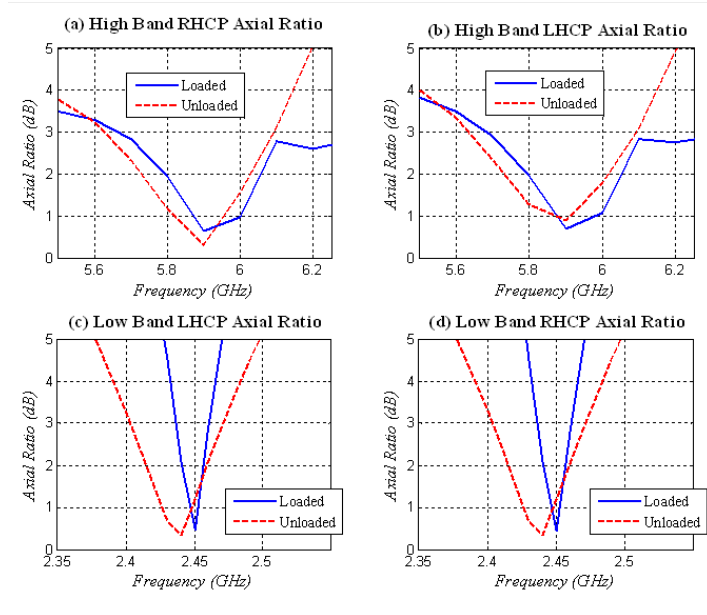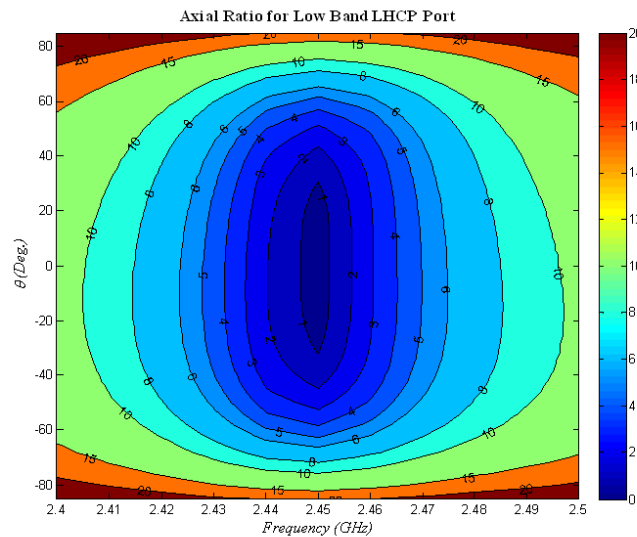

Figure 3-10: Comparison of the axial ratio for a dual-band, dual-CP antenna elements with and without the introduction of a dual-substrate capacitive loading technique for size reduction of the low band element

Figure 3-11: Axial ratio vs. frequency vs. theta for the low band LHCP port of a dual-band, dual-CP antenna element including dual-substrate capacitive loading for size reduction

Thus, the dual-substrate capacitive loading structure proposed in [14] can effectively be incorporated into the dual-band, dual-polarized antenna element, resulting in an element capable of operating over two distinct frequency bands with orthogonal senses of CP while occupying a small enough footprint for array applications. The small footprint allows for wide scanning coverage in an array environment. The resulting size reduction is not obtained without drawback as outlined in the comparison of Table 2. Despite these drawbacks, the addition of the capacitive loading results in a nearly 50% size reduction. The capacitive loading structure had a negligible effect on the performance of the high band performance of the element.

4   Hybrid Array Analysis Technique

Several techniques can be used to adequately study the performance of the dual-band, dual-polarized antenna element in an array environment. Typically, the first look at the performance of an element placed in an array comes from the use of periodic boundary conditions. These boundary conditions simulate the infinite periodic extension of the element and make the element appear as if it is surrounded by an infinite number of uniformly excited elements. Once the element pattern is calculated using this approach, it can be multiplied by an array factor to reveal an approximate array pattern. This approach has the advantage of requiring limited computational resources because the computational domain consists of a single unit-cell of the array. However, this approach assumes that all elements are identical and thus neglects changes in mutual coupling and edge effects that occur for elements near the outer perimeter of the array.

The classical approach for calculation of the radiation pattern for an antenna array involves multiplying the antenna pattern of an isolated element by an array factor accounting for the spatial distribution, amplitude weighting, and phase weighting of the array elements. The shortcomings of the classical approach lie in its inability to account for mutual coupling effects between elements in an array [19]. In order to include mutual coupling effects, active element patterns are used in place of an isolated element pattern to provide a more complete result. The active element pattern provides the radiation pattern of the entire array when a single element is fed and all other elements are terminated in a conjugately matched termination [19-21]. The active element pattern can be obtained through measurements and/or simulations. When the active element pattern is multiplied by the proper array factor, the array pattern including mutual coupling effects is obtained.

The work in [23] describes approaches using open-circuited active element patterns and short-circuited active element patterns. In these approaches, the element patterns contain the magnitude and phase information accounting for the spatial phase variation for the given element, and thus the pattern for each individual element is required. It is mentioned that symmetry can be used to reduce the number of patterns that are required, but this is still a large number of elements for large arrays. In this paper, a hybrid approach is developed and utilized that requires the calculation of only nine active element patterns. The phase information for each element will be included by taking the phase-adjusted unit-excitation active element pattern and using it as an active element pattern for all elements present in a similar electromagnetic and geometric environment. The phase-adjusted unit-excitation active element pattern is discussed in [19], and it is a modified version of the unit-excitation active element pattern in which the spatial phase dependence has been removed. The phase-adjusted patterns will change when the geometry changes. However, if the proper phase-adjusted patterns are selected for the appropriate

locations within a large array, the hybrid technique presented can be used to provide an excellent approximation to the overall array pattern. The theory and application of this technique will be described in the remainder of this section.

The classical array pattern is calculated using (7), where $g_{isol}(\theta, \varphi)$ is the element pattern of one of the array elements in an isolated environment (typically a free-space environment), $\hat{r}$ is a unit vector directed from the origin to the observation point, and $\mathbf{r_i}$ is the vector from the origin to the location of the current element. This approach assumes that the current distribution at each element is identical, and hence is not impacted by mutual coupling. The classical approach is sufficient for many array applications where the mutual coupling between elements is insignificant; however, (7) can be made more accurate if it is modified to include the active element pattern.

$$E(\theta, \varphi) = g_{isol}(\theta, \varphi) \sum_{i=1}^{N_{TOT}} I_i e^{jk\hat{r}\cdot r_i} \tag{7}$$

The unit-excitation active element pattern, $g_u^i(\theta, \varphi)$, represents the radiation pattern of the entire array when only a single element is excited by a unit voltage with its associated generator impedance (Z_{gq}). All other elements are loaded by their characteristic impedances. The set of unit-excitation element patterns contain all effects of radiative mutual coupling. As a result, (8) provides an exact representation of the array pattern. It should be noted that (8) does not contain the typical spatial-phase term found in array patterns. This is because the spatial-phase term is already included in the unit-excitation active element pattern. As a result, this pattern is unique to the geometrical location of the given element. In order to use the unit-excitation active element pattern in other geometries, it can be modified to the phase-adjusted, unit-excitation active element pattern using (9). The phase-adjusted quantity removes the spatial-phase term from the element. The expression in (8) is modified to (10) when the phase-adjusted quantity is used. It should be noted that the expression in (10) is still an exact representation of the array pattern.

$$E(\theta, \varphi) = \sum_{i=1}^{N_{TOT}} I_i g_u^i(\theta, \varphi) \tag{8}$$

$$g_p^i(\theta, \varphi) = g_u^i(\theta, \varphi) e^{-jk\hat{r}\cdot r_i} \tag{9}$$

$$E(\theta, \varphi) = \sum_{i=1}^{N_{TOT}} I_i(\theta, \varphi) \, g_p^i(\theta, \varphi) e^{jk\hat{r}\cdot r_i} \tag{10}$$

The unit-excitation active element pattern is different for every element within the array due to the unique geometrical location of each element. This requires the measurement, calculation, or simulation of the pattern for every individual element within the array. In order to simplify the process, the average active element pattern can be used to approximate the result. As the size of the array increases, the majority of the elements within the array have nearly identical phase-adjusted, unit-excitation active element patterns. Subsequently, these patterns can be approximated by the average active element pattern, $g_{av}(\theta, \varphi)$. This pattern can be obtained through simulations using periodic boundary conditions to make the element appear as if it is in an infinite array environment. Once the average active element pattern is known, (11) can be applied to provide an approximation of the array pattern. This approach is accurate for very large arrays, but it typically fails for smaller arrays due to the significant variation of the active element patterns across the array.

$$E(\theta, \varphi) = \boldsymbol{g_{av}}(\theta, \varphi) \sum_{i=1}^{N_{TOT}} I_i e^{jk\hat{r} \cdot \boldsymbol{r}_i} \tag{11}$$

For arrays of small to moderate size, the average active element pattern approach can have shortcomings because of the variation of element performance across the array. An exact solution can be obtained by simulating the entire array using commercial software, but this technique can be time consuming and taxing to typical computational resources. Another method to obtain an exact solution is to construct the entire array, measure the unit-excitation active element pattern of each element, and add the contributions analytically. While this technique requires a large time commitment to measuring many element patterns, it is not without benefit. After all of the element patterns are measured, they can be combined analytically to provide the antenna array pattern for any scanned pattern by introducing the proper amplitude and phase weighting. This eliminates the need to design, build, and test many beamforming networks for characterizing the array. However, it would be nice to have access to a close approximation of the array pattern without the potentially costly – both in time and money – process of constructing a large array. In order to accomplish this, an approach is presented that utilizes different average active element patterns selected based on the location of the element within the array. In the discussion presented here, the necessary set of average active element patterns is obtained by simulating – or measuring – a 3x3 array. Higher levels of accuracy can be obtained by simulating larger arrays at the expense of time and/or cost.

The hybrid array pattern calculation technique is illustrated in Figure 4-1. The left of this figure shows a 3x3 array, with the elements numbered 1 through 9. The unit-excitation active element pattern for each element in this array is simulated (or measured), and the phase-adjusted unit-excitation active element pattern is calculated by applying (9). The phase-adjusted patterns are then used to represent the average active element pattern for the region of the array indicated by the large array illustrated on the right hand side of this figure. This technique utilizes the assumption that the majority of mutual coupling effects come from the elements immediately surrounding the driven element. This approach will not result in the exact pattern that would be obtained using (8) or (10), but it will have a higher level of accuracy than the approach that assumes an identical active element pattern for all elements within the array. Additionally, the hybrid approach eliminates the need for simulating and/or measuring the active element pattern for every element within in potentially large finite array, thus providing a significant savings in both time and computational resources.

After the nine average active element patterns are simulated or measured, they can be summed to provide the array pattern including mutual coupling effects. For example, element 4 has elements 7, 8, 5, 2, and 1 as neighbors. This environment is similar to that of all edge elements excluding corners on the left-hand side of the larger array. Using this approach, the pattern for the moderately sized 10x10 array shown above can be evaluated by completing the simulation of a small 3x3 array and applying the hybrid calculation technique. This can be extended to any array size larger than 3x3 with no added complexity. The algorithm used for this calculation is shown in (12). In this algorithm, $\boldsymbol{g_{av}^q}$ is the phase-adjusted unit-excitation element pattern for the given element (and it will be used as the average active element pattern for the corresponding region), N_q is the number of elements in the q_{th} region ($1 < q < 9$), $\boldsymbol{r_{i,q}}$ is the vector from the origin to the ith element in the qth region, and $I_{i,q}$ is the complex weight for the ith element in the qth region.
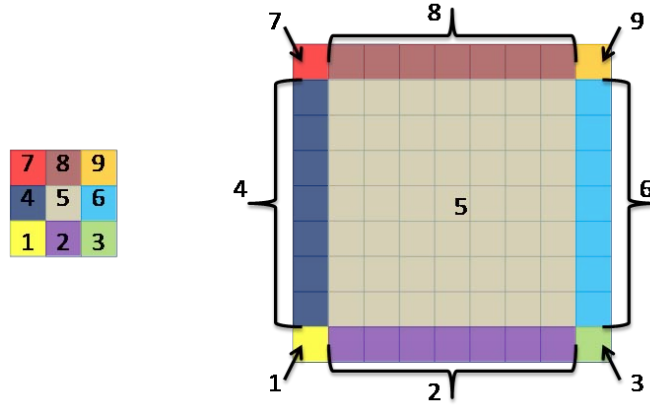
Figure 4-1: Illustration of the calculation domain for the hybrid array pattern calculation technique

$$E(\theta, \varphi) = \sum_{q=1}^{9} \left\{ \boldsymbol{g}_{av}^{q}(\theta, \varphi) \sum_{i=1}^{N_q} I_{i,q} e^{jk\hat{r}\cdot r_{i,q}} \right\} \tag{12}$$

5   Dual-Band, Dual-Polarized Array Analysis

5.1   Active Element Results

The approximate active element performance of the dual-band, dual-CP antenna element was obtained through infinite array simulations in CST Microwave Studio – a computational electromagnetics software package employing the finite integration technique (FIT) [14]. The size of the low band radiator was reduced by introducing the dual-substrate capacitive loading technique described in [7, 8]. The array element spacing is 3.15 cm (1.204"). This spacing is equivalent to 0.609λ in the high frequency band and 0.257λ in the low band. The maximum scan angle, θ_0, before the onset of grating lobes can be determined from (13). The array lattice provides grating-lobe free scanning at the high frequency to angles less than 40° off of broadside. At the low frequency, the fine element spacing will not produce grating lobes at any angles in the visible region.

$$\theta_0 = sin^{-1}\left(\frac{\lambda}{d} - 1\right) \tag{13}$$

The infinite array simulations provide the approximate active element impedance match. This parameter shows the input match to a given port when all other ports in the array are excited with the same amplitude and phase. The resulting VSWR is plotted in Figure 5-1(a). The low band ports exhibit a VSWR < 2.0:1 over the majority of the 2.45 GHz ISM frequency band. The high band element operates with a broad impedance bandwidth that more than covers the entire 5.8 GHz ISM band. The high frequency ports exhibit a broader bandwidth than the low frequency element for two main reasons. Firstly, the high band square ring slot element inherently operates over a broader frequency band than the shorted square ring low band element. Secondly, the low band element uses a dual-substrate capacitive loading structure to reduce the element size; this capacitive loading results in a decreased impedance bandwidth.

377

The active element axial ratio is plotted in Figure 5-1(b). The low band ports (RHCP and LHCP) have an axial ratio < 3.0dB from 2.44 – 2.52 GHz (3.2% bandwidth). The minimum axial ratio occurs at 2.45GHz for each polarization (AR_{min} = 0.4dB). The high band ports have broad axial ratio coverage. The LHCP polarization has an axial ratio < 3dB from 5.25 – 6.08 GHz with a minimum axial ratio of 0.5dB at 5.9 GHz , and the RHCP polarization covers 4.82 – 6.08 GHz with a minimum axial ratio of 0.18dB at 5.9GHz. The two polarizations exhibit slightly different axial ratio performance due to the slightly asymmetric feeding. One of the two feed lines crosses over the other near the center of the element because they are printed on opposing sides of the thin feed substrate layer; the feed line on the bottom (LHCP) exhibits slightly degraded axial ratio bandwidth compared to the other port. However, both ports have an axial ratio <1.5dB over the entire 5.8 GHz ISM band.

The active element axial ratio is plotted as a function of frequency and angle for the low and high frequency bands in Figures 5-2(a)-(b) respectively. The contour plots show that the dual-band dual-CP element maintains good axial ratio performance well off of broadside in both frequency bands, a result that is critical in allowing the dual-band dual-CP array to maintain good axial ratio at scanned conditions.

(a) Low band (top) and high band (bottom) active element VSWR (simulated)

(b) Low band (top) and high band (bottom) active element axial ratio (simulated)
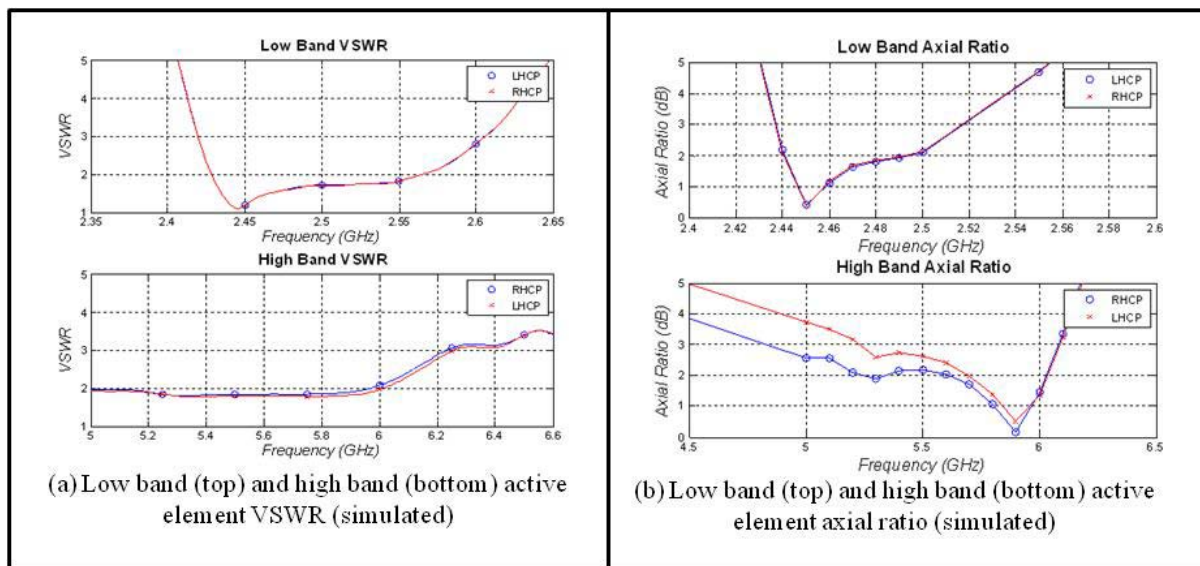
Figure 5-1: Simulated active element VSWR and axial ratio for the capacitively loaded dual-band, dual-CP antenna element

378

(a) Active axial ratio vs. frequency vs. theta for the high band RHCP port of a dual-band, dual-CP antenna element

(b) Active axial ratio vs. frequency vs. theta for the low band LHCP port of a dual-band, dual-CP antenna element
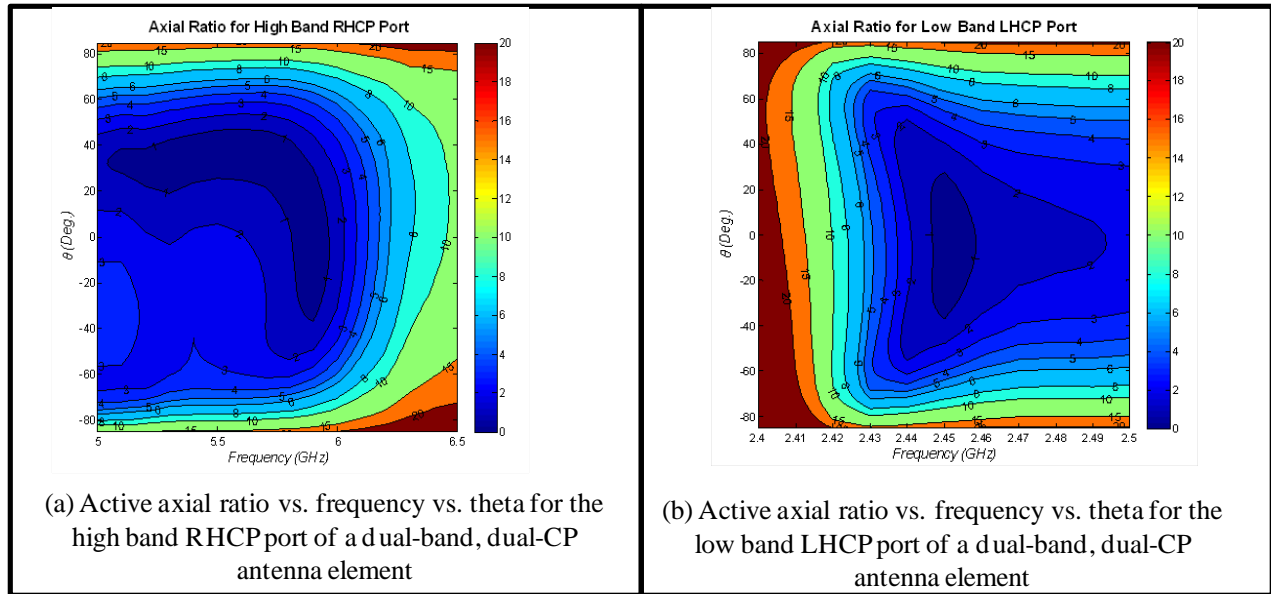
Figure 5-2: Simulated active element axial ratio vs. frequency vs. theta for the capacitively loaded dual-band, dual-CP antenna element

5.2   Dual-Band, Dual-Polarized 3x3 Array Results

The infinite array simulations were performed to provide an approximation of the element's performance in an array environment. The next step in the array analysis procedure used in this study was to simulate the element in a 3x3 array. This simulation will provide the necessary active element patterns that will be used in the technique described in Section 4. An illustration of the 3x3 array that was simulated in CST Microwave Studio [17] is shown in Figure 5-3.

(a) Top View   (b) Isometric View
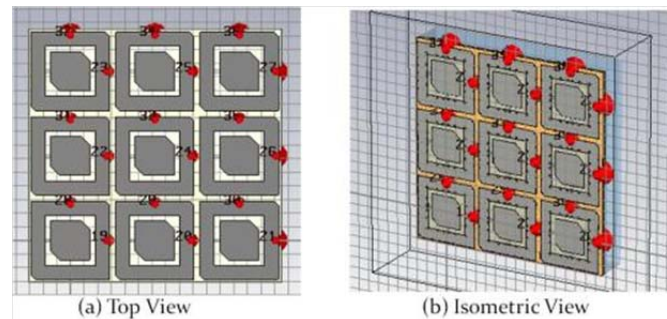
Figure 5-3: Simulation model of a 3x3 array of dual-band, dual-CP antenna elements

The results of the 3x3 array simulation revealed the importance of using the hybrid method for array analysis. The active element patterns for the low band RHCP port are plotted in Figure 5-4. The frequency for these plots is 2.44 GHz. These radiation patterns are for the φ=0° plane (x-z plane). Figure 5-4(a) shows the pattern for the center element (element 5 in the hybrid technique). This element is used to represent all elements in the core region of the antenna, and it has a performance analogous to that obtained via infinite array simulations. This active element pattern exhibits a maximum value at broadside (θ=0°) and extremely high XPD. The active element patterns for the corner elements (elements

379

1, 3, 7, 9 in the hybrid technique) are shown in Figure 5-4(b). These patterns are normalized to the maximum value of the center element case. The results show degraded performance in many aspects of the pattern. The maximum value is reduced significantly, the pattern becomes squinted off of broadside, and the *cross-polarized* component is increased. Similar active element pattern performance is seen in the edge elements (elements 2, 4, 6, and 8 in the hybrid technique).

The results for the center element closely resemble the patterns obtained via infinite array analysis. Conversely, the elements around the outer perimeter of the 3x3 array exhibit asymmetries, increased cross-polarization levels, and decreased gain. The active element patterns show that the edge effects and asymmetrical mutual coupling provide distortions in pattern performance that would be ignored if the infinite array pattern was used to approximate the performance of all elements in the array.

(a) Low band RHCP active element pattern for the center element of the 3x3 array of dual-band, dual-CP antenna elements

(b) Low band RHCP active element pattern for the corner elements of the 3x3 array of dual-band, dual-CP antenna elements

(c) Low band RHCP active element pattern for the edge elements of the 3x3 array of dual-band, dual-CP antenna elements
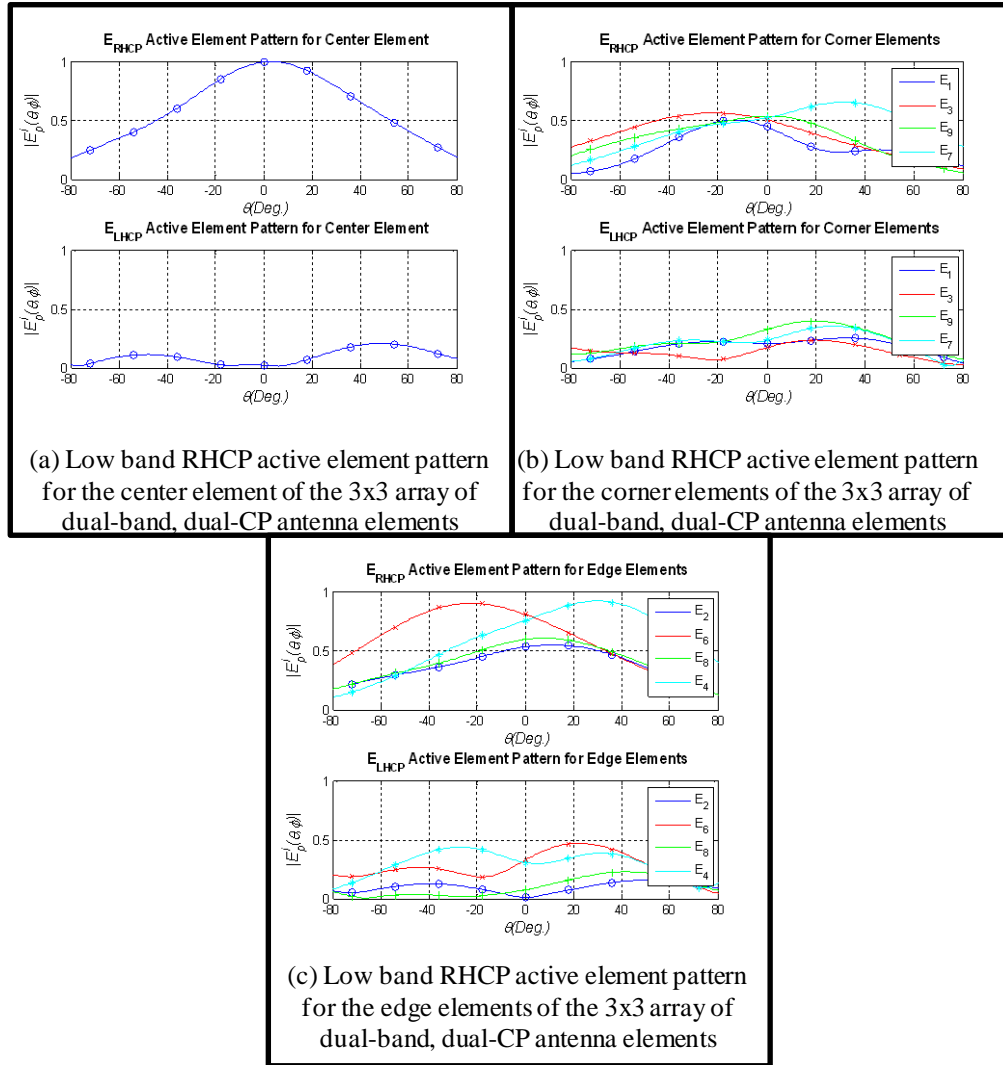
Figure 5-4: Low band active element patterns obtained from 3x3 array simulation

5.3   Dual-Band, Dual-Polarized Array Performance

The radiation pattern for the dual-band, dual-CP antenna array was calculated using the multiple active element hybrid technique for three array sizes (12 elements x 12 elements, 24x24, and 48x48). The three

sizes were intended to show the results using the hybrid technique for a small, moderate and large antenna array. For the low band radiators, the antenna patterns were calculated using the individual feeding technique and a quad-element technique that combines 2x2 subarrays of low band elements into a larger effective element. The remainder of this section will show the calculated array patterns for the low band radiators, the performance analysis, and a comparison between the two feeding techniques.

5.3.1 Low Band Performance

The size of the low band radiator was reduced to allow for spacing at the high frequency suitable for grating lobe-free scanning. This size reduction resulted in a small footprint at the low frequency, and thus the low frequency aperture is oversampled. The size reduction results in a larger than necessary number of potentially expensive and lossy components (such as attenuators and/or phase shifters). If the spacing at the low frequency were doubled, the elements would then be separated by 0.514λ, a spacing allowing scanning to $70.7°$ before the onset of grating lobes according to (13). This element spacing can be accomplished by feeding groups of four elements together at the low frequency; this group of four elements will be referred to as the *quad-element*.

The quad-element is illustrated in Figure 5-5. The phase centers of four dual-band, dual-CP elements are indicated as (x_{pi}, y_{pi}), where i = 1, 2, 3, or 4. For the quad-element feeding, these four elements are excited by a simple four-way power splitter. In doing so, these four elements are fed with equal amplitude and phase. The effective phase center of the quad-element is indicated by (x_{eff}, y_{eff}). When the array is scanned, the scanning phase shift is determined using the effective phase center. The use of this feeding technique eliminates 75% of the required phase shifters and attenuators necessary for low frequency operation. The quad-element feeding is only used for the low frequency elements. In Figure 5-5, the high frequency radiators still have phase centers at (x_{pi}, y_{pi}).

The phase centers for the 12x12 antenna array are shown in Figure 5-6. This figure shows the phase centers for two feeding techniques, individual feeding and quad-element feeding. *Individual Feeding* refers to the case where all elements are fed individually, requiring components at each element. The *Quad-element* feeding technique was previously described. At the low frequency limit, this array is electrically small (3.084λ x 3.084λ).
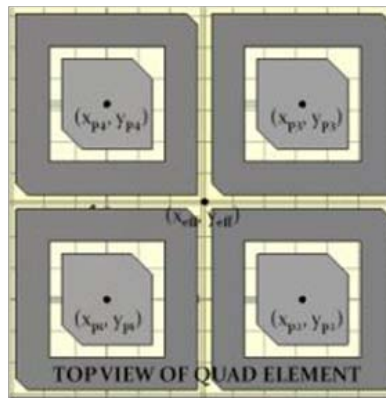

Figure 5-5: Illustration of the quad-element feeding technique used to simplify the feed network for the low band radiators in the dual-band, dual-CP antenna array
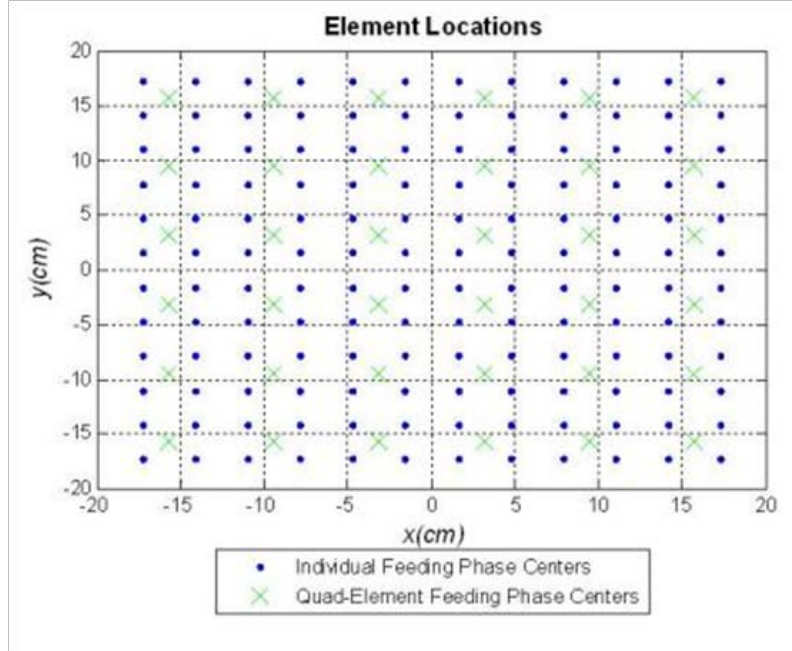
Figure 5-6: Phase center locations for the individual and quad-element feeding for the 12x12 dual-band, dual-CP antenna array

The array patterns for θ_0=0°, 15°, 30°, and 45° degrees are plotted in Figure 5-7 for the low band RHCP port in the φ=90° plane using individual element feeding. Figure 5-7(a) shows the *co-polarized* components, and Figure 14(b) provides the *cross-polarized* components. The element pattern is overlaid on both of these plots to show that the array pattern drops off proportionally to the element pattern at θ_0. The RHCP and LHCP pattern for the quad-element feeding is compared to the individual feeding in Figures 5-8. The normalized maximum value drops off faster at wide scan angles for the quad-element feeding, but not drastically. At θ_0=45°, the quad-element case exhibits a maximum value 1.8dB lower than that of the individual element feeding case. The individual feeding technique requires more potentially high loss phase shifters that would most likely decrease the gain of the individual feeding below that of the quad-element feeding. The quad-element feeding showed higher XPD at wide scan angles than the individual element feeding. The improved XPD leads to an axial ratio value closer to unity, thus improving the performance of the array at wide scan angles for CP operation.
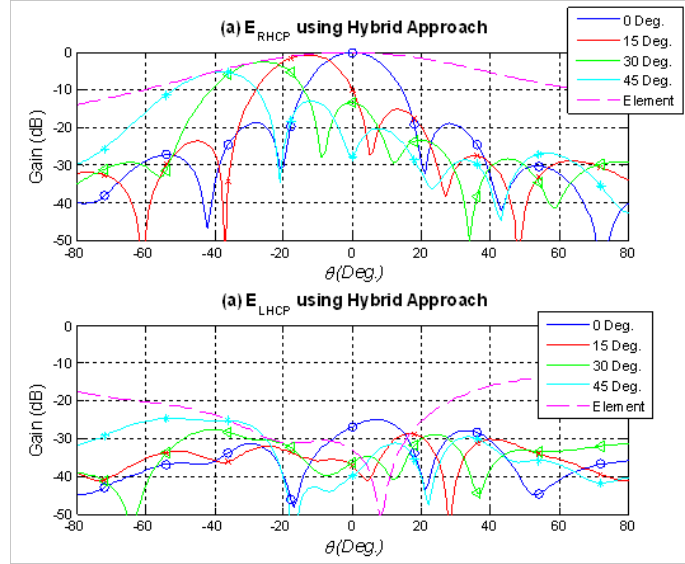
Figure 5-7: Co- and cross-pol scanned array patterns for the low band radiators in a 12x12 array
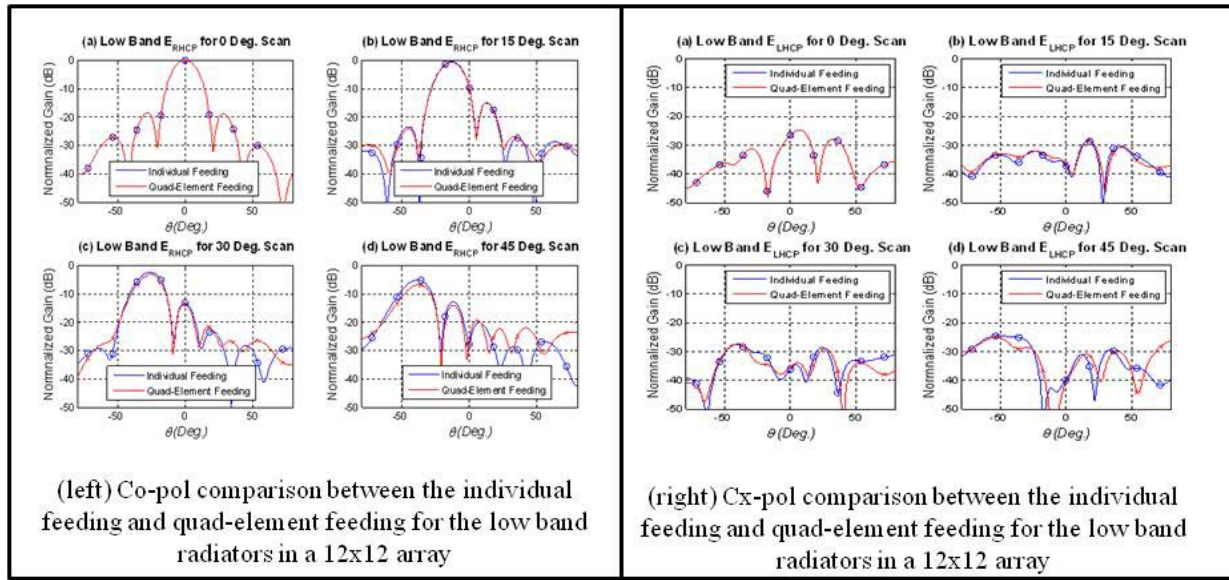
Figure 5-8: Comparison of co- and cross-polarized 12x12 array patterns for the low band radiators using individual and quad-feeding

The XPD and axial ratio performance for the low band RHCP radiators of the dual-band, dual-CP antenna array is provided in Figure 5-9. Figure 5-9 contains four subplots: XPD for individual feeding, XPD for quad-element feeding, AR for individual feeding and AR for quad-element feeding. Moreover, Figure 5-9 has data points indicating the value for all three array sizes that were discussed. The results show that the low band RHCP radiators of the dual-band, dual-CP antenna element provide excellent CP performance in an antenna array environment. The low band radiator maintains an axial ratio better than 2.0 dB for scans less than 30°, and the AR remains less than 3.0dB for scans up to 45°.
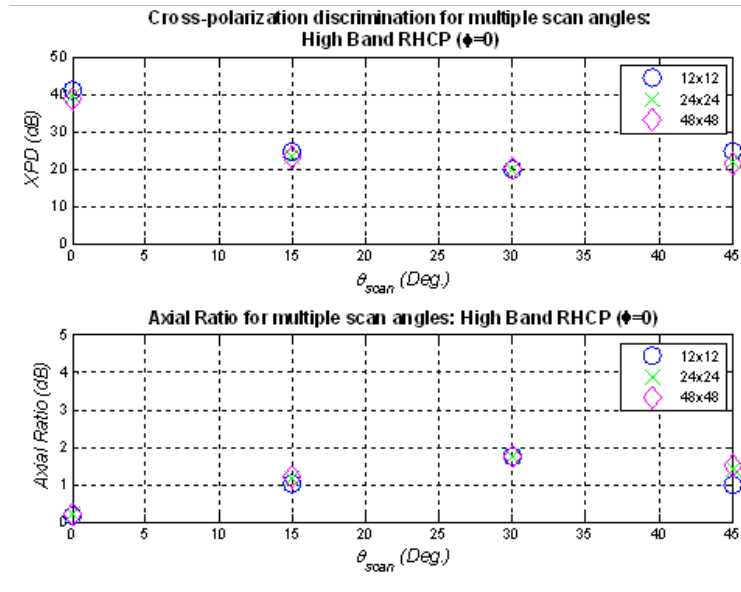
383
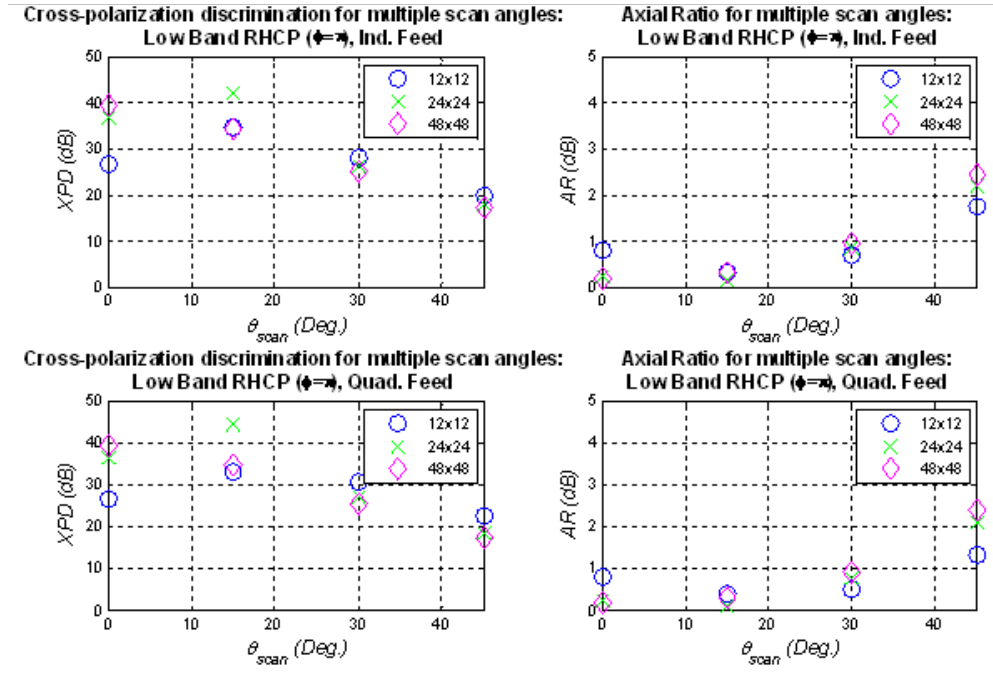
Figure 5-9: Calculated cross-polarization and axial ratio for the low band RHCP radiators of dual-band, dual-CP antenna arrays of various sizes

5.3.2   High Band Array Performance

The 0.609λ spacing at 5.9GHz allows scanning of the main beam up to 40° off of broadside before grating lobes appear in the pattern. This section will show high band calculated results for the three array sizes at various scan angles accompanied by performance analysis.

The scanned array patterns for the RHCP high band radiators of the 12x12 and 24x24 arrays are shown in Figure 5-10. In each of these figures, (a) shows the co-polarized patterns normalized to the maximum value of the broadside case, while the patterns in (b) show the cross-polarized components. The normalization is done to show the reduction in maximum gain as the array is scanned. The gain reduction is proportional to the overlaid element pattern until grating lobes begin to appear. This is evident in the 45° scan case. The main lobe maximum value has dropped off much faster than the element pattern, and a grating lobe is visible in the range from 50°<θ<80°. The cross-polarized patterns of Figure 5-10 illustrate the excellent XPD for the array. As mentioned before, a high XPD corresponds to an axial ratio near unity.

The XPD and axial ratio performance for the high band RHCP radiators of the dual-band, dual-CP antenna is provided in Figures 5-11. Each of these figures contains two subplots: XPD and AR. The results show that the high band radiators of the dual-band, dual-CP antenna element provides excellent CP performance in an antenna array environment. The high band radiator maintains an axial ratio better than 2.0 dB for scans less than 45°. The element spacing is slightly over 0.6λ in the high frequency band causing grating lobes to appear in the visible region when the array is scanned past 40°.

| (left) Co- and cross-pol scanned array patterns for the high band radiators in a 12x12 array | (right) Co- and cross-pol scanned array patterns for the high band radiators in a 24x24 array |
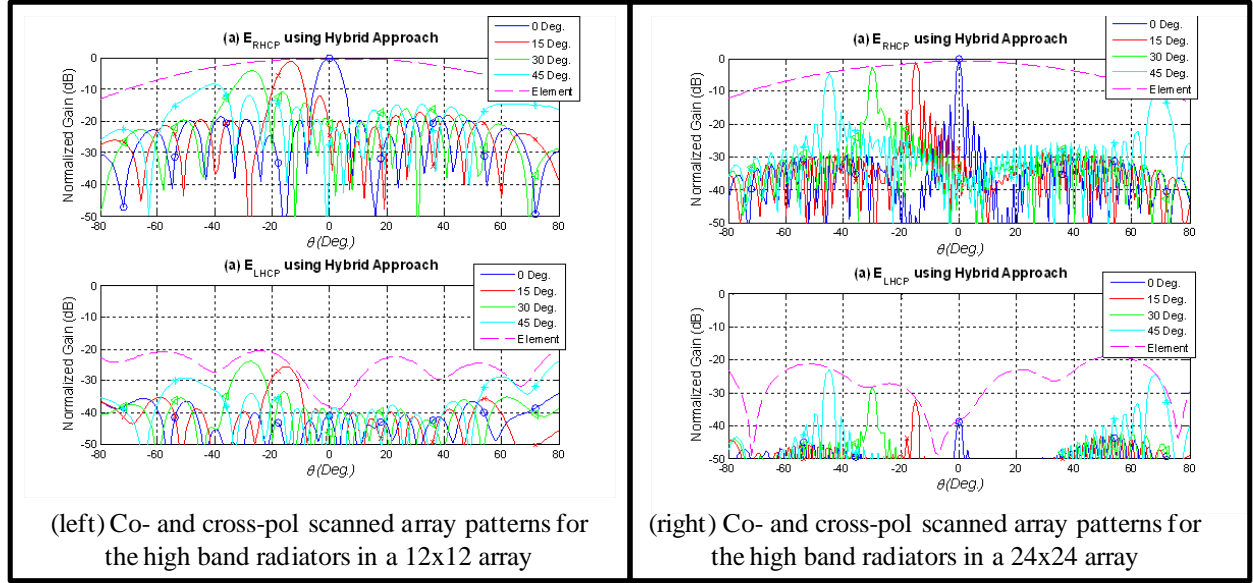
Figure 5-10: Co- and cross-polarized array patterns for the high band radiators of a 12x12 and 24x24 array

Figure 5-11: Calculated cross-polarization and axial ratio for the high band RHCP radiators of dual-band, dual-CP antenna arrays of various sizes

6   Conclusions

A novel dual-band element has been designed that provides dual-CP performance in two distinct frequency bands. The element, consisting of two concentric radiating elements, was built and tested to verify the concept and performance shown in simulations. The measured results show good agreement with the simulations, this establishing a high confidence level in the validity of the simulation models used in this dissertation. Moreover, the measured results confirm the ability of this element to generate

dual-circular polarization at two distinct frequency bands while providing a lightweight, low-profile, printed circuit design capable of facilitating system integration.

A dual-substrate capacitive loading structure was incorporated into the dual-band, dual-polarized antenna element to reduce the footprint of the element. This allows a dual-band element with a large frequency ratio to be placed in an array environment conducive to scanning the main beam at the high frequency without the introduction of grating lobes. The capacitive loading structure reduces the size of the low frequency element while leaving the high band element performance unchanged. The size reduction, however, is not obtained without drawbacks. The operational bandwidth of the low band element – in terms of impedance match and axial ratio – is reduced by the increased quality factor of the element generated by the increased element capacitance.

A hybrid calculation technique using multiple active element patterns is developed and applied to investigate the performance of this element within an array. In this technique, a 3x3 array of elements is simulated to arrive at nine active element patterns. Each element in the array is assigned one of these nine active element patterns to serve as its active element pattern. The pattern is chosen based on the geometrical location and boundary conditions of the given element within the array. This approach presents a compromise between the time-efficient infinite array analysis and the exact result of the active element pattern approach.

The results of the array analysis indicate that the dual-band, dual-CP element provides an attractive option for applications requiring dual-band apertures requiring dual-frequency operation and main beam scanning. The dual-ISM band antenna array permits scanning up to 70° off of broadside at 2.44 GHz before the onset of grating lobes. At the high frequency band, grating lobe-free scanning is achieved for angles up to 40° off of broadside. The cross-polarized discrimination (XPD) and axial ratio holds up extremely well for both polarizations and both frequency bands. At 2.44 GHz, the axial ratio remains below 2.0dB for scans less than 30°. The high frequency polarizations experience an axial ratio better than 2dB over the entire grating lobe-free scanning region. The low profile, low cost, and light weight nature of the element used in this array make it advantageous for use in large apertures.

References

[1] P. K. Hughes and J. Y. Choe, "Overview of advanced multifunction RF system (AMRFS)," in Phased Array Systems and Technology, 2000. Proceedings. 2000 IEEE International Conference on, 2000, pp. 21-24.
[2] G. C. Tavik, C. L. Hilterbrick, J. B. Evins, J. J. Alter, J. G. Crnkovich, Jr., J. W. de Graaf, W. Habicht, II, G. P. Hrin, S. A. Lessin, D. C. Wu, and S. M. Hagewood, "The advanced multifunction RF concept," Microwave Theory and Techniques, IEEE Transactions on, vol. 53, pp. 1009-1020, 2005.
[3] R. M. Sorbello and A. I. Zaghloul, "Wideband, high-efficiency, circularly polarized slot elements," in Antennas and Propagation Society International Symposium, 1989. AP-S. Digest, 1989, pp. 1473-1476 vol.3.
[4] R. M. Sorbello and A. I. Zaghloul, "Orhotgonally Polarized Dual-Band Printed Circuit Antenna Employing Radiating Element Capacitively Coupled to Feedlines," U. S. P. Office, Ed.: Comast, 1996.
[5] C. B. Ravipati and A. I. Zaghloul, "A hybrid antenna element for dual-band applications," in Antennas and Propagation Society International Symposium, 2004. IEEE, 2004, pp. 4020-4023 Vol.4.

[6] A. I. Zaghloul and W. M. Dorsey, "Dual-Band Reduced-Size Circularly Polarized Co-Planer Printed-Circuit Antenna Element," in International Union of Radio Science (URSI) Electromagnetic Theory Symposium (EMTS) Ottawa, ON, Canada, 2007.

[7] W. M. Dorsey, J. A. Valenzi, and A. I. Zaghloul, "Dual-Substrate Capacitive Loading Technique in Linearly and Circularly Polarized Annular Ring Antennas," Monticello, IL, 2007.

[8] W. M. Dorsey and A. I. Zaghloul, "Size reduction and bandwidth enhancement of shorted annular ring (SAR) antenna," in Antennas and Propagation International Symposium, 2007 IEEE, 2007, pp. 897-900.

[9] W. M. Dorsey and A. I. Zaghloul, "Dual-Band Array Calculations Using Hybrid Calculation Technique," U.S Naval Research Laboratory, Washington, DC 2009.

[10] K. Chang and L. H. Hsieh, *Microwave Ring Circuits and Related Structures*, 2 ed. Hoboken: John Wiley & Sons, Inc., 2004.

[11] Row, J.-S., "The design of a squarer-ring slot antenna for circular polarization," *Antennas and Propagation, IEEE Transactions on* , vol.53, no.6, pp. 1967-1972, June 2005.

[12] Kin-Lu Wong; Chien-Chin Huang; Wen-Shan Chen, "Printed ring slot antenna for circular polarization," *Antennas and Propagation, IEEE Transactions on* , vol.50, no.1, pp.75-77, Jan 2002.

[13] M. Niroojazi and M. N. Azarmanesh, "Practical design of single feed truncated corner microstrip antenna," in *Communication Networks and Services Research, 2004. Proceedings. Second Annual Conference on*, 2004, pp. 25-29.

[14] W. M. Dorsey and A. I. Zaghloul, "Dual-Polarized Dual-Band Antenna Element for ISM Band Application", *IEEE International Symposium on Antennas and Propagation*, Charleston, SC, June 2009.

[15] K. Itoh and M. Yamamoto, "A slot-coupled microstrip array antenna with a triplate line feed where parallel-plate mode is suppressed efficiently," in *Antennas and Propagation Society International Symposium, 1997. IEEE., 1997 Digest*, 1997, pp. 2135-2138 vol.4.

[16] A. Bhattacharyya, O. Fordham, and L. Yaozhong, "Analysis of stripline-fed slot-coupled patch antennas with vias for parallel-plate mode suppression," *Antennas and Propagation, IEEE Transactions on,* vol. 46, pp. 538-545, 1998.

[17] "CST Microwave Studio," 2006B ed.

[18] W. L. Stutzman, *Polarization in Electromagnetic Systems*. Norwood, MA: Artech House, 1993.

[19] D. F. Kelley and W. L. Stutzman, "Array antenna pattern modeling methods that include mutual coupling effects," Antennas and Propagation, IEEE Transactions on, vol. 41, pp. 1625-1632, 1993.

[20] D. M. Pozar, "The active element pattern," Antennas and Propagation, IEEE Transactions on, vol. 42, pp. 1176-1178, 1994.

[21] D. M. Pozar, "A relation between the active input impedance and the active element pattern of a phased array," Antennas and Propagation, IEEE Transactions on, vol. 51, pp. 2486-2489, 2003.

[22] D. F. Kelley, "Relationships between active element patterns and mutual impedance matrices in phased array antennas," in Antennas and Propagation Society International Symposium, 2002. IEEE, 2002, pp. 524-527 vol.1.

Abstract

METAMATERIAL LOADED RADIATING ELEMENTS FOR USE IN INTEGRATED ARRAYS

Authors

Michael J. Buckley, Lee M. Paulsen, Jeremiah D. Wolf, Michael D. Davidson,
Dennis L Manson, James B. West

Advanced Technology Center
Rockwell Collins, Inc.
400 Collins Rd. NE. M/S: 108-102
Cedar Rapids, IA 52498

Abstract – **Metamaterial loaded radiating elements for use in integrated arrays are discussed. Measured results for a 3D metamaterial loaded radiating element that scans from 0 to 70 degrees (half conical angle) in the E plane over a frequency band from 14 to 18 GHz and scans from 0 to 70 degrees (half conical angle) in the H plane over a frequency band from 14 to 17 GHz are presented. A 2D metamaterial loaded radiating element with 2D scan from 0 to 70 degrees (half conical angle) from 12 to 18 GHz is introduced. The advantages of a 2D metamaterial compared to a 3D metamaterial are discussed**

Table of Contents

List of Figures

1. Introduction

There is significant interest in developing multifunction radar systems with SAR, GMTI, and Sense and Avoid capability on UAV's [1, 2]. The antenna for a multifunction radar system on a UAV must be relatively broadband, low profile, environmentally hardened, and offer easy connectivity to T/R modules. Depending on the radar system, the antenna may be a gimbaled array, a 1D scanned array, or a 2D scanned array. A printed circuit board planar antenna meets the packaging requirements; however conventional planar radiating elements typically have narrow bandwidth and/or scan volume. For the active array case, the antenna radiating elements must be capable of operating in a triangular grid. A radiating element that requires a rectangular grid incurs a 15% penalty in size, weight, power, and cost.

In this paper, we present the measured results of a 3D metamaterial loaded radiating element in a triangular grid. We also discuss a 2D metamaterial radiating element in a triangular grid and compare the 2D metamaterial to the 3D metamaterial. The 2D metamaterial loaded radiating element has the potential to be integrated into a UAV structure and function as a load bearing antenna. Stripline is used for the feed transmission line in both cases in order to eliminate back radiation from the feed network, to allow a multilayer PCB architecture that includes the RF manifold distribution network, and to permit easy integration of the T/R modules. The PCB radiating element stack consists of Arlon CLTE or equivalently Rogers 6002 (dk ~ 2.94) and, in the 2D metamaterial radiating element case, a covering layer of Astroquartz. Astroquartz is a commonly used radome material. The use of Astroquartz and Arlon CLTE or Rogers 6002 reduces manufacturing costs incurred by using nonstandard PCB materials such as foams and also eliminates water absorption problems caused by foams.

2. 3D Metamaterial Wide Scan Radiating Element

The details of the 3D metamaterial radiating element are discussed in [3]. A cross sectional view of the 3D metamaterial radiating element is shown in Figure 1 and a top down view of 4 unit cells with dipoles and 3D metamaterial is shown in Figure 2. In Figure 2, note that the 3D metamaterial wide scan radiating element is arranged in a triangular grid. As noted above, compared to a rectangular grid, a triangular grid offers a 15 % reduction in radiating elements for a given scan volume. Customers are usually cost sensitive.
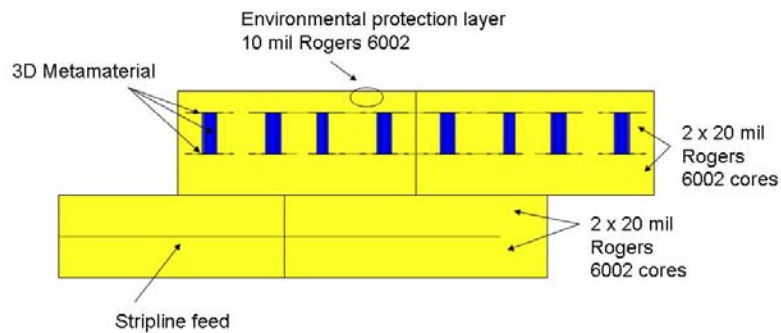
Figure 1. Cross sectional view of the metamaterial loaded wide scan radiating element. The wide scan radiating element is a stripline fed aperture coupled radiating element with a 3D metamaterial.

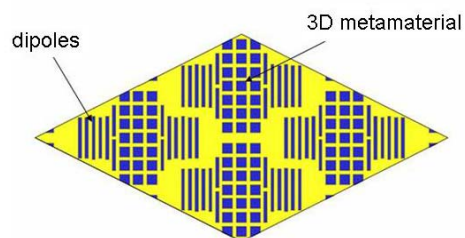**Figure 1 Cross Sectional View of 3D Metamaterial Radiating Element**

Fig 2. A top down view of 4 unit cells with dipoles and 3D metamaterial is shown. The nonuniform arrangement of the metamerial is done in order to maximize radiating element performance. An 80 ohm stripline feed excites each unit cell.

Figure 2 Top Down View of 4 Unit Cells with Dipoles and 3D Metamaterial

The wide scan radiating element consists of an 80 ohm stripline feed layer, a slot in the ground plane, two layers of radiating dipoles, a single layer of 3D metamaterial, and a 10 mil environmental protection layer. Using a 10 mil core of Rogers 6002 or Arlon CLTE eliminates the common problem of salt fog etching away the top layer of metal in a planar radiating element. A view of the stripline feed and ground plane is shown in Figure 3.

The slot is symmetric. In conjunction with the symmetric dipoles and the metamaterial arrangement in the unit cell, the cross polar radiation is zero at array normal and in the E plane scan.
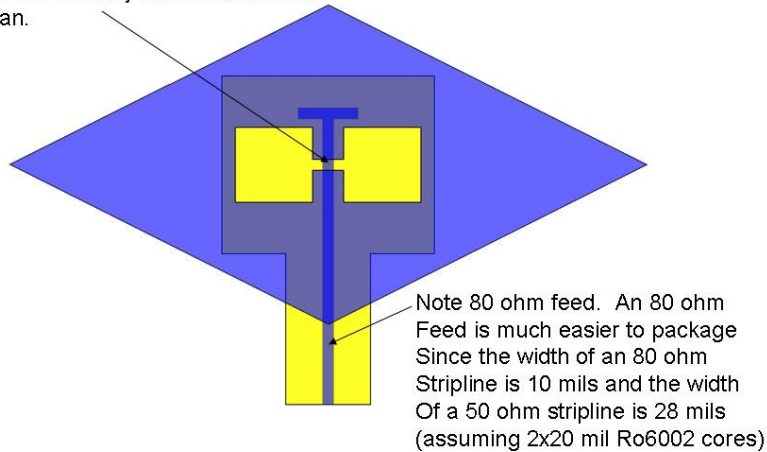
Note 80 ohm feed. An 80 ohm Feed is much easier to package Since the width of an 80 ohm Stripline is 10 mils and the width Of a 50 ohm stripline is 28 mils (assuming 2x20 mil Ro6002 cores)

Fig. 3 The 80 ohm stripline feed and the slot in ground plane of the 3D metamaterial wide scan radiating element.

Figure 3 Stripline Feed and Ground Plane

The 3D metamaterial wide scan radiating element was tested in a compact range at Rockwell Collins. E and H copol and xpol patterns were taken. (Figure 4)
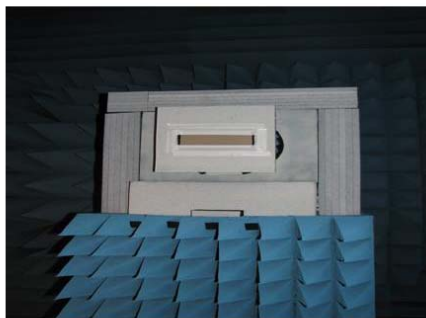
fractional array in far field chamber on pedestal

fractional array in far field chamber

Figure 4 Pictures of the 3D Metamaterial Wide Scan Radiating Element in a Rockwell Collins' Compact Range.

Figure 5 shows the E plane copol pattern from 12 – 14.5 GHz. The lower limit of the frequency band is 14.0 GHz.
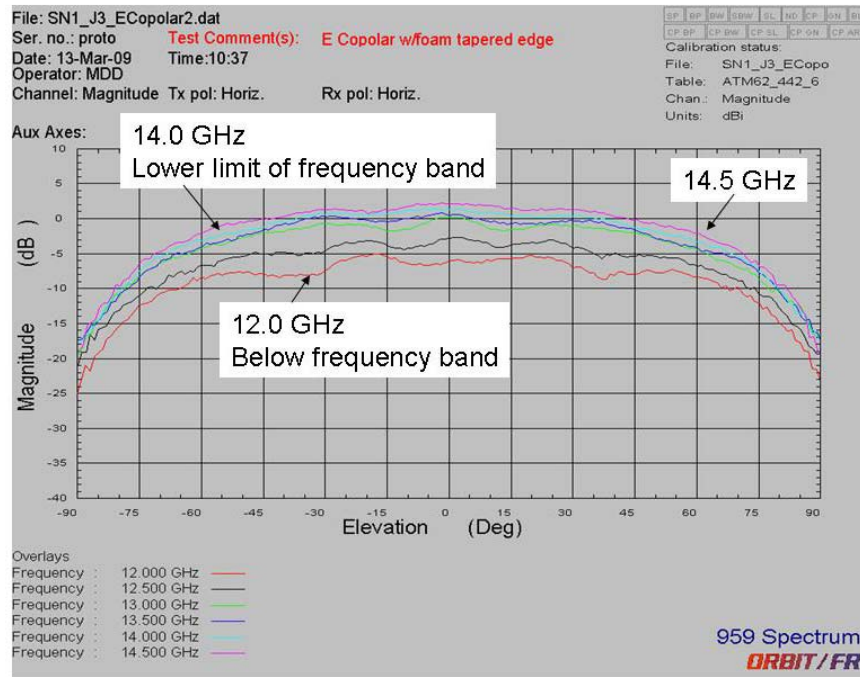

Figure 5 E plane copol pattern for the 3D Metamaterial Wide Scan Radiating Element

Figure 6 shows the E plane copol pattern from 15 – 18 GHz. The upper limit of the E plane frequency band is 18.0 GHz.
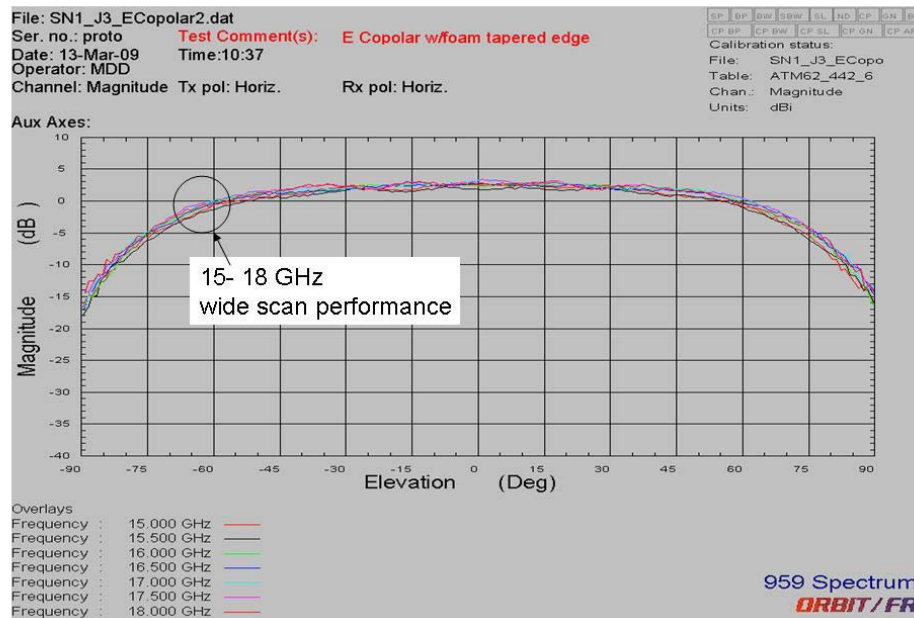

Figure 6 E plane copol Pattern from 15 – 18 GHz

Figure 7 shows the E plane copol and xpol patterns at 16 GHz. Similar results were obtained at other frequencies for the E plane scan. The xpol pattern is of interest because, given the symmetry in the radiating element, the xpol pattern should be in the noise of the measurement. If the xpol pattern is not in the noise, it is an indication of a range problem or manufacturing issue with the radiating element.
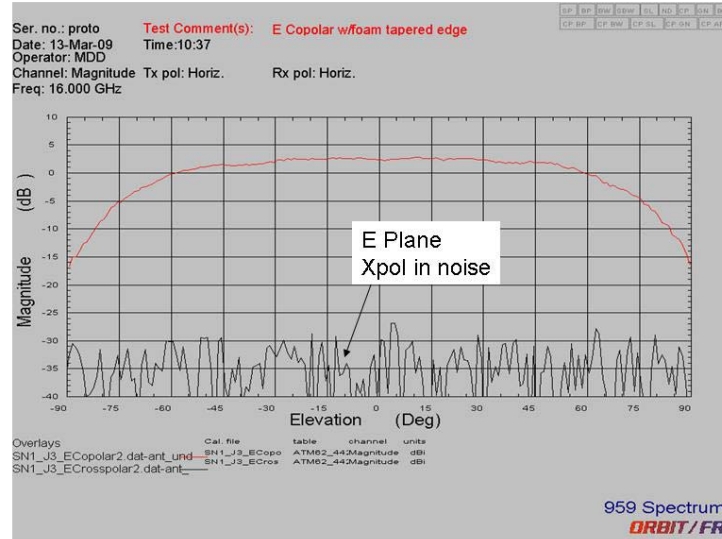

Figure 7 Plot of E plane Copol and Xpol Pattern at 16 GHz

Figure 8 is a plot of the copol H plane pattern from 12 – 14.5 GHz. The lower limit of the frequency band is 14.0 GHz.
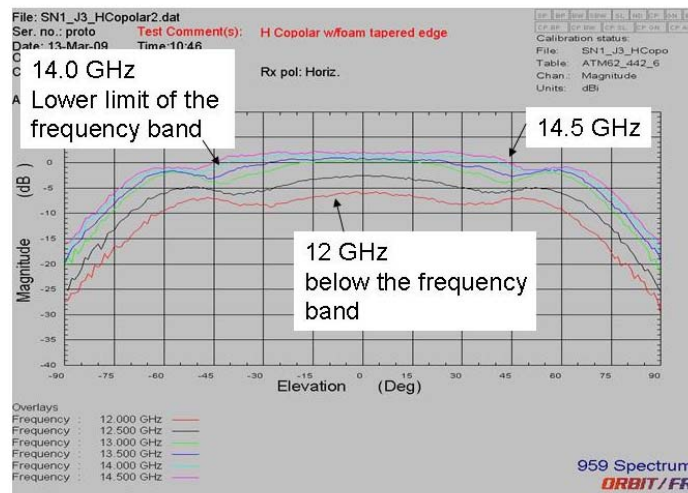

Figure 8 Plot of the Copol H Plane Pattern from 12 – 14.5 GHz

Figure 9 is a plot of the H plane copol pattern for the 3D metamaterial wide scan radiating element from 15 – 18 GHz. The upper limit of the frequency band in the H plane is 17.0 GHz.
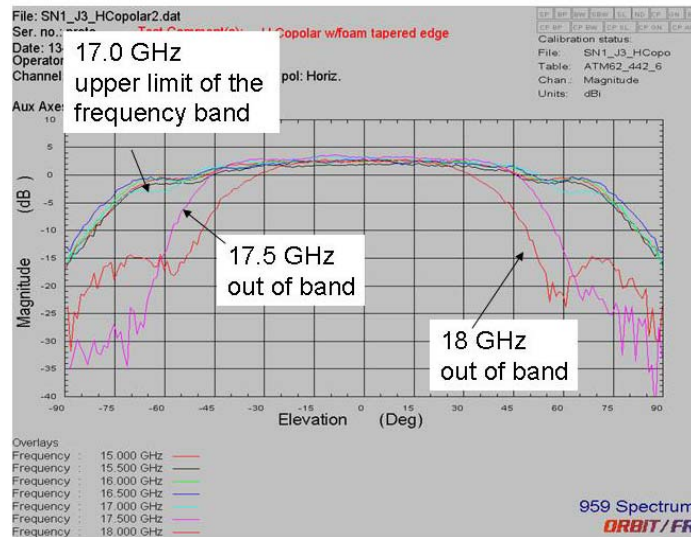
Figure 9 Plot of the H Plane Copol Pattern for the 3D Metamaterial Wide Scan Radiating Element from 15 – 18 GHz

Note that the scan in the H plane falls off sharply outside upper limit of the frequency band.

Figure 10 shows the H plane copol and xpol patterns at 16 GHz. Similar results were obtained at other frequencies for the H plane scan. As noted above, the xpol pattern is of interest because, given the symmetry in the radiating element, the xpol pattern should be in the noise of the measurement. If the xpol pattern is not in the noise, it is an indication of a range problem or manufacturing issue with the radiating element.
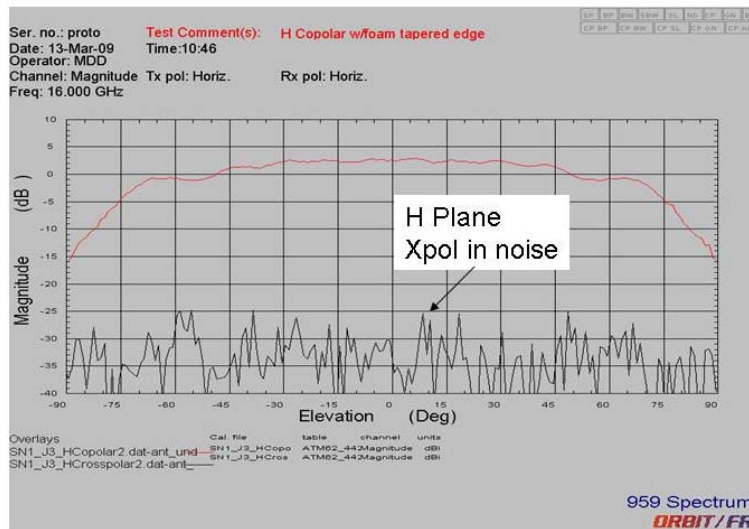

Figure 10 H Plane Copol and Xpol Patterns at 16 GHz

The principal CEM modeling tool used in this paper is Ansoft HFSS [4]. Figure 11 is a comparison of the HFSS calculated active element pattern for the E plane at 18 GHz with

the measured E plane pattern. 18.0 GHz is the upper limit of the frequency band for the E plane. The HFSS calculated E plane pattern does not include the effects of a Gore 100 to measurement system interconnect.
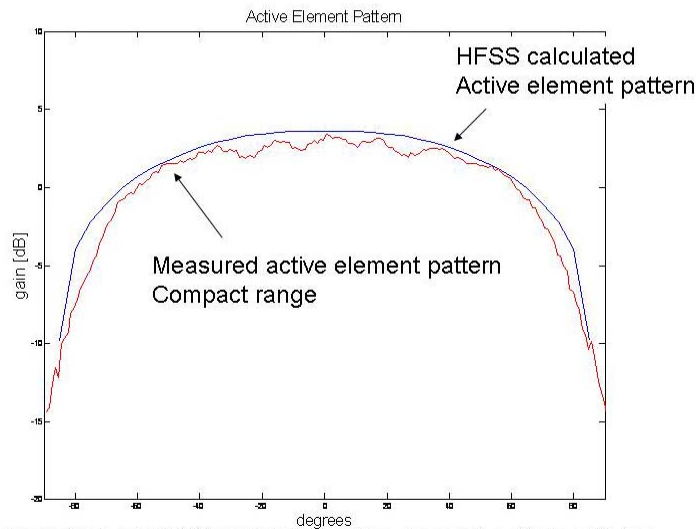

Figure 11 Comparison of HFSS Calculated Active Element Pattern with the Measured Active Element for the E plane at 18 GHz

Figure 12 is a comparison of the HFSS calculated active element pattern for the H plane at 17.0 GHz. 17.0 GHz is the upper limit of the frequency band for the H plane. In the H plane at 17.0 GHz, the measured active element pattern is not as wide as the HFSS calculated active element pattern. In the H plane, a surface wave is present just above the upper limit of the frequency band. If the pcb adhesives, FEP and Speedboard C, were too thick, and/or the dielectric constant of the Teflon material is slightly high (but still within range, typically 2.9 < e' < 2.98), the surface wave will be pulled within the scan volume. If one of the 20 mil Arlon CLTE cores is replaced with an Arlon CLTE 15 mil core, the surface wave effects will be pushed out of the scan volume.
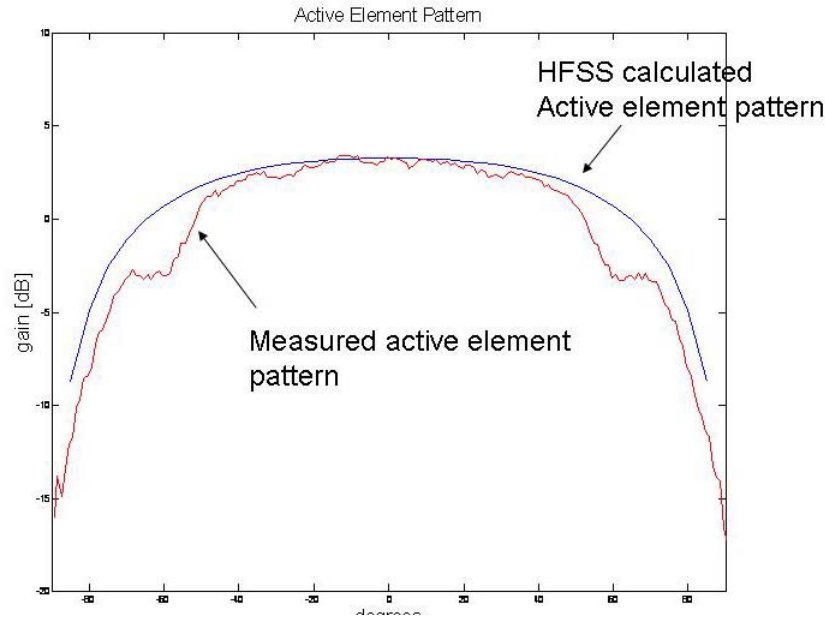
Figure 12 Comparison of HFSS Calculated Active Element Pattern with the Measured Active Element for the H Plane at 17.0 GHz

3. 2D Metamaterial Wide Band and Scan Radiating Element

One of the limitations of the 3D metamaterial is that the 3D metamaterial must be identical for two layers of the printed circuit board. In addition, the volume of the 3D metamaterial typically forces the dipoles on adjacent layers to have an identical arrangement. In this section we will discuss a 2D metamaterial that offers more flexibility than the 3D metamaterial. Figure 13 shows a unit cell of the 3D metamaterial and a unit cell of the 2D metamaterial. The dimensions of the unit cells of the 2D and 3D metamaterial are much less than a free space wavelength and much less than a radiating element unit cell dimensions.
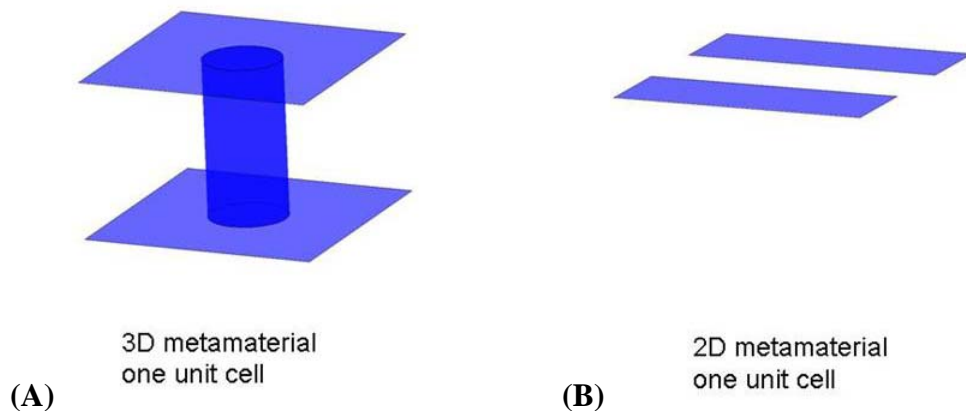

(A)   **(B)**

Figure 13 (A) Unit Cell of 3D Metamaterial and (B) Unit Cell of 2D Metamaterial

The 2D metamaterial was used in the design of a linearly polarized 12-18 GHz radiating element with 70 degree half conical scan angle. A cross sectional view of the radiating element is shown in Figure 14. The 2D metamaterial radiating element contains a built in 30 mil Astroquartz radome. This type of radiating element has the potential to be a load bearing structure in a UAV. This would enable the inclusion of sophisticated radar in a small UAV. Note that this radiating element can operate in a triangular grid. A small UAV does not have the power to afford the luxury of a rectangular grid radiating element. Power and cooling problems would also arise from a rectangular grid radiating element. This radiating element is only .183 free space wavelengths including the stripline feed layer in depth at the highest frequency. A small UAV has a limited volume for a radar system.
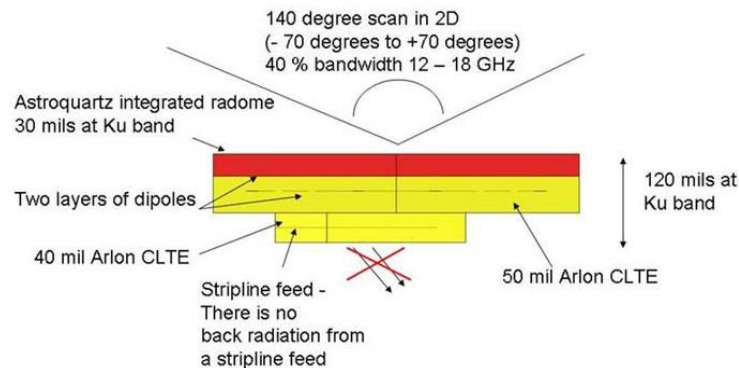

Figure 14 cross sectional view of Rockwell Collns 2D Metamaterial Radiating Element

The wide scan radiating element consists of an 50 ohm stripline feed layer, a slot in the ground plane, two layers of radiating dipoles and 2D metamaterial, and a 30 mil Astroquartz top cover. Figure 15 shows a view of the stripline feed. This is a very simple feed structure, particularly for a planar radiating element that operates from 12 to 18 GHz.
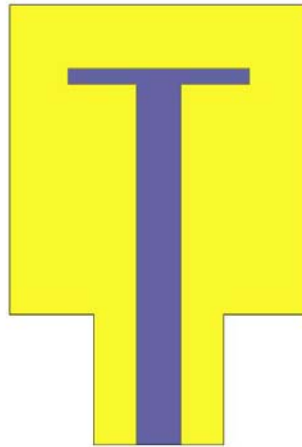

Figure 15 Top Down View of Stripline Feed of 2D Metamaterial Loaded Radiating Element

Two layers of dipoles and 2D metamaterial are used to couple the electromagnetic energy from the slots to free space. The combination of dipoles and 2D metamaterial results in a design with greater bandwidth and scan capability than dipoles alone. A four element section of the lower layer of dipoles and 2D metamaterial is shown in Figure 16.
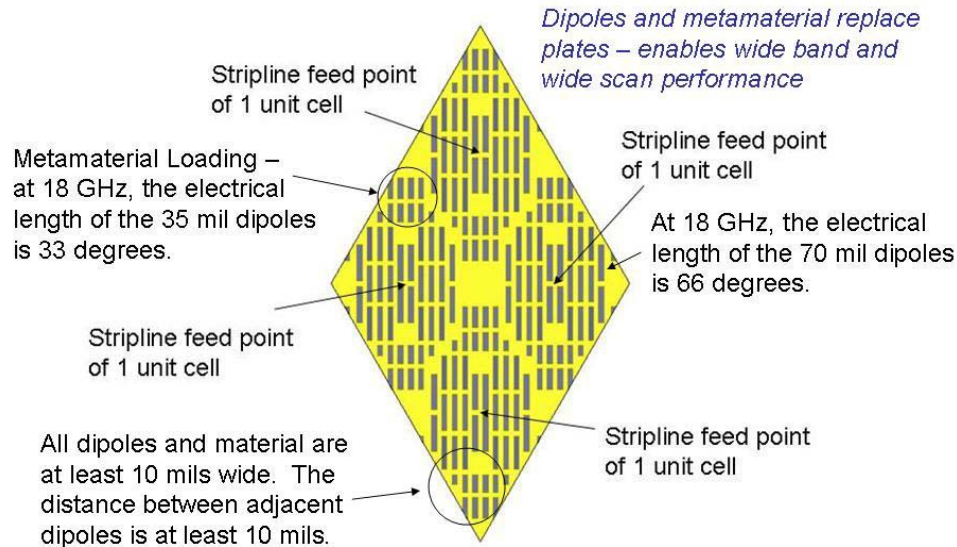
Figure 16 Top Down View of Lower Layer of Dipoles of 2D Metamaterial Loaded Radiating Element

A four element section of the upper layer of dipoles and 2D metamaterial is shown in Figure 17. Note that the upper layer of dipoles and 2D metamaterial is different from the lower layer of dipoles and 2D metamaterial. The use of 2D metamaterial enables the upper and lower layers to be different, resulting in great tuning capability.
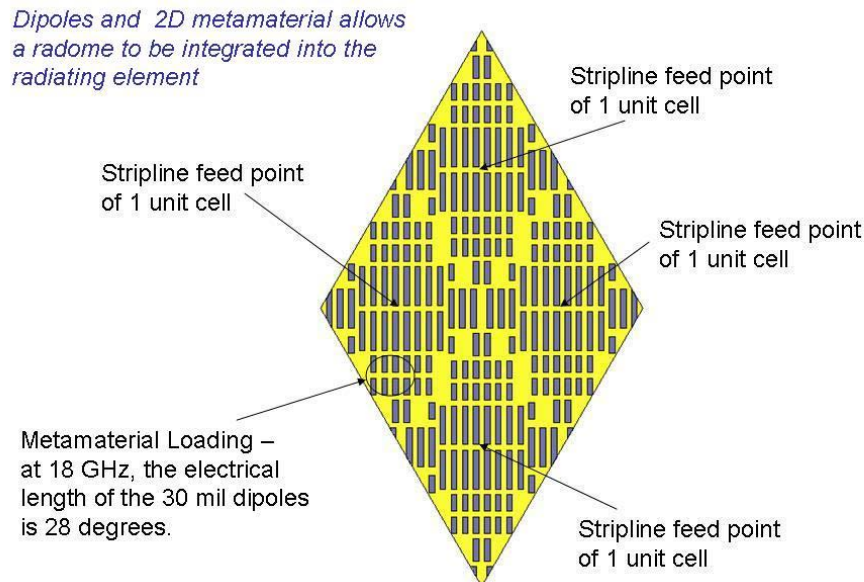
Figure 17 Top Down View of Upper Layer of Dipole of the 2D Metamaterial Loaded Radiating Element

Figure 18 and Figure 19 are plots of the 2D metamaterial loaded radiating element for the E plane scan. The radiating element's performance is excellent out to 70 degree scan.
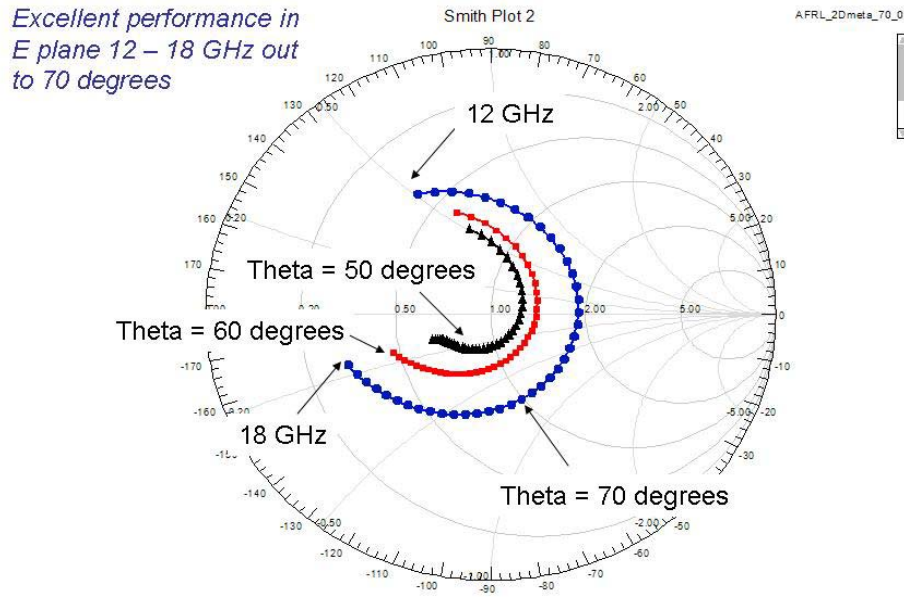
Figure 18 Smith Chart Plot of Active Element Impedance – theta=50, 60, and 70 Degrees
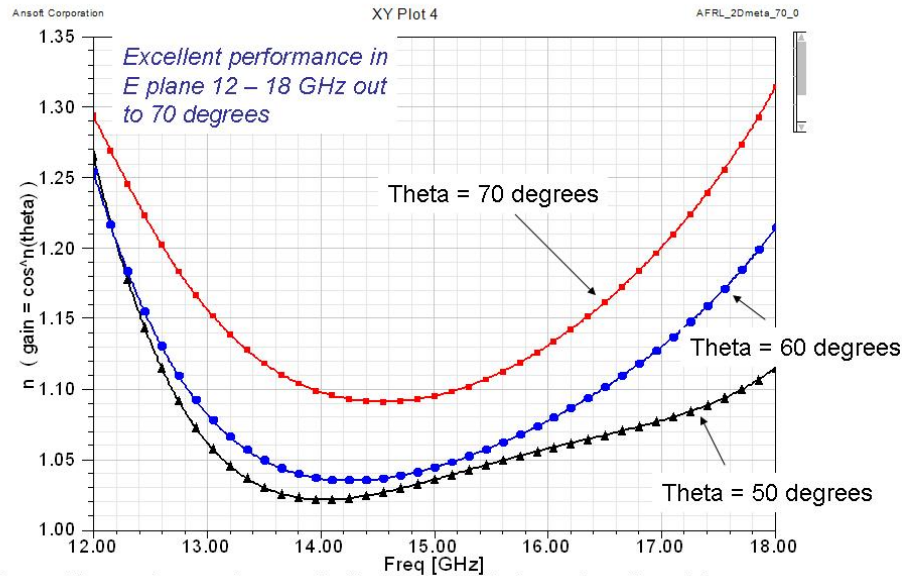
Figure 19. n, where gain = cos^n(theta), is plotted as a function of frequency of the 2D metamaterial loaded radiating element for theta = 50, 60, and 70 degrees.

Figure 19 Plot as Function of Frequency

Figure 20 and Figure 21 are plots of the 2D metamaterial loaded radiating element for the phi = 30.11 degree scan. The closest grating lobe is along the phi = 59.88 degree scan.

With no close grating lobes in the phi = 30.11 degree scan, the impedance and propagating constants of the evanescent floquet modes are relatively constant over frequency and scan. The radiating element should be well matched along the phi = 30.11 degree scan.
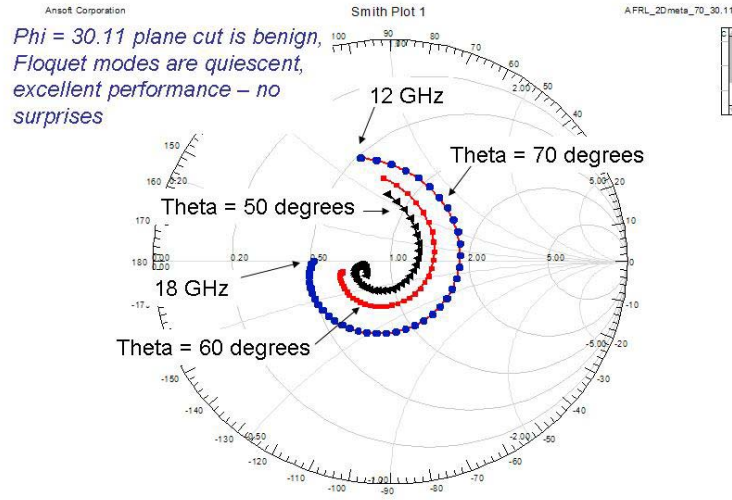
Figure 20 Smith Chart of 2D Metamaterial Loaded Radiating Element - phi=30.11 degree Scan
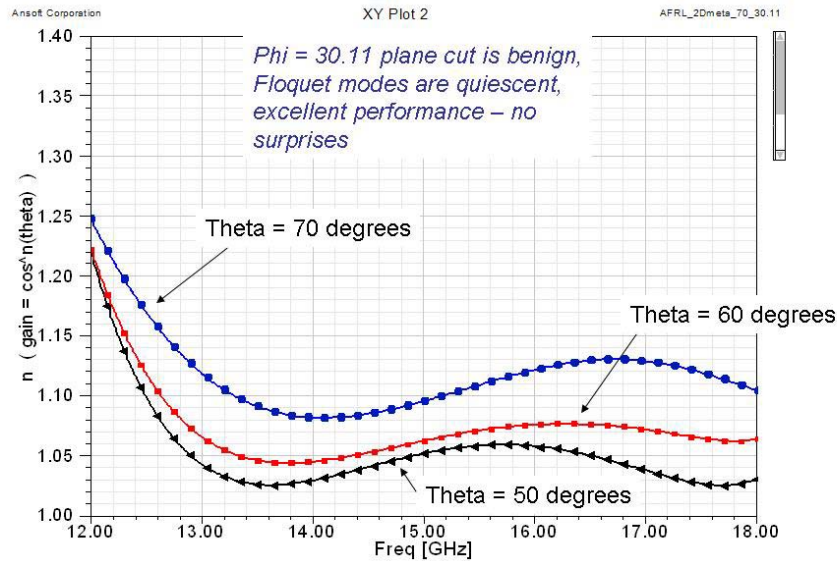
Figure 21 Plot as Function of Frequency for of 2D Metamaterial Loaded Radiating Element - phi=30.11 degree Scan

Figure 22 and Figure 23 are plots of the 2D metamaterial loaded radiating element for phi = 59.88 degree scan. The phi = 59.88 degree plane cut is the plane where a grating lobe is closest to visible space [5]. This is the plane cut for which the impedance and

propagating constants of the evanescent floquet modes change the most over frequency and scan in theta. This is an important plane cut to check.
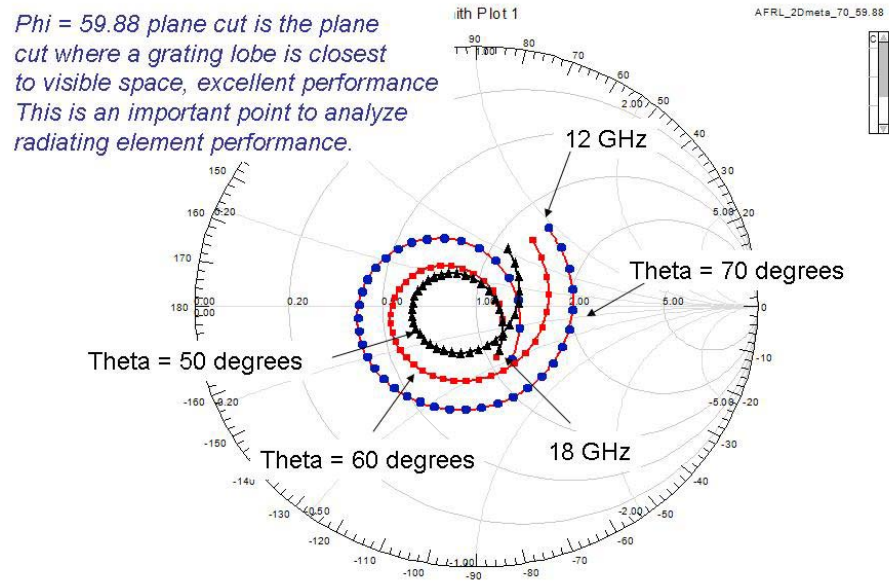
Figure 22 Smith Chart of 2D Metamaterial Loaded Radiating Element for phi = 59.88 degree scan
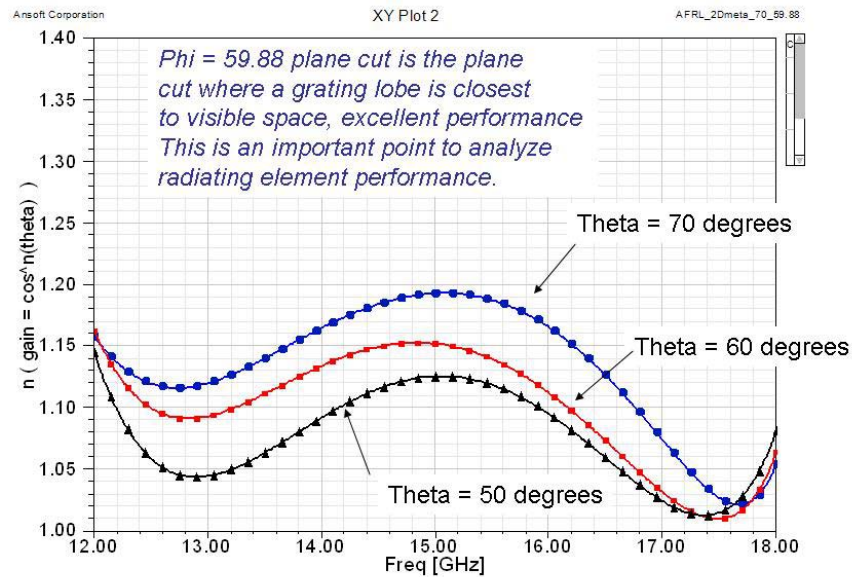
Figure 23 Plot of of 2D Metamaterial Loaded Radiating Element for phi = 59.88 degree scan

The H plane scan performance, phi = 90 degrees, is shown in Figure 24 and Figure 25.
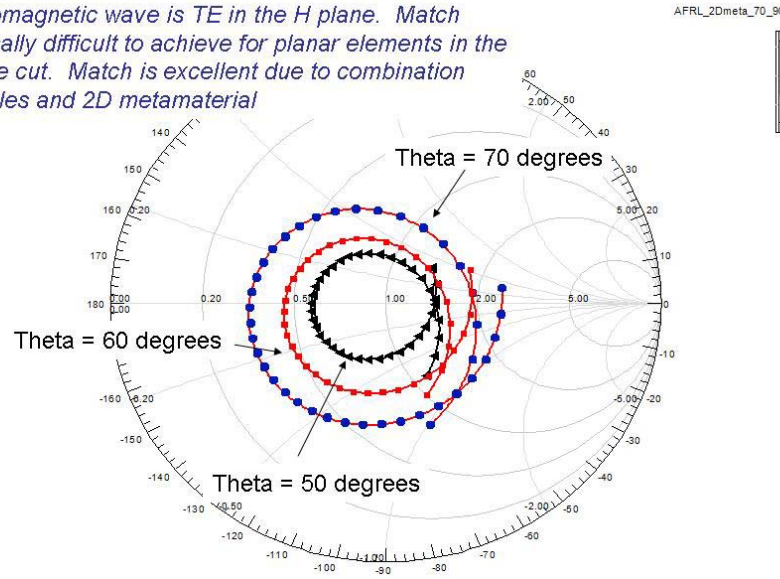
Figure 24 Smith Chart of H Plane Scan Performance
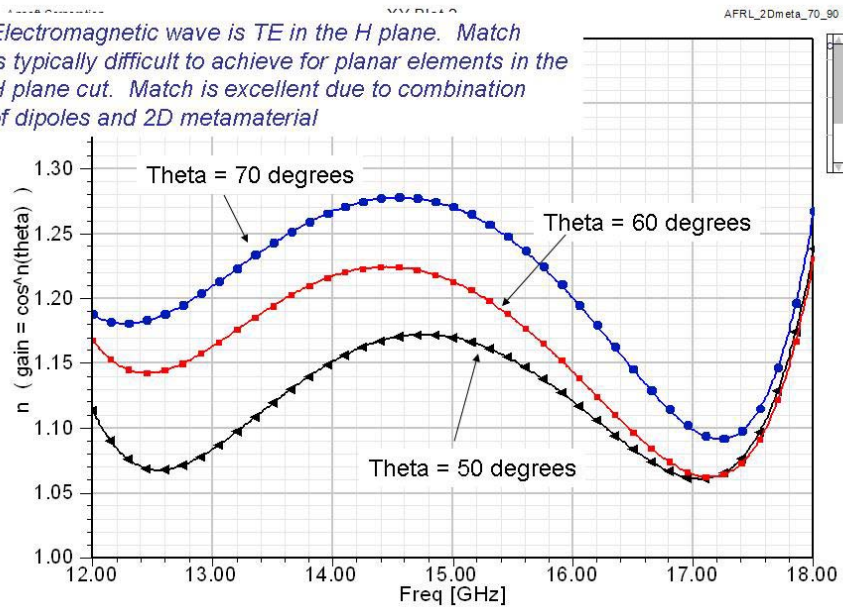
Figure 25 Plot Chart of H Plane Scan Performance

The effect of the electrically small metamaterial can be seen in Figure 26 and 27. Figure 26 is a plot of the H plane active element impedance of the radiating element with and without 2D metamaterial loading. Figure 28 is a plot of n, where gain = cos^n(theta), as a function of frequency.
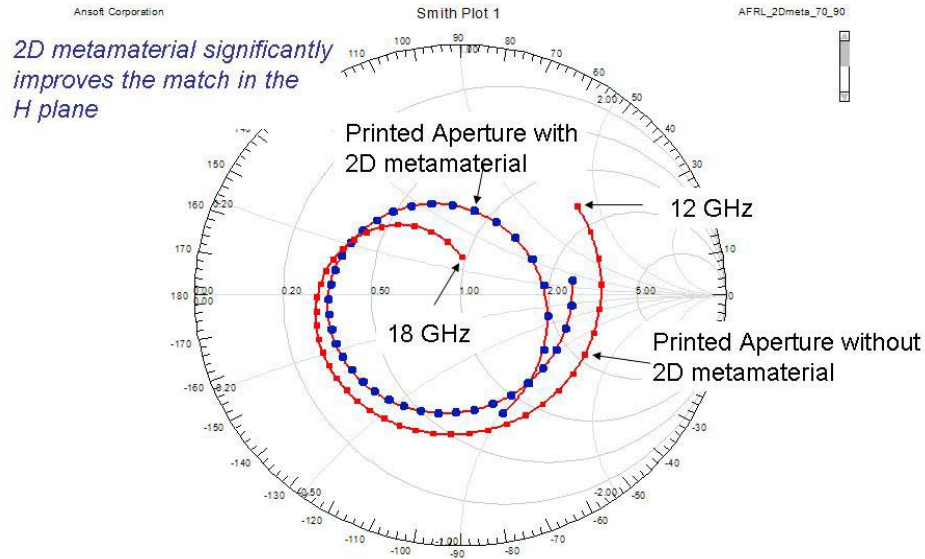
Figure 26 Effect of Electrically Small Metamaterial – Smith Chart - H Plane Plot
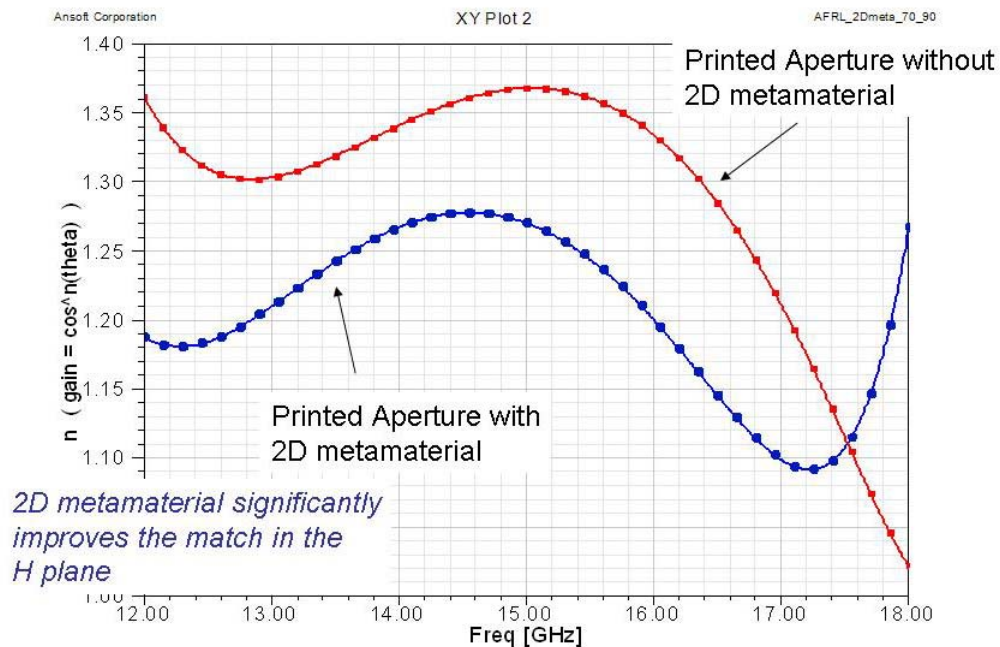
Figure 27 Effect of Electrically Small Metamaterial – Plot of n

4. Conclusions

The 3D metamaterial radiating element basically works. The E plane shows good scan performance from 14 to 18 GHz out to 70 degree half conical angle scan. The H plane works well from 14 to 16.5 GHz out to 70 degree half conical angle scan. The frequency band can be extended in the H plane by reducing the height of the aperture stack slightly.

The 2D metamaterial radiating has a computed frequency band of 12 to 18 GHz with two dimensional scan out to 70 degree half conical scan angle. The 2D metamaterial radiating element has a 30 mil Astroquartz radome and has the potential to be a load bearing antenna in a small UAV. A 2D metamaterial fractional array is currently being built in order to measure the scan performance.

Both the 3D metamaterial radiating element and the 2D metamaterial radiating element can operate in a triangular grid which minimizes size, weight, and power requirements for a given scan volume.

5. References

[1] N. Llombart, A. Neto, G. Gerini, and P. de Maagt, "1-D Scanning Arrays on Dense Dielectrics Using PCS-EBG Technology," *IEEE Trans. Antennas Propag.*, vol. 55, no. 1, pp.26-35, Jan. 2007.

[2] R. Erickson, R. Gunnarsson, T. Martin, L. –G. Huss, L. Pettersson, P. Andersson, A. Ouacha, "Wideband and Wide Scan Phased Array Microstrip Patch Antennas for Small Platforms," Antennas and Propagation, 2007 EuCAP 2007 The Second European Conference on, 11-16 Nov. 2007 Page(s):1-6

[3] M. Buckley, L. Paulsen, J. Wolf, and J. West, "Stripline Fed Low Profile Radiating Elements for Use in Integrated Arrays," 2008 Antenna Applications Symposium, Allerton Park, Monticello, Illinois, pp. 60-85, Sept 16 – 18, 2008

[4] www.ansoft.com

[5] D. Pozar, and D. Schaubert, "Scan Blindness in Infinite Phased Arrays of Printed Dipoles," *IEEE Trans. Antennas Propag.*, vol. 32, no. 6, pp.602-612, June 1984.

Interleaved Dual-Band Printed Antenna Element for Phased Array Applications

R. L. Li[1], T. Wu[1], K. Naishadham[2], L.Yang[1], and M. M. Tentzeris[1]

Georgia Institute of Technology, Atlanta, GA, USA

Corresponding author's e-mail: <u>krishna.naishadham@gtri.gatech.edu</u>

Abstract

Light-weight phased array antennas for aerospace applications require utilizing the same antenna aperture to provide multiple functions with dissimilar radiation pattern specifications (e.g., multi-band operation for communications and tracking). In this paper, we present a novel antenna *element* design for dual-band phased array configuration, comprising nested printed dipoles with balanced individual feeds for each band. The folded dipoles are assumed to be resonant at octave-separated frequency bands (1 GHz and 2 GHz for the design reported herein), and printed on photographic paper (dielectric constant of 3) using low-cost photolithography and ink-jet printing technology. In order to reduce the back-lobe and also to improve the impedance bandwidth, a ground plane is inserted 0.13 λ below the antenna substrate, where λ is the wavelength at 1 GHz. Each dipole is gap-fed in a balanced mode by voltage induced electromagnetically from a microstrip line on the other side of the substrate. The feed line includes a stub for improving the impedance match. Two high-band elements are each nested in one leg of a low-band folded dipole, with a spacing of half-wavelength at 2 GHz to produce an array pattern without grating lobes. This nested element configuration has been simulated, fabricated and measured, and excellent corroboration observed between simulated and measured data. The return loss shows well-centered low and high bands with 10-dB bandwidth of at least 5% for each, and isolation better than -15 dB between the bands. In both bands, the measured co-polarized gain is about 5.3 to 7 dBi in the two principal planes, with cross-polarization less than -25 dBi in the H-plane. Currently, this low-cost light-weight nested antenna element is being integrated into a dual-band phased array. The scan performance of this array will be reported in another paper.

---

[1] Georgia Electronic Design Center (GEDC), ECE Department

[2] Georgia Tech Research Institute (GTRI), Sensors and Electromagnetic Applications Laboratory

1. Introduction

In aerospace and wireless communications, there is a pressing need to minimize the size, weight and power requirements of antenna arrays, while simultaneously requiring multiple radiation functions using the same physical aperture. For example, the array may require shared aperture capability to facilitate full-duplex operation with polarization diversity, and multiple isolated frequency bands for communications, telemetry, radar, etc. This paper presents a novel planar radiating element utilizing the same physical aperture for two sub-bands of an octave-separated dual-band array antenna. The array design and its operation utilizing the proposed radiating elements will be the subject of another paper.

One approach to design multi-band array antennas is to use a single wideband radiating aperture and process the received signals with an integrated front-end comprising wideband power dividers and wideband feeds to the elements. Ultra-wideband (UWB) antenna elements have been designed and fabricated that can potentially provide a shared aperture capability [1]-[4]. However, these antennas require expensive, heavy, and bulky front-ends to channelize the signals into multiple frequency bands required for communications and radar signal processing, where narrow bandwidths are typically allocated for each function. UWB apertures designed for multiple communication purposes in FCC licensed bands use short discrete pulses to modulate low-power signals. In order to maintain pattern uniformity over a wide bandwidth, large physical aperture is needed. Furthermore, there may be a few narrow-band communications channels within the UWB band, such as wireless local-area network (WLAN) IEEE802.11a and HIPERLAN/2 WLAN operating in the 5–6 GHz band, which form a subset of UWB (3.1 to 10. 6 GHz). In order to prevent interference to these channels from the UWB radiator, band-notched antennas have been developed, which mitigate the need for high-Q band-reject filters [5]. The associated complexity of receiver deign escalates considerably if UWB operation is required in an array configuration.

Several researchers have looked at designing planar light-weight antennas with isolated frequency bands, using a single feed to excite both bands [6]-[18]. A T-shaped planar monopole antenna with two asymmetric horizontal strips to produce the lower and upper resonant modes has been investigated in [6] and [7] to cover the 2.4/5.2 GHz bands. The authors in [8] presented the design of a planar L-shaped monopole antenna fed by a microstrip line, using a shorted parasitic inverted-L wire to facilitate tri-band operation. By adjusting the coupling between the parasitic and driven elements, two resonant modes are excited, one covering 2.4 GHz band and the other producing 5.2/5.8 GHz dual-band radiation. In [9], a dual-band antenna for 2.4/5 GHz operation is designed

utilizing coupling between driven and parasitic strips of a uni-planar monopole occupying a small form-factor. The concept of adjusting reactive coupling between parasitic and driven elements has been used in planar patch antenna geometries to produce dual-band operation [10]-[18], including the use of flat-plate radiator above a ground plane with a shorted parasitic strip on the same face [10], printing two dissimilar coupled monopoles on either side of a substrate [11], the use of slots and shorted pins on patches to produce modes with widely separated resonant frequencies [12]-[15], and the use of notches or other conductor perturbation to produce multiple modes [16]-[18]. However, none of these design approaches are suitable for dual-frequency array operation, because they are all based on single feed design, and depend on radiating element shaping or parasitic coupling to produce multiple band operation. Multiple feeds will be necessary, either at the element level or sub-array level, to facilitate different imaging, tracking or other signal processing functions, and to enable MIMO communications and adaptive beam-forming. Also, for scanning purposes, it is desirable to have separate feeds for each frequency band, with the ability to control amplitude and phase either at the element level or at the sub-array level, and to have a simpler design for the element itself.

The concept of array antennas with widely separated frequency bands, such as PCS, GSM communications bands, L and S radar bands, etc., sharing the same physical aperture is a challenging problem, and has been mostly unexplored. A novel design of dual-band, dual-linearly polarized microstrip antenna arrays for synthetic aperture radar applications, with a frequency ratio of about 1:3, has been presented in [19]. Stacked microstrip dipoles and square patches are used as the radiating elements at S- and X-bands, respectively. The microstrip dipoles are proximity-coupled and the square patches are probe-fed. The measured impedance bandwidth (VSWR $\leq$ 2) of the prototype array reaches 8.9% and 17% for S- and X-bands, respectively, and the measured isolation between polarizations for both bands is better than -20 dB. Low cross-polarization levels (less than -26 dB and -31 dB for S- and X-bands, respectively) have been observed.

In this paper, we present a novel antenna element design for dual-band phased array configuration, comprising interleaved printed dipoles with balanced individual feeds for each band. The folded dipoles are resonant at octave-separated frequency bands, and printed on photographic paper (dielectric constant of 3) using low-cost photolithography and ink-jet printing technology [20]-[23]. This nested element configuration has been simulated, fabricated and measured, and excellent corroboration observed between simulated and measured data. Currently, this low-cost light-weight nested antenna element is being integrated into a dual-band phased array. The scan performance of this array will be reported in another paper.

2. Antenna Design Approach

The proposed antenna design approach involves using nested or interleaved elements to provide adequate isolation between channels. As an example, Figure 1 depicts a novel antenna design for dual-band phased array application, which consists of nested printed dipoles with balanced individual feeds for each band. The folded dipoles are assumed to be resonant at two frequency bands with an octave separation (1 GHz and 2 GHz for the design reported herein). In order to reduce the backlobe and also to improve the impedance bandwidth, a ground plane is inserted 0.13 λ below the antenna substrate, where λ is the wavelength at 1 GHz. Each dipole is gap-fed in a balanced mode by voltage induced electromagnetically from a microstrip line on the other side of the substrate (see the inset in Figure 1). The feed line includes a stub for improving the impedance match. One high-band element is nested in each leg of the low-band folded dipole, with a spacing of half-wavelength (at 2 GHz) to provide grating-lobe-free operation in the array environment. A pair of high-band elements are also inserted vertically half-way between two low-band elements. This self-similar design and placement of dual-band elements offers the capability to use the extended single physical aperture for multiple antenna functions, and can also be integrated with independent elements (such as patches) in stacked layers if more than two bands are desired. However, feed design and beam-former design become very complicated as we add more frequency bands or antenna functions.
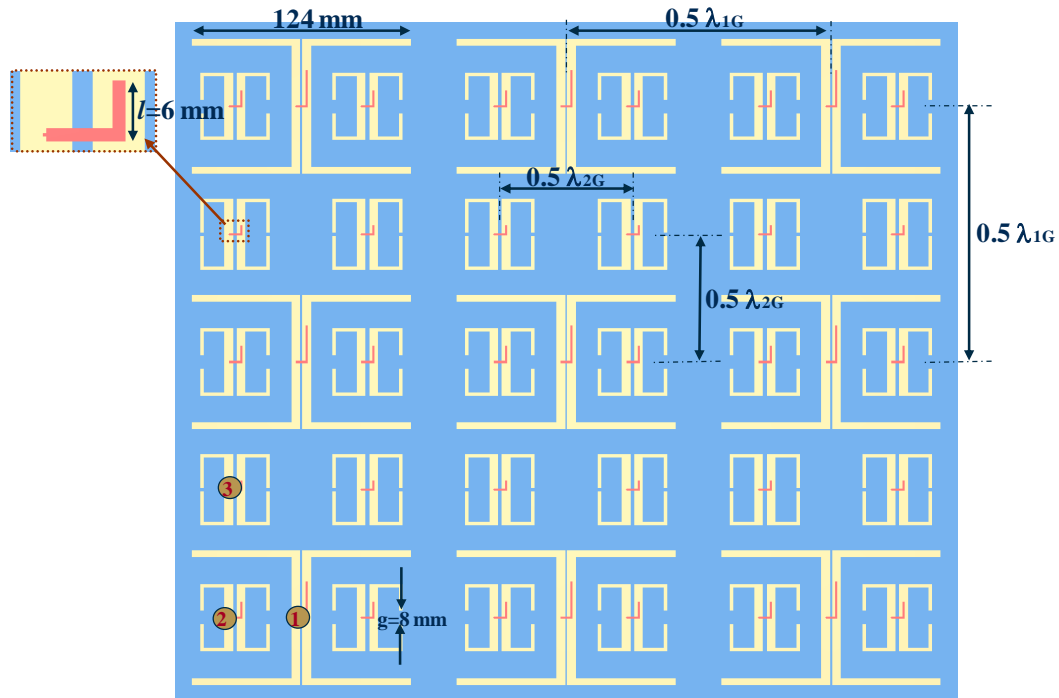
Figure 1. Top view of a nested element-array for dual-band operation.

A single dual-band nested element is shown in Figure 2. The feed line is on the other side of the substrate. The distance from the center of the dipole to the gap is about half wavelength at its resonant frequency. Because of mutual coupling, the gap for the high-band dipole is adjusted to be shorter than that of the low-band one. The length of each dipole is optimized to tune the low-band dipole to 1 GHz and the high-band one to 2 GHz. The dipole is on the bottom side of the substrate (see Figure 3) and the microstrip feed line is on the top side. The stub connected to each feed line can be adjusted in length for impedance matching.
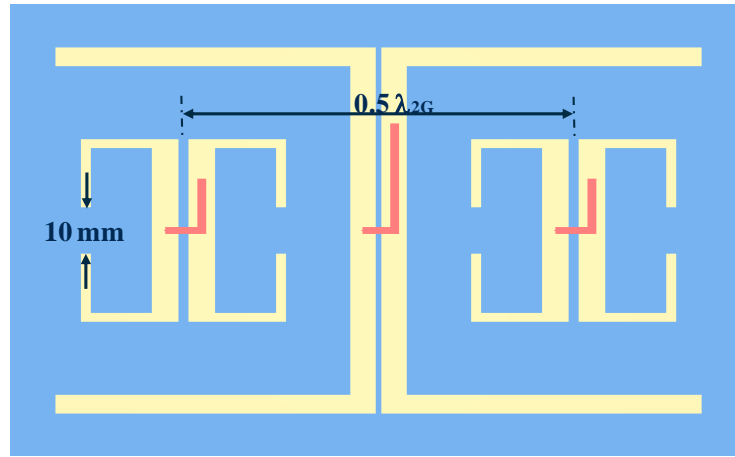
Figure 2. Dual-band nested element.
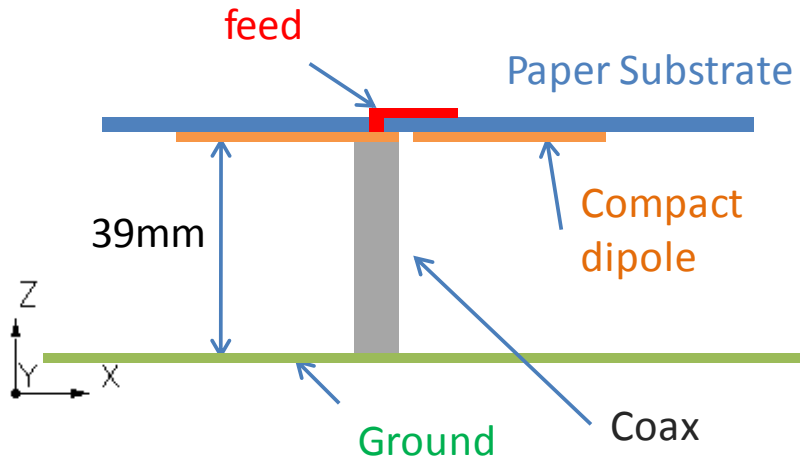
Figure 3. Feed configuration for the dual-band element.

The antenna and the feed line are printed on photographic paper using inkjet printing technology [20]-[23]. The substrate has the dimensions 200 mm x 160 mm x 0.52 mm, and a dielectric constant of 3.1. The ground plane, of size 200 mm x 160 mm, is

positioned 0.125 λ below the substrate at the lower frequency, or 0.25 λ at the higher frequency. It means that we achieve broader bandwidth at 2 GHz compared to that at 1 GHz. Also, the ground plane is necessary for mounting on a vehicle surface, and serves to improve the efficiency by minimizing the back-lobe. As shown in Figure 3, the center conductor of a coaxial cable is connected to the microstrip feed line, which impresses a voltage at the gap between the two dipole arms. One end of the cable shield is connected to one antenna arm, and the other end is terminated on the reflector. In order to minimize perturbation of antenna currents, we use SSMA connectors, with one feed per antenna.

3. Results and Discussion

The dual-band antenna has been designed using the commercial time-domain simulator, *Microstripes*, and optimized for good match (VSWR better than 1.5) at 1 GHz and 2 GHz. The optimized antenna has been fabricated and its radiation pattern as well as reflection coefficient have been characterized. Figure 4 shows the fabricated antenna trace comprising the dual-band elements. For clarity, the feed configuration and ground plane are not shown.
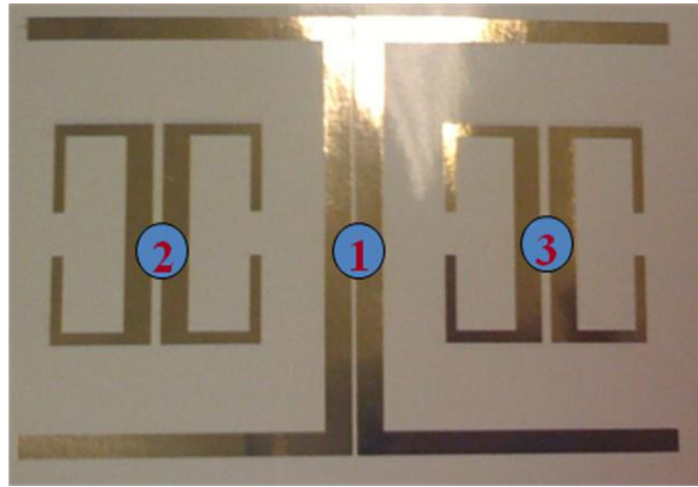
Figure 4. Fabricated antenna geometry.

The comparison of simulated and measured scattering parameters is depicted in Figure 5. The antenna elements are numbered as indicated in Figure 4. Excellent agreement is observed between the two sets of data, with measured return loss of the low-band at -18 dB and that at high-band at -16 dB. Because the ground plane is located at quarter wavelength of the higher center frequency, the bandwidth in the high-band is larger than that of the low-band. The measured return loss of the two high-bands show similar variation with frequency. The isolation between the low-band element and either of the two high-band elements is observed to be between -18 dB and -16 dB around 2

GHz, and -25 dB at 1 GHz. Therefore, it is anticipated that the interference between the two bands in an array environment will not be significant.
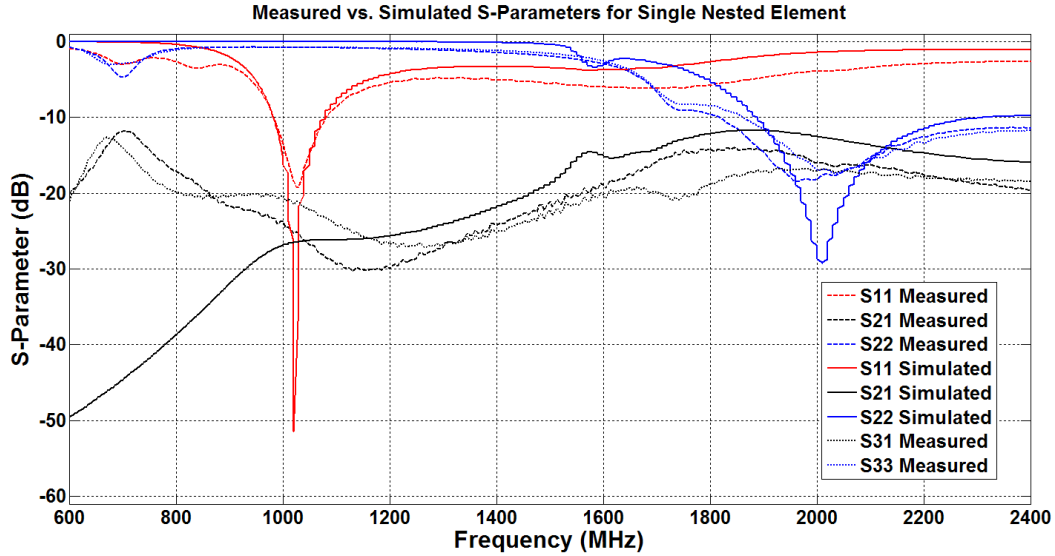
Figure 5. Comparison between measured and simulated scattering parameters.

The radiation pattern and gain of the antenna has been measured in an anechoic chamber at GTRI. Figure 6 compares the simulated and measured E-plane patterns at the low band frequency of 1 GHz. The measured peak gain is 7 dBi whereas the simulated *directivity* is 8.2 dBi. Considering the losses in the antenna, anticipated to be few tenths of a dB, and the systematic as well as random measurement errors attributed to the chamber and the equipment, which are collectively estimated as 0.5 dB, it appears that the simulated and measured gain values are reasonably close. The measured cross-polarization is better than -20 dB over the entire azimuth angle range.

Figure 6. Comparison of simulated and measured E-plane patterns at 1 GHz.

Figure 7. Comparison of simulated and measured H-plane patterns at 1 GHz.

Figure 7 compares the simulated and measured H-plane patterns at the low band frequency of 1 GHz. The measured peak gain is 6.9 dBi whereas the simulated directivity is 8.2 dBi. Considering the losses in the antenna and the measurement errors, as alluded to earlier, it appears that the simulated and measured gain values are reasonably close. The measured cross-polarization is better than -18 dB over the entire azimuth angle

range. The beamwidth, measured at 0 dBi reference in both graphs (Figures 6 and 7), is somewhat broader for the H-plane pattern than the E-plane pattern. This is typical of printed dipoles because of the uneven influence of ground plane currents in the two principal planes. In summary, the agreement in the simulated and measured patterns in both of these figures is within the measurement accuracy.

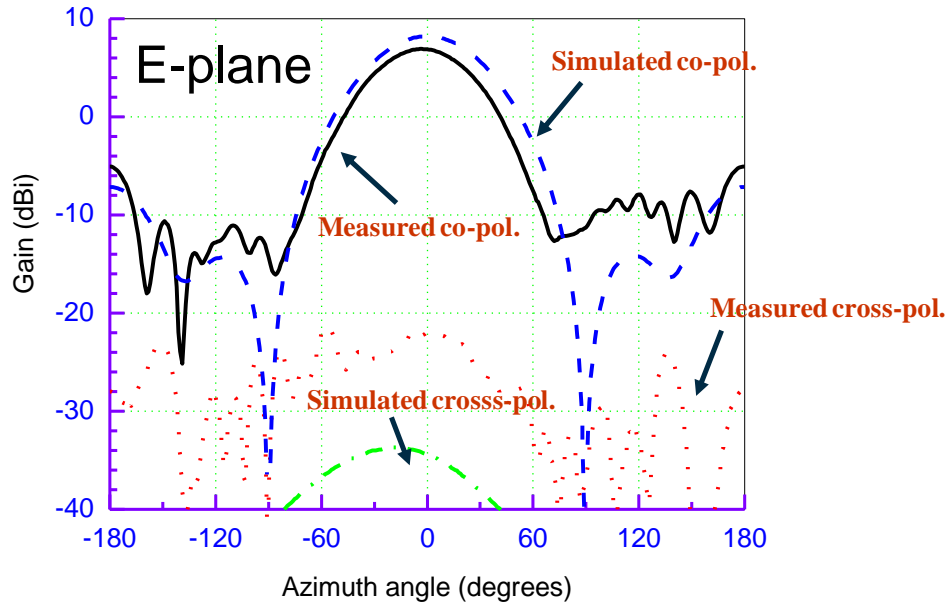Figure 8 compares the simulated and measured E-plane patterns of element no. 2 at the high band frequency of 2 GHz. The pattern is asymmetric for both measured and simulated gain because of influence of the other high-band element nearby. A similar result (not plotted) has been observed for element no. 3. The measured peak gain is 6 dBi whereas the simulated *directivity* is 7.7 dBi. This discrepancy is larger than that in the low-band pattern in Figure 6, and can be explained by the higher cross-polarization measured. Nonetheless, the agreement between measured and simulated data in the pattern is gratifying given that the high-band elements are separated by only a half wavelength, and are completely interleaved within the low-band element. It is also interesting that the measured pattern has lower sidelobes than the simulated pattern in spite of the higher measured cross-polarization level.

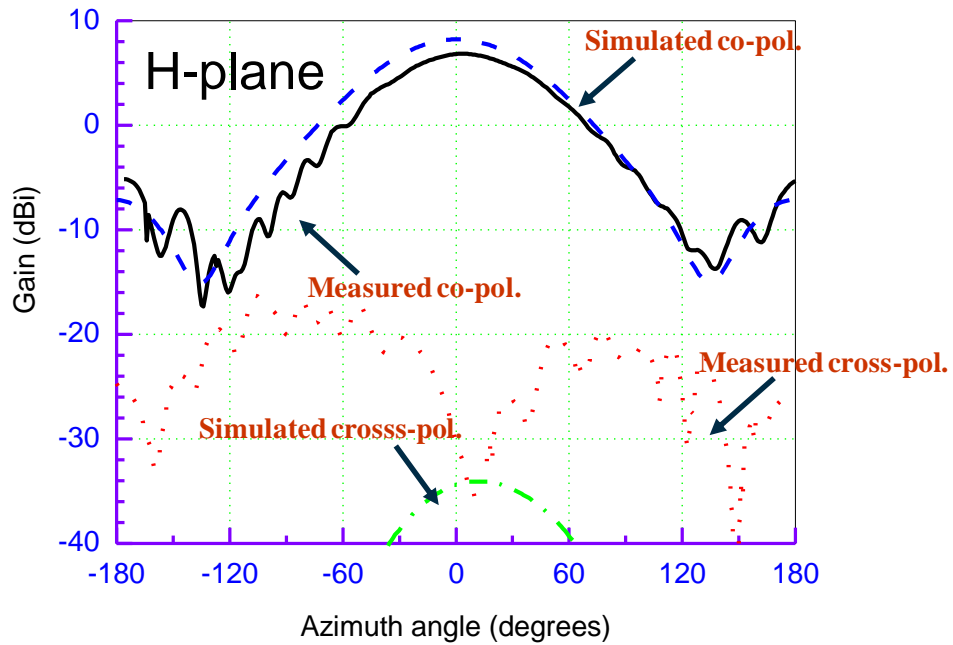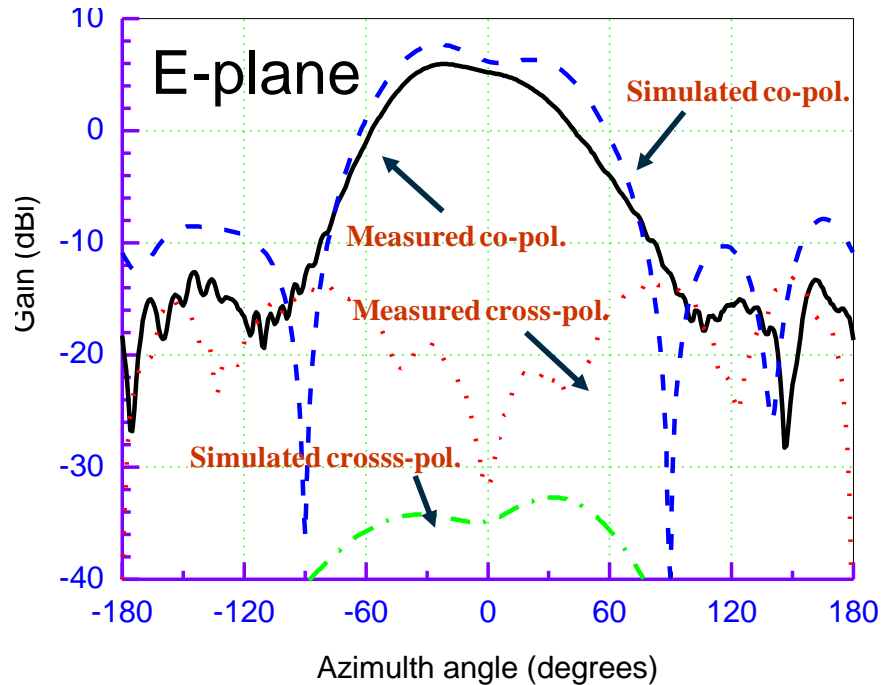Figure 8. Comparison of simulated and measured E-plane patterns at 2 GHz.
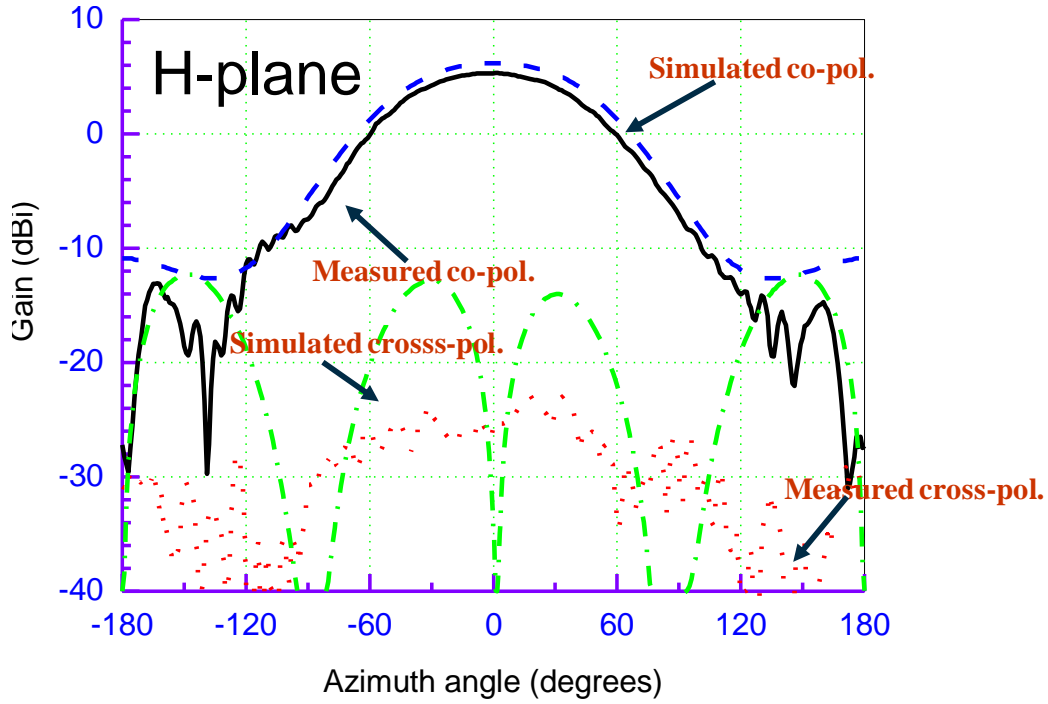
Figure 9. Comparison of simulated and measured H-plane patterns at 2 GHz.

Figure 9 compares the simulated and measured H-plane patterns of element no. 2 at the high band frequency of 2 GHz. This pattern is considerably less asymmetric for both measured and simulated gain in contrast to the E-plane pattern in Figure 8. A similar result (not plotted) has been observed for element no. 3. The measured peak gain is 5.3 dBi whereas the simulated *directivity* is 6.2 dBi. The lower cross-polarization levels in the measured pattern yields a good agreement in the two gain values. The measured cross-polarization is better than -24 dBi and is considerably better than the cross-polarization in the simulated pattern in the direction of the main beam. In an array implementation, it appears that high-band elements placed along the H-plane will have less coupling than those in the E-plane.

4. Conclusions

We have presented a novel antenna element design for dual-band phased array configuration, comprising nested printed dipoles with balanced individual feeds for each band. The folded dipoles are resonant at octave-separated frequency bands (1 GHz and 2 GHz for the design reported herein), and fabricated using low-cost photolithography and ink-jet printing technology. Each dipole is gap-fed in a balanced mode by voltage induced electromagnetically from a microstrip line on the other side of the substrate. The feed line includes a stub for improving the impedance match. This nested element

configuration has been simulated, fabricated and measured, and excellent corroboration observed between simulated and measured data. The return loss shows well-centered low and high bands with 10-dB return loss bandwidth of at least 5% for each, and isolation better than -15 dB between the bands. In both bands, the measured co-polarized gain is about 5.3 to 7 dBi in the two principal planes, with cross-polarization less than -25 dBi in the H-plane. It has been shown that the shielding provided by the interleaved design reduces coupling between the high-band elements in the H-plane. Currently, this low-cost light-weight nested antenna element is being integrated into a dual-band phased array. The scan performance of this array will be reported in another paper.

References

[1] F-W. Yao and S-S. Zhong, "Broadband and high-gain microstrip slot antenna," *Microw. Opt. Technol. Lett*, vol. 48, no. 11, pp. 2210-2212, Nov. 2006.

[2] T. G. Ma and S. K. Jeng, "Planar miniature tapered-slot-fed annular slot antennas for ultra-wideband radios," *IEEE Trans. Antennas Propag*., vol. 53, pp. 1194–1202, Mar. 2005.

[3] Y. C. Lin and K. J. Hung, "Compact ultrawideband rectangular aperture antenna and band-notched designs," *IEEE Trans. Antennas Propag*., vol. 54, pp. 3075–3081, Nov. 2006.

[4] T.-Y. Yun, C. Wang, P. Zepeda, C. T. Rodenbeck, M. R. Coutant, M. Li, and K. Chang, "A 1-21 GHz low-cost, multi-frequency and full-duplex phased array antenna system," *IEEE Trans. Antennas Propag*., vol. 50, no. 5, pp. 641-650, May 2002.

[5] W. S. Lee, D. Z. Kim, K. J. Kim, and J. W. Yu, "Wideband planar monopole antennas with dual band-notched characteristics," *IEEE Trans. Microw. Theory Tech*., vol. 54, no. 6, pp. 2800–2806, June 2006.

[6] Y.-L. Kuo and K.-L. Wong, "Printed double-T monopole antenna for 2.4/5.2 GHz dual-band WLAN operations," *IEEE Trans. Antennas Propag*., vol. 51, no. 9, pp. 2187-2192, Sep. 2003.

[7] S.-B. Chen, Y.-C. Jiao, W. Wang, and Zhang, F.-S., "Modified T-shaped planar monopole antennas for multiband operation," *IEEE Trans. Microw. Theory Tech*, vol. 54, no. 8, pp. 3267-3270, Aug. 2006.

[8] J.-Y. Jan and L.-C. Tseng, "Small planar monopole antenna with a shorted parasitic inverted-L wire for wireless communications in the 2.4, 5.2, and 5.8-GHz bands," *IEEE Trans. Antennas Propag*., vol. 52, no. 7, pp. 1903-1905, July 2004.

[9] L.-C. Chou and K.-L. Wong, "Uni-planar dual-band monopole antenna for 2.4/5 GHz WLAN operation in the laptop computer," *IEEE Trans. Antennas Propag.*, vol. 55, no. 12, pp. 3739-3741, Dec. 2007.

[10] K.-L. Wong, L.-C. Chou, and C.-M. Su, "Dual-band flat-plate antenna with a shorted parasitic element for laptop applications," *IEEE Trans. Antennas Propag.*, vol. 53, no. 1, pp. 539-544, Jan. 2005.

[11] R. L. Li, B. Pan, J. Laskar, and M. M. Tentzeris, "A novel low-profile broadband dual-frequency planar antenna for wireless handsets," *IEEE Trans. Antennas Propag.*, vol. 56, no. 4, pp. 1155-1162, Apr. 2008.

[12] B. F. Wang and Y. T. Lo, "Microstrip antennas for dual-frequency operation," *IEEE Trans. Antennas Propag.*, vol. 32, no. 9, pp. 938-943, Sep. 1984.

[13] S. Maci and G. B. Gentili, "Dual-frequency patch antennas," *IEEE Antennas and Propagation Magazine*, vol. 39, no. 6, pp. 13-20, Dec. 1997.

[14] J.-H. Lu, "Single-feed dual-frequency rectangular microstrip antenna with pair of step-slots," *Electronics Letters*, vol. 35, no. 5, pp. 354-355, Mar. 1999.

[15] H. Nakano, K. Vichien "Dual-frequency patch antenna with a rectangular notch," *Electronics Letters*, vol. 25, no. 16, pp.1067-1068, 1989.

[16] J.-H. Lu, "Broadband dual-Frequency operation of circular patch antennas and arrays with a pair of L-shaped slots," *IEEE Trans. Antennas Propag.*, vol. 51, no. 5, pp. 1018-1023, May 2003.

[17] K. Oh, B. Kim and J. Choi, "Design of dual and wideband aperture stacked patch antenna with double-sided notches," *Electronics Letters*, vol. 40, no. 11, pp.643-645, 2004.

[18] P. Li, K. M. Luk, and K. L. Lau, "A dual-feed dual-band L-probe patch antenna," *IEEE Trans. Antennas Propag.*, vol. 53, no. 7, pp. 2321-2323, July 2005.

[19] X. Qu, S.S. Zhong, Y.M. Zhang, and W. Wang, "Design of an S/X dual-band dual-polarised microstrip antenna array for SAR applications," *IET Microw. Antennas Propag.*, vol. 1, no. 2, pp. 513-517, April 2007.

[20] D. C. Thompson, O. Tantot, H. Jallageas, G. E. Ponchak, M. M. Tentzeris, and J. Papapolymerou, "Characterization of Liquid Crystal Polymer (LCP) Material and Transmission Lines on LCP Substrates from 30 to 110 GHz," *IEEE Trans. Microwave Theory Tech.*, vol. 52, no. 4, pp. 1343-1352, April 2004.

[21] L. Yang, A. Rida, R. Vyas, and M. M. Tentzeris, "RFID Tag and RF Structures on a Paper Substrate Using Inkjet-Printing Technology," *IEEE Trans. Microwave Theory Tech.*, vol. 55, no. 12, pp. 2894-2901, Dec. 2007.

[22] M. Berggren, T. Kugler, T. Remonen, D. Nilsson, M. Chen, and P. Norberg, "Paper electronics and electronic paper," in *Proc. IEEE Polymers and Adhesives in Microelectron. Photon. Conf.*, Oct. 2001, pp. 300–303.

[23] B. Farrell and M. St. Lawrence, "The processing of liquid crystalline polymer printed circuits," in *Proc. IEEE Electronic Components and Technology Conf.*, May 2002, pp. 667–671.

ANALYSIS OF THE EFFICIENCY IMPROVEMENTS OF A DIRECTLY-DRIVEN ANTENNA-BASED AM TRANSMITTER

Olusola O. Olaode[1], William T. Joines[1], and W. Devereux Palmer[2]
[1]Department of Electrical and Computer Engineering,
Duke University, Durham NC 27708
[2]US Army Research Office, Durham NC 27703

Abstract-The operation of a traditional radio transmitter is limited by the frequency range over which the antenna input impedance can be conjugately matched to the power amplifier output impedance. This limitation is particularly strong when an electrically-small antenna is used. US patent number 5,402,133 "Synthesizer Radiating Systems and Methods" by Joseph Merenda suggested that this limitation can be overcome by driving the antenna directly with a digital version of the desired signal, such as that produced by a pulse-width modulator, through a pair of switching transistors, and using the antenna reactance to convert the digital input signal back into an analog radiated signal. The practicality of the Merenda method was demonstrated using an unmodulated carrier at 1 MHz by Palmer *et al.* in a paper presented at the 2008 Antenna Applications Symposium at Allerton. This work builds upon that result by demonstrating that an AM signal can in fact be encoded and transmitted with an electrically-small antenna by using this method, and by comparing the radiated power available from the directly-driven antenna (DDA) system to that of a traditional linear, conjugately matched transmitter.

1. Introduction

Modern wireless systems increasingly require more compact, portable, wide-band, and efficient transmitter architectures. In conditions where depletable power supply sources are used to power mobile devices, it is especially important that they are efficient. The research described in this paper is oriented towards the investigation of alternative transmitter architectures for US Army ground mobile wireless communications. Therefore, it is our expectation that the integration of this technology into actual Army radios, prove to be more efficient than the existing radios. Since 80% of the Army's

ground mobile wireless communication is conducted in the HF to VHF bands, the focus of this work, which is to improve the efficiency of the transmitter architecture, will center on the AM band where commercial components are readily available. A block diagram of a simple amplitude modulation (AM) transmitter is shown in the upper half of Figure 1.

The most notable in terms of efficiency and cost are the power amplifier and matching stages. Conventional AM transmitters have often employed class A, B, or AB linear amplifiers in the output stage, all of which are known to draw significant bias current to or from the load; thus, producing considerable power loss in the output power amplifier. In order to mitigate these losses, designers of wireless transmission systems have explored the use of higher-efficiency class-D amplifiers to replace the PA component in the traditional architecture shown in the upper half of Figure 1.

In comparison to class A (efficiency: 25% [1]) or class B (efficiency: 78.5% [1]), class D amplifiers can theoretically provide an efficiency of unity. Due to the non-linearity of the class-D amplifier, it is expected to yield a higher Total Harmonic Distortion (THD) compared with their linear counterparts. However, when designed carefully, an output filter improves the THD to <1% [1]. Therefore, the class D amplifier provides the optimum compromise between THD and efficiency.
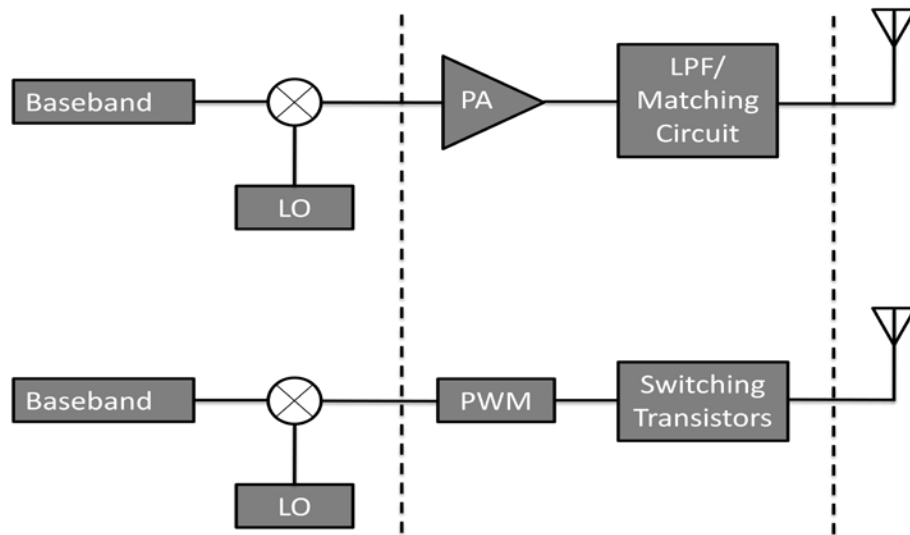

Figure 1. Block diagram showing the architectures of the (upper) conventional and (lower) digitally-driven antenna (DDA) AM transmitters. Glossary of terms - LO: Local Oscillator, PA: Power Amplifier, PWM: Pulse-Width Modulator, LPF: Low-Pass Filter.

Another approach taken by some researchers in improving the efficiency of a wireless transmitter circuit is to use a filter-less class D amplifier. Muggler et al. were able to obtain 86% power efficiency with their filter-free design [3]. However, in that application, the full-bridge configuration of the class D amplifier was used to differentially power the output speaker. This approach required pulse-width generation for each half-circuit of the H-bridge class D amplifier and pre-amplifier stage.

A dramatically different approach was proposed by Joseph T. Merenda (formerly of Hazeltine Corporation). Merenda (Patent # 5,402,133) proposed a system in which a radio signal can be digitized through a pulse width modulator and used to control the switching rate of a pair of complimentary transistors in a class D amplifier configuration. The signal is subsequently radiated by electrically small antenna systems (antennas whose physical sizes are small relative to excitation wavelength [2]). This approach was proven to result in improved bandwidth and efficiency in getting signals to the antenna and forms the basis of the work described in this report.

The lower block diagram in Figure 1 shows the architecture of the DDA system. Modulation of an information signal is performed in an identical manner in both the DDA and the conventional systems except that the power amplifier and low-pass filter/matching network stages in the conventional architecture are replaced with a pulse-width modulator and complimentary switching transistors in the DDA architecture. Details on the contributions of the PWM/switching transistor networks combinations are to be presented later in the paper.

2. Digitally Driven Antenna Circuit Design and Architecture

2.1   Pulse Width Modulator

The Pulse Width Modulation (PWM) in the DDA architecture is performed by a comparator amplifier as shown in Figure 2. An audio signal that has been modulated with a high-frequency local oscillator (Modulated Carrier, V_{MC}) is driven into the positive terminal of the comparator and sampled through a much-higher frequency sawtooth waveform (Reference, V_{REF}). The output of the comparator is low when the magnitude of the reference exceeds the baseband and high otherwise; hence resulting in the pulse-width modulation. For a given input level, the sawtooth frequency determines the frequency of the comparator's output [1] while the baseband frequency determines its duty cycle. Therefore, for an accurate signal reconstruction, the frequency of the reference waveform should be at least ten times that of the baseband [1].
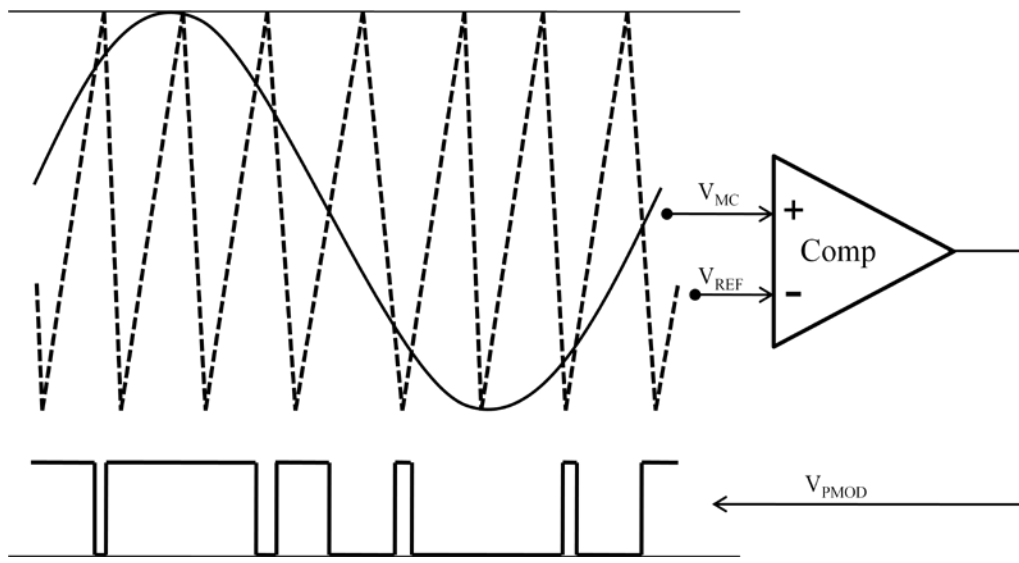
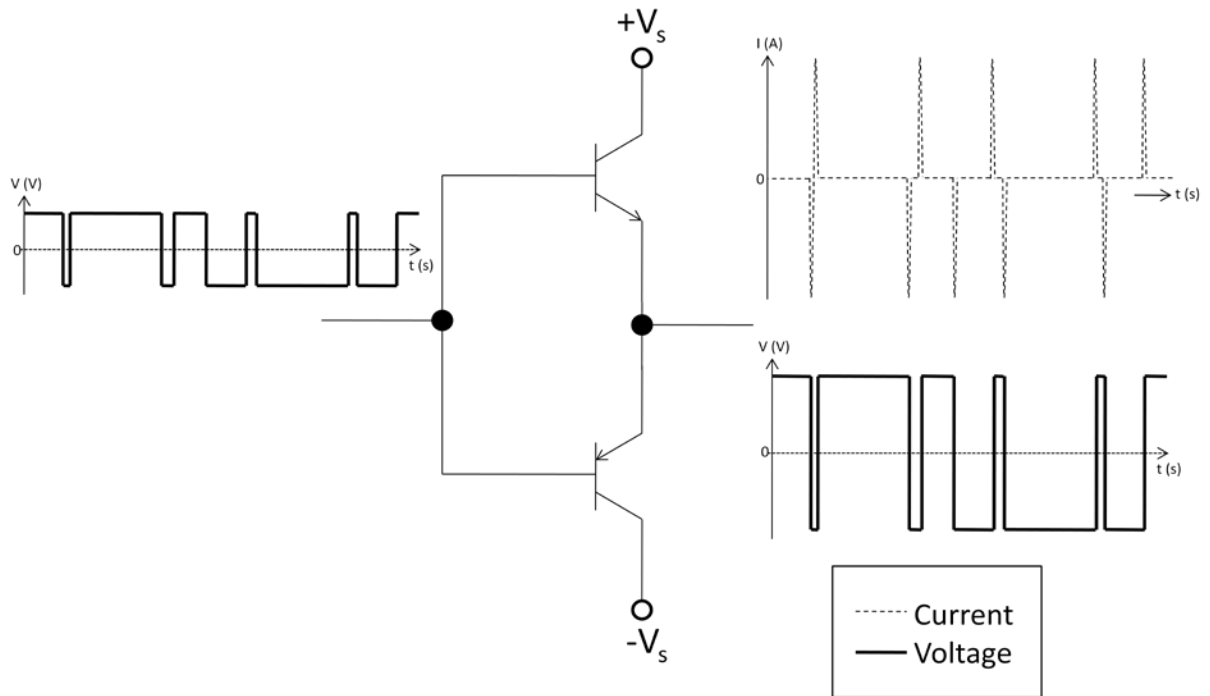Figure 2. Pulse Width Modulation stage. *Glossary of terms* - Comp: Comparator

Figure 3. Class D amplifier switching amplifier stage.

2.2   Switching Transistor Network

The digitized version of the modulated carrier signal from the PWM stage discussed in the previous section is driven directly into a class D amplifier shown in Figure 3. The class D amplifier used in this study comprises of a pair of complimentary bipolar junction transistors driven either in cutoff or saturation. Therefore, the output is a copy of the input pulse train but at a higher current level, oscillating between the amplifier's rail voltages ($+V_S$ and $-V_S$). Furthermore, current spikes are generated only during the transition times of the voltage signal. The information contained in the modulated carrier signal and encoded in the separation of the current spikes is converted to analog by the antenna reactance, radiated and recovered at the receiver end. Because current flows to the antenna only in very short bursts, the power efficiency of the transmitter output stage may be increased.

2.3   Transmit and Receive Antenna Selection

This section covers both the dipole antenna used as a transmitter and a ferrite rod loop antenna used as a receiver. Geometrically small and portable radios require electrically small antennas. A half-wavelength dipole antenna at resonance was used for this study (see Figure 5). The electrical length was $\lambda/3300$ at 1MHz carrier frequency. Such dipole antennas can be represented by resonant RLC circuits [4], [5], [6], [7]. For example, [7] suggested that a dipole antenna can be represented with a four-element equivalent circuit in Figure 4. Calculation of the equivalent impedance seen looking in Figure 4 suggests a much higher capacitive component and a very small radiation resistance, which is expected in electrically small antennas.
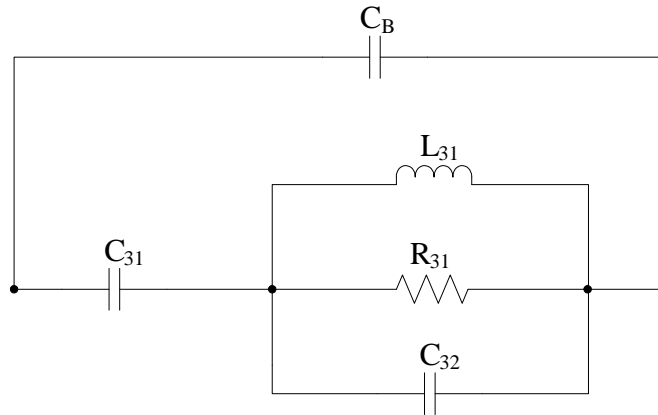
Figure 4. R-L-C representation of a Dipole Antenna. Adapted from [7].

Based on the equations provided in [7] and reproduced here for convenience, theoretical values of C31, L31, R31, C32 were calculated and are shown below.

$$C_{31} = \left\{ \frac{12.0674\,h}{log\left(\frac{2h}{c}\right)-0.7245} \right\} pF \tag{1a}$$

$$C_{32} = 2h \left\{ \frac{0.89075}{[log\,(2h/c)]^{0.8006}-0.861} - 0.02541 \right\} pF \tag{1b}$$

$$L_{31} = 0.2h\{[1.4813\,log(2h/c)]^{1.012} - 0.6188\}\,\mu H \tag{1c}$$

$$R_{31} = \{0.41288[log(2h/c)]^2 + 7.40754(2h/c)^{-0.02389} - 7.27408\,\}\,k\Omega \tag{1d}$$

$$C_{31} = 0.5468\,pF \tag{2a}$$

$$C_{32} = 0.115\,pF \tag{2b}$$

$$L_{31} = 0.0179\,\mu H \tag{2c}$$

$$R_{31} = 0.6952\,k\Omega \tag{2d}$$

Analysis of the total impedance of the circuit in Figure 4 using the theoretical values of C_{31}, L_{31}, R_{31}, C_{32} obtained in equations (2a)-(2d) suggests C_{31} as dominant. Hence, L_{31}, R_{31}, C_{32} can be ignored. The capacitance introduced by the balun is estimated as that of two concentric hollow cylinders 8cm in length and with 0.55cm radius and 0.17cm thickness, as calculated in equation (3).

$$C_B = \frac{2\pi\varepsilon_0}{\ln\left(\frac{a}{c}\right)} \cdot b = \frac{2\pi\cdot 8.854\cdot 10^{-12}}{\ln\left(\frac{0.0055}{0.0017}\right)} \cdot 0.08 = 3.8pF \tag{3}$$

For the receive antenna, we used a 470μH antenna. Therefore, a combination of both transmit (0.5468pF capacitor) and receive (470μH inductor) antennas constitutes a filter; albeit the first few harmonics are still permitted and a dedicated filter may be necessary based on the application environment.
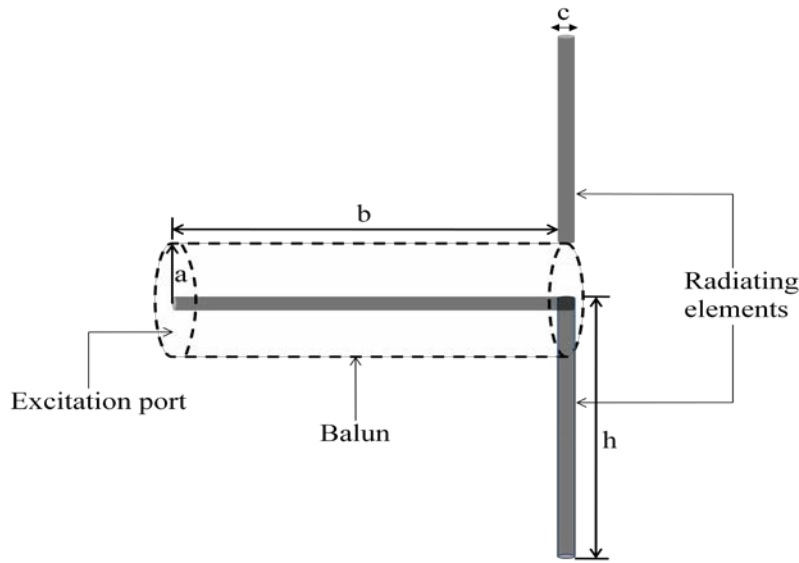
Figure 5. 3-D sketch of the Dipole Antenna used for this study. h = 4.55cm, c = 0.17cm, a = 0.55cm, b = 8cm. Radiating elements and balun are made of copper. SMA connector at the excitation port facilitates interfacing to circuit.

3.   Measurement Setup

As indicated earlier, the goal of the work described in this report is to investigate potential efficiency improvement of the DDA over conventional transmitter architectures. Therefore, it is important that both architectures are kept identical except in the output stage, and that measurements are made under the same conditions. Figures 6 and 7 depict the two architectures. In both cases, an audio signal with bandwidth approximately 20 kHz is coupled from a music player in to an AM transmitter kit, manufactured by Ramsey Electronics, LLC. The transmitter circuit is optimized to produce an amplitude-modulated carrier sine wave at a frequency of approximately 1MHz. A copy of the schematic has been provided in Figure 9 for reference purposes.

In the conventional AM transmitter circuit (upper half of Figure 8), the carrier-modulated sine wave is amplified with a low-power audio amplifier (LM386) commonly employed in commercially-available AM radios and transmitted to a low pass filter prior to propagation by the transmit dipole antenna. The low pass filter facilitates a further suppression of spurious content in the received frequency spectrum. A highly-inductive receive antenna (470μF) commonly in use in commercial AM radios was placed at a
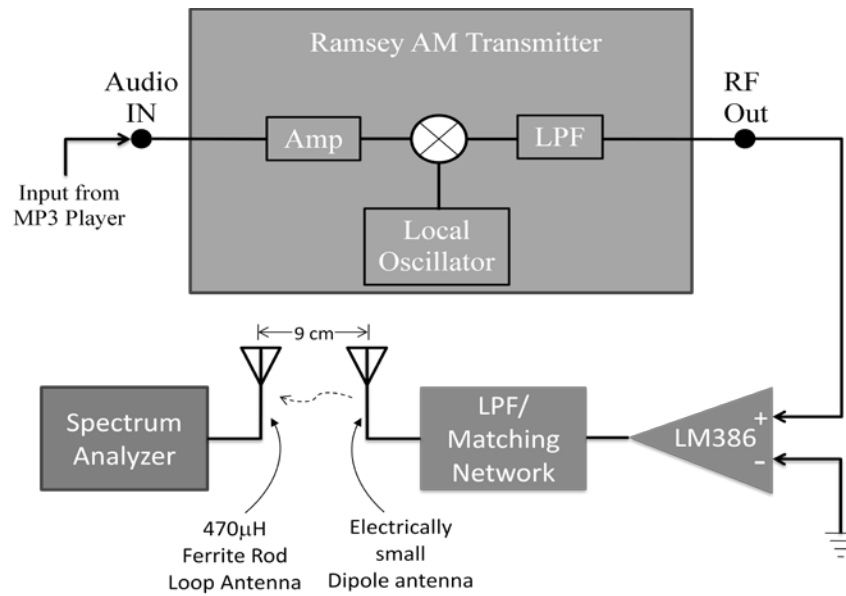
Figure 6. Measurement setup of the Conventional AM transmitter architecture. *Glossary of terms* – LPF: Low Pass Filter, Amp: Amplifier. Ramsey AM Transmitter refers to the AM1C AM transmitter kit produced by Ramsey Electronics.
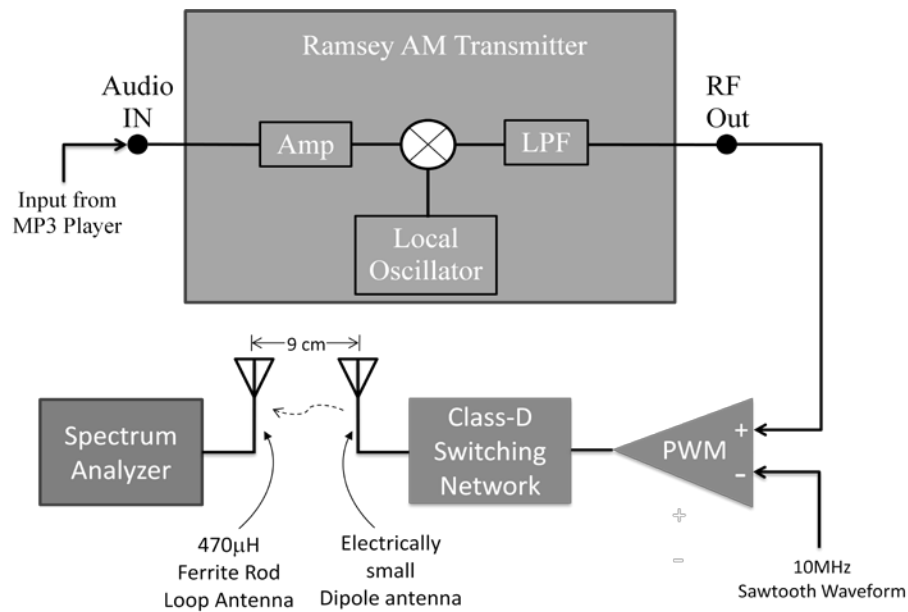
Figure 7. Measurement setup of the DDA AM transmitter architecture. *Glossary of terms* – LPF: Low Pass Filter, Amp: Amplifier. Ramsey AM Transmitter refers to the AM1C AM transmitter kit produced by Ramsey Electronics.
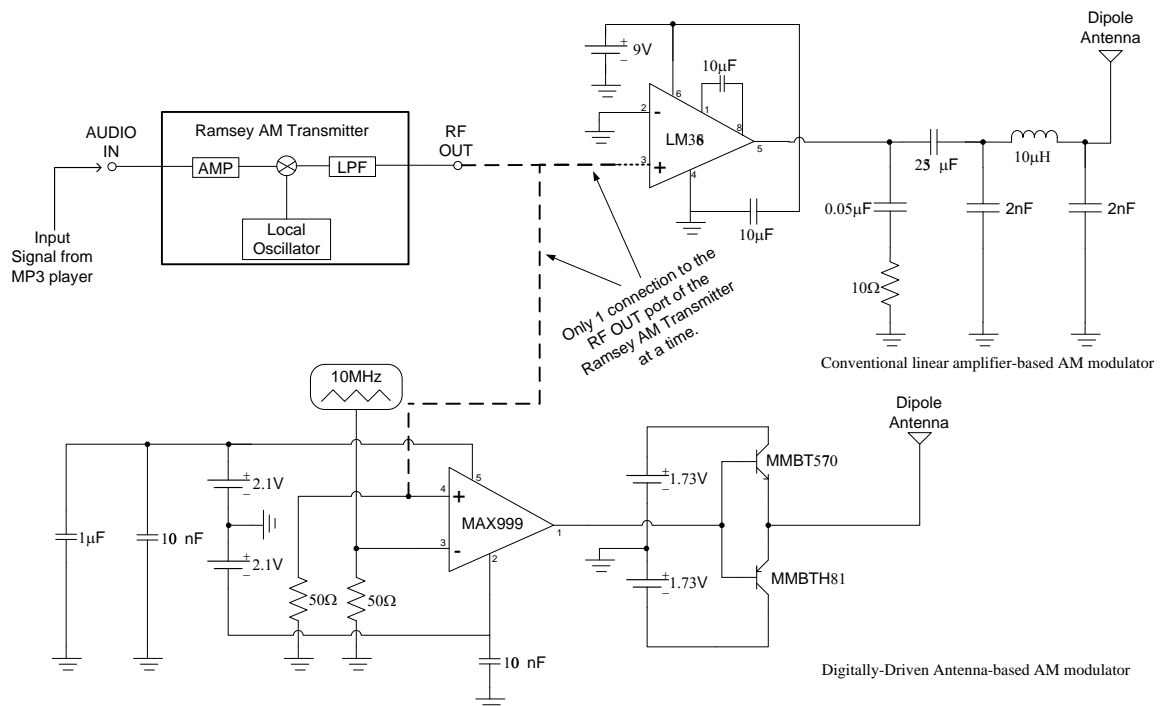
Figure 8. Schematic-level representation of Figures 6 and 7. Ramsey AM Transmitter refers to the AM1C AM transmitter kit produced by Ramsey Electronics.
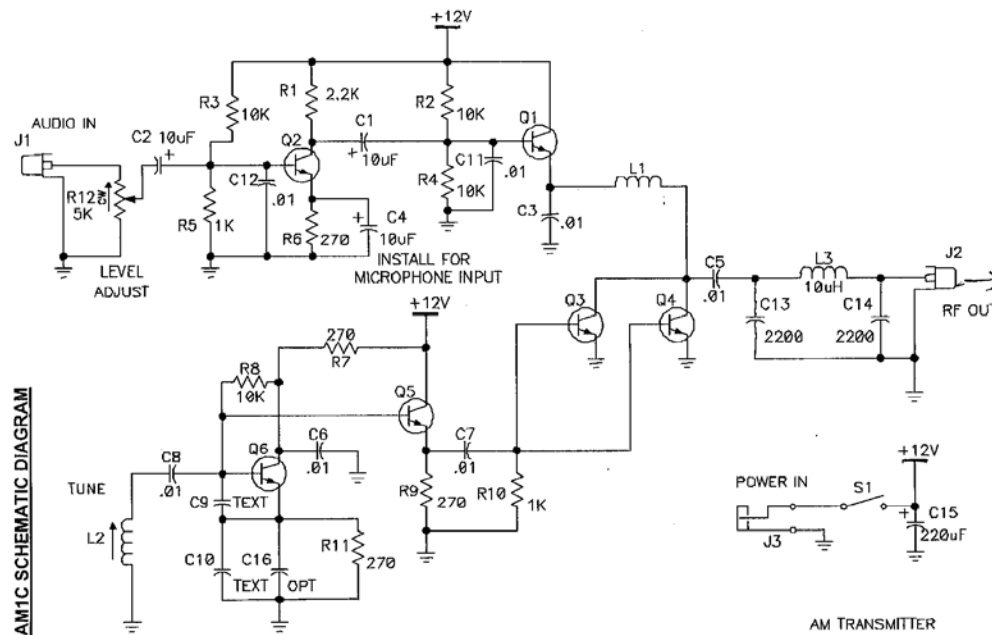
Figure 9. Schematic of the Ramsey AM Transmitter. *Courtesy: Ramsey Electronics, LLC*.

distance of 9cm for both transmit architectures. The measurement results are discussed in the following section.

4.   Results

To qualitatively compare the performance of the two AM transmitter architectures, the modulated 1MHz carrier signal was set to a given power level and the signal received on the portable tabletop AM radio receiver was tuned to the carrier frequency. The AM radio was gradually moved away from the dipole (transmit) antenna along the plane of the peak broadside radiation pattern. It is noteworthy to mention that both transmitters reproduced the signal from the music player in a clear, recognizable way although the DDA-based transmitter yielded a much higher-fidelity reproduction of the original signal despite the fact that the DDA architecture does not include an explicit filtering mechanism on the output. In addition, the broadcast signal still could be heard a few feet beyond where the signal produced by the conventional transmitter architecture became unintelligible. Given that the testing conditions for the two architectures were otherwise identical, the observation described above signifies that more of the modulated carrier signal power is radiated in the DDA case than in the conventional circuit case. Therefore, these qualitative observations strongly suggest that the DDA transmitter produces a more efficient coupling of the signal to the electrically-small transmit antenna.

To quantify the relative performance, the radiated frequency spectrum was measured at the receive antenna end placed at a distance of 9 cm using each architecture. The distance of 9 cm while arbitrary, is well in the far field region of the transmit antenna as estimated by Equation 4 [10] and also minimizes interference from the test equipment and active transmission lines. The power magnitude at the carrier frequency of 1 MHz was measured and compared in both cases. Figure 9 indicates a power magnitude of -81.2 dBm or 7.6 pW in the conventional AM transmitter case while Figure 10 indicates a power magnitude of -70.1 dBm or 97.7 pW in the DDA transmitter case. This represents an improvement of 11 dB or 13X with the DDA transmitter in contrast to the non-DDA transmitter, while also maintaining a smaller visual signature (layout).

$$r_{ff} = \frac{2D^2}{\lambda} \hspace{4cm} (4)$$

Where r_{ff} is radial distance from the dipole antenna, D is the largest dimension of the antenna and λ is the smallest wavelength radiated.
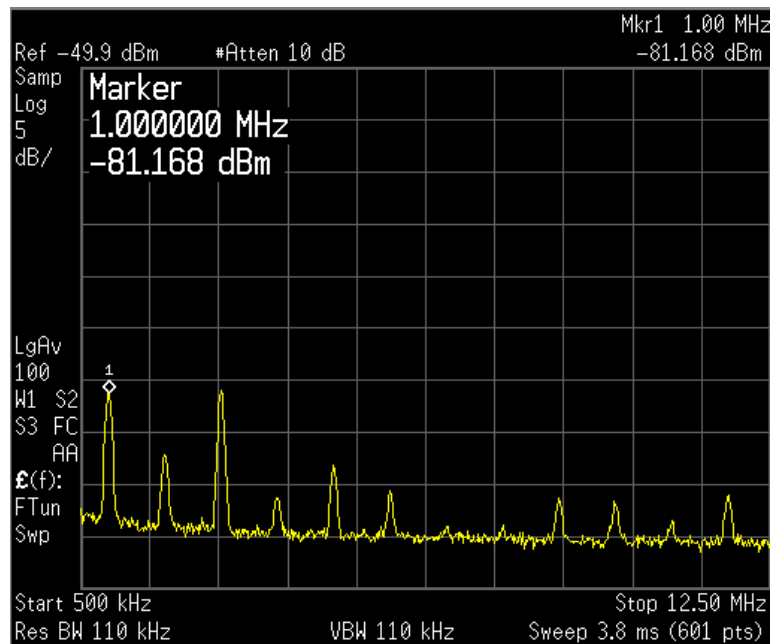
Figure 9. Radiated frequency spectrum observed at 9 cm from the transmit dipole antenna using the conventional AM circuit architecture.
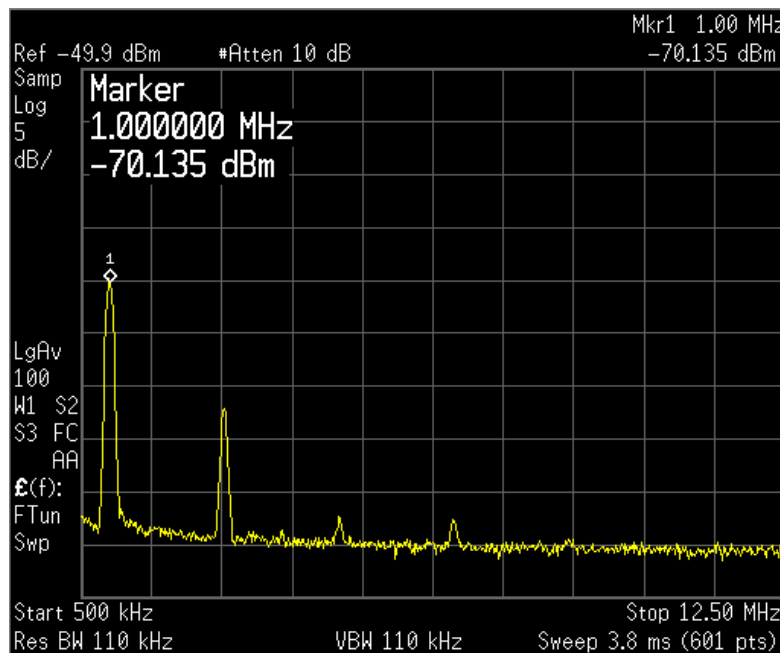
Figure 10. Radiated frequency spectrum observed at 9 cm from the transmit dipole antenna using the DDA architecture.

5. Conclusion and Future Research

The potential for the DDA architecture to break the performance bounds of the traditional transmitter architecture make it an attractive research area for potential use in US Army ground mobile wireless communications. In this work, the ability of the DDA architecture to transmit an AM signal at 1 MHz with higher power than can be produced by the conventional transmitter architecture strongly suggests that the DDA architecture produces more efficient coupling of the modulated carrier to an electrically-small transmit antenna. Many research questions remain, including analysis and control of the spectral content of the radiated signal, comparison of the relative efficiency, size, and cost of the DDA and conventional architectures, PWM clock rate and stability requirements as a function of modulation complexity, and the effect of the transmit antenna design on the filtering properties of the DDA architecture. The DDA architecture also introduces more fundamental questions, potentially requiring new definitions for standard antenna terms such as "match" and "near field" in the DDA context where the assumptions used in analysis of steady state operation no longer apply.

6. Acknowledgement

7. References

[1] *Class D Audio Amplifiers Save Battery Life*, Maxim Integrated Products, Sunnyvale, CA, AN1760, 2002.

[2] J.T. Merenda, "Synthesizer Radiating Systems and Methods," U.S. Patent 5 402 133, March 28, 1995.

[3] P. Muggler, W. Chen, C. Jones, P. Dagli, and N. Yadzi, "A Filter Free Class D Audio Amplifier with 86% Power Efficiency," *IEEE Symposium on Circuits and Systems*, vol. 1, pp. 1036-1039, May 2004.

[4] R. G. Brown, R. A. Sharpe, W. L. Hughes and R. E. Post, Lines, Waves, and Antennas, New York: Wiley, 1973, pp. 339-346.

[5] H. Jasik, Antenna Engineering Handbook, New York: McGraw-Hill, 1961, pp. 2-11.

[6] R. W. P. King, The Theory of Linear Antennas, Cambridge: Harvard University Press, 1956, p. 176.

[7] T. G. Tang, Q. M. Tieng, and M. W. Gunn, "Equivalent circuit of a dipole antenna using frequency-independent lumped elements," IEEE Trans. Antennas and Propagation, vol. 41, no. 1, pp. 100–103, January 1993.

[8] S. B. Wang, A. M. Niknejad, and R. W. Brodersen, "Modeling omnidirectional small antennas for uwb applications," in Conf. Rec. IEEE Antennas and Propagation International Symposium, 2004.

[9] W.D. Palmer, W.T. Joines, and S.D. Keller. "Transmission of a 1 MHz Signal Using a Directly Driven Antenna System," Antenna Applications Symposium at Allerton, Monticello IL, September 16-18, 2008.

[10] W. L. Stutzman, G. A. Thiele, Antenna Theory and Design, New York: John Wiley & Sons, Inc, 1998, p. 413.

Design, Fabrication and Characterization of Electrically Small, Plasmonic Resonator Antennas

Vasundara V. Varadan
Microwave & Optics laboratory for Imaging & Characterization
Department of Electrical Engineering
University of Arkansas, Fayetteville, AR 72701
E-mail: vvvesm@uark.edu

Abstract

Metamaterials are composed of plasmonic resonators such as the ubiquitous split ring resonator (SRR). *Here, we propose to excite the SRR resonator directly by capacitive/inductive coupling to realize efficient, electrically small antennas.* A major advantage is that an impedance matching network is not needed. Exciting applications of interest to the military and commercial sectors can be realized. Due to scalability, we can design plasmonic resonator antennas for applications ranging from GPS frequencies to mm wave frequencies. The very high field localization and absence of fringing fields makes them very attractive for reducing inter-element spacing in array antennas. We will present design and measured results for plasmonic resonator antennas at S-, X- and B-bands on FR4 and Dupont 951 dielectric substrates using PCB and LTCC methods for fabrication. The performance will be compared to microstrip patch antennas operating at the same frequency on the same substrate. Numerical simulations of the EM fields in the vicinity of the plasmonic radiator will demonstrate the high localization of the field. The realized electrical size of the plasmonic antenna radiating element is 0.06 – 0.1 λ. The efficiency ranges from 50-85% with bandwidths ~ 5–10%.

1.0 Introduction

There is increased need for miniaturization of antennas for communication systems mounted on military vehicles. Metamaterials provide a convenient platform for this realization because plasmonic resonances occur at subwavelength sizes of the resonators (SRR) as suggested by Pendry [1]. The size of the SRR is much less than the wavelength at resonance (~0.1λ). The geometric parameters - ring radius, gap and line width determine the resonance frequency. The resonance frequency increases with decreasing size and the scaling applies from RF to optical frequencies. Harold Wheeler is famous for stating in 1947, "But antennas and propagation will always retain their identity, being immune to miniaturization and digitization". Fifty years later, with advances in theory, materials, fabrication methods as well as defence and market driven forces have resulted in a quest for increasingly small antennas that perform as well or better than their bigger counterparts. Currently metamaterials are proposed as substrates for microstrip patch

431

antennas and conventional dipole antennas but the research has achieved size reduction at the expense of gain, Erentok *et al.* [2], Varadan & Kim [3, 4], Alici & Ozbay [5].

Metamaterials have been proposed as substrates for microstrip patch antennas to reduce the electrical size of the antenna. Metamaterials are composed of plasmonic resonators such as the ubiquitous split ring resonator (SRR). *Here, we propose to excite the SRR resonator directly by inductive coupling to realize efficient, electrically small antennas.* Thus the SRR is the radiating element or antenna. Indeed, if a microstrip patch were to be placed at a very small distance above the SRR, the operating frequency would still be very close to the plasmonic resonance frequency of the SRR, the effect of the microstrip patch would be to provide capacitive coupling to the SRR that will lower the operating frequency of the antenna. A major advantage of plasmonic resonator antennas is that they can be excited by inductive coupling and hence do not need impedance matching networks. The direct excitation of the plasmonic resonator is a new concept and leads to many exciting applications of interest in military and commercial applications. Metamaterials scale over the entire range of the non-ionizing electromagnetic spectrum. Hence, it is possible to design plasmonic resonator antennas for applications ranging from GPS frequencies to mm wave frequencies. Another important advantage of the plasmonic resonator antenna is the very high field localization and absence of fringing fields. This makes them very attractive for antenna array applications.

We first give a justification for why we call this a plasmonic resonator antenna as well as reasons why an SRR is an effective radiator at its resonance frequency, then we give examples of design simulation for X- and Ku- bands as well as GPS frequencies using an SRR as the antenna element, we have also explored Hilbert curve modifications of an SRR for further decreasing the radiator size at GPS frequencies.

2.0 Justification for the Terminology Plasmonic Radiator Antenna

The aim of this paper is to demonstrate that metamaterial resonators, that are electrically small (size $\leq 0.1\lambda$) can be excited by capacitive or inductive coupling (parasitic coupling) to serve as the radiating element of an antenna with acceptable radiation efficiency. The antenna radiates at a frequency that is in the equivalent magnetic plasma region as we will show in this section. Further the antenna has good radiation efficiency only at this frequency. Hence we call the directly excited metamaterial structure as a plasmonic resonator antenna. In contrast to previous research involving metamaterials as the substrate for a conventional antenna or the design of metamaterial inspired antennas, here we propose the excitation of a metamaterial structure (for eg. an SRR) at its resonance frequency. Elsewhere (Varadan & Ji [6]), we have shown that an SRR radiates effectively only at its resonance frequency, at other frequencies it is passive. At the resonance frequency, the wavelength is an order of magnitude larger than the size of the SRR. Thus this resonance is very different from the resonance of patch antenna, a dielectric resonator antenna or a half wavelength dipole antenna. The resonance frequency of conventional

antennas corresponds to resonator sizes ~0.25 to 0.5λ. This is the reason why we refer to the SRR antenna as a plasmonic resonator antenna so we can distinguish this type of antenna from λ/2 resonance antennas. The name also has a basis in the seminal paper by Pendry [7] which proposed that a collection of electrically small split rings could be described as a effective medium with magnetic properties that displays highly dispersive behavior and even negative permeability values in a small range of frequencies. The Lorentz model to describe the frequency dependence of the permeability (or permittivity) is given by

$$\frac{\mu(\omega)}{\mu_0} = \mu_s + \frac{F\omega^2}{\omega^2 - \omega_0^2 + i\Gamma\omega} = \mu_s + \frac{F\omega^2\left(\omega^2 - \omega_0^2\right) - i\Gamma F\omega^3}{\left(\omega^2 - \omega_0^2\right)^2 + \Gamma^2\omega^2} \tag{1}$$

where 'μ_s' is the static or frequency independent value of the property away from resonance, 'F' defines the strength of the resonance, 'ω' is the operating frequency. 'Γ' is a damping factor, 'ω_r' is the resonance frequency. Pendry [7] defined a frequency ω_0 below which, the permeability increases with ω and above which it is a decreasing function of ω. In other words, at ω_0, the slope of the μ-ω dispersion curve changes from positive to negative and the value of Re(μ) can also become negative. The frequency range in which Re(μ) is negative may termed as a magnetic plasma region according to Pendry [7] and a frequency ω_{mp} can be defined as the frequency above which Re(μ) becomes positive. In analogy with an electron plasma, this frequency is called the magnetic plasma frequency. Varadan and Tellakula [8] extracted the permittivity and permeability of a periodic arrangement of SRRs with their gaps parallel (SRR1) and perpendicular (SRR3) to the incident electric field by measuring the reflected and transmitted field S-parameters for a slab of finite thickness. The measurements and the extracted material properties show excellent agreement with HFSS full wave simulation. Extraction of material properties is done using the Nicholson-Weir-Ross method. Later Varadan and Ro [9] showed that the permeability and permittivity could be fitted exactly with the Lorentz model proposed by Pendry [7] and the result is given in Fig. 1.
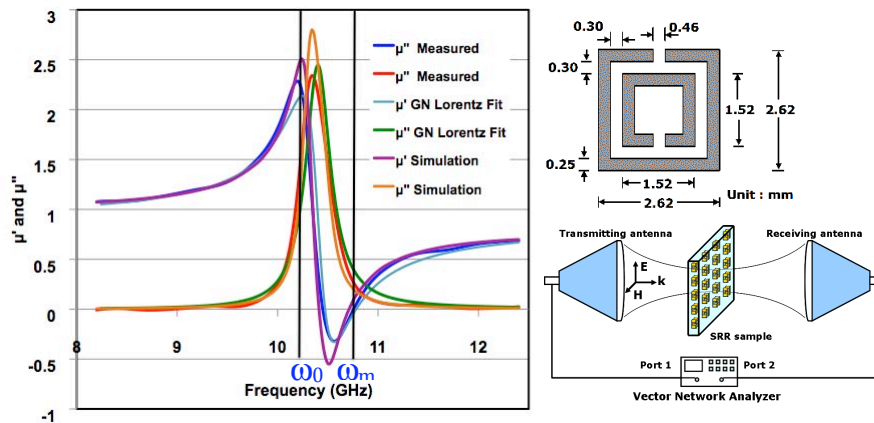
Figure 1: Complex permeability of a periodic distribution of Cu SRR3s printed on an FR4 substrate (ε=4.4-j0.088) in X-band. The graph is a comparison of the extracted permeability from S-parameter measurements using a Free Space system shown on left, the dimensions of the SRR are shown on top right and the unit cell dimension is 5 mm. Permeability extracted from HFSS full wave simulation of the slab of SRRs agrees well with the experimental extraction. Further the Lorentz model of Eq. 1 was fitted to the experimental data using a Gauss-Newton fit yielding F=–076, Γ=0.31 and ω_r=10.4 GHz. From the graph, we note that for SRRs, ω_0=10.2 GHz and ω_{mp}=10.73 GHz. At the resonance frequency μ'=0.

The results in Fig. 1 have also been obtained for the case of SRR1 with its gap parallel to the incident electric field, see [8]. Its resonance frequency is also at 10.4 GHz. Thus this resonance frequency may be attributed to the geometry, dimensions and substrate properties and has nothing to do with the lattice or the polarization of the incident wave.

We next computed the far field in air scattered by a single SRR printed on FR4 at off resonance and resonance frequencies using the HFSS full wave simulator. This calculation is closer to the antenna application and is indicative of how effective the SRR is as a radiator and at what frequency. In Fig. 2 below the scattered far field in air plotted at three different frequencies.

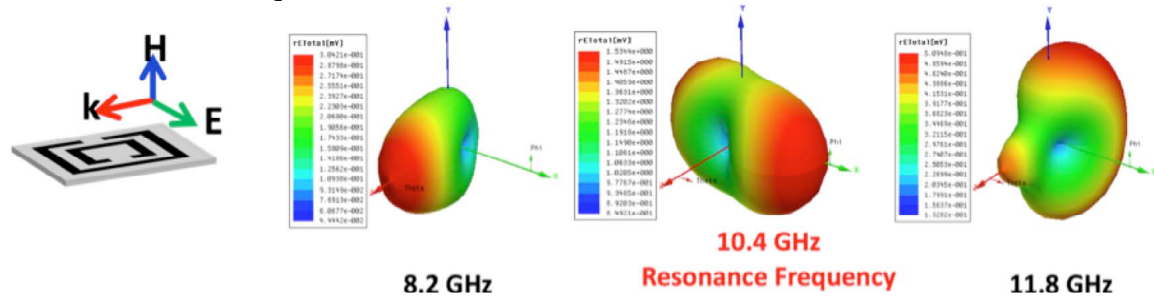Figure 2: Far field scattered by a single SRR in air computed at two non-resonant frequencies and the resonance frequency of the SRR3. The radiated field strength is about one order of magnitude larger at the resonance frequency and displays a perfect dipole pattern that is oriented perpendicular to the gap of the SRR and parallel to the electric field. An identical result (not shown) is obtained for SRR1, the dipole field is again perpendicular to the gap but perpendicular to the incident electric field, Varadan & Ji [6].

We have established that the magnetic plasma frequency region for this SRR geometry is 10.4 GHz to 10.72 GHz and the SRR is effective as an antenna element precisely in this frequency region, hence it is appropriate to call it a plasmonic resonator antenna.

3.0 Simulation of the Performance of a Plasmonic Resonator Antenna

The performance of the SRR as an antenna element when excited by a microstrip feed line is considered next. For convenience in fabrication of the antenna and the probe feed excitation, it is more convenient to consider Dupont 951 as the substrate with ε_r=7.4– j0.026. An SRR is printed on top of the substrate. The upper right figure in Figure 3, shows the simulated geometry. There is a ground plane below the 1 mm thick 951 substrate. A microstrip feed line (not shown) can be designed under a dielectric layer introduced below the ground plane. A probe feed attached to the microstrip line can be inserted via the ground plane into the substrate under one edge of the SRR. Another probe is connected to the ground plane. This results in an electric field excitation of the SRR since the probe functions as two wire Tx line. Using the LTCC method, this design can be fabricated conveniently since it is easy to make via holes for the feed probes. To obtain a resonance in the Ku-band, the size of the SRR was increased (dimensions shown in Fig. 3) for the higher permittivity substrate. Ansoft HFSS was used to simulate the return loss of the SRR antenna, the radiation efficiency and the radiation pattern. The

resonance frequency of this SRR is at 17 GHz where it has a return loss of -18dB and a radiation efficiency of 83% and a gain of 5.2 dBi. The gain is substantially improved due to the presence of the ground plane interferes constructively with the radiated field because the substrate electrical thickness of 1mm is approximately $\lambda/4$ at 17 GHz.
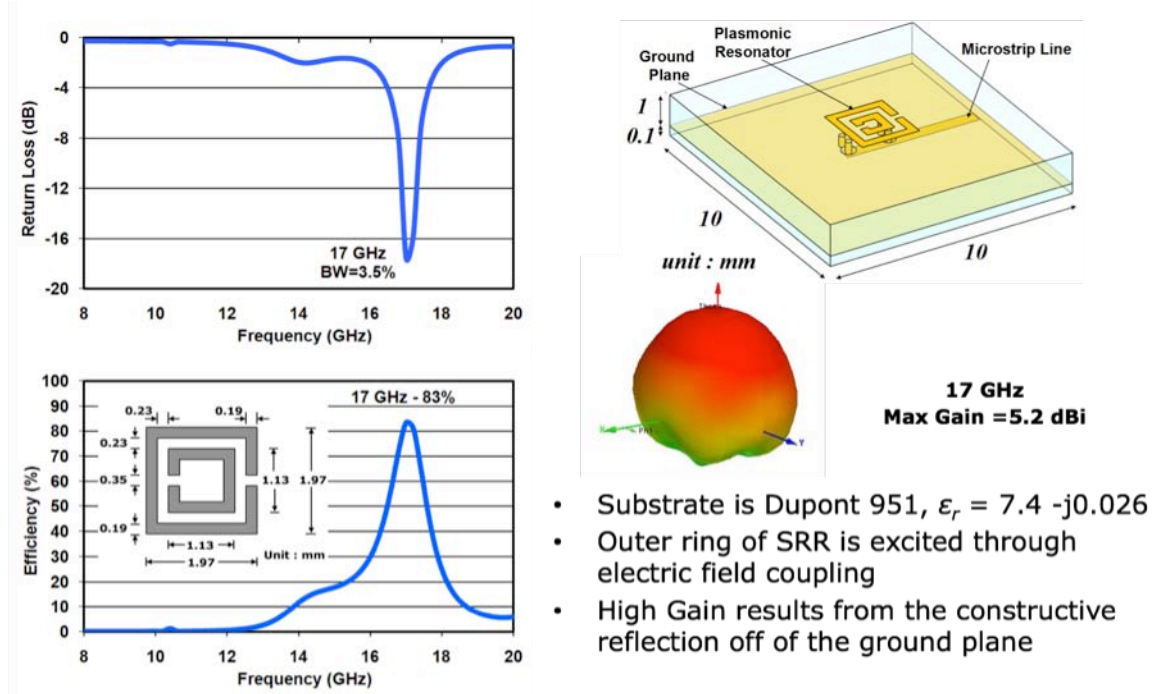
Figure 3: Performance of an SRR plasmonic resonator antenna printed on Dupont 951 with a ground plane and excited by double probe feed as shown. The performance of the antenna is independent of the size of the ground plane. The ground plane dimension was chosen as 10mm for ease of fabrication and measurements. The physical size of the radiator is 1.97 mm and its electrical size at resonance is $0.1\lambda_0$.

4.0 Fractal Plasmonic Resonator Antenna for GPS Applications

Several researchers have considered fractal geometries to decrease the overall size of microstrip patch antennas (Jaggard [10,11], Lakhtakia *et al.* [12,13], Werner *et al.* [14]). Fractals exhibit self similarity and scaling and for GPS antenna applications, Mandelbrot [15]. At GPS frequencies ~ 1.5 GHz, the size of a conventional microstrip patch antenna would be prohibitively large, but as shown by Vinoy *et al.* [16,17], a third order Hilbert curve VHF antenna is only $\lambda/10$ in size. Encouraged by this result as well as the performance of the SRR antenna at higher frequencies, we performed design simulation of a Hilbert curve SRR antenna with an operating frequency of 1.5 GHz. In Figure 4, we show the reduction in size achieved by a Hilbert curve SRR relative to an SRR for a comparable resonance frequency and return loss using full wave simulation. The size reduction is almost 50% and the size of Hilbert curve SRR with a resonance frequency of

1.5 GHz is 12.6 mm or $0.06\lambda_0$. Next we simulate the performance of a Hilbert curve SRR antenna using a very small dipole (3mm) placed in close proximity (0.25 mm) to the SRR. The thickness of the Dupont 951 substrate used was 40mm. Results are compared for the performance of the antenna without a ground plane, with a ground plane and with an ideal perfect magnetic conductor ground plane (perfect reflection with zero phase change). It is well known, that at low frequencies, a conventional PEC ground plane will results in a 180° phase change leading to destructive interference of the reflected signal for very thin substrates such as the one used here.
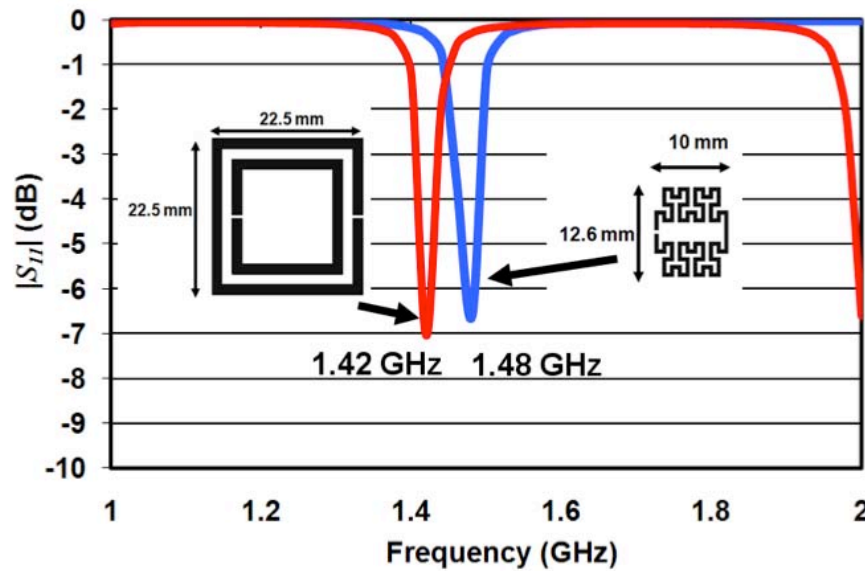
Figure 4: Comparison of the return loss from an SRR relative to a Hilbert curve SRR with a nominal resonance frequency of 1.5 GHz.

Much research is being done in the development of magnetic ground planes following the pioneering research of Sievenpiper *et al.* [18] who demonstrated that such ground planes can be constructed by using EBG structures and that the performance of antennas with thin substrates can be greatly improved relative to conventional PEC ground planes that result in poor radiation efficiency. Research is being pursued on the development of such magnetic ground planes for application to low frequency plasmonic resonator antennas sucha s the one shown in Fig. 5 where we have used a virtual but ideal PMC ground plane.

5.0 Fabrication and Characterization of the Performance of Plasmonic Resonator Antennas

The Low Temperature Co-fired Ceramics (LTCC) technique is a well established multilayer technology that is in use by the packaging industry for RF and MW applications. It is used to produce multilayer hybrid integrated circuits, which can include resistors, inductors, capacitors, and active components in the same package. The LTCC process can be used to great advantage for the fabrication of plasmonic resonator

antennas because probe feeds, electric or magnetic ground planes, power dividers, etc. can be easily integrated into one package. In addition using the multilayer technology it is easy to create different types of superstrates and substrates of the desired thickness as called for by the design. The radiating elements can be on the surface or they can be embedded. Thus the LTCC method is a very versatile, economical and rapid method for the fabrication of plasmonic resonator antennas.
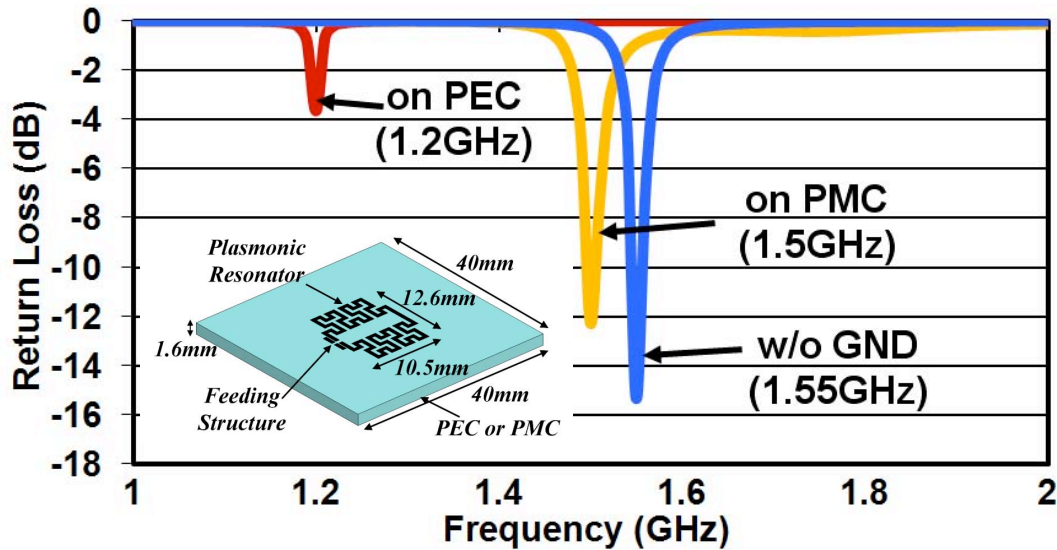
Figure 5: Return loss from a Hilbert curve SRR antenna excited by an adjacent miniature dipole. The return loss is very good when there is no ground plane, but with a PEC ground lane the return loss is only -4dB but with a virtual PMC ground plane, the return loss is –12 dB which is acceptable

The characterization of the performance of such antennas consists in the measurement of the return loss of the antenna as well as the measurement of the radiation pattern. The return loss is easily measured using a vector network analyzer. For the measurement of the antenna pattern, we have developed a new method using horn lens focused Gaussian beam antenna as the probe antenna using a free space system [8]. The advantage of this method is that the antenna pattern of small antennas such as the plasmonic resonator antenna can be mapped without using an anechoic chamber. Our initial results using conventional horn antennas as the test antenna have provided very good results that are in agreement with published data for these antennas. Fabrication and characterization of plasmonic resonator antennas in ongoing research and we expect to present results in the near future.

Acknowledgements

References

[1]   J. B. Pendry, A. J. Holden, W. J. Stewart and I. Youngs, "Extremely Low Frequency Plasmons in Metallic Mesostructures", Physical Review Letters, Volume 76, Number 25, 4773-4776, 17 June 1996

[2]   A. Erentok, R. W. Ziolkowsk*i,* "Metamaterial-Inspired Efficient Electrically Small Antennas", IEEE Trans. Antennas & Propagation, 691, 2008.

[3]   V. V. Varadan and I. K. Kim, "Compact, Multiband, Plasmonic resonator Antenna," IEEE AP International Symposium, 2009, Charleston, SC.

[4]   I. K. Kim and V. V. Varadan, "Effect of capacitive coupling between split-ring resonators," IEEE *Antennas and Propagation International Symposium*, Jul. 2008

[5]   K. B. Alici and E. Ozbay, "Electrically small split ring resonator antennas," *Journal of Applied Physics*, vol. 101, 083104, Apr. 2007.

[6]   V.V. Varadan and L. Ji, " Multipole moments of radiating Split Ring Resonators", Metmaterials'2009, London, UK.

[7]   J.B. Pendry, A. J. Holden, D. J. Robbins and W.J. Stewart, "Magnetism from conductors and enhanced nonlinear phenomena," *IEEE Trans. on Microwave Theory and Tech.*, vol. 47, no. 11, pp.2075-2084, Nov. 1999.

[8]   V. V. Varadan and A. R. Tellakula, "Effective properties of split-ring resonator metamaterials using measured scattering parameters: Effect of gap orientation," *Journal of Applied Physics*, vol. 100, 034910, Aug. 2006.

[9]   V.V. Varadan and R. Ro, "Analyticity, Causality, Energy Conservation and the Sign of the Imaginary Part of the Permittivity and Permeability" IEEE AP International Symposium, 2006.

[10]   D. L. Jaggard, "On Fractal Electrodynamics," in H. N. Kritikos and D. L. Jaggard (eds.), *Recent Advances in Electromagnetic Theory,* New York, Springer-Verlag, 1990, pp. 183-224.

[11]   D. L. Jaggard, "Fractal Electrodynamics and Modeling," in H. L. Bertoni and L. B. Felson (eds.), *Directions in Electromagnetic Wave Modeling,* New York, Plenum Publishing Co., 1991, pp. 435-446.

[12]   Lakhtakia, V. K. Varadan and V. V. Varadan, "Timeharmonic and Time-dependent Radiation by Bifractal Dipole Arrays*,"Int. J. Electronics,* 63,6, 1987, pp. 819-824.

[13]   A. Lakhtakia, N. S. Holter, and V. K. Varadan, "Self-similarity in Diffraction by a Self-similar Fractal Screen," *IEEE Transactions on Antennas and Propagation,* AP-35, 2, February 1987, pp. 236- 239.

[14]   D. H. Werner, R. L. Haup, and P. L. Werner, "Fractal Antenna Engineering: The Theory and Design of Fractal Antenna Arrays", J, IEEE Antennas and Propagation Magazine, Vol. 41, No. 5, October I999, 37-59.

[15]   B. B. Mandelbrot, *The Fractal Geometry of Nature,* New York, W. H. Freeman, 1983.

[16]   Vinoy, K.J.; Abraham, J.K.; Varadan, V.K.; "On the relationship between fractal dimension and the performance of multi-resonant dipole antennas using Koch curves", IEEE Tans. Antennas and Propagation, Volume 51, Issue 9, Sep 2003 Page(s):2296 - 2303

[17]   K. J. Vinoy, K. A. Jose, V. K. Varadan, and V. V. Varadan, "Hilbert curve fractal antenna: a small resonant antenna for VHF / UHF applications", Microwave and Optical Technology Letters / Vol. 29, No. 4, May 20 2001, 215-219.

[18]   Sievenpiper, D., L. Zhang, R. F. J. Broas, N.G. Alexopolous and E. Yablonovitch, " High-Impedance Electromagnetic Surfaces with Forbidden Frequency Band", Trans. IEEE MTT, Vol. 47, 2059, 1999.

Optimization of the Bandwidth of Electrically Small Planar Antennas

Steven R. Best

MITRE
M/S E087
202 Burlington Road
Bedford, MA 01730

sbest@mitre.org
(781) 271-8879

Abstract: The bandwidth limitations of resonant, electrically small antennas that fully occupy a spherical volume are well defined by the inverse of the Chu-limit or the lower bound on quality factor. Recently, Gustafsson et al developed lower bounds for the *Q* of antennas of arbitrary shape. We have previously described antenna designs fully occupying a spherical volume and a cylindrical volume that exhibit *Q's* close to the Chu-limit and close to the Gustafsson limit, respectively.

In many applications, there is a requirement for electrically small planar antennas. It is understood that the *Q* of an electrically small planar antenna cannot approach the *Q* of a spherical or cylindrical antenna, where all have the same value of *ka* and fully occupy their respective total available volumes. Comparing the *Q's* of planar antennas to the lower bound for spherical or cylindrical antennas does not provide sufficient insight into how well the antenna performs relative to the theoretical performance that can be achieved in the planar shape. Recently, Gustafsson et al presented the limit on achievable *Q* for planar antennas as a function of their length-to-diameter ratio. In this paper, we present several designs for electrically small, thin planar antennas and compare their *Q's* to the Gustafsson limit.

Introduction

When designing electrically small antennas there are a number of **performance properties to consider. These include the antenna's impedance,** which provides information on the match to the transmitter and/or receiver **as well as the antenna's operating bandwidth; the antenna's radiation efficiency; and the antenna's radiation patterns.**

Most electrically small antennas exhibit radiation patterns consistent with those of a fundamental, single mode dipole or monopole. In some

instances, where the radiating structure is arbitrarily shaped or includes an arbitrarily shaped ground plane, the radiation pattern may deviate from that of a fundamental dipole or monopole. In many wireless applications, where the link is principally established through multipath, the antenna's radiation pattern may be a secondary concern.

The small antenna's radiation efficiency can often be made reasonably high with suitable design approaches and suitable choice of materials. However, there are instances where a low radiation efficiency may be necessary or desirable in order to increase the operating bandwidth of the antenna to meet system requirements and/or make it less sensitive to frequency shifts that may occur due to changes in the operating environment.

Impedance matching the electrically small antenna at a single frequency is often straight-forward through changes in the antenna design or easy using external lumped matching components. When comparing the performance properties of different electrically small antenna, presumably where they have the same size and occupy the same volume, the critical performance property to consider is bandwidth or Q. These are generally the limiting performance properties in the design of an electrically small antenna of a given size.

In this paper, we focus on the design of several planar antennas with the purpose of comparing their $Q's$ to the lower bound defined by Gustafsson et al. We verify that, as predicted by Gustafsson, there is an optimum value of length-to-diameter ratio for achieving the lowest Q or the widest possible bandwidth. We assume here that all of the antennas exhibit a single resonance within their impedance bandwidth and exhibit fundamental mode radiation patterns.

Background

The material that appears in this section has been previously published in the open literature[1] and is included here for completeness.

The lower bound on Q [1]-[2], Q_{lb}, often referred to as the Chu-limit, establishes the theoretical minimum value of Q that can be achieved as a function of the antenna's occupied spherical volume, which is defined by the

---

[1] The text contained in this section has been extracted and edited from the following: S. R. Best, "A Comparison of the Cylindrical Folded Helix Q to the Gustafsson Limit," *EuCap 2009*, Berlin, Germany, March 2009.

value of **ka**, where **k** is the free space wavenumber $2\pi/\lambda$, and **a** is the radius of an imaginary sphere circumscribing the maximum dimension of the antenna. The lower bound on **Q** for the general, single mode (fundamental TE or TM mode), lossy antenna is given by

$$Q_{lb} = \eta_r \left(\frac{1}{(ka)^3} + \frac{1}{ka} \right) \tag{1}$$

where η_r **is the antenna's radiation efficiency.**

To achieve a **Q** that most closely approaches the lower bound of Equation 1, the small antenna must utilize the full spherical volume defined by the value of **ka**. The lowest possible **Q** is achieved when the antenna conductor(s) are confined to the outermost regions of the spherical volume [3]–[5].

In most practical applications, the constraint on the occupied volume of a small antenna is not defined by a spherical shape. Typically, the small antenna must fit within a volume of arbitrary shape or in many cases, a cylindrical or planar shape. In these instances, the antenna **Q** will not approach the lower bound as closely as does the **Q** of the spherical shaped antenna. Without an appropriate adjustment in the lower bound of Equation 1 for differences in antenna shape, the engineer has no measure of how well the arbitrary shaped antenna performances relative to theoretical limits.

Recently, Gustafsson et al derived a lower bound on **Q** for arbitrary shaped antennas [6], thus providing the engineer with the capability of determining how well the general small antenna performs relative to theoretical limits. Gustafsson also defined specific lower bounds for antennas having a cylindrical shape [6] - [7], and recently, antennas having a planar shape.

The exact **Q** of an electrically small, tuned or self-resonant antenna is given by [1], [8]

$$Q(\omega_0) = \frac{\omega_0 |W|}{P} \tag{2}$$

where **W** is internal energy and **P** is the total power accepted by the antenna, which includes both power dissipated in the form of radiation and heat within the antenna structure. ω_0 is the radian frequency ($2\pi f_0$) where the antenna is naturally self-resonant, tuned, or made to be self-resonant. If the tuned small antenna exhibits a single impedance resonance within its

defined **VSWR** bandwidth, its **Q** can be accurately approximated at any frequency, ω, from its impedance properties using [8]

$$Q(\omega) \approx \frac{\omega}{2R(\omega)} \sqrt{R'(\omega)^2 + \left(X'(\omega) + \frac{|X(\omega)|}{\omega} \right)^2} \qquad (3)$$

where $R'(\omega)$ and $X'(\omega)$ are the frequency derivatives of the antenna's feed point resistance and reactance, respectively.

In recent years there has been substantial interest in developing electrically small antennas that are impedance matched, exhibit low **Q** and have high radiation efficiency. One antenna that was designed with the objective of achieving these characteristics is the folded spherical helix [3] – [4] depicted in Figure 1.
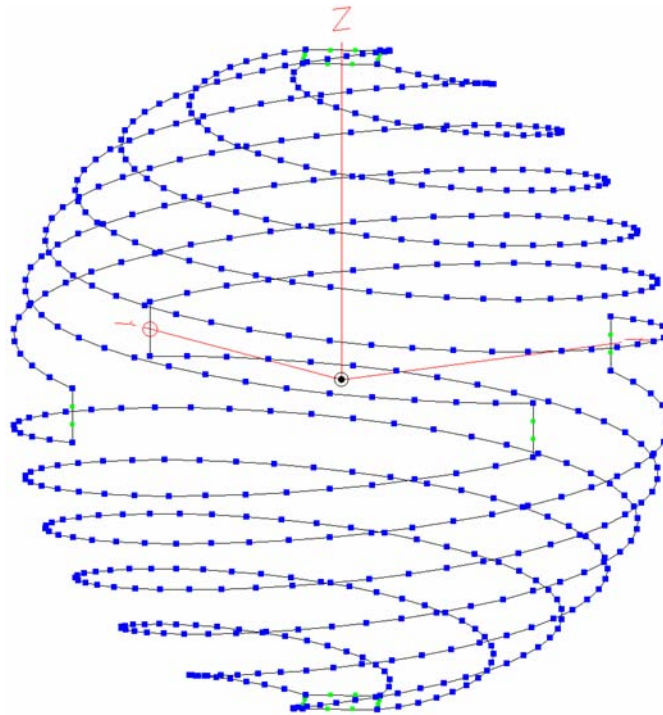

Fig. 1 The 4-arm spherical folded helix antenna.

The advantage of the folded spherical helix design is that it utilizes the entire spherical volume where all of the conductors are wound on the outside of

the imaginary spherical shape. Multiple folded arms are used to both impedance match the antenna and reduce its *Q*. In this case, four folded arms are used to match the antenna to a 50Ω characteristic impedance. There is a single feed point in the antenna at the center of one of the short vertical sections of conductor.

At a value of *ka* = 0.265, the folded spherical helix is self-resonant with a total resistance (including both radiation and loss terms) of 47.6Ω, a radiation efficiency of 97.1% and a *Q* of 84.64, approximately 1.52 times the lower bound of 55.61. For *ka* < 0.5, this value of *Q* is consistent with the practical, minimum achievable *Q* predicted by Thal for spherical wire antennas [5].

The spherical folded helix discussed above utilizes the full spherical volume defined by a specific value of *ka*. In doing so, the design is able to be adjusted to achieve a *Q* that closely approaches the lower bound. Similarly, for the cylindrical shape, a cylindrical folded helix was designed using the same principles with the exception that the conductors are wound on the outside surface of an imaginary cylinder. The dimensions of the antenna (its overall length, overall diameter and conductor length) are set so as to maintain self-resonance at the same value of *ka* (0.265) as that of the folded spherical helix.

In a design approach similar to that used with the folded spherical helix, self-resonance is achieved by adjusting the arm length in each of the folded arms. Adjustment of the arm length changes the total self-inductance of the structure, tuning out the inherent self-capacitance associated with the small dipole-like design. Once self-resonance is achieved, the resonant resistance is increased by adding folded arms to the structure. Since the cylindrical folded helix does not occupy the same overall volume as the spherical folded helix having the same value of *ka*, it will not exhibit as low a *Q*. The basic configuration of a 4-arm cylindrical folded helix is depicted in Figure 2.

In encompassing the cylindrical folded helix within the same spherical volume (*ka*) as the folded spherical helix, there are a vast number of length-to-diameter ratios that can be chosen. As expected and quantified by Gustafsson et al, the minimum achievable *Q* for the antenna will vary as a function of its length-to-diameter ratio. Additionally, with this type of antenna design, the resonant resistance is a function of $(\ell/\lambda)^2$, where ℓ is the overall length of the cylinder. As a result, the resonant radiation resistance and antenna *VSWR* will also change as a function of length-to-diameter ratio for a fixed number of turns.
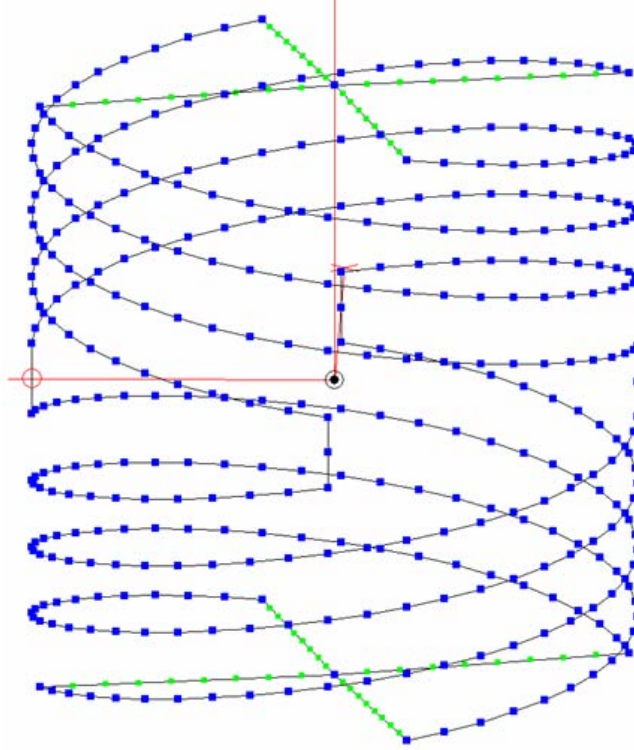
Fig. 2 The 4-arm cylindrical folded helix antenna.

A number of 4-arm folded helices with different length to diameter ratios were studied. The ratio of the antenna *Q* to the lower bound (the Chu limit) of Equation 1 was calculated and compared against the Gustafsson limit for cylindrical shaped antennas [7]. This comparison is presented in Figure 3. Note that in calculating the Gustafsson limit presented in Figure 3, it was assumed that the antennas have a *ka* much less than 1, are purely vertically polarized and that the maximum achievable directivity is 1.5. In all cases, the *Q* of the antenna is above or at the Gustafsson limit.

The objective of the present work is to perform a similar study for planar antennas as a function of their length-to-diameter ratio. We compare a number of different planar antennas, consider simple techniques to impedance match them and then compare their *Q's* to the Gustafsson limit.
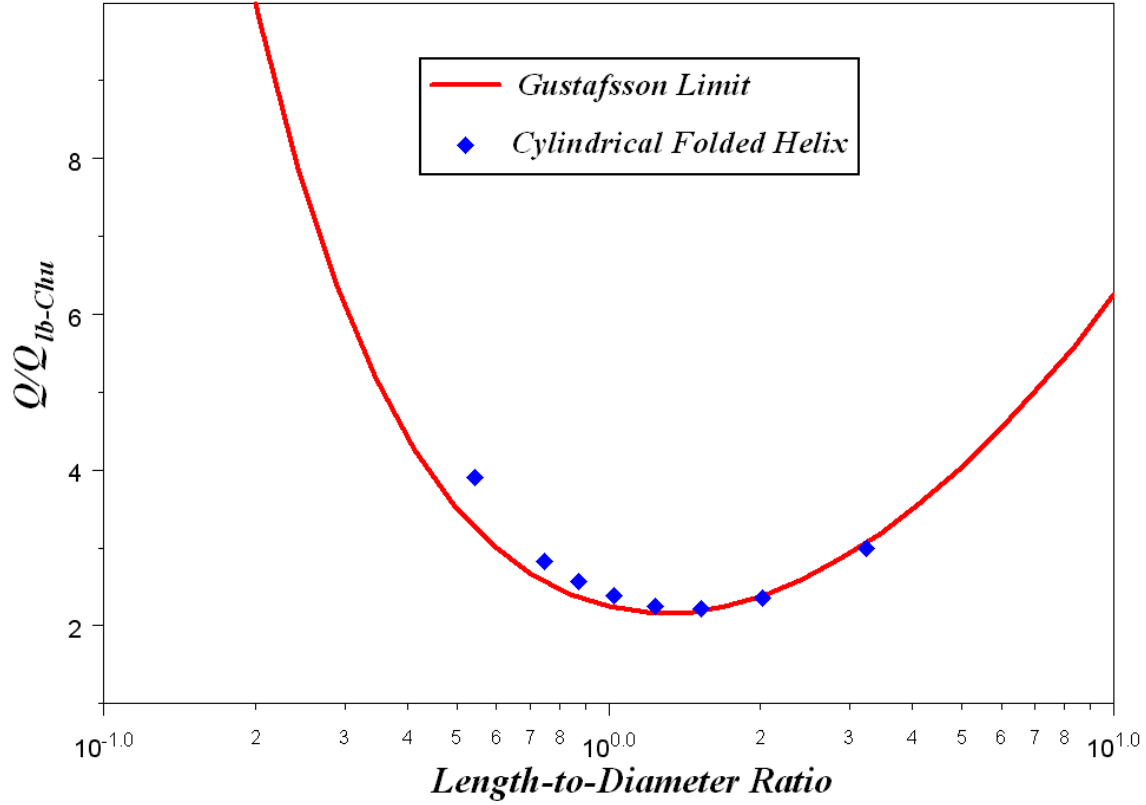
Fig. 3 Comparison of the cylindrical folded helix *Q* to the Gustafsson limit.

Planar Antennas

In the previous section, we described two similar antenna designs that exhibit *Q's* which approach and meet theoretical limits. In this section, we describe several planar antennas that are designed with the same objective, namely to develop antennas having a planar geometry which exhibit a matched impedance and *Q's* that meet theoretical limits. While the Chu-limit provides an absolute minimum for antenna *Q* as a function of occupied spherical volume, it provides no insight into what value of *Q* can be practically achieved using a planar geometry.

Gustafsson provided data for the minimum achievable *Q* for planar antennas as a function of their length-to-diameter ratio [7]. It was assumed that the antennas are electrically small, exhibit a single resonance within their defined operating bandwidth and that they have a directivity equal to 1.5. A plot of the Gustafsson limit, expressed as the ratio of antenna *Q* to the Chu-Limit (Q/Q_{lb}), is presented in Figure 4. From Figure 4, it is seen that the

446

optimum length-to-diameter ratio for the planar dipole antenna is approximately 1.9.

The design approach used with the planar antennas describe here is essentially identical to that used with the spherical and cylindrical folded helices with the exception that the antenna geometry is confined to a 2D planar area. The antenna designs presented here are straight-forward. Their initial dimensions were chosen to approximate the length of the two helices, having a nominal dipole length of approximately 8.36 cm. The width of the planar antennas was varied to change the antenna length-to-diameter ratio. With only a few exceptions, all of the antennas considered here have a conductor diameter of 1 mm and they were designed to operate near a frequency of 300 MHz, where the value of *ka* would be less than 0.5.
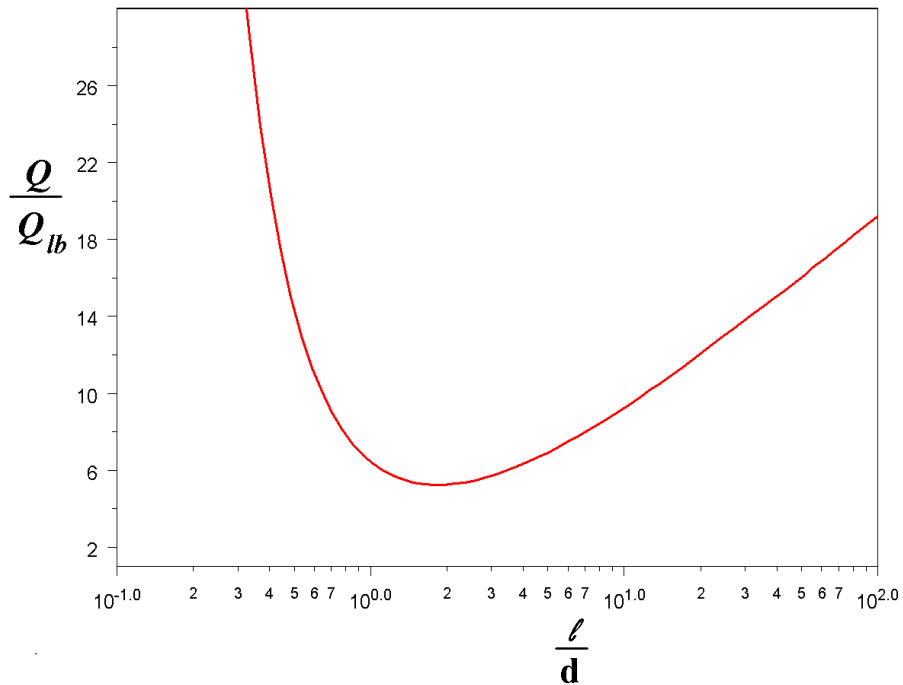

Figure 4. The Gustafsson limit for electrically small planar antennas as a function of length-to-diameter ratio.

The initial and perhaps most obvious geometry for designing an electrically small planar antenna is a meander line structure as illustrated by the meander line configurations presented in Figure 5. The first antenna considered is meander line M1, which has an overall dipole length of 7.96 cm and a diameter of 4 cm, corresponding to a length-to-diameter ratio of 1.99. It is resonant at a frequency of 329.7 MHz, corresponding to a *ka* equal to

0.308. It has a resonant radiation resistance of 3.1Ω and a *Q* of 166.8[2], corresponding to a *Q/Q$_{lb}$* ratio of 4.4. Its radiation efficiency is 63.7%. Before comparing its *Q* to the Gustafsson limit, we will describe a number of other small planar designs considered here.

In many applications, it is desirable to design the antenna to exhibit a resonant impedance equal to 50Ω. In some applications, such as small super directive arrays, it may be desirable that the antenna exhibit a substantially higher resonant resistance. The other meander line antennas presented in Figure 5 are designs implemented to achieve an impedance match relative to 50Ω, or higher impedance as may be necessary in other applications. Achieving an impedance match with the small planar antennas considered in this work is somewhat trivial as it is easily implemented using a near-field reactive coupling matching element approach or a shunt-stub, parallel inductor approach.

The other configurations presented in Figure 5 are design variations that match the antenna impedance to 50Ω or another, higher arbitrary value. Configurations M2 through M4 use a near-field, reactive coupling matching approach where the electrically small dipole, to the left of the meander line, is matched using the resonant meander line structure. This approach is a common technique used in impedance matching electrically small loops and it has more recently been used by Erentok and Ziolkowski in many of their small antenna designs [9]. Configuration M5 uses a shunt-stub (parallel inductor) to match the meander line antenna to 50Ω. A comparison of the antenna impedances is presented in Figure 6. As is seen in Figure 6, the antennas can be easily modified for an impedance match to 50Ω or another, **higher characteristic impedance.   The antennas' other performance** properties will be compared shortly after discussing several other planar antenna designs.

In addition to the simple meander line antennas shown in Figure 5, there are numerous antenna configurations and geometries that may be used to implement electrically small planar antennas. Only a few representative configurations can be described here. Several alternate approaches to designing small planar antennas are illustrated in Figures 7 and 8.

The antennas presented in Figure 7 are meander line geometries where the meandering is oriented in a manner similar to that of a planar inductor. This approach to winding the conductor is generally more effective in that it

---

[2] In this paper, we calculate the *Q*'s of the antennas assuming that the wires are perfectly conducting.

requires less total wire length to achieve resonance relative to the configurations presented in Figure 5. One of the performance drawbacks is that it typically introduces some level of orthogonal TE mode radiation, resulting in minor overhead null fill.
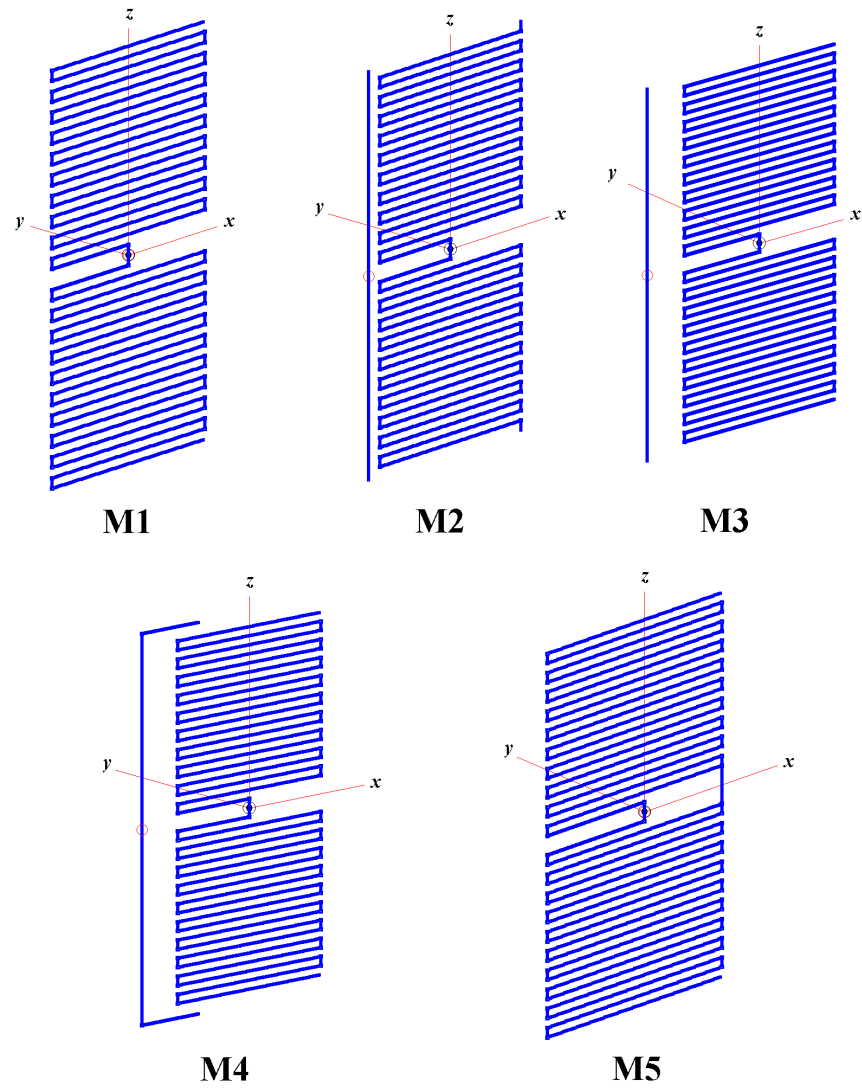

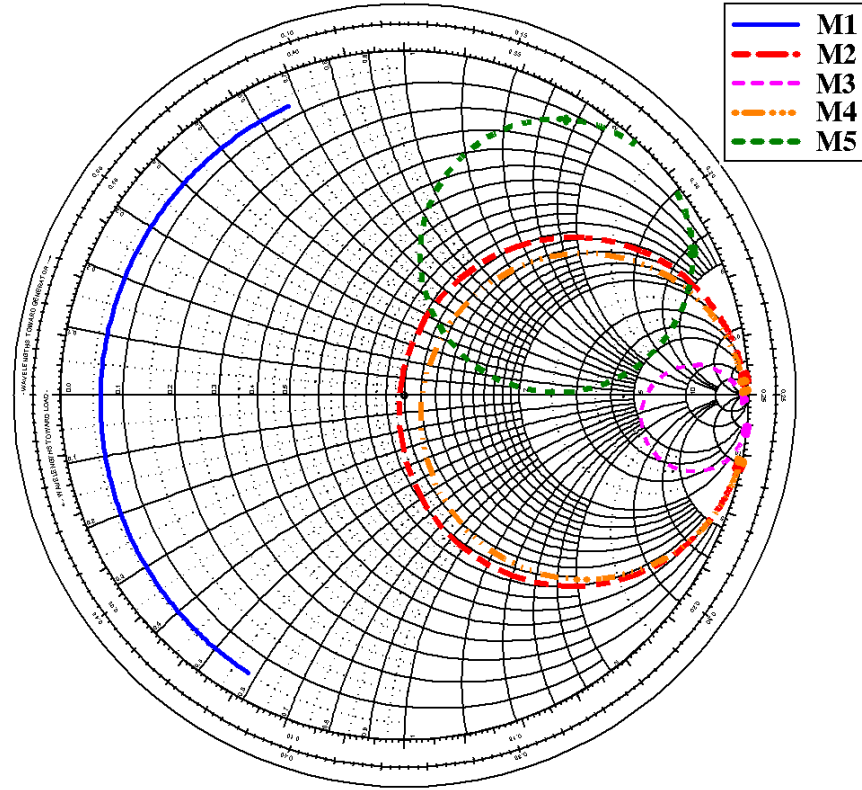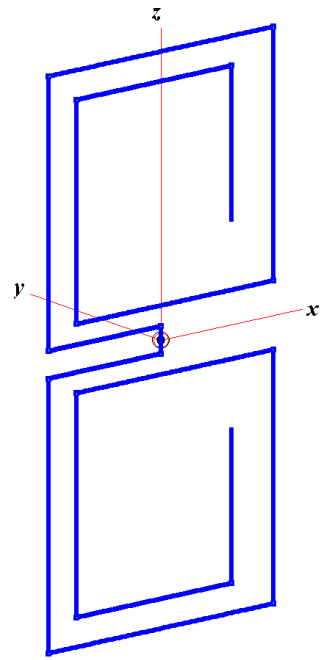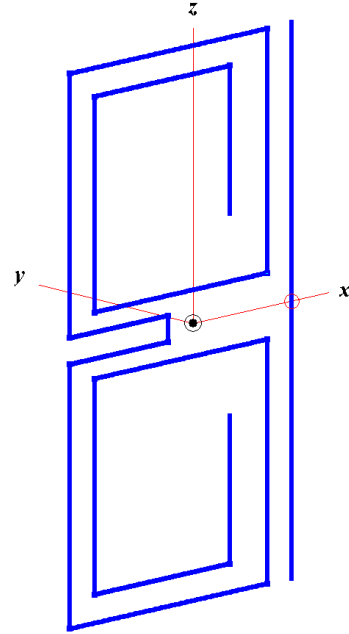**Figure 5. The electrically small planar meander line antennas.**

Figure 6. The feed point impedance of the electrically small planar meander line antennas.

Antenna configuration W1 has an overall dipole length of 8.36 cm and a diameter of 4 cm, corresponding to a length-to-diameter ratio of 2.09. It is resonant at a frequency of 319.3 MHz, corresponding to a *ka* equal to 0.31. It has a resonant radiation resistance of 2.3Ω and a *Q* of 325.9, corresponding to a *Q/Q_{lb}* ratio of 8.86, which is substantially higher than that of meander line M1. Its radiation efficiency is 77.1%.

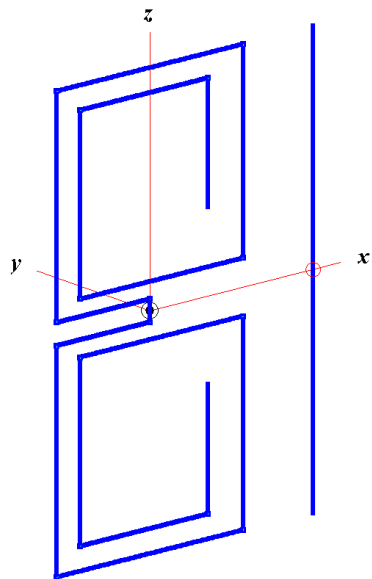Antenna configurations W2 and W3 use near field, reactive coupling matching to achieve the impedance match relative to 50Ω and an arbitrary characteristic impedance of 355Ω, respectively. Antenna configuration W4 uses a shunt-stub, parallel inductor approach to achieve an impedance match relative to 50Ω.

W1

W3
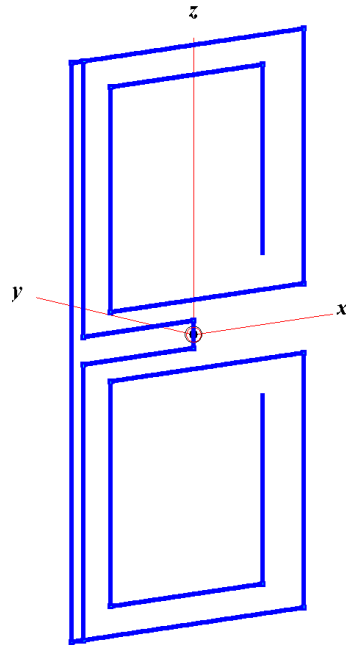
Figure 7. Electrically small planar meander line antennas wound in a manner similar to planar inductors.
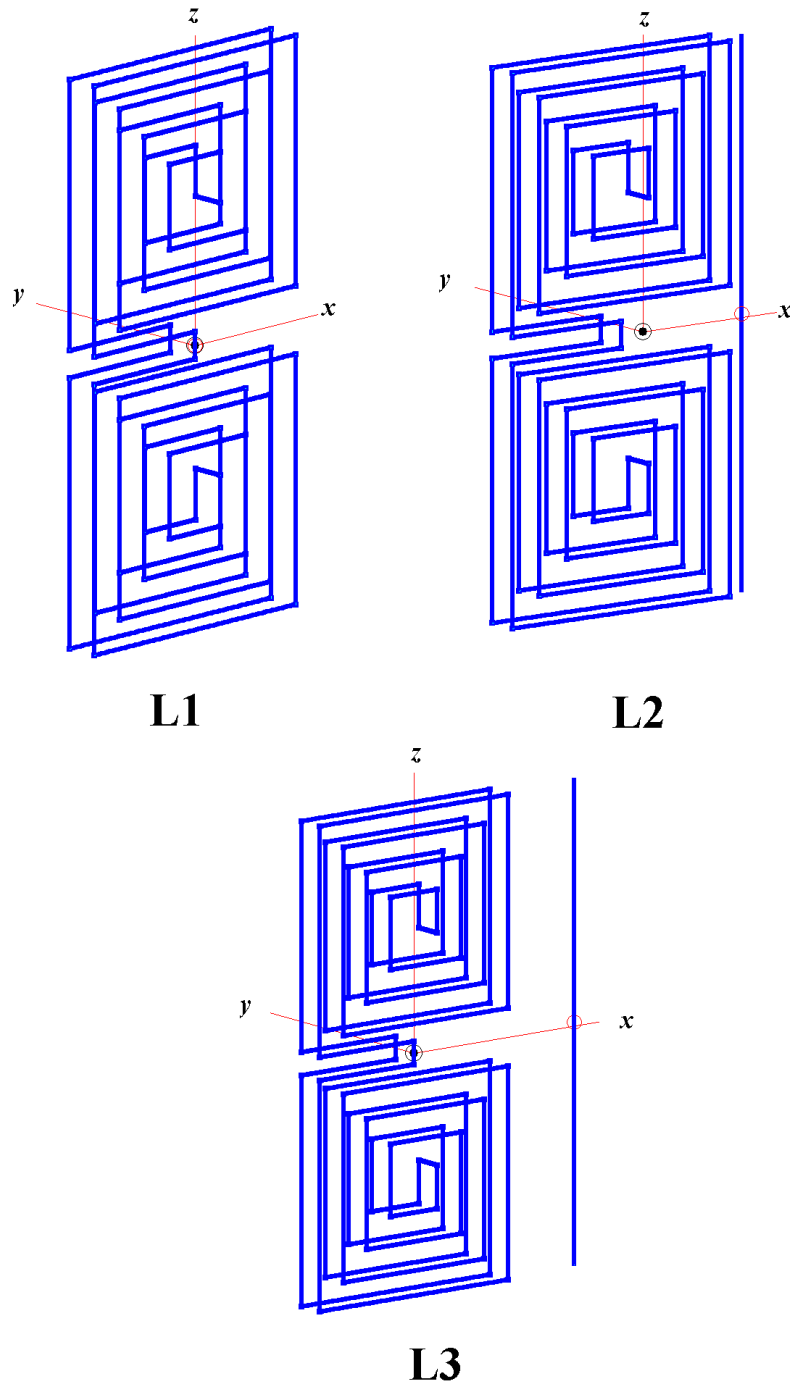
Figure 8. Electrically small planar meander line loop antennas.

The antenna configurations illustrated in Figure 8 are loop antennas derived from the planar meander line antenna W1. The loop nature of the design is created by mirroring the meander line dipole and short-circuiting the two dipoles together at their end points to form a single loop. The increase in wire length in the structure is necessary for a loop antenna to be operated

near its first series resonance in nearly the same frequency range as the meander line dipole antennas. These antennas are presented primarily to illustrate that these electrically small planar loops, operated at their first series resonance, will behave in a manner consistent with the small dipole in terms of their performance properties.

Antenna configuration L1 has an overall dipole length of 8.36 cm and a diameter of 4 cm, corresponding to a length-to-diameter ratio of 2.09. It is resonant at a frequency of 245.7 MHz, corresponding to a *ka* equal to 0.239. It has a resonant radiation resistance of 5.5Ω and a *Q* of 723.6, corresponding to a *Q/Q$_{lb}$* ratio of 9.3, which is higher than that of both meander line M1 and W1. Its radiation efficiency is 70.3%.

Although configuration L1 is a loop antenna in that it is short-circuited at its end points and exhibits a first natural resonance that is an antiresonance, its current distribution and radiation properties are more consistent with those of a small electric dipole rather than a small magnetic dipole. However, much like antenna configuration W1, it does exhibit significant cross polarization and overhead null fill as illustrated in Figure 9. The radiation pattern of meander lines M1 through M5 are identically consistent with those of a straight-wire dipole antenna.

Antenna configurations L2 and L3 use near field, reactive coupling matching to achieve the impedance match relative to 50Ω and an arbitrary characteristic impedance of 304Ω, respectively.

A comparison of the performance properties of all the antennas is presented in Table 1. The ratio of *Q/Q$_{lb}$* for each antenna is presented and compared to the Gustafsson limit is Figure 10. We note that all of the antennas can be easily matched to 50Ω using reactive coupling matching or a shunt stub acting as a parallel inductor. The radiation efficiencies of the antennas are reasonable and in some cases can be improved by using a larger conductor diameter. In some cases, such as the M1 through M5 configurations, the conductor diameter cannot be increased due to space limitations. Finally, we note that in terms of antenna quality factor compared to the lower bound, the meander line M1 and M5 offer optimum performance and in fact exhibit a *Q/Q$_{lb}$* ratio less than the Gustafsson limit.
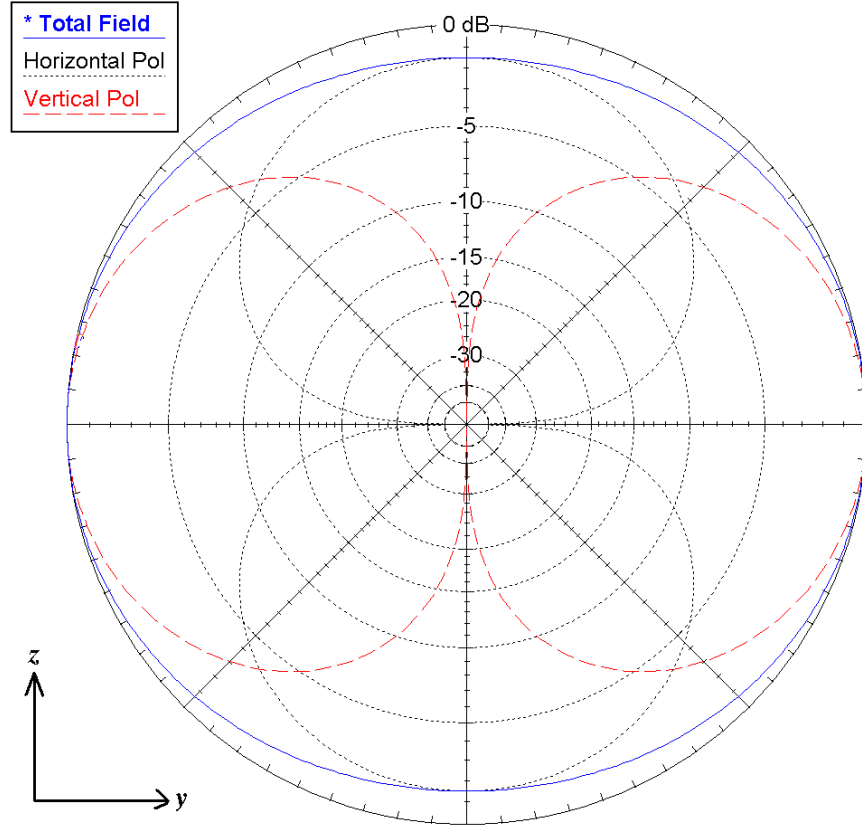
Figure 9. Radiation pattern of the electrically small planar antenna L1. The radiation pattern for the theta sweep plane is shown.

Table 1. Performance comparison of the electrically small planar antennas.

| Antenna Configuration	Frequency (MHz)	Overall Height (λ)	ka	l/d	Radiation Resistance (Ω)	Radiation Efficiency (%)	Q	Q/Q_{lb}
M1	329.7	0.088	0.308	1.99	3.1	63.7	166.8	4.44
M2	309.7	0.086	0.305	1.935	48.4	52.0	263.3	6.86
M3	324.8	0.091	0.332	1.672	285.8	59.6	202.4	6.65
M4	315.0	0.090	0.328	1.720	55.4	51.2	279.4	8.93
M5	313.9	0.083	0.301	1.769	65.3	61.8	176.4	4.41
W1	319.3	0.089	0.31	2.09	2.3	77.1	325.9	8.86
W2	309.9	0.087	0.309	1.867	52.5	72.8	418.5	11.32
W3	317.3	0.089	0.334	1.527	355.5	75.7	366.5	12.27
W4	331.5	0.092	0.325	1.99	57.1	79.3	324.6	10.08
L1	245.7	0.069	0.239	2.09	5.5	70.3	723.6	9.3
L2	239.5	0.067	0.237	1.90	35.6	67.14	844.7	10.67
L3	244.6	0.068	0.251	1.64	304.7	69.2	788.9	11.73
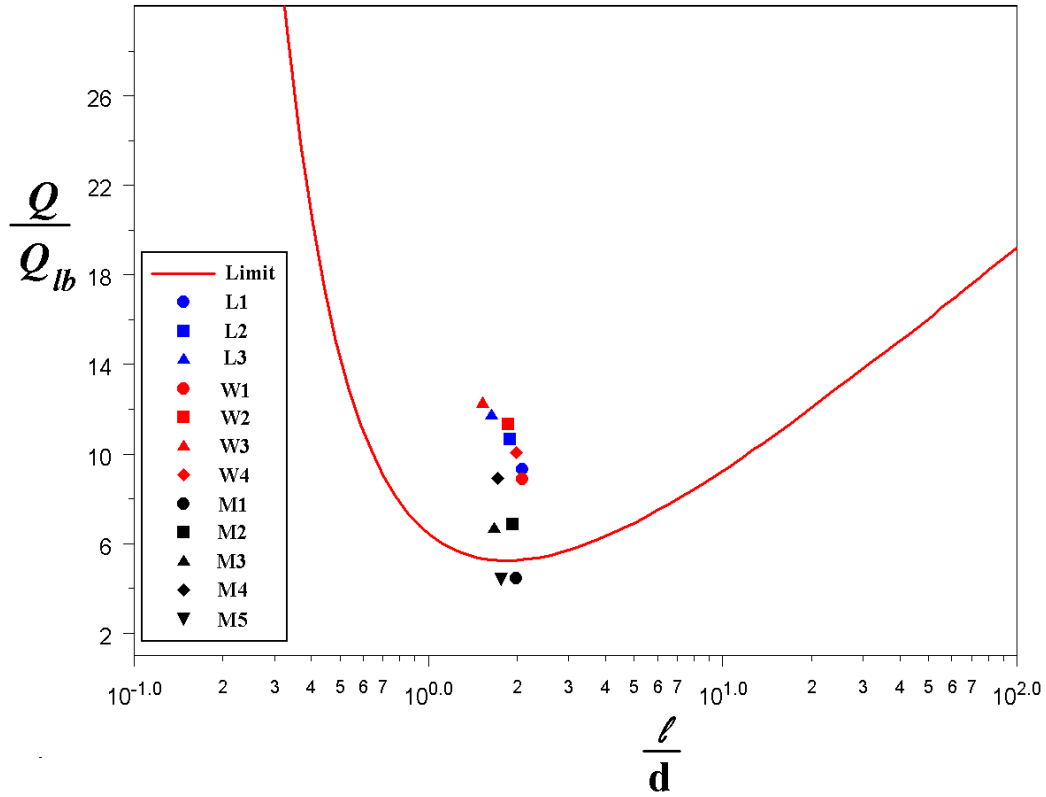
Figure 10. Comparison of the ratio Q/Q_{lb} for the electrically small planar antennas relative to the Gustafsson limit.

The fact that meander line M1 and M5 exhibit a Q/Q_{lb} ratio less than the Gustafsson limit may be expected to some extent as Gustafsson assumes that the lower bound on Q is given by $1/(ka)^3$ rather than Equation 1. To investigate this further and validate the relative behavior predicted by the Gustafsson limit, namely that a length-to-diameter ratio slightly less than 2 is optimum, we consider several other configurations where the length-to-diameter ratios of the antennas are varied relative to the previous configurations. These are illustrated in Figures 11 and 12.

The antenna configurations M1A and M2A are simply multiple arm folded dipole versions of the meander line M1. With an increase in the number of **folded arms, there is a decrease in the antenna's length**-to-diameter ratio **and an increase in the antenna's radiation resistance, exactly as occurs with** the folded spherical and cylindrical helix antennas.

The antenna configurations M3A and M4A are also derived from meander line antenna M1. They have a decreased width and an increased length. **These changes obviously translate into an increase in the antenna's length**-to-diameter ratio.

A comparison of the performance properties of all these antennas is presented in Table 2. The ratio of Q/Q_{lb} for each antenna is presented and compared to the Gustafsson limit is Figure 13.
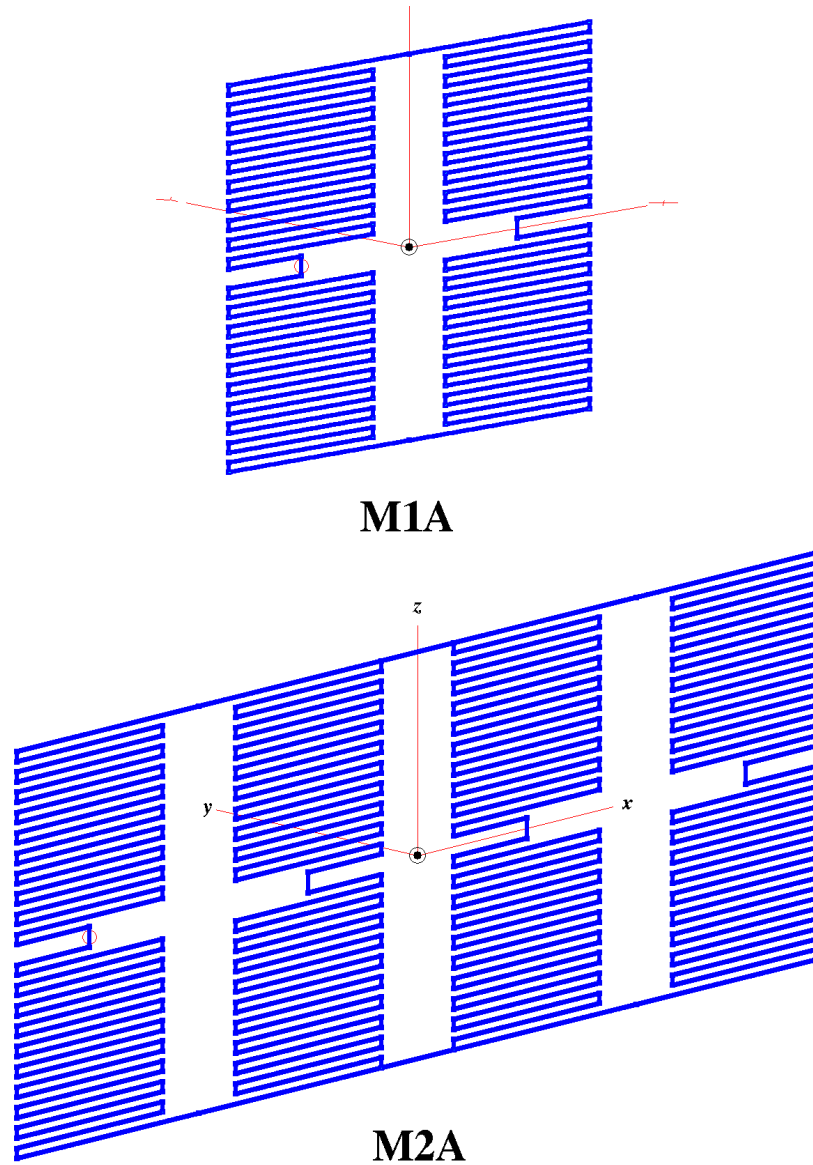
Figure 11. Electrically small planar antennas with decreased length-to-diameter ratios – M1A and M2A.

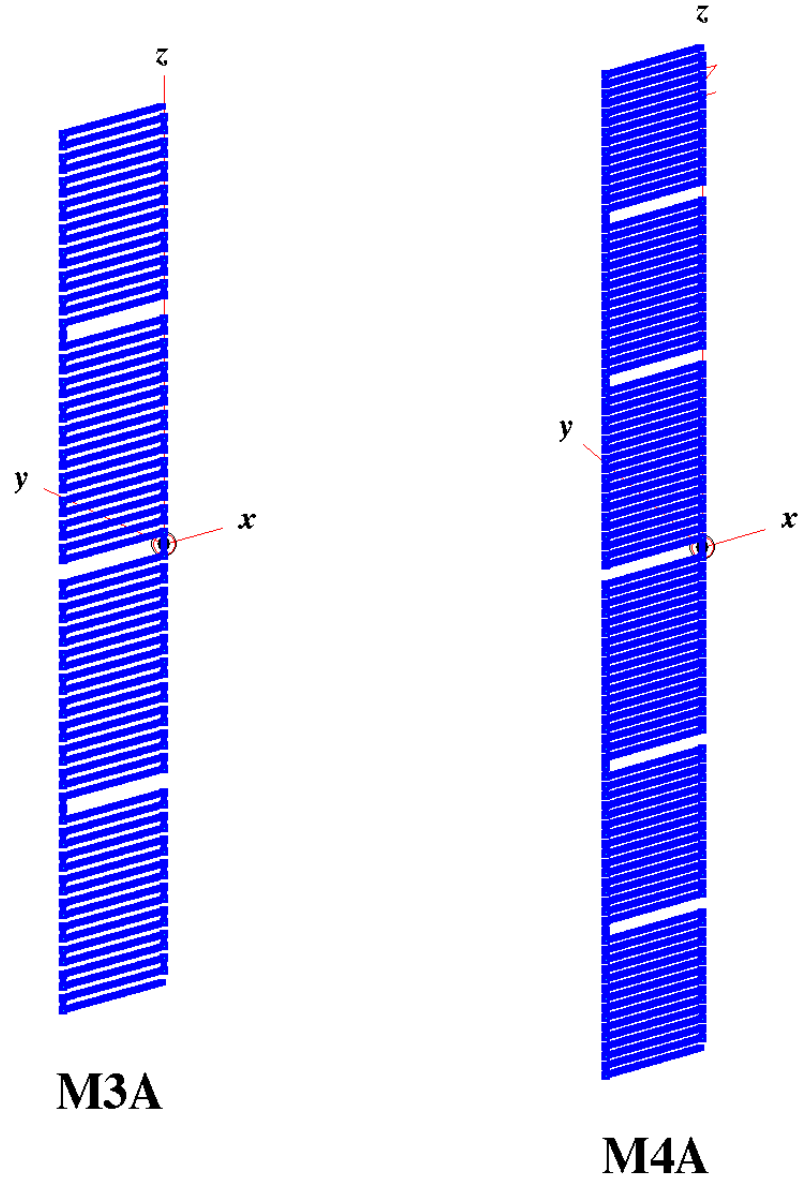**Figure 12. Electrically small planar antennas with increased length-to-diameter ratios – M3A and M4A.**

As expected, the ratio of Q/Q_{lb} increases with either an increase or decrease in length-to-diameter ratio, illustrating that for optimum bandwidth, the electrically small planar antenna should have a length-to-diameter ratio slightly less than 2.

Table 2. Performance comparison of the electrically small planar antennas, M1A, M2A, M3A, and M4A.

Antenna Configuration	Frequency (MHz)	Overall Height (λ)	ka	l/d	Radiation Resistance (Ω)	Radiation Efficiency (%)	Q	Q/Q_{lb}
M1	329.7	0.088	0.308	1.99	3.1	63.7	166.8	4.44
M1A	338.3	0.089	0.453	0.796	13.4	78.5	82.8	6.40
M2A	346.3	0.092	0.849	0.362	51.4	87.5	43.7	15.56
M3A	341	0.168	0.531	7.37	9.5	85.9	53.12	6.21
M4A	260.1	0.18	0.567	10.35	10.7	85.1	50.76	7
CSTM4A	281.9	0.19	0.614	10.35	14.4	-	31.2	5.25
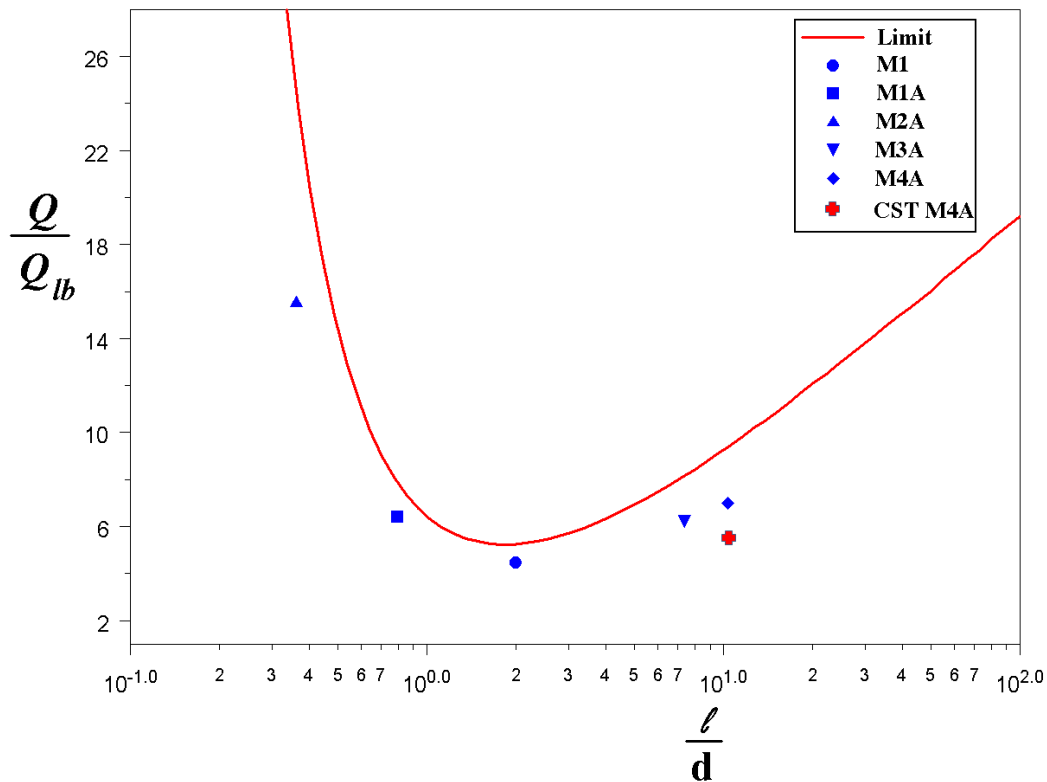
Figure 13. Comparison of the ratio Q/Q_{lb} for the electrically small planar antennas (M1A through M4A) relative to the Gustafsson limit.

We note however, that the Q/Q_{lb} ratios for the antennas are much lower than the Gustafsson limit causing us to question the validity of the simulations or possibly the statement of the limit. We have communicated our concern to Gustafsson and are discussing the matter at the time of

458

writing. To validate the simulations to some extent, we modeled the M4A **antenna configuration in CST's Microwave Studio and obtained similar** results. The Q/Q_{lb} ratio determined from the Microwave Studio simiulations is depicted in Figure 13.

While our investigation of this topic is ongoing, we are confident that the behavior predicted by the Gustafsson limit is valid in that optimum length-to-diameter ratio for the electrically small planar antenna is slightly less than 2.

Discussion

We have modeled and compared the performance properties of several electrically small planar antennas for the purpose of comparing their quality factors to the lower bound and the Gustafsson limit. Our primary objective is to utilize these comparisons for the purposes of optimizing the bandwidth of electrically small planar antennas. We emphasize at this time that we are only considering small antennas that exhibit a single resonance within their defined operating bandwidth.

As expected from the Gustafsson limit, the optimum bandwidth of the small planar antenna is a function of its length-to-diameter ratio. We have also demonstrated that, in some cases, it is somewhat trivial to impedance match these antennas using near field reactive coupling or shunt stub parallel inductor. We note that efficient matching often becomes more of a challenge at lower frequencies and smaller antenna sizes.

Future work in this area is taking into account that many planar antennas operate in conjunction with a dielectric substrate which has the effect of **lowering the antenna's operating frequency. We are additionally considering** planar antennas that operate against in-line ground planes. In these applications, the antenna size is not limited to the antenna geometry but must include some portion of the ground plane as it is often the dominat source of radiation.

References

[1]   L. J. Chu, "Physical Limitations on Omni-Directional Antennas," *J. Appl. Phys.*, Vol. 9, pp. 1163-1175, 1948.
[2]   **J. S. McLean, "A Re**-Examination of the Fundamental Limits on the Radiation Q of   **Electrically Small Antennas,"** *IEEE Trans. Antennas Propagat.*, Vol. 44, pp. 672-676, May 1996.

[3] S. R. Best, "The Radiation Properties of Electrically Small Folded Spherical Helix Antennas," *IEEE Trans. Antennas Propagat.*, Vol. 52, No. 4, pp. 953-960, Apr 2004.

[4] S. R. Best, "Low Q Electrically Small Linear and Elliptical Polarized Spherical Dipole Antennas," *IEEE Trans. Antennas Propagat.*, Vol. 53, No. 3, pp. 1047-1053, Mar 2005.

[5] H. L. Thal, "New Radiation Q Limits for Spherical Wire Antennas," *IEEE Trans. Antennas Propagat.*, Vol. 54, No. 10, pp. 2757-2763, Oct 2006.

[6] M. Gustafsson, C. Sohl, and G. Kristensson, "Physical Limitations on Antennas of Arbitrary Shape," Lund University Report: LUTEDX/(TEAT-7153)/1-36/(2007), July 2007.

[7] M. Gustafsson, Private Communication.

[8] A. D. Yaghjian and S. R. Best, "Impedance, Bandwidth and Q of Antennas," *IEEE Trans. Antennas and Propagat.*, Vol. 53, No. 4, pp. 1298-1324,Apr 2005.

[9] A. Erentok, and R. W. Ziolkowski, "Metamaterial-Inspired Efficient Electrically Small Antennas," *IEEE Trans. Antennas and Propagat.*, Vol. 56, No. 3, pp. 691-707, Mar 2008.

A WIDEBAND DIPOLE ARRAY FOR DIRECTED ENERGY APPLICATIONS AND DIGITAL TV RECEPTION

F. Scirè Scappuzzo[1,4], D. D. Harty[2], B. Janice[2], H. Steyskal[3], and S. N. Makarov[2]
[1] Physical Sciences Inc., Andover, MA, USA
[2] Worcester Polytechnic Institute, Worcester, MA, USA
[3] Consultant, Concord, MA, USA
[4] Swiss Federal Institute of Technology, ETH, Zurich, CH
fscire@psicorp.com   makarov@wpi.edu

Abstract: The present study investigates a broadside small linearly-polarized wideband UHF non-scanning array for directed energy applications. The array radiator is a new volumetric ribcage dipole configuration. Its performance is compared to the performance of two well-known wideband dipole configurations: the wide-blade dipole and the droopy-blade dipole. A tapered PCB-based planar microstrip balun is used. We present theoretical, simulation (Ansoft HFSS), as well as measurement results for the isolated element and for a finite array. We also discuss possible commercial applications (e.g. Digital TV) for the sub-arrays.

Keywords: Broadband Dipoles, Arrays, Finite arrays, Broadband arrays

1. Selection of a single dipole radiator with ground plane

The array performance relies upon the single radiator, although the impedance bandwidth may considerably change (increase or decrease) due to mutual coupling. The gain bandwidth of the single radiator is not important for large arrays, but may have a significant influence on the radiation pattern for small arrays.

1.1 Conventional candidates

If we want the single radiator to withstand high power, we may choose two different solutions: either a PCB design with planar geometry and thick traces (rather expensive), or a metal-sheet design with a planar or non-planar geometry (less expensive). The non-planar geometry, if any, should be simple to manufacture.

The single radiator should possess a large impedance bandwidth and a large gain bandwidth. In order to compare different results we understand the impedance bandwidth as the frequency band where VSWR is less than 2 (return loss is less than -10 dB) and the gain bandwidth as the band where the gain variations of the main beam are less than 3 dB. To estimate the gain bandwidth, the dipole antenna should be possibly located over an infinite ground plane.

461

Conventional dipole antenna/array configurations include:

   i.   the planar wideband dipole (blade, bowtie, diamond, elliptical, etc.) –see [1];
   ii. the sleeve volumetric dipole –see [2];
   iii. the droopy-blade dipole –see [3]-[5] ;
   iv. the folded dipole of different variations –see [6]-[9];
   v.   the planar dipole (diamond, bowtie, blade) above a EBG ground plane –see [10],[11];
   vi. a hybrid of the dipole and the Vivaldi antenna – the so-called "bunny ear antenna" – see [12],[13].

A wide variety of planar shapes may be considered – see [14]. Other related antenna/array dipole configurations may be found in Refs. [15]-[21].

For a droopy-blade dipole, Kerkhoff, and Ellingson [3] obtained good pattern uniformity (gain bandwidth) of 1.8:1 and a slightly lower impedance bandwidth.

For a Fourpoint diamond-like planar dipole antenna with a tuning plate (a variation of a folded dipole above a ground plane), Suh *et al* [8] obtained the gain bandwidth of less than 2:1, but 2.75:1 and higher impedance bandwidth.

For a diamond-like planar dipole above a EBG ground plane, Akhoondzadeh-Asl *et al* [10] obtained 1.4:1 gain bandwidth, but large 2.5:1 impedance bandwidth.

It follows from this analysis that a single radiator that has 2:1 or better impedance bandwidth and at the same time 2:1 or better gain bandwidth should certainly reflect the present state of the art.

1.2   Rib cage dipole above a ground plane

We introduce a new, yet simple broadband volumetric dipole construction shown in Figure 1b. We call this antenna "ribcage dipole" naming it after an initial design that was resembling the human rib cage.

The ribcage dipole is similar to the droopy-blade dipole because it occupies the volume beneath the antenna and provides a capacitive coupling to the ground plane; however, it is different because it forms a well-confined metal cavity. On the other hand, when the sleeves or ribs are missing, the ribcage dipole is reduced to the planar wide-blade dipole. The ribcage structure with rectangular metal-sheet wings enables a low-cost design.

First, we compare the performance of the ribcage dipole to the performance of the standard (not wideband) blade dipole above a metal ground plane. The geometry for both, a standard dipole and a ribcage dipole, including critical dimensions is shown in Figures 1a and 1b, respectively.
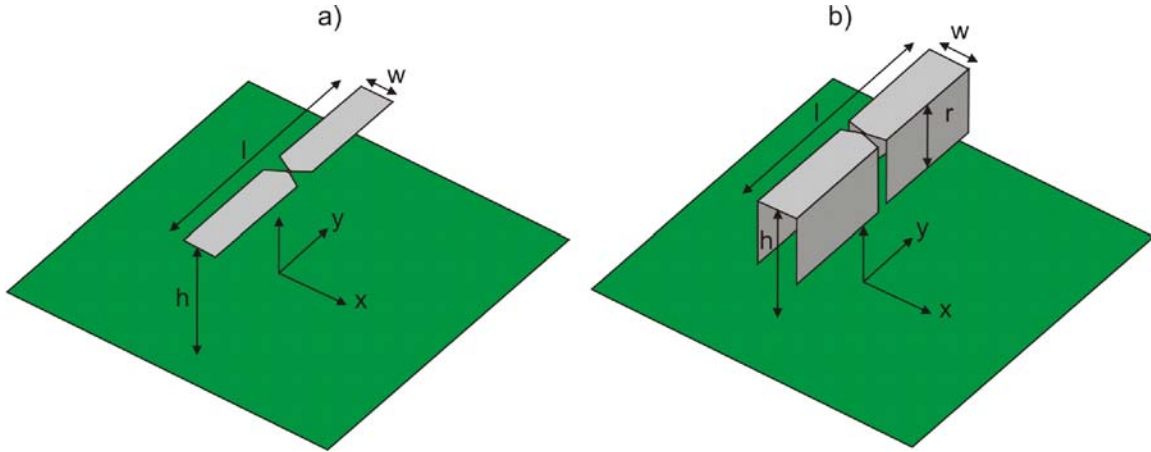
Figure 1. a) Standard dipole above finite ground plane; b) Ribcage dipole above finite ground plane. The two radiators a) and b) have the same length, l, and width, W. The geometry parameters are listed in Table 1.

Figure 2 presents the simulated return loss for the two antennas of Figure 1 with the dimensions given in Table 1. The dipoles were fed by lamped port with characteristic impedance of 50 Ohm. In this study we focus on the UHF band. Clearly, the ribcage demonstrates a broadband behavior, similar to the wide-blade dipole and the droopy-blade dipole.

All simulations are performed in Ansoft HFSS11, with the PML boundary, with final meshes of about 20,000 tetrahedra, and with a good convergence history. For parametric optimization, the fast frequency sweep is used; all final results have been controlled using discrete frequency sweep.
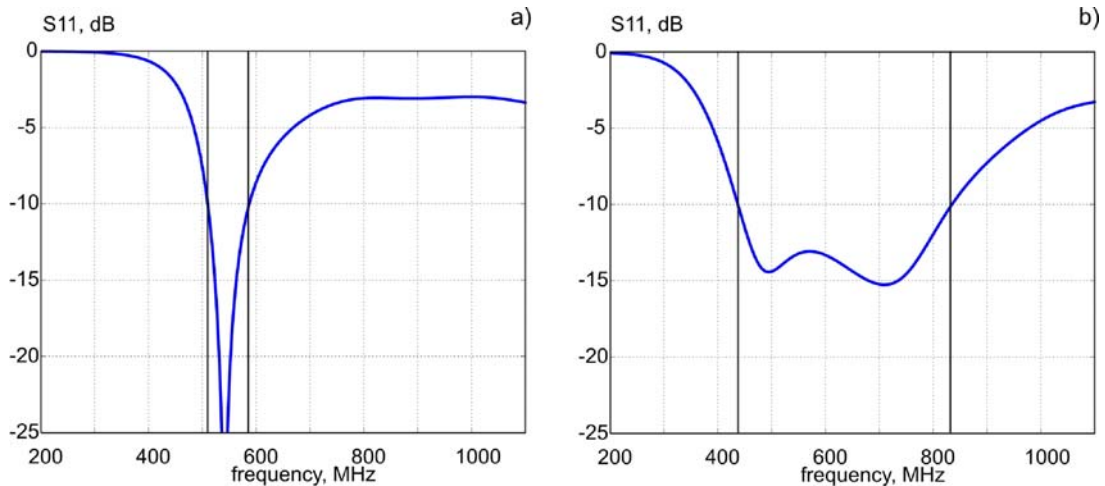

Figure 2. Simulated impedance bandwidth for two antennas shown in Figure 1. a) Blade dipole, with f_C =548 MHz, λ_C =547mm, B=509-587 MHz; b) ribcage dipole, with f_C =636 MHz, λ_C=471mm, and B=436-836 MHz.

463

Table 1. Geometry Parameters for the Antennas of Figure 1, used in Figure 2

Antenna	Height above Ground Plane	Width	Total Length	Rib (Sleeve) Depth	Ground Plane
Blade dipole	h=105mm h/λ_C =0.19	w=30mm	l=220mm	NA	300×300mm
Ribcage dipole	h=160mm h/λ_C =0.34	w=30mm	l=220mm	r = 70mm	300×300mm

1.3   Ribcage dipole, wide-blade dipole and droopy-blade dipole comparison

Once the broadband behavior of the isolated ribcage dipole over the ground plane is established, a legitimate question to ask is the following: how is the performance of the ribcage dipole compared to the performance of wideband dipole configurations such as the planar wide-blade dipole and the droopy-blade dipole? The configurations under study are shown in Figure 3 that depicts a ribcage dipole (a), a planar wide-blade dipole (b), and a droopy-blade dipole (c) of same length, total width, and height over a fixed size ground plane.
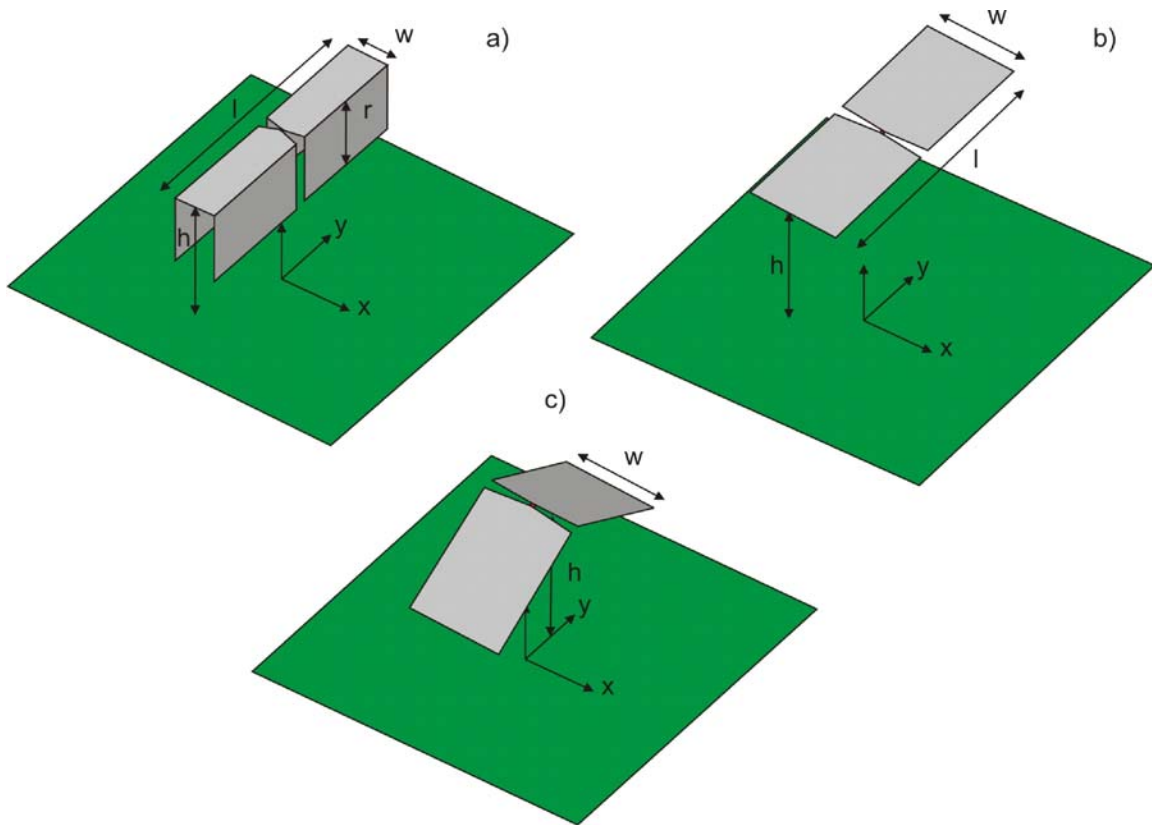

Figure 3. Ribcage dipole (a); planar wide-blade dipole (b); and droopy-blade dipole (c).

We are interested in evaluating which isolated radiator element among the wide-blade dipole, the droopy-blade dipole, and the ribcage dipole, potentially provides the best performance, keeping in mind both, the impedance bandwidth and the gain bandwidth.

When placed above a finite or infinite ground plane, at heights $0.40 > h/\lambda_C > 0.25$, all three antenna elements generally indicate a broadband behavior. The distance from the ground plane, h, should be such that $h < 0.40\lambda_C$ to preserve the broadside dipole pattern at the center frequency. As the antenna height above the ground plane increases, the impedance bandwidth increases, but the gain bandwidth generally decreases (the dipole half-donut pattern is destroyed). Thus, smaller heights are more beneficial for wide gain bandwidth and larger heights are more beneficial for wide impedance bandwidth, in all three antennas of Figure 3.

1.3.1   Wide-blade dipole and droopy-blade dipole comparison

For the *same* height above the ground plane and for the same antenna length (from end to end) the planar wide-blade dipole and the droopy-blade dipole show opposite behaviors in terms of impedance bandwidth and gain bandwidth performance. To illustrate this observation we consider the following numerical experiment:

  i.   fix the antenna length *l*, from end to end;
  ii. fix the antenna height (from the delta-gap feed) at h= 0.7*l* (150mm);
  iii. fix the ground plane size at 300×300mm;
  iv. fix the flare angle for the droopy-blade dipole at 30°;
  v.   allow the width of the antenna, W, to vary from 0.1*l* to 0.7*l*.
  vi. allow the feed flare angle (very important for impedance matching) to vary.
  vii. simulate the different configurations using Ansoft HFSS.

Over 200 representative combinations were simulated in either case to achieve optimized results. We selected the antenna geometries with the *largest* possible impedance bandwidth. The results of the optimization are shown in Figure 4. Table 2 lists the corresponding antenna parameters.

Analyzing Figure 4 we may conclude that the wide-blade dipole has a potentially larger impedance bandwidth than the droopy-blade dipole of the same length and height, *disregarding* of the most favorable dipole width. This result was replicated also at other antenna heights (160mm and 170mm).

On the other hand, the wide-blade dipole has a considerable gain variation with frequency (i.e. an undesirable antenna pattern variation over the frequency) and thus a smaller gain bandwidth than the droopy-blade dipole. This result has been confirmed at other antenna heights (160mm and 170mm). In conclusion, either radiator element (wide-blade dipole or droopy-blade dipole) has its own advantages and disadvantages in terms of impedance bandwidth and gain bandwidth performance.
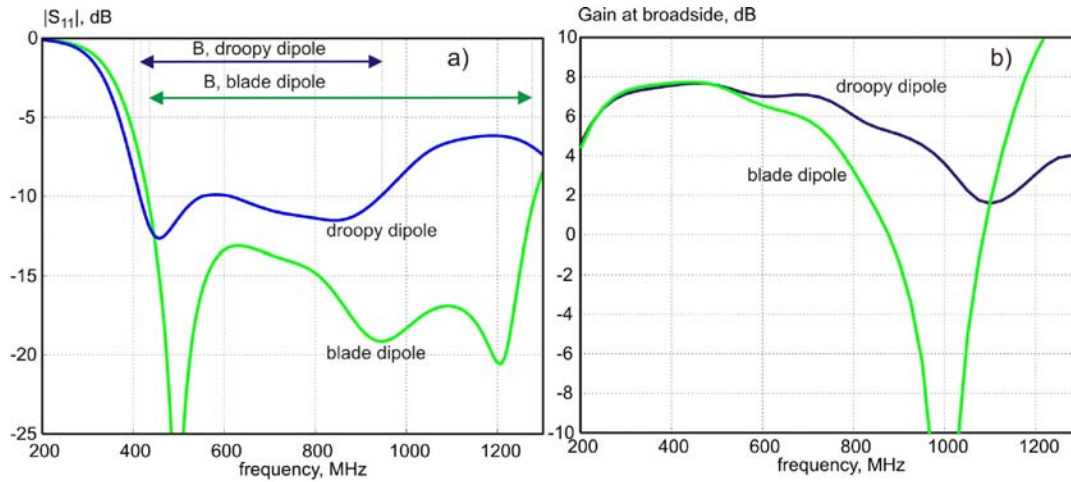
Figure 4. Return loss and broadside gain for the planar blade dipole and the droopy-blade dipole, respectively. Both antennas are optimized for maximum impedance bandwidth. Impedance bandwidth of the blade dipole is ~3.0:1; impedance bandwidth of the droopy-blade dipole is ~2.3:1.

Table 2. Geometry Parameters Corresponding to Two Antennas in Figure 4

Antenna	Height over Ground Plane	Width	Total Length	Sleeve Depth	GP
Wide-blade dipole	h=150mm	w=120mm	l=220mm	NA	300×300mm
Droopy-blade dipole	h=150mm	w=140mm	l=220mm	NA	300×300mm

1.3.2 Ribcage dipole and droopy-blade dipole comparison

The ribcage dipole is reduced to the wide-blade dipole when the sleeve length is zero. Therefore, it could indeed replicate the large impedance bandwidth of the wide-blade dipole of Figure 4. But, could the ribcage dipole be designed to, also, replicate the performance of the droopy-blade dipole (i.e. wide gain bandwidth)? To answer this question we have repeated the procedure adopted in Section 1.3.1 to match the performance of the droopy-blade dipole of Figure 4 with a ribcage dipole. In this case the overall width of the ribcage dipole includes the blade width plus twice the sleeve length - see Figure 3a. A typical matching result is shown in Figure 5. The antenna parameters are given in Table 3.

Figure 5 displays a close match between the impedance and gain bandwidths of the ribcage and the droopy-blade dipole; however, an even better match may be obtained by letting the ribcage overall width differ from the droopy dipole. As an example, Figure 6 shows the same droopy dipole of Figure 5 compared with a new ribcage dipole with overall width of 145 mm (25+60×2) instead of 140mm. The corresponding geometry parameters are given in Table 4.
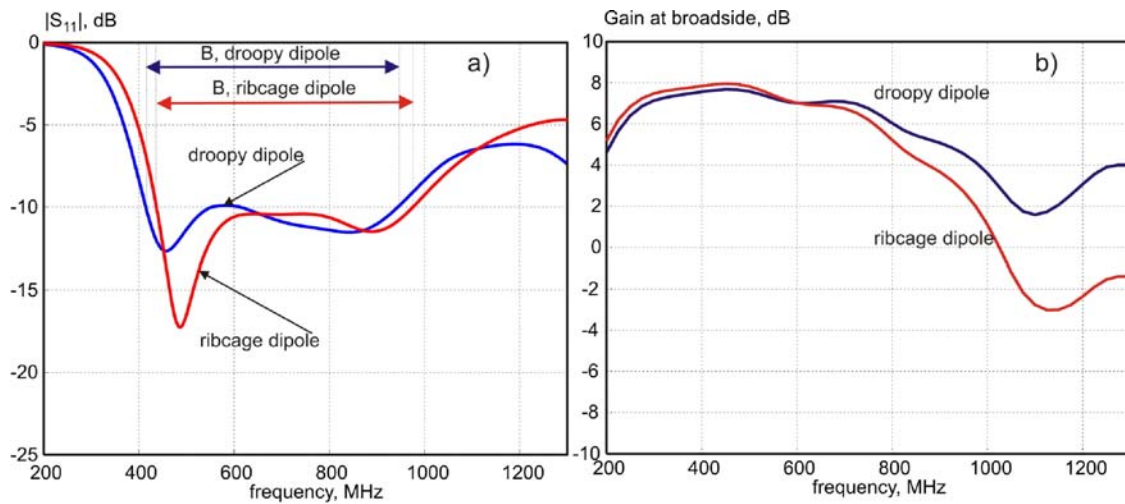
Figure 5. Return loss and broadside gain for the ribcage dipole and the droopy-blade dipole of same length, height, and overall width. The impedance bandwidth of the ribcage dipole is ~2.2:1.

Table 3. Geometry parameters corresponding to two antennas in Figure 5. The overall width of the ribcage (40+50×2=140mm) is equal to the width of the droopy-blade dipole (140mm).

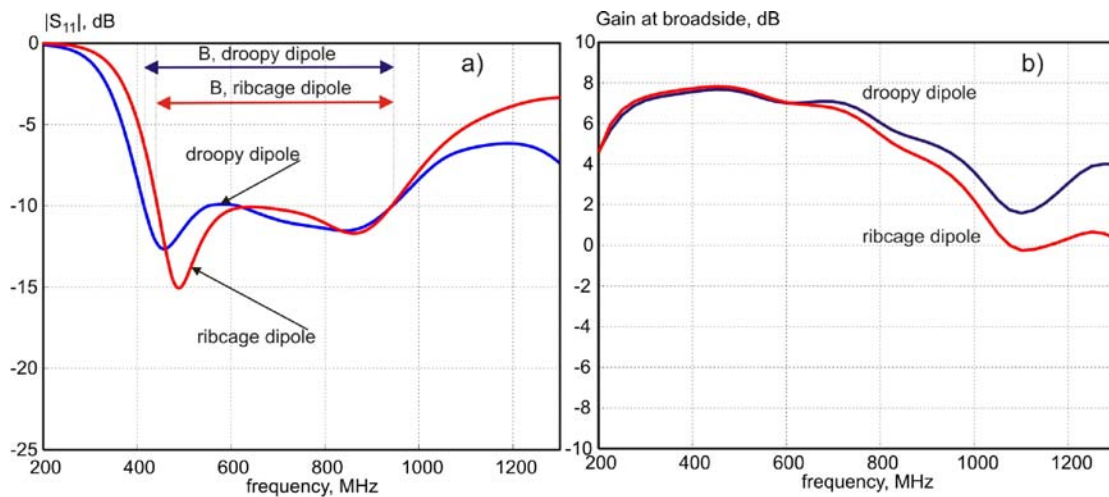| Antenna	Height from Ground Plane	Overall Width	Total Length	Sleeve Depth	GP
Ribcage dipole	h=150mm	w=40mm	l=220mm	50mm	300×300mm
Droopy dipole	h=150mm	w=140mm	l=220mm	NA	300×300mm

Figure 6. Return loss and broadside gain for the ribcage dipole and the droopy-blade dipole having the same overall length, the same height, and the overall width different by 5 mm.

467

Table 4. Geometry parameters corresponding to two antennas in Figure 6.
The overall width of the ribcage (25+60×2=145mm) is slightly larger than the
width of the droopy-blade dipole (140mm).

Antenna	Height from Ground Plane	Width	Length	Sleeve Depth	GP
Ribcage dipole	h=150mm	w=25mm	l=220mm	60mm	300×300mm
Droopy-blade dipole	h=150mm	w=140mm	l=220mm	NA	300×300mm

1.4   Advantages of the ribcage dipole

In this section we will discuss the advantages of the ribcage dipole. First, it should be noted that the ribcage dipole occupies significantly less overall volume (narrower design) than the wide-blade dipole and droopy-blade dipole over a ground plane when the sleeves length is non-zero. Second, the ribcage dipole can be designed to have better combined impedance/gain bandwidth performance.

Indeed, analyzing the preceding discussion, we may notice that the ribcage dipole is perhaps not better or worse than either of the two other configurations; rather, it *includes* both, the wide-blade dipole and the droopy-blade dipole, as two degenerate cases. When the sleeves are missing, it reduces to the blade dipole; when the sleeves are long as in Figure 6 (Table 4) the performance is similar to that of the droopy-blade dipole.

Since the ribcage dipole has two additional independent parameters (dipole width and sleeve length) it is capable of achieving an intermediate behavior: a larger impedance bandwidth than for the droopy-blade dipole and a better radiation pattern than the wide-blade dipole. Figure 7 provides evidence of our findings.

It is critical to note that with carefully optimized sleeve length the ribcage dipole is capable of providing larger impedance bandwidth among all three candidates, while keeping the gain bandwidth higher than the wide-blade dipole's. This conclusion is confirmed by the results of the optimizations shown in Figure 8.

In conclusion, such design flexibility may be of significant importance for single radiators as well as small arrays (2×2, 4×4, or even 8×8). For small arrays both, the impedance bandwidth and the gain bandwidth of the isolated element may have a significant influence on the antenna array behavior.
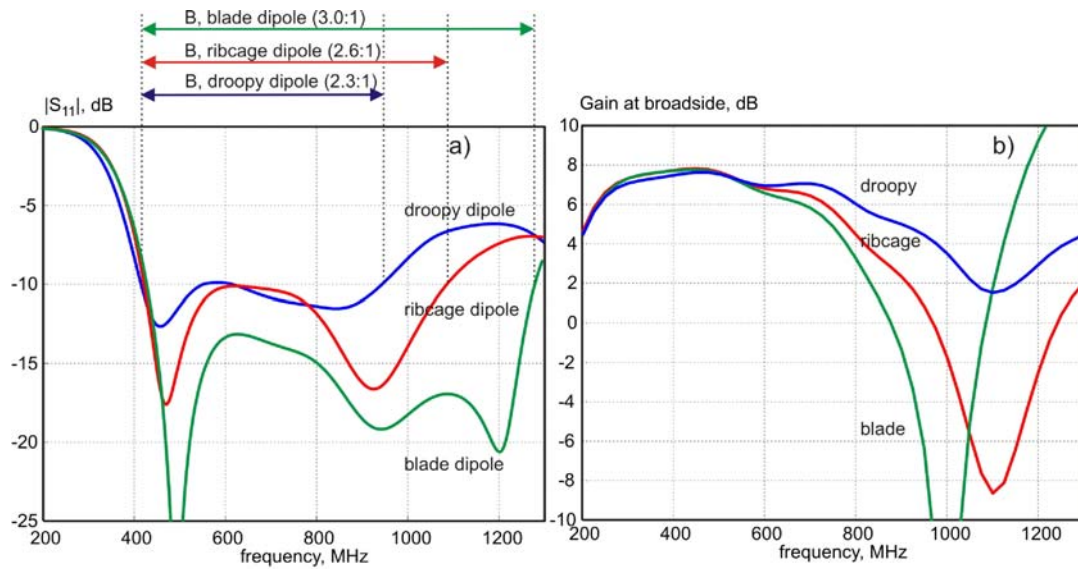
Figure 7. Return loss and broadside gain for the ribcage dipole, droopy-blade dipole, and the wide-blade dipole of same length, height, and ground plane spacing (h=150 mm). The droopy-blade dipole and the wide-blade dipole have been optimized for the maximum possible bandwidth. The antenna geometries are listed in Table 5.

Table 5. Geometry parameters corresponding to three antennas in Figure 7. The overall width of the ribcage (55+40×2=135mm) is slightly less than the width of the droopy-blade dipole (140mm).

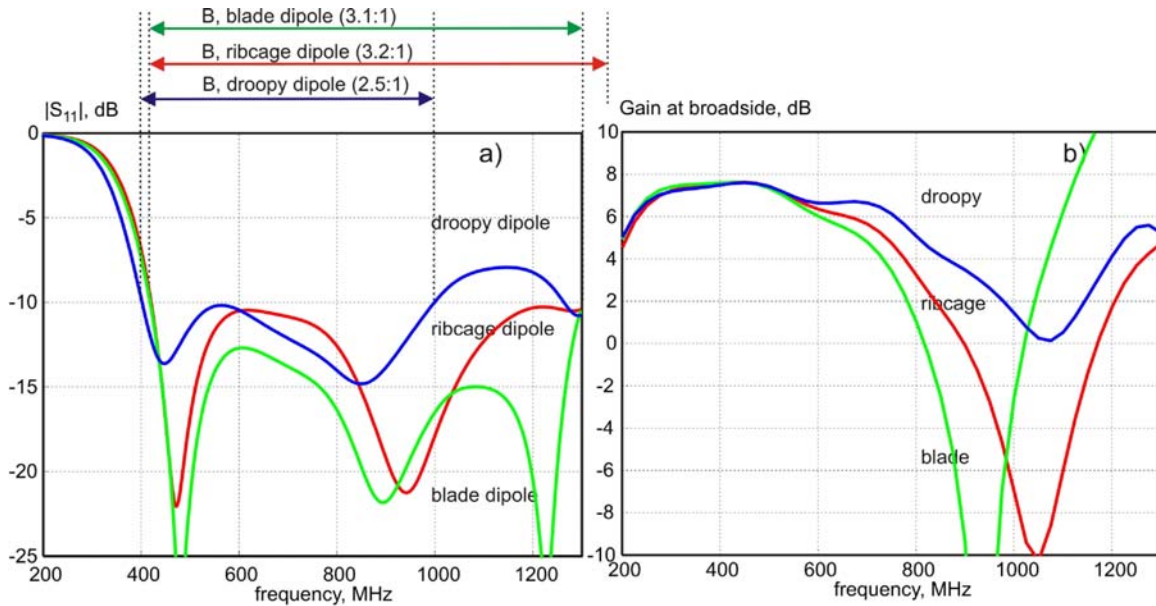| Antenna	Height From Ground Plane	Width	Length	Sleeve Depth	GP
Ribcage dipole	h=150mm	w=55mm	l=220mm	40mm	300×300mm
Droopy-blade dipole	h=150mm	w=140mm	l=220mm	NA	300×300mm
Wide-Blade dipole	h=150mm	w=120mm	l=220mm	NA	300×300mm

Figure 8. Return loss and broadside gain for the ribcage dipole, droopy-blade dipole, and wide-blade dipole of same length and height from the ground plane (h=160mm). The droopy-blade dipole and the wide-blade dipole have been optimized for the maximum possible bandwidth. The antenna geometries are listed in Table 6.

Table 6. Geometry parameters corresponding to three antennas in Figure 7.
The overall width of the ribcage (50+40×2=130mm) is slightly less than the width of the droopy-blade dipole (140mm).

Antenna	**Height from Ground Plane**	**Width**	**Length**	**Sleeve Depth**	**GP**
Ribcage dipole	**h=160mm**	**w=50mm**	**l=220mm**	**40mm**	**300×300mm**
Droopy-blade dipole	**h=160mm**	**w=140mm**	**l=220mm**	NA	**300×300mm**
Wide-Blade dipole	**h=160mm**	**w=120mm**	**l=220mm**	NA	**300×300mm**

1.5   Tapered microstrip balun

We have chosen to implement a taper microstrip balun for the ribcage dipole antenna feed. The optimized balun is shown in Figure 9. The use of this type of balun is common for broadband linearly-polarized dipoles over a ground plane [1],[10]. The balun is printed on a 125 mil thick FR4 using thick copper traces and is soldered to an N-type male connector in the ground plane. The microstrip trace itself may also be tapered. The typical trace width is 5-6mm.
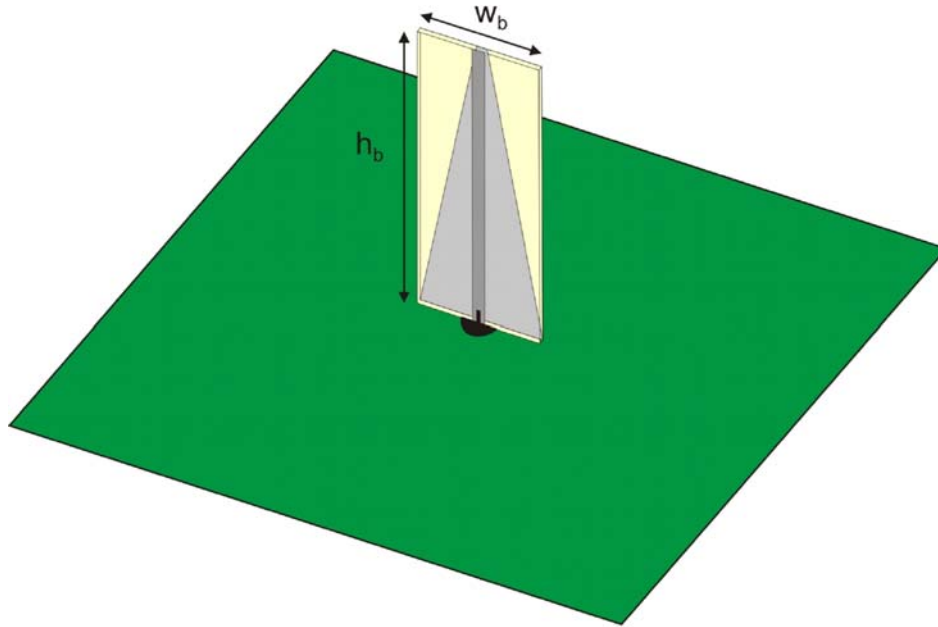
Figure 9. Microstrip tapered balun optimized for the ribcage dipole antenna of Table 7.

We have investigated different tapering profiles including triangular, exponential, and Chebyshev's profiles, but did not find a significant improvement in the impedance bandwidth compared to the simple triangular profile.

Compared to the center-fed ribcage dipole, the isolated ribcage radiator with the balun maybe optimized for a slightly lower or a similar impedance bandwidth.

1.6   Experimental results and comparisons with simulations

Two ribcage dipoles including the printed balun were built and tested. One of the ribcage antennas is shown in Figure 10a. The antenna parameters are given in Table 7. Figure 10b shows a comparison between simulations and return loss measurements performed using an E8356A Agilent Vector Network Analyzer. The simulations and experimental results are in good agreement. We partially explain the differences in the middle of the band by a detuning effect of two Teflon posts seen in Figure 10a. These posts have not been considered in the simulations. Better agreement is obtained when the posts are removed from the antenna construction.

Figure 11 shows the antenna performance when the Teflon posts removed. The remaining disagreement may be due to a feed assembly uncertainty, the effect of the coaxial connector, or (most likely) a slightly different dielectric constant of FR4 used in the balun.
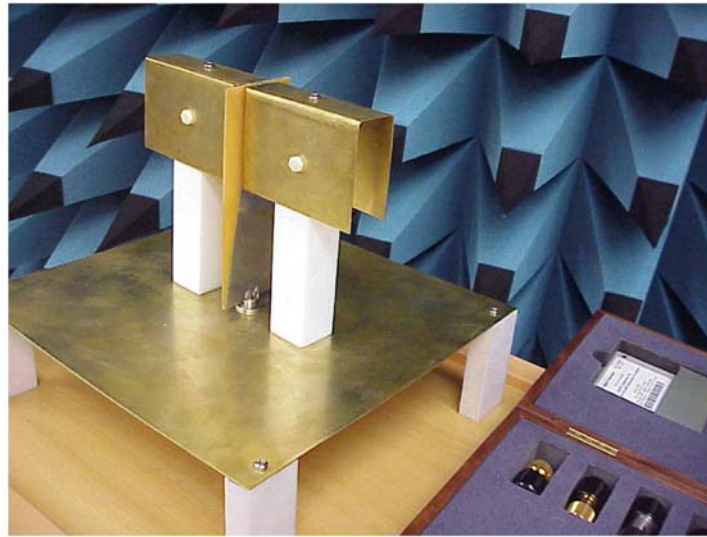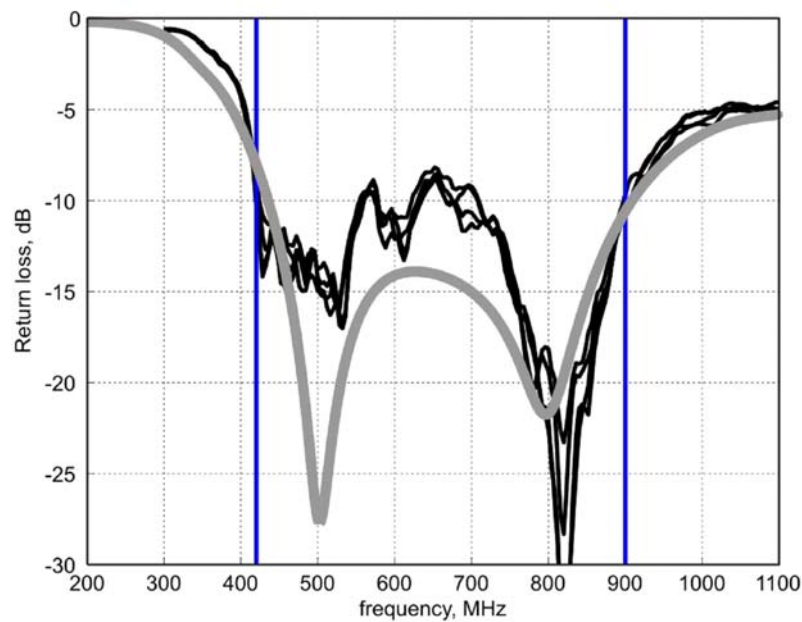
Figure 10. a) Ribcage dipole antenna with ground plane and additional Teflon posts for mechanical support. b) Comparison between simulations and experiments. Return loss of the ribcage dipole above 300×300 mm ground plane. The thick curve indicates simulations; the thin curves indicate our experimental results.

Table 7. Geometry parameters used in Figure 10

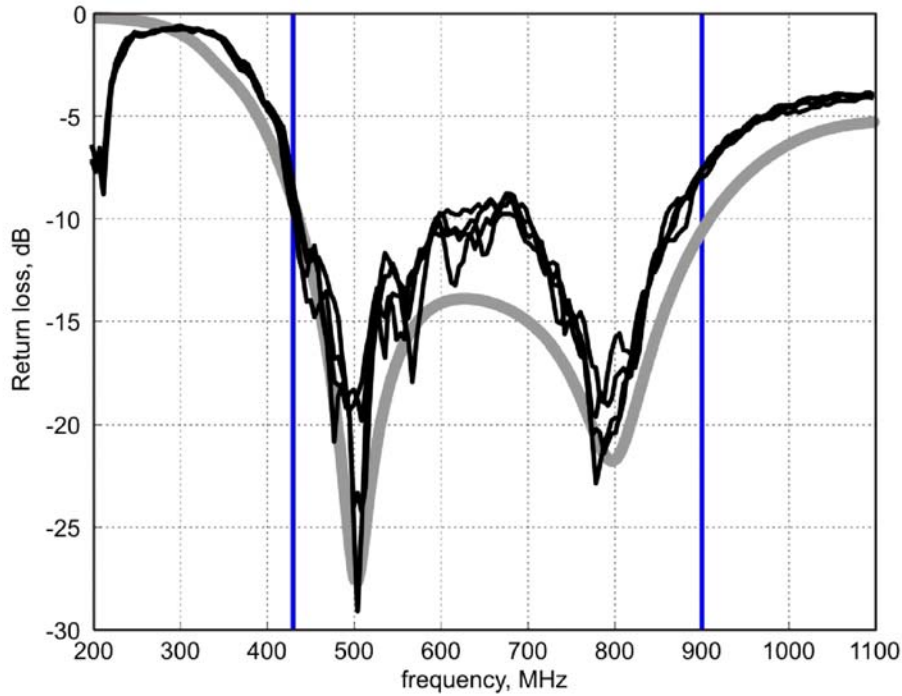| Antenna	Height from Ground Plane	Width	Total Length	Sleeve Depth	Ground Plane
Ribcage Dipole f_C =670 MHz B=430-910 MHz (2.1:1)	**h=175mm** h/λ_C =0.39	**w=35mm**	**L=210mm**	**r=70mm**	**300×300mm**

Figure 11. The same comparison as in Figure 10b), but without the Teflon posts. The experimental data at low frequencies (below 300 MHz) should be ignored.

2.   Antenna array performance

We are interested in investigating how the ribcage dipole would perform as a single element of an antenna array. To this end our goal is twofold:

 i.   build a one octave (500MHz-1000MHz) 8x8 antenna array and achieve ~20 dB gain over the band (while maintaining low sidelobes);

 ii. build a small, low-cost, 4x4 array (from 400MHz to 1000MHz) for digital TV reception.

473

In either case, we shall use the ribcage dipoles as radiators, augmented with the tapered microstrip balun.

2.1   Unit cell optimization

Figure 12 shows the optimized unit cell array element with balun simulated using Ansoft HFSS. We have used periodic boundary conditions (see [22],[23] for a discussion of the numerical accuracy) and a Floquet wave port at the top boundary. The Floquet port expands the radiated field into a full set of Floquet modes (plane waves) that are sufficient to describe any outgoing field from a unit cell at different scan angles.
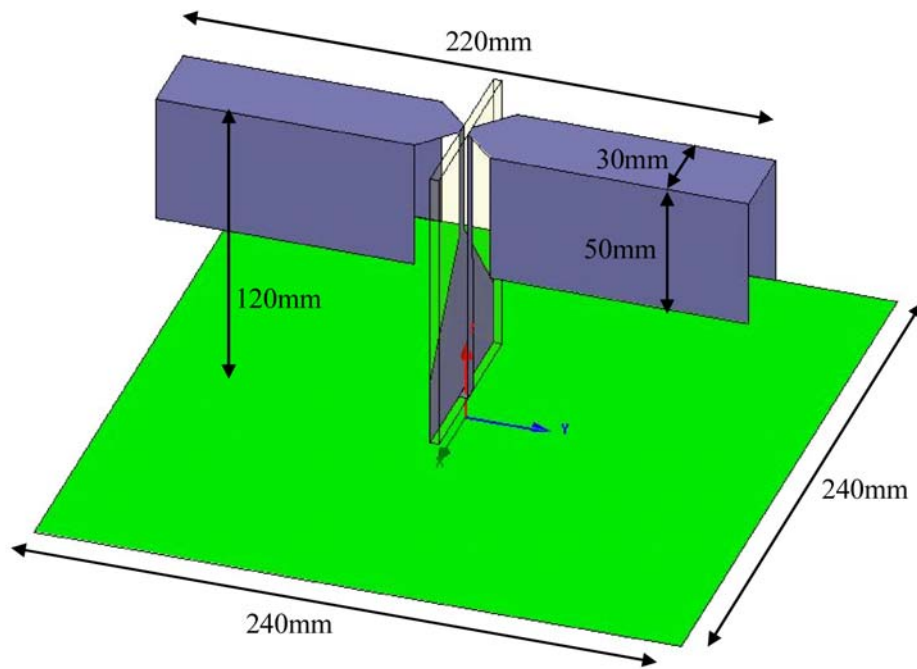

Figure 12. An optimized unit cell of the array with the balun.

When the unit cell size does not exceed $\lambda_0/2$, only one Floquet mode can propagate in the vertical direction; the other plane waves are evanescent and very quickly decay with increasing z. Therefore, the number of modes reaching the Floquet port located at the very top of the unit cell may be very small.

In the presence of the Floquet port, the antenna impedance cannot be calculated from the self-impedance of the antenna lumped port. We must use the self-reflection coefficient, S_{11}, of the antenna port, which is found when all other modes of the Floquet port are terminated into matched loads (e.g. exactly into impedance of free space). The antenna's impedance is then obtained in the form

$$Z = 50\Omega\frac{1+S_{11}}{1-S_{11}}, \quad S_{11} = |S_{11}|\exp(j\angle S_{11}) \tag{1}$$

Figure 13 shows the optimized active return loss for the unit cell array with balun. The optimization involved an extensive search in the space of available radiator/balun parameters. The final (discrete) frequency sweep has a resolution of 2 MHz. The resonances and antiresonances seen in Figure 13 are due to the resonant behavior of the balun. The resulting active impedance bandwidth at broadside is from 428 to 1024 MHz, or ~2.1:1.
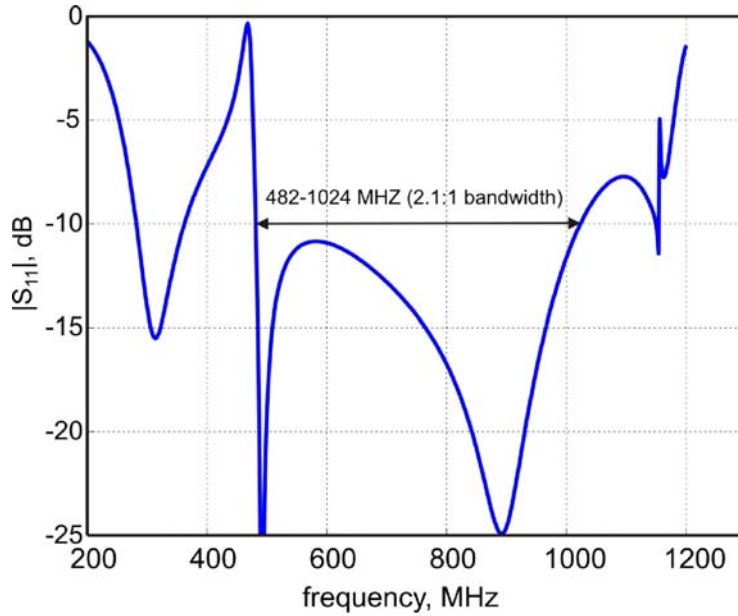

Figure 13. Active (scan) return loss at broadside for the optimized unit cell array with balun.

2.2   Feeding network

We have considered implementing several feeding network configurations for the 8x8 array of ribcage dipoles. As an example, in Figure 14 we show a feeding network that is composed of 2:1, 4:1, and 8:1 equal-split Wilkinson power dividers.
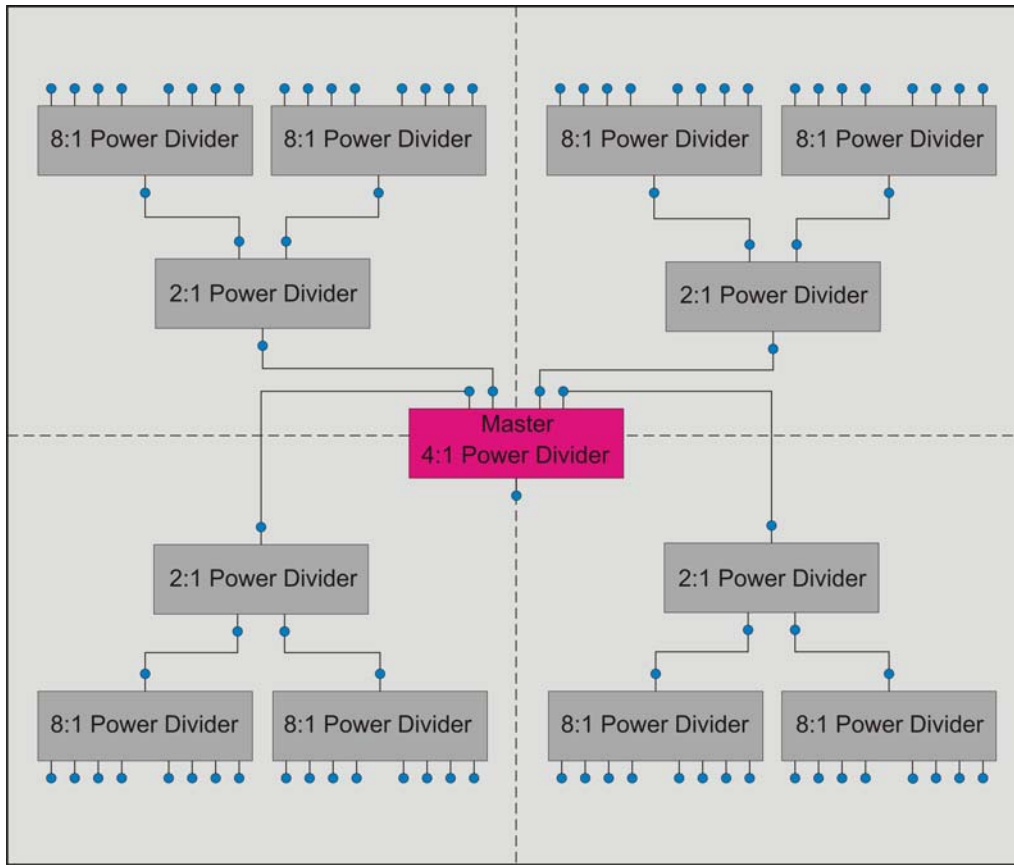
Figure 14. Feeding network for the 8×8 non-scanning array of ribcage dipoles.

We have built custom one-section Wilkinson power dividers (1:2, 1:4, and 1:8) on 125 mil thick FR4. The dividers along with their dimensions are shown in Figure 15. The power dividers have been carefully designed and optimized in Ansoft HFSS for the desired bandwidth (0.5-1.0 GHz).

Smaller sizes may be achieved at the expense of a slightly worse performance.

Figure 16 gives the corresponding S-parameters obtained from Ansoft HFSS simulations, taking into account the loss tangent of FR4. The corresponding hardware prototypes are shown in Figure 17.
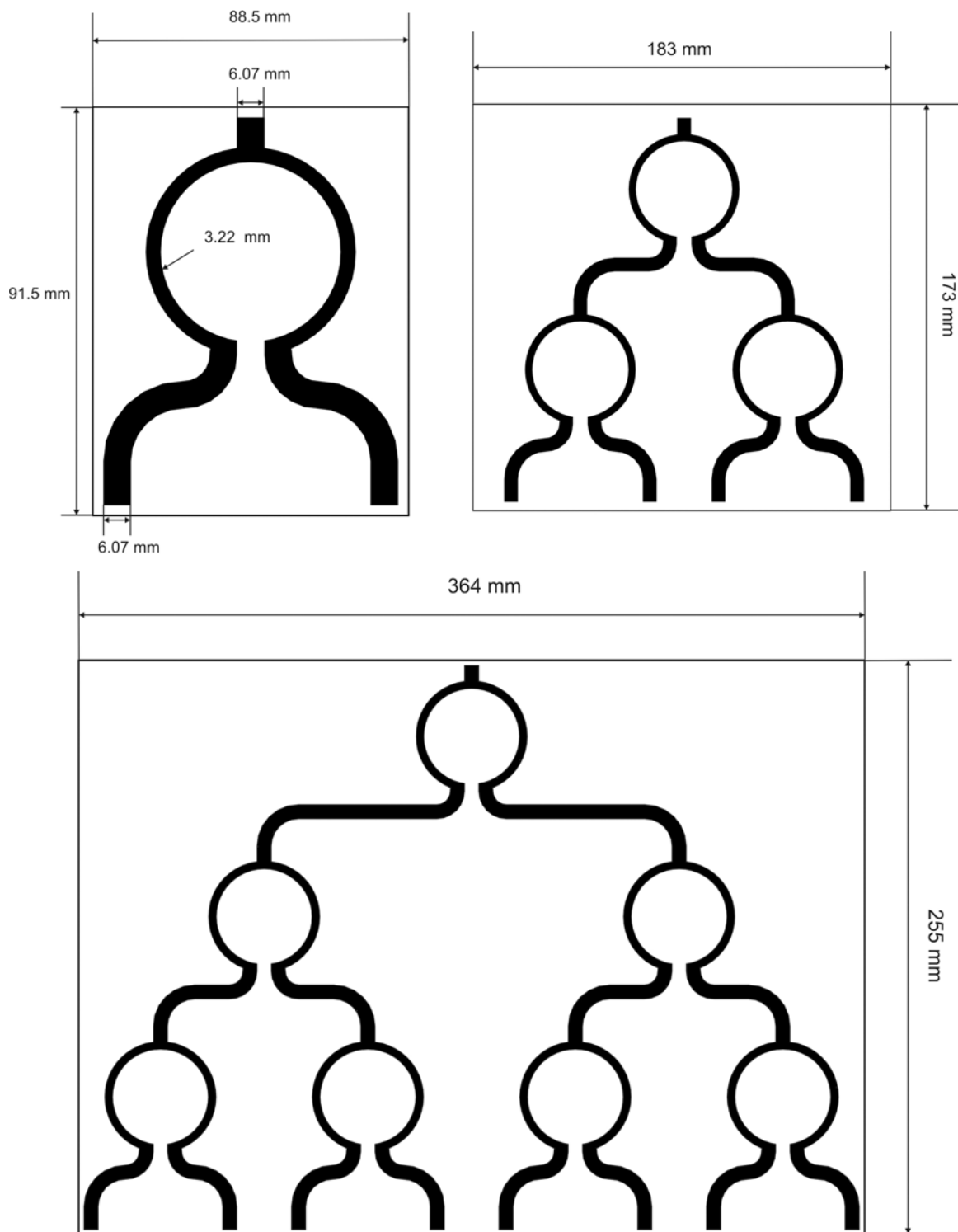
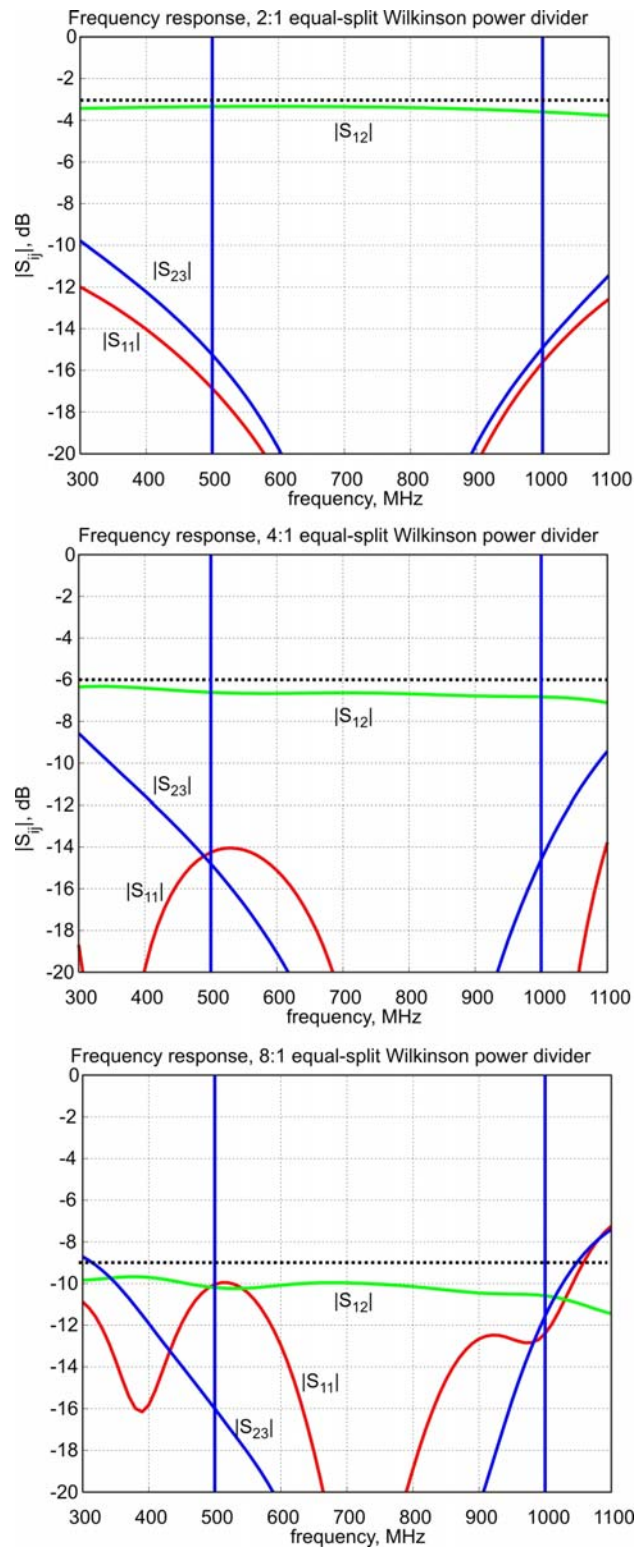Figure 15. Optimized power dividers and dimensions in the 0.5-1.0 GHz band.

Figure 16. S-Parameters of the custom power dividers of Figure 15, over the band from 500 MHz to 1 GHz.
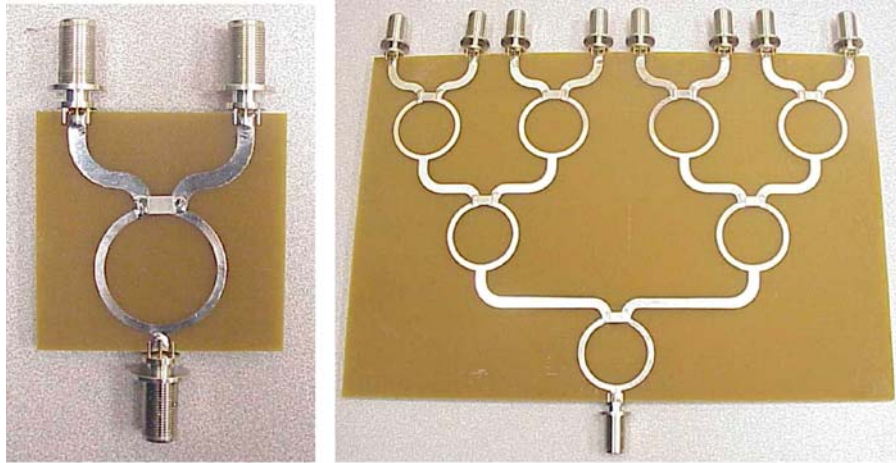
Figure 17. Hardware implementation of the power dividers of Figure 15. The base is 125 mil FR4 with solid ground plane.

The 2:1 dividers have an average loss of 0.4dB over the band, the 4:1 divider has 0.6 dB average loss, and the 8:1 dividers have 1.1dB average loss, as shown in Figure 16. We therefore expect the average loss of the divider network to be 2.1 dB. The cable/connector loss of about 0.4 dB should be added, which gives a total loss in the feeding network of about 2.5 dB. For a smaller 4x4 array, the total loss in the feeding network is estimated at about 1.4 dB using the same power dividers.

2.3   Antenna pattern modeling

2.3.1   Modeling method

Modeling a finite 8×8 elements antenna array of ribcage dipoles with the balun in Ansoft HFSS requires approximately 21 hours to run and more than 70 GB of memory on a 64-bit Windows machine, when a satisfactory accuracy is required. This makes numerical optimization of the array cumbersome; therefore, we resort to an approximate analysis which exploits the symmetries of the array and the array excitation. This procedure reduces the analysis to a single 6×6 subarray. With Ansoft HFSS a 6×6 array of ribcage dipoles simulation takes approximately 6 hours and requires about 20 GB of memory.

We have developed a simple algorithm that allows us to express the total array field pattern for the 8x8 antenna array as a combination of a number of 6x6 sub-arrays of the original array. The procedure is depicted in Figures 18 and 19.

The total array field pattern can be expressed as the superposition of the four array field patterns of Figure 18, when the quadrants Q1, Q2, Q3 andQ4 are excited one at time. Thus, only 16 elements are excited at any one time, while the remaining elements are passive and match-terminated (50Ω).
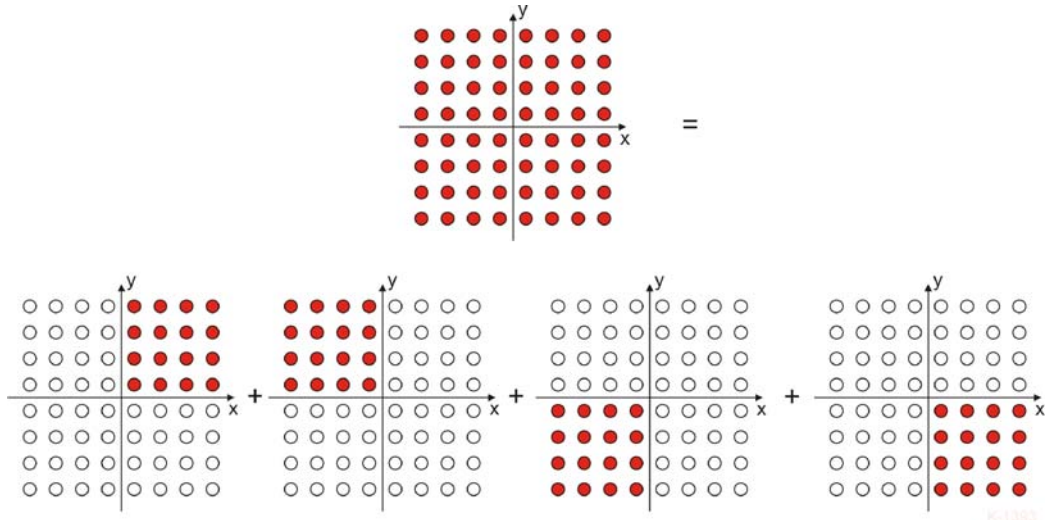
Figure 18. A fully excited array can be viewed as the superposition of four partially excited arrays. The full red circles denote active elements; the empty circles denote passive elements.

We now introduce an approximation. We truncate the passive arrays by removing the two outermost rows and columns, as in Figure 19. This implies that we ignore the scattering off the outermost elements and perturb the diffraction at the weakly illuminated edge of the finite ground plane. However, this should introduce only minor effects on the radiation pattern of the active sub-array, which still is surrounded by two rows and columns of passive elements. The result of this approximation is that we now have four 6x6 arrays, which can be analyzed separately with Ansoft HFSS.
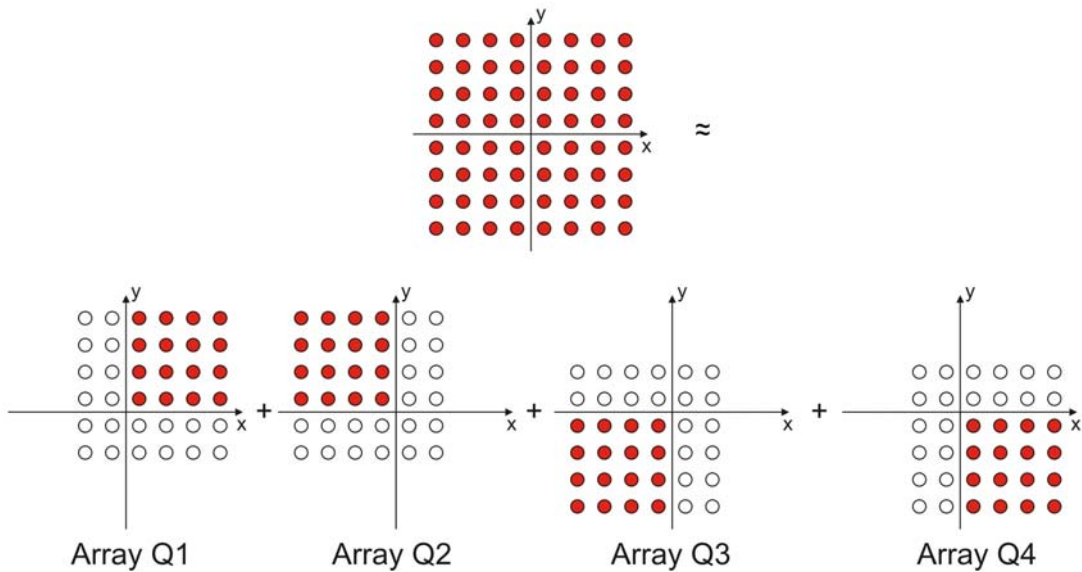

Figure 19. The four 6×6 arrays used to approximate the 8×8 array. The full red circles denote active elements; the empty circles denote passive elements.

480

Further simplification results when the array excitation is symmetric with respect to the x- and y-axes. In this case the excitation of Q3 can be viewed as the negative of the excitation of Q1 rotated 180 deg. about the z-axis. Therefore, the field pattern $\mathbf{E}_{Q3}$ of Q3 is derived from the far field pattern $\mathbf{E}_{Q1}$ of Q1 by

$$\mathbf{E}_{Q3}(\theta,\varphi) = -\mathbf{E}_{Q1}(\theta,\varphi-\pi) \tag{2}$$

where θ and φ are the conventional spherical coordinates. Furthermore, we note that the arrays Q2 and Q4 are the mirror images of Q1 and Q3, respectively, so that in our case where the dipole elements are parallel to the x-axis, it can be shown that

$$E_{Q2,\theta}(\theta,\varphi) = -E_{Q1,\theta}(\theta, \pi-\varphi) \tag{3}$$

$$E_{Q2,\varphi}(\theta,\varphi) = E_{Q1,\varphi}(\theta, \pi-\varphi) \tag{4}$$

$$E_{Q4,\theta}(\theta,\varphi) = E_{Q1,\theta}(\theta, -\varphi) \tag{5}$$

$$E_{Q4,\varphi}(\theta,\varphi) = -E_{Q1,\varphi}(\theta, -\varphi) \tag{6}$$

As a result we obtain a highly accurate representation for the far field of the 8×8 array in terms of the computed far field of a single 6×6 array. The Q1 sub-array is illustrated in Figure 20.

Finally, the array directivity D is obtained by simple pattern integration,

$$D = 4\pi \frac{\left|E_{max}\right|^2}{\iint \left|E(\theta,\varphi)\right|^2 \sin\theta \; d\theta d\varphi} \tag{7}$$

A representative Q1 array pattern at 0.75 GHz is shown in Figure 21. Based on repeated computer runs we estimate the relative error $\Delta P/P_{max} < 0.0003$, where ΔP is the pattern error at any one point and P_{max} is the maximum power pattern value.
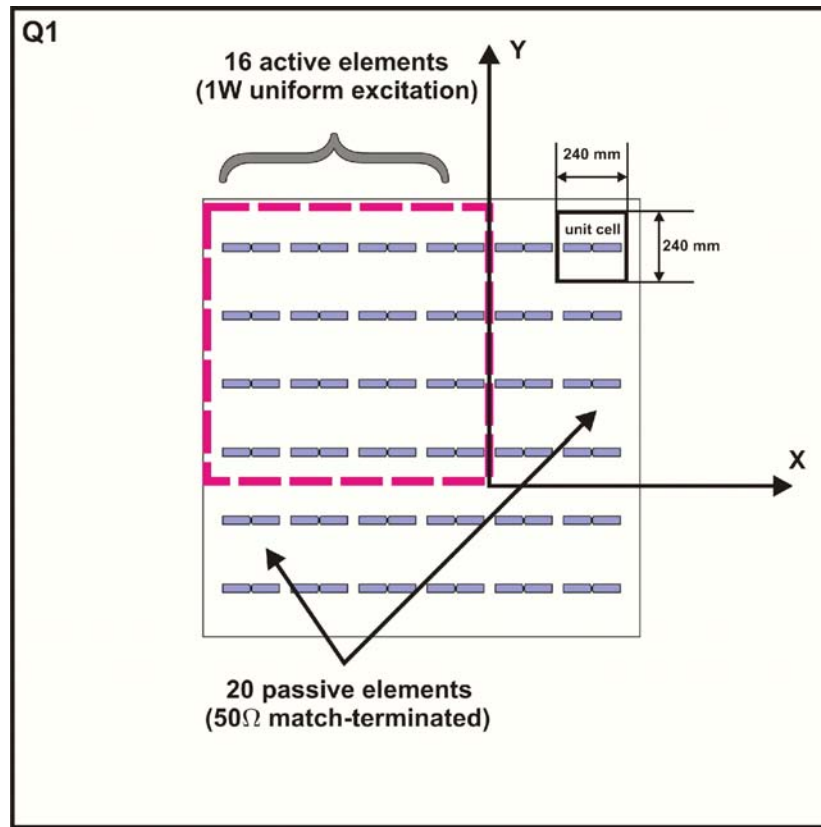
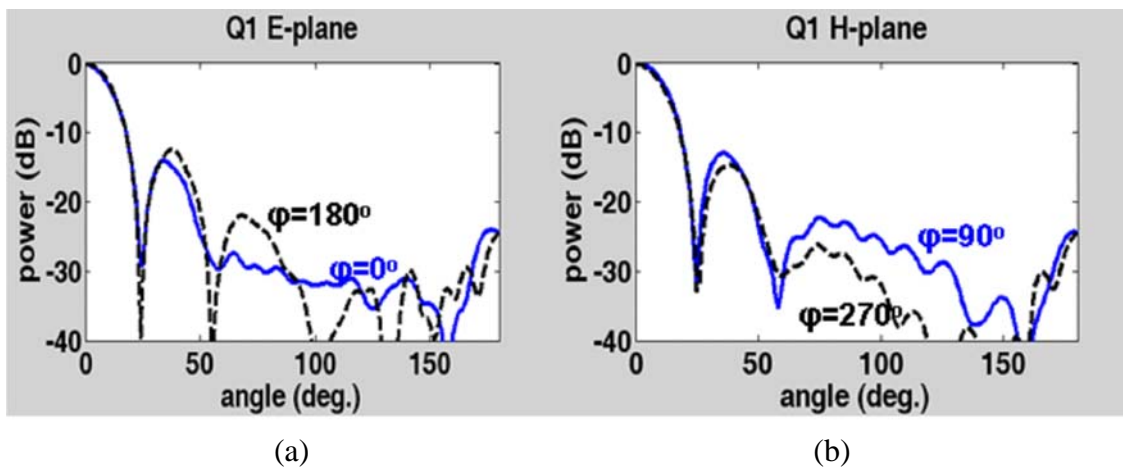Figure 20. Q1 sub-array model, with 16 active elements and 20 passive elements.

(a)   (b)

Figure 21. Q1 array pattern at 750 MHz: a) E-plane, and b) H-plane.

2.3.2 Computational results

The corresponding total array pattern for the 1.92 x 1.92 m antenna array of ribcage dipoles (8×8 array) at 0.75 GHz is shown in Figure 22. The array elements are excited individually with uniform amplitude, i.e. the array model does not include the corporate feed. The gain based on pattern integration is 24.75 dB, which is 0.15 dB higher than the aperture gain 24.6 dB computed from $(4\pi A/\lambda^2)$, where A denotes the aperture area. This is within the numerical accuracy of the computations.
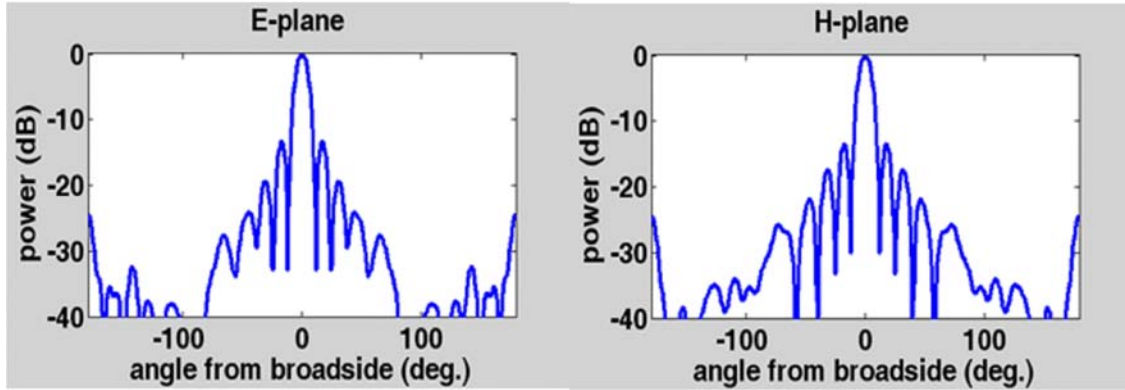
Figure 22. The ribcage dipole 8x8 antenna array pattern at the center frequency of 750 MHz.

Table 8 lists the data on the broadside gain for the 8×8 ribcage array with the 240mm×240mm unit cell at UHF frequencies.

Table. 8. Estimated broadside gain of the 8×8 ribcage array with the 240mm×240mm unit cell at different frequencies. The overall array size is 1920×1920mm.

Frequency	Aperture Gain, $10\log_{10}(4\pi A/\lambda^2)$, dB	Gain Computed from the Composite Array Model (four 6×6 subarrays)	Total Gain (array gain minus net loss in the feeding network - see Section 2.2)
500 MHz	21.1 dB	21.5 dB	19.0 dB
750 MHz	24.6 dB	24.7 dB	22.2 dB
1000 MHz	27.1 dB	26.4 dB	23.9 dB

3.   Conclusions

The present paper has introduced and discussed the use of the wideband ribcage dipole as a single radiator and in a small array environment. The ribcage dipole combines the advantages of the planar blade dipole (wide impedance bandwidth) and of the droopy blade dipole (wide gain bandwidth and smaller gain variation with frequency).

As an isolated element over a ground plane, the ribcage dipole may have an impedance bandwidth up to 3.2:1 while maintaining better pattern stability than the planar blade dipole.

The unit-cell (infinite array) impedance bandwidth of the ribcage dipole with the tapered microstrip balun was 2.1:1 at broadside.

As an example, we have constructed and simulated the performance of a 500 MHz-1GHz 8×8 non-scanning array of ribcage dipoles of overall size 1.920×1.920m. The bandwidth of the array was 2:1. The gain of the finite 8×8 array was modeled using a 6×6 sub-array model. The broadside gain, taking into account the computed loss in the power splitter network, varies from 19 dB at the lover band edge to 23.9 dB at the upper band edge.

A small array of ribcage dipoles may be used for directed energy applications as well as for digital TV reception in the UHF sub-band from 400 to 900 MHz. In the latter case, the present results shall be recomputed with matching impedance of 75Ω.

4.   Acknowledgements

5.   References

[1]. Jeong Il Kim Joung Myoun Kim, Young Joong Yoon, and Cheol Sig Pyo, "Wideband printed fat dipole fed by tapered microstrip balun," *2003 IEEE AP-S International Symposium*, vol. 3, June 2003, pp. 32 – 35.
[2]. M. I. Borgford and A. K. Kong, "Design of a very broadband dipole," *1988 IEEE AP-S International Symposium*, vol. 2, June 1988, pp. 812 – 815.
[3]. A. Kerkhoff, and S. Ellingson, "A wideband planar dipole antenna for use in the long wavelength demonstrator array (LWDA)," *IEEE AP-S International Symposium*, July 2005, vol. 1B, pp. 553-556.

[4]. S. Ellingson and A. Kerkhoff, "Comparison of two candidate elements for a 30-90 MHz radio telescope array," *IEEE AP-S International Symposium*, July 2005, vol. 1A, pp. 590-593.

[5]. E. B. Rodal, M. C. Detro, D. R. Gildea, and J. M. Janky, *Antenna with Curved Dipole Elements*, US Patent # 5,173,715, Dec. 22nd, 1992.

[6]. P. G. Elliot, "*Folded cross grid dipole antenna*," U.S. Patent #5796372, Aug. 18, 1998.

[7]. Seong-Youp Suh, W. L. Stutzman, and W. A. Davis, "Low-profile, dual-polarized broadband antennas," *2003 IEEE Antennas and Propagation Society International Symposium*, vol. 2, June 2003, pp. 256 – 259.

[8]. Seong-Youp Suh, W. Stutzman, A. Davis, A. Waltho, K. Skeba, and J. Schiffer, "A novel low-profile, dual-polarization, multi-band base-station antenna element – the Fourpoint Antenna," *2004 IEEE 60th Vehicular Technology Conference*, 2004. VTC2004-Fall, vol. 1, 26-29 Sept. 2004, pp. 225 – 229.

[9]. Seong-Youp Suh, W. Stutzman, W. Davis, A. Waltho, K. Skeba, and J. Schiffer, "Bandwidth improvement for crossed-dipole type antennas using a tuning plate," *2005 IEEE Antennas and Propagation Society International Symposium*, vol. 2A, July 2005, pp. 487 – 490.

[10]. L. Akhoondzadeh-Asl, D. J. Kern, P.S. Hall, and D. H. Werner, "Wideband Dipoles on Electromagnetic Bandgap Ground Planes", *IEEE Trans. Antennas Propagation*, vol. 55, no 9, Sept. 2007, pp. 2426-2434.

[11]. S. Best, and D. Hanna, "Design of a broadband dipole in close proximity to an EBG ground plane," *IEEE Antennas and Propagation Magazine*, vol. 50, no. 6, Dec. 2008, pp. 52 – 64.

[12]. J. J. Lee, S. Livingston, and R. Koenig, "Performance of a wideband (3-14 GHz) dual-pol array," *IEEE AP-S International Symposium*, June 2004, vol. 2, pp. 551-554.

[13]. J. J. Lee, S. Livingstone, and R. Koenig, "A low-profile wide-band (5:1) dual-pol array," *IEEE Antennas and Wireless Propagation Letter*, vol. 2, 2003, pp. 46-49.

[14]. P. Cerny and M. Mazanek, "Optimized Ultra Wideband Dipole Antenna", *18th Int. Conf. on Applied Electromagnetics and Communications*, 2005, Oct. 2005, pp. 1-4.

[15]. S. R. Best, "A Study of the Performance Properties of Small Antennas," *Antenna Applications Sym.*, Monticello, IL, 2007, pp. 193-219.

[16]. M. Goettl and R. Kinker, "*Dual-polarized dipole antenna element*," U.S. Patent #6940465, Sep. 6, 2005.

[17]. P. G. Elliot, "*Stacked crossed grid dipole antenna array element*," U.S. Patent #5418544, May 23, 1995.

[18]. P. G. Elliot, "Octave Bandwidth Microwave Scanning Array", *1995 Antenna Applications Symposium Proc.*, Monticello, IL, Sep. 1995, 19 p.

[19]. P. G. Elliot and A. E. Rzhanov, "Octave bandwidth printed circuit phased array element," *2006 IEEE Antennas and Propagation Society International Symposium*, July 2006, pp. 3743 – 3745.

[20]. S. Makarov and F. Scire' Scappuzzo, "Multipath rejection by virtue of a choke ring for a broadband droopy turnstile antenna," *2007 Antenna Applications Symposium Proc.*, Monticello, IL, Sep. 2007, pp. 467-507.

[21]. B. Kaswarra, W. Quddus, F. Scire' Scappuzzo, and S. Makarov, " Circular Polarization Bandwidth for a Bowtie Turnstile Over a Ground Plane," *Proc. IEEE AP-S International Symposium on Antennas and Propagation*, Honolulu, June 2007, pp. 3544-3547.

[22]. S. Makarov, A. Puzella, and Vishwanath Iyer, "Scan impedance for an infinite dipole array: accurate theory model compared to numerical software," *IEEE APS Magazine,* vol. 50, no. 6, Dec. 2008, pp. 132-149.

[23]. S. Makarov and A. Puzella, "Scan impedance for an infinite dipole array: Hansen's formulas vs. Ansoft HFSS simulations," *IEEE APS Magazine*, vol. 49, no. 4, Aug. 2007, pp. 143-156.

RECENT ADVANCES AND APPLICATIONS OF THE CONTINUOUS TRANSVERSE STUB (CTS) ARRAY ANTENNA

William Milroy
ThinKom Solutions, Inc.
20000 Mariner Ave. Torrance, CA 90503 (USA)
BillM@thin-kom.com

Abstract: Originally invented in the early 1990's, the "Continuous Transverse Stub (CTS)" array antenna has more recently enjoyed increased adoption in a broad range of Microwave and Millimeter-Wave Radar and Communication applications. These products embody both staring and scanning (phased-array) extensions of the original technology, improved and adapted for the challenging demands of various fixed, ground-mobile, and aeronautical users and platforms. Utilizing over-moded parallel-plate (TEm) transmission line as both its feed and radiator basis, this low-profile planar array technology exhibits a number of favorable properties in terms of antenna efficiency, operating bandwidth, sidelobe control, polarization diversity, active scan impedance, and overall tolerance insensitivity. This paper will briefly describe and quantify the technical basis and design properties of the CTS array by way of specific examples including Commercial and Government low-profile antenna products for Radar, Point-to-Point (PTP) communication, Man-Portable SATCOM, and high data rate Satellite-on-the-Move (SOTM) applications.

Introduction

Since its original invention in 1991 [1], the Continuous Transverse Stub (CTS) array has been successfully demonstrated in over 50 separate embodiments, supporting specific applications in operating frequencies ranging from C-band (3 GHz) through W-band (94 GHz) and with continuous bandwidths approaching two octaves. Continuously improved and evolved since its first inception, the CTS antenna together with its variant, the Variation Inclination Continuous Transverse Stub (VICTS) array, now enjoys broad application in a wide variety of applications. To date, over 65 US and Foreign patents now cover the technology and this portfolio continues to grow. Previous publications [2], [3] have provided general background to the technology and others [4], [5] have provided details of relevant designs. This paper will strive to provide an update on the latest improvements in the technology as well as specific examples of current representative applications.

1.0 The CTS Array – Theory of Operation

The CTS array differs markedly from other planar array and Electronically-Scanned Array (ESA) implementations in terms of architecture, radiator realization, coupling

mechanism(s), and transmission-line properties. Figure 1.0-1 illustrates the canonical architecture of a typical CTS antenna, realized as an array of broad *continuous transverse* radiating *stubs*, finite in height, extending from the upper conductive plate of an open parallel-plate transmission-line structure, and internally excited by a (generic) linear source. These transverse-oriented stubs interrupt longitudinal current components within the parallel-plate structure and in doing so, efficiently couple and radiate propagating energy from the parallel-plate structure into free-space as a linearly-polarized wave. This simple architecture allows for a (typically) complex two-dimensional planar array to be instead realized as an "extrusion" of a one-dimensional (constant cross-section) geometry. This has the favorable effect of replacing a conventional "$NxN=N^2$" element structure (of discrete radiators, couplers, etc.) with a less complex "monolithic" array comprised of "N" integrated coupler/radiator features. The close proximity and parallel orientation of the radiating stubs typically equate to unusually strong (and interestingly, beneficial) mutual coupling, therefore requiring the rigorous simulation of the effective active impedance of each stub exploiting the periodicity of the structure.
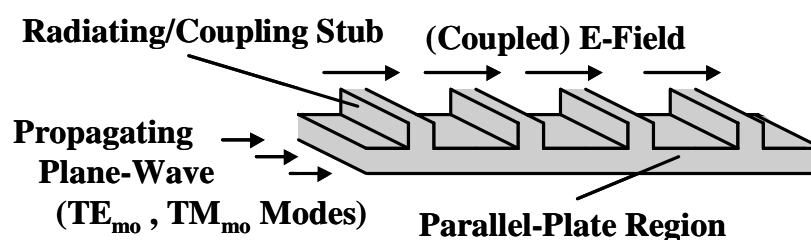

Figure 1.0-1. Basic CTS Radiator /Coupler Configuration (Series-Fed Architecture)

The simple "tee" cross-section of the integrated CTS coupler/radiator forms an inherently low-"Q" (non-resonant) element which exhibits significant advantages (as compared to resonant slot or patch radiators) in terms of wide-angle scanning capability, polarization purity, bandwidth, and dimensional insensitivity. As an additional benefit, the utilization of a simple parallel-plate cross-section as the basis for the transmission-line structure fully exploits the low dissipative loss, dimensional insensitivity, wide operating bandwidth, and low-dispersion typical of propagation within an air- or dielectrically-filled parallel-plate transmission-line structure. In many applications, these qualities contrast favorably in comparison to waveguide, microstrip, and strip-line transmission-line structures with respect to these attributes.

1.1 CTS Stub Radiator

Due to its long "continuous" nature, the CTS radiator can be accurately considered as a filamentary magnetic current source with a minimum of fringing contributions and with a commensurately high-purity (linear) polarization characteristic.   For near-broadside operation, the active impedance of the radiator is closely modeled as an abrupt parallel-plate step transition between the individual dielectrically-filled stub-radiator of parallel-plate spacing (width) "b" and the air-filled parallel-plate region of spacing "s," synonymous, via Perfect-Electric-Conductor (PEC) image-planes corresponding to the stub-to-stub inter-element spacing.   In addition, the (typical) recessed nature of the ground-plane region spanning the individual radiating stubs forms an equivalent "choked" series-inductive region which, from an equivalent-circuit standpoint, is series-connected with the radiating stub surface and can (and does) modify the active impedance of the stub as compared to a flush-mounted ground-plane.   Fringing capacitance contributions at both the stub-to-freespace interface and stub-to-stub "choke" regions are added for improved fidelity in an equivalent-circuit model.   The active impedance of the stub (referenced to its radiating surface) is generally on the open-circuit region of the Smith Chart with the real component predominating (i.e. generally non-reactive,) meaning that the resultant "Q" of the stub radiator is beneficially quite low (making the non-resonant stub inherently broadband and robust with respect to tolerances.)

For non-broadside and scanned applications, a Floquet-based mode-matching solution [6] provides accurate (infinite-array) active-impedance modeling over frequency, E-plane, and H-plane scan.   Because of the continuous nature of the stub radiator (as compared to a conventional 2-D radiator lattice) H-plane scanning (in the plane of the radiating stub) is pseudo-optical in nature with no local "blind-zone" phenomenology. E-plane scan characteristics, owing to the periodic nature of the stubs in this plane, are more conventional in nature with traditional grating-lobe driven constraints on inter-element spacing and operating frequency.

1.2 Parallel-Plate-to-Radiating Stub Coupling

Internal coupling from the parallel-plate transmission-line region to the radiating stub is controlled (to first-order) by the relative width of the individual stub relative to the height of the parallel-plate base structure. Similar to the radiator-itself, this internal coupling structure is generally non-resonant in nature, modeling (to zeroth-order) as a simple resistive voltage-divider.) For higher-fidelity, an equivalent-circuit model for the 3-port junction, employing fringing capacitance and series-reactance terms, may be employed.   It is interesting to note that the 3-port scattering properties of the isolated coupling junction are completely independent of any E-plane scanning and that the H-plane scan-dependence of the junction is well-behaved (owing to the continuous nature of the junction in that scan plane, internal to the parallel-plate region.)

1.3 Excitation (and Scan) Control

For series-fed CTS arrays as previously described, the control of amplitude coupling (and resultant aperture excitation) in the E-plane is controlled primarily through selective control of the radiating stub width and/or parallel-plate base height. In series-fed traveling-wave implementations, where large dynamic coupling ranges are required in order to minimize power-to-the-load (residual uncoupled power) and to provide for low antenna sidelobe tapers, practical coupling ranges between -2 dB and -30 dB can be readily achieved. Similarly, for series-fed standing-wave implementations, this same broad coupling range allows for the efficient realization of both extremely short (2 element) and extremely long (50+ element) feeds (CTS arrays.)

Excitation in the H-plane of the array is set primarily by the excitation of the line-feed "launcher" into the parallel-plate region. A wide variety of continuous and discrete, fixed and scanning, line-feed implementations have been successfully integrated with the CTS array for this purpose. Generically, these feeds excite a finite number of $TE_{m,o}$ or $TM_{m,o}$ modes (dependent on the width and edge-wall termination of the parallel-plate region). Some examples include: a sectoral (H-plane) horn; an electro-mechanical scanning line-feed; and an N-element linear phased array of Transmit/Receive (TR) modules. For cases in which an electronic scanning line-source is employed, the CTS array faithfully transforms the scanned *linear* phase-front emanating from the line-feed (typically a mode-limited finite Fourier Series representation of the imposed aperture taper and inclined phase-front) into a scanned plane-wave, oriented in the *H-plane* and radiating at an inclined angle with respect to the surface of the CTS array. Other potential scanning implementations include: *Digital Beam Forming* (DBF), *Rotman Lens, Butler Matrix,* and *Photonically-Controlled* scanning line-feeds. Figure 1.3-1 illustrates the applicable geometry for H-plane scanning typical with the CTS array.
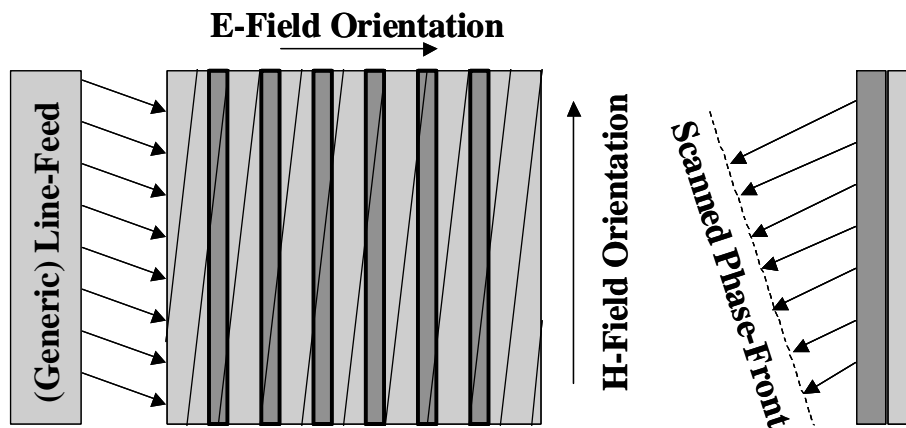

Figure 1.3-1. (Scanning) Line-Feed Excitation of the Parallel-Plate Region

1.4 Parallel-Fed Variants

A useful variant of the series-fed CTS array is one that is parallel-fed (i.e. true-time-delay to every radiator.) Such implementations [7] enjoy the previously described radiator active impedance, scan capability, and wide bandwidth benefits together with the inherent low-loss, dispersion-free, tolerance insensitive, wideband attributes of the parallel-plate transmission-line media, in a structure capable of support much higher continuous/instantaneous bandwidths beyond that which is otherwise achievable in conventional series-fed (standing- or traveling-wave fed) architectures. Employing this method, CTS antennas capable of supporting up to two-octaves (4:1) of continuous bandwidth have been successfully demonstrated [8], [9]. Figure 1.4-1 illustrates an early prototype example of a Parallel-fed variant of the CTS array. Note the integrated (parallel-plate) corporate-feed structure clearly visible in the left-hand side of the array.
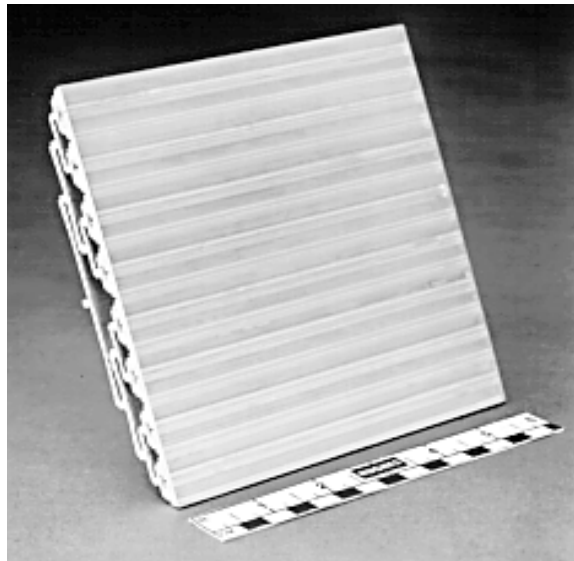

Figure 1.4-1. Parallel-Fed Wideband CTS Array (5 to 20 GHz)

1.5 Dual-Polarized Variants

Dual-polarized variants of the single-polarized CTS are achieved by exploiting the unique "open" internal electromagnetic architecture of the basic (single-polarized) design through the simultaneous launching, distribution, and subsequent radiation of two orthogonal plane-wave (finite-mode) excitations sharing the common parallel-plate region. As described previously, in terms of efficiency and performance as a radiator, the parallel-plate based radiating "stub" behaves (and models) similarly to a linear

filamentary magnetic current source and therefore exhibits excellent frequency-independent polarization purity (axial ratio) as compared to the band-limited (mode- and fringing-limited) performance of typical slot-, patch-, and/or waveguide-based radiator alternatives. Similarly, the Dual-Polarized variant of the CTS accurately models as two orthogonal arrays of filamentary magnetic current sources, with inherently high isolation and polarization purity between the orthogonal polarization components. It is important to note that the ability to launch, support, (and couple) two simultaneous orthogonal modes within a single common parallel-plate region is strictly contingent on the absence of any interconnecting features between opposing parallel-plate surfaces which would otherwise interrupt/corrupt the x- and y-propagating modes bounded between them.

Figure 1.5-1 illustrates a representative dual-polarized CTS array, suitable for Direct Broadcast Satellite (DBS) reception over the 12.20 to 12.70 GHz frequency band. This antenna is fabricated exclusively utilizing low-cost commercially-available materials (aluminum, low-density foam, and plastic) and processes (stamping, extruding, and injection molding), requiring no supplemental conductive bonding, brazing, gasketing, or interconnects of any kind. The "checkerboard" pattern formed by the orthogonal dual-polarized radiating stubs are clearly visible (in white) on the aperture surface.

Figure 1.5-1. Dual-Polarized CTS Array (Ku-band)

1.6 Dual-Band Variants

For applications requiring simultaneous dual-polarized operation over very broad and/or multiple frequency bandwidths (such as FSS VSAT antennas), the parallel-plate geometry of the CTS array may be further exploited to support this multi-functionality while preserving the simple low-cost attributes of the CTS structure. Series-fed CTS arrays support dual-band operation through the incorporation of passive dichroic parallel-plate features which enable distinct primary and secondary bands, thereby providing for two co-boresighted broadside beams at two distinct offset frequencies. Alternatively, in the case of dual-polarized/dual-band series-fed CTS arrays, the interelement spacing of the radiating elements for each of the two orthogonal polarizations may be staggered in order to support distinct operating frequencies. In the case of parallel-fed CTS arrays, dichroic (non-contacting) coupling features within the shared parallel-plate region provide the requisite corporate feed components (E-plane bends and reactive 3-port tees) to support dual-band operation [10].

A CTS antenna exhibiting the aforementioned broadband dual-polarization capability was successfully designed, fabricated, and demonstrated under funding from the United States Air Force (AFRL). Capable of supporting both the 17.7 to 21.2 GHz receive and 43.5 to 45.5 GHz transmit frequency bands simultaneously with dual-polarization (RHCP and LHCP) in both bands, this 3" x 3" x 0.7" aperture exhibited a minimum cross-polarization isolation of 22 dB (Axial Ratio < 1.4 dB) in a low-cost low-profile multi-layer form factor requiring no interconnects or RF critical joints. Figure 1.6-1 illustrates this dual-polarized/dual-band CTS aperture in subarray form.
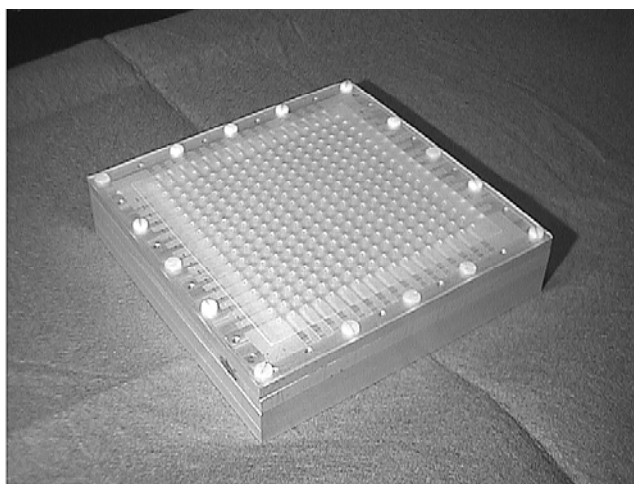

Figure 1.6-1. Dual-Polarized/Dual-Band (K/Q) CTS Array

1.7 Cylindrical-Conformal Variants

In some specialized applications, it is highly desired to provide high-gain antenna performance in a non-planar conformal form-factor. Exploiting the fact that the local interelement spacing of the individual stub radiators within a series-fed CTS array may be freely varied over a relatively broad range, it is then possible to use this variation to deterministically compensate for progressive phase errors created by a non-planar aperture shape. In the case of a cylindrical shape, the induced phase error is quadratic, leading to a generally linear variation in interelement spacing in order to compensate for it. Figure 1.7-1 shows a center-fed series-fed cylindrical CTS array employing such a technique, wherein the interelement spacing (and stub widths) at the edges of the array differ significantly than those at the center of the antenna.
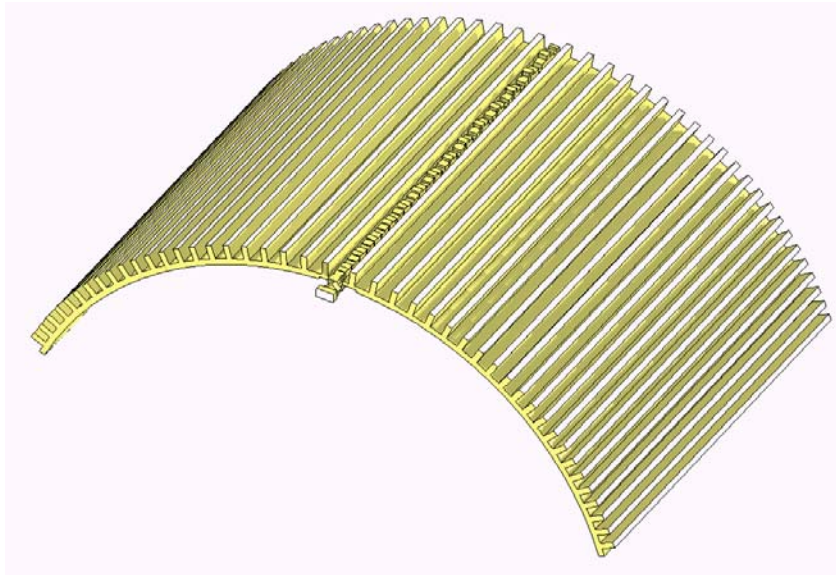

Figure 1.7-1. High-Gain Cylindrical CTS Array (with Azimuth Plane Pattern)

2.0 The Variable Inclination Continuous Transverse Stub (VICTS)

As a direct extrapolation of the basic CTS array, the Variable Inclination Continuous Transverse Stub (VICTS) array [11] employs a novel two-dimensional scan mechanism which is 100% mechanical, involving the simple rotation (common and differential) of two coplanar plates, one (upper) comprised of a one-dimensional lattice of continuous radiating stubs and the second (lower) forming the base of the parallel-plate region formed and bounded between the non-contacting (RF choked) upper and lower plates. Since all wave propagation within the VICTS occurs in air, ohmic loss is minimized to

the greatest extent possible, leading to ohmic efficiencies greater than 85% with overall efficiencies greater than 65% percent. Because of this unusually high efficiency and well-behaved scan impedance, even at extreme scan angles, the VICTS array typically requires 30% to 75% less area than a conventional phased array in order to meet the same level of performance.
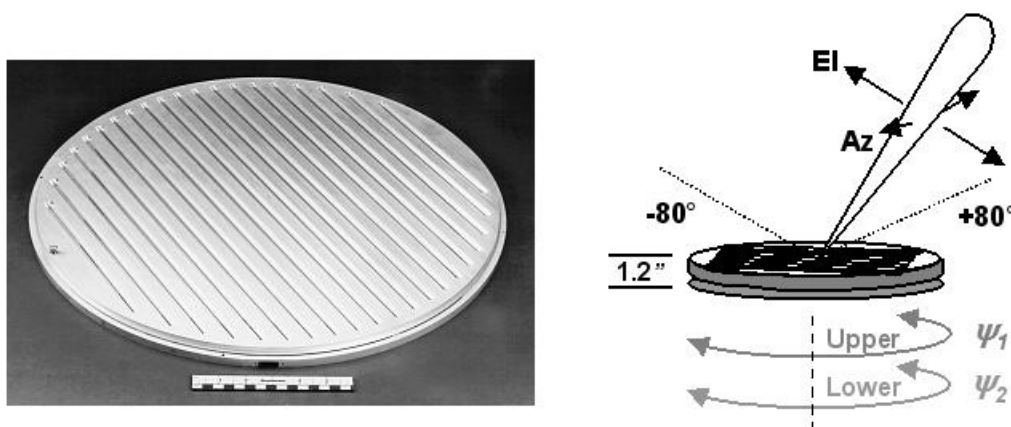

Figure 2.0-1. VICTS Array Scan Geometry

The (instantaneous) bandwidth properties of the VICTS may be further enhanced by sub-division of the aperture into subarrays in a manner as depicted in Figure 2.0-2. Individual subarrays are interconnected via a (passive waveguide) true-time-delay network whose individual line-lengths and dispersion properties are carefully chosen in order to provide a frequency-independent (array-factor) beam-pointing characteristic at specific scan angle(s). In this way, the frequency-stabilized array-factor dominates over the frequency-dependent beam position of the individual subarrays, thereby providing the desired enhancement in terms of instantaneous bandwidth (beam stability over frequency.) This feeding technique allows the VICTS array to meet the wider instantaneous bandwidths as required for Synthetic Aperture Radar (SAR) applications and in SATCOM applications employing hopped or spread-spectrum waveforms. It is important to note that the described sub-division of the aperture is done at the subarray feed level with all subarrays sharing a common (generally non-partitioned) parallel-plate region and a common (rotating) stub aperture (i.e. the subarray implementation adds very little to the complexity or recurring cost of the overall product.)
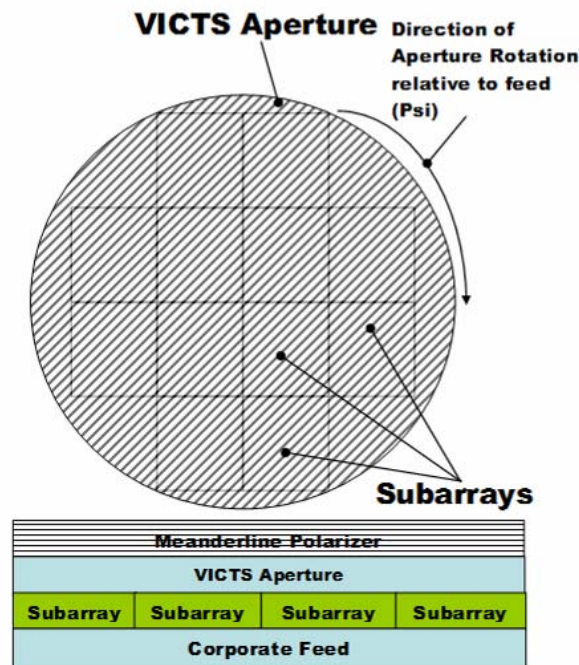
Figure 2.0-2. Subarray Feeding (Modularization) of the VICTS Array

2.1 VICTS Radiator Geometry – Scan and Active Impedance Characteristics

As the VICTS array is generally designed for scanning (rather than fixed broadside) applications, a Floquet-based [6] or similar model is generally utilized in order to accurately characterize the variation in active impedance (complex reflection coefficient referenced at the upper-most surface of the radiating stub) over arbitrary scan angle. In practice, for a given operating frequency, stub interelement spacing, effective dielectric constant in the parallel-plate region, and (second-order) stub radiator reactive loading, there is a deterministic relationship between the relative mechanical rotation angle of the stub radiating aperture (relative to the feeding base) and the resultant direction in spherical coordinates (theta, phi) of the VICTS antenna's scanned beam. This is generally a curved characteristic as measured in the reference plane of the radiating aperture with primary movement in the theta-direction (primarily H-plane oriented) and secondary movement in the phi-plane (primarily E-plane oriented.) This means that the primary scan mechanism for the VICTS array is pseudo-optical in nature, in that scanning is primarily in the plane of the continuous radiating stubs – and not in the orthogonal "array" plane. This phenomenology results in several advantages. One, scan angle in the (primary) H-plane of the VICTS aperture is (to first-order) independent of frequency meaning that the VICTS array naturally supports a wider instantaneous bandwidth as compared to a scanned array composed of discrete periodically-spaced radiating elements. Second, because the scanning profile (the curved continuous path in theta-/phi-space) is both deterministic and compound in

496

nature (composed of both E- and H-plane components), the active impedance of the VICTS radiating stub is unusually well-behaved over the entire scan volume with no blind-zones and very stable (low) reflection coefficient magnitudes even at extreme scan angles (approaching end-fire.)

2.2 Grating Lobe Management

The radiator (stub) interelement spacing in VICTS arrays in terms of wavelength, is generally large in comparison to those employed in conventional phased-arrays supporting large scan volumes. This is necessitated by the typical requirement to support broadside operation, which necessarily requires the stubs in the traveling-wave (series) fed aperture to be spaced at roughly (λo/$\varepsilon_r^{0.5}$) which would appear (upon initial examination) to be far too loose to support a broad grating-lobe-free scan volume. This would certainly be the case if the VICTS array were required to support arbitrarily large scan angles in the E-plane (orthogonal to the radiating stubs), but this is fortunately not the case. To the contrary, as previously mentioned, the primary scan plane for the VICTS array is in the H-plane, the plane in which grating lobe phenomenology is completely absent due to the continuous nature of the radiating stubs. Hence, the relatively loose interelement spacing employed in the E-plane of the VICTS array does not limit the array's capability to support large grating-lobe-free scan volumes.

2.3 Excitation Control

Conventional CTS arrays employ variation in individual radiating stub widths (and position) in order to provide desired amplitude (and phase) aperture excitations in support of efficient E-plane low-sidelobe operation. This method would be problematic in the case of a VICTS array, since the relative locations of the coupling/radiating stubs vary widely as the radiating aperture is rotated relative to the feed/base. Instead, in the case of the VICTS array, all radiating stubs are stipulated to be strictly identical in terms of cross-section and instead the base height (the parallel-plate spacing in the interconnecting transmission-line structure bounded by the upper conducting surface of the base/feed and the lower conducting surface of the rotating aperture) is varied in order to provide for the requisite range in stub coupling values. In the orthogonal H-plane, aperture excitation in the VICTS array is controlled by the characteristics of the line-feed launching into the parallel-plate region, in a manner identical to that employed in conventional CTS arrays.

2.4 Polarization Options

The polarization of radiating stubs (equivalent filamentary magnetic current sources) employed in both CTS and VICTS arrays is inherently linear (with high polarization purity). In the case of CTS arrays, the addition of orthogonal radiating stub elements

provides complete polarization diversity allowing for fixed-linear, tracking-linear, or circular polarization through appropriate combining of the two orthogonal components. In the case of the VICTS array, owing to its requisite traveling-wave (series) fed phenomenology in support of its scanning mechanism, the addition of a orthogonal set of radiators is not practical. The VICTS array therefore generally relies on the use of an integrated polarizer in most applications. For those applications requiring support of circular-polarization, a novel variant of the meanderline polarizer is employed in order to support switchable RHCP and/or LHCP. This particular polarizer design employs a "detuning" method plus an additional non-conventional trace layer in order to accommodate conformal near-field mounting of the polarizer (mounted well within the evanescent region of the loosely-spaced radiating stubs) and to support low axial-ratio (high circular polarization purity) performance out to extreme scan angles (in excess of 75 degrees from broadside.) For those applications requiring switchable and/or tracking-linear polarization, a novel compact "twisting-grid" polarizer (customized to the aforementioned near-field/evanescent region immediately above the aperture) is generally employed.

Figure 2.0-3 illustrates an exploded diagram for a typical VICTS implementation showing the relative locations and orientation of the polarizer, aperture, top feed, and corporate feed components.
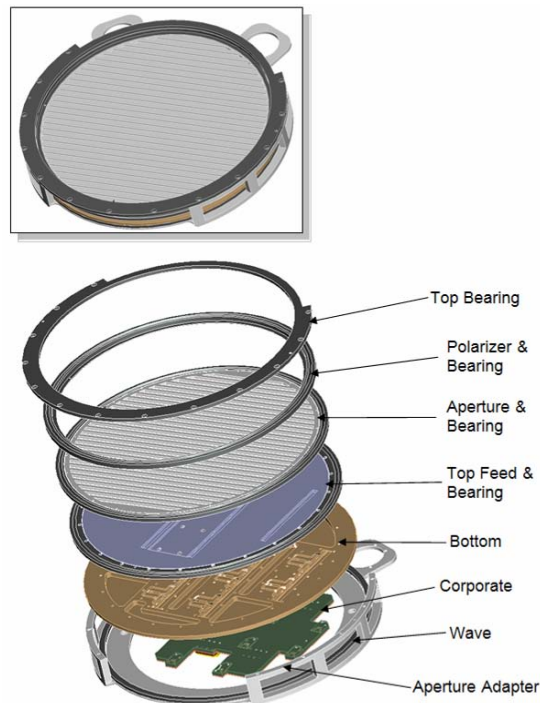

Figure 2.0-3. Exploded Diagram – Typical VICTS Assembly

3.0 Representative Applications of the CTS and VICTS Arrays

The "Continuous Transverse Stub (CTS)" array and its related variant, the "Variable Inclination Continuous Transverse Stub (VICTS)" array, have enjoyed increasing adoption in a broad range of Microwave and Millimeter-Wave Radar and Communication applications. These include Commercial and Government low-profile antenna products for Radar, Point-to-Point (PTP) communication, Man-Portable SATCOM, and high data rate Satellite-on-the-Move (SOTM) applications. The following will describe representative examples of these applications.

3.1 Fixed Terrestrial: Point-to-Point (11, 15, 23, 26, 38, 70/80 GHz)

Since 1998, the employees of ThinKom have successfully fielded 40,000 commercial MMW (23, 26, and 38 GHz) Point-to-Point antennas in collaboration with and support of Harris Corporation's Microstar® MMW PTP Radio products. Figure 3.1-1 illustrates the 38 GHz version of this product together with an exploded diagram of it's assembly and Figure 3.1-2 illustrates the measured (very low sidelobe) pattern and high efficiency gain metrics (80% aperture efficiency, 65% total efficiency) for the 38 GHz CTS antenna product. This is a parallel-fed CTS array employing (non-precision) aluminum extrusions, plated injection-molded plastic feed assemblies, and a silk-screened (Ag conductive paint) 45 degree twist polarizer which provides for vertically- and horizontally-oriented linear polarization, despite the standard diamond-orientation mounting of the antenna (which would otherwise provide slant 45 degree orientation.)

As compared to the shrouded-parabolic dish that it replaces, this antenna is 50% broader in bandwidth, 20% higher in efficiency, 6 to 15 dB lower in sidelobes, 70% lower in profile, 40% lighter in weight, and significantly lower in manufacturing cost. These antennas meet all applicable international regulatory specifications (for highest performance categories) including FCC, BAPT, MPT, and ETSI, replacing larger parabolic dishes for the same applications. For example, an 18" x 18" 11 GHz CTS Array exhibits the same sidelobe mask contour (critical for adjacent site isolation) as that of a much larger 48"D parabolic dish.

Similarly architected versions of the 23, 26, and 38 GHz CTS Arrays have been successfully demonstrated at 11, 15, and 70/80 GHz in support of evolving domestic and international Point-to-Point Microwave Radio markets.

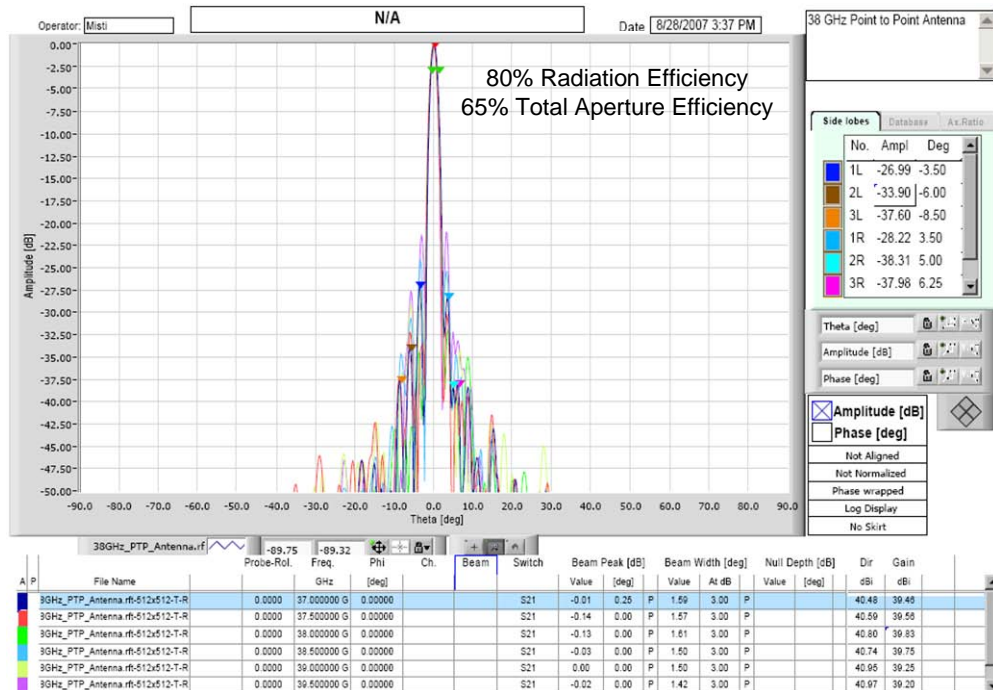**Figure 3.1-1. 38 GHz Point-to-Point CTS Antenna (with Exploded View)**

Figure 3.1-2. Measured Azimuth Plane Pattern (38 GHz PTP CTS)

3.2 Cylindrical-Conformal (MW through MMW Frequencies)

A representative example of the Cylindrical CTS array is currently in full-scale production and deployment for specific Government applications. This particular design supports low-sidelobe performance and high-efficiency in a compact conformal form-factor. The radiating aperture and integrated line-feed of this antenna are fabricated monolithically as a single injection-molded plastic component which is subsequently conductively-plated. Figure 3.2-1 shows the assembled antenna (with interconnecting waveguide and frame) together with a measured azimuth-plane antenna pattern. Commercial applications of this technology include high-gain conformal light/telephone pole-mounted antennas for video camera and cell-site back-haul at frequencies of 2.5, 5, 24, and 60 GHz.
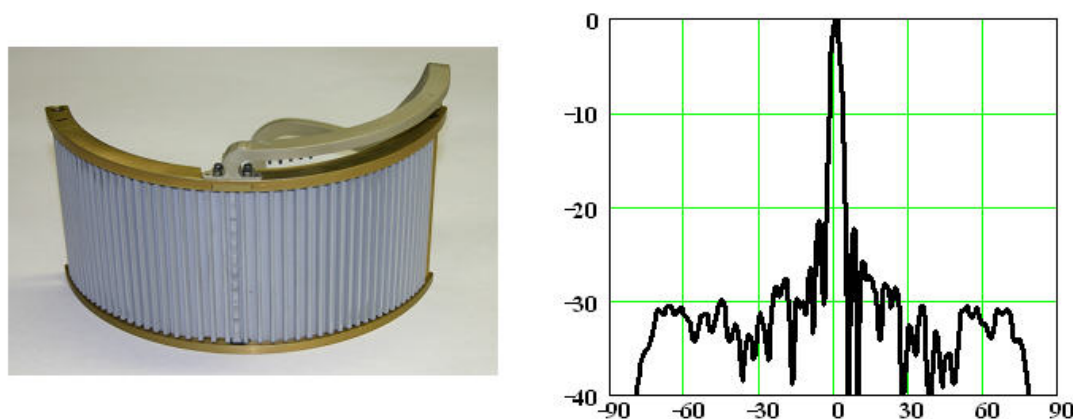

Figure 3.2-1. Cylindrical CTS Array (with Measured Azimuth-Plane Pattern)

3.3 SATCOM Man-Portable (X, Ku, Ka, K/Ka and K/Q Frequency Bands)

Lightweight Low-profile Dual- and Single-polarized CTS Arrays for Man-portable ("Manpack" or "Rucksack") SATCOM applications are currently entering full-scale production. X-band (Dual-Polarized/Dual-Band) versions have successfully completed Operational Evaluation with the US Army and a Ku-band version capable of supporting full international Ku-band SATCOM will soon be field-tested. These units are fabricated from plated injection-molded plastic, yet meet the full rigors and rough-handling associated with "real-world" field operations. A 9.5" x 14.5" Ka-band version of this antenna has been link-tested on the US Government's Global Broadcast Service (GBS) Satellite network. Figure 3.3-1 depicts a 10" x 30" X-band and the 9.5" x 14.5" Ka-band antennas. Figure 3.3-2 shows the measured sidelobe patterns and gain for the Ka-band antenna, with total antenna efficiency of approximately 75% and G/T of 14 dB/K.
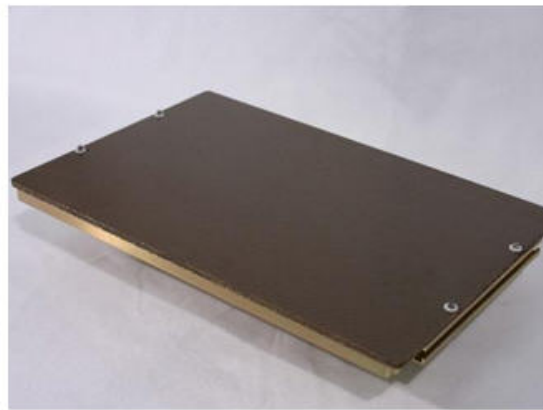
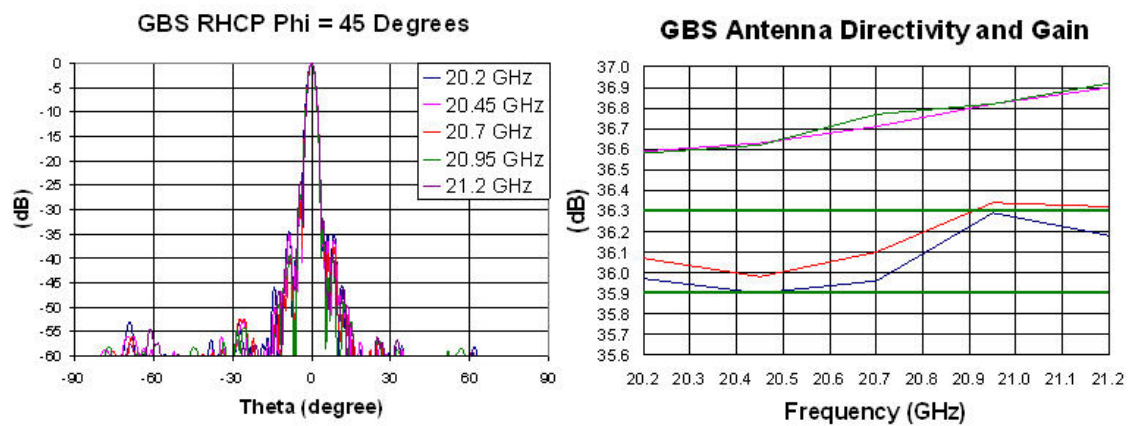**Figure 3.3-1. X-band and Ka-band ThinPack® CTS Antennas**

Figure 3.3-2. Ka-band ThinPack® CTS Antenna Performance

3.4 Ground-Mobile SATCOM "Communication-on-the-Move" (COTM)

Both CTS and VICTS arrays are currently in development for Ground-Mobile "Communication on the Move" SATCOM applications for both Government and Commercial users.

3.4.1 Gimbaled Low-Profile CTS Antennas (X, Ku, K/Ka, K/Q) for COTM

A gimbaled Dual-Polarized X-band CTS Antenna has been successfully demonstrated and field-tested for Satellite-on-the-Move (SOTM) applications. This unit works with existing XTAR and Skynet satellite networks and is fully-compatible with the X-band component of the US Government's Wideband Global Service (WGS.) This particular design supports 7.25-7.75 GHz on Receive and 7.90-8.40 GHz on Transmit with sufficient G/T and Transmit gain to enable 1 to 2 Mbps two-way SATCOM data rates while "on-the-move." Figure 3.4.1-1 shows the (Dual-Polarized/Dual-Band) CTS array for this particular design and Figure 3.4.1-2 illustrates the fully-integrated SOTM antenna subsystem (including elevation-over-azimuth positioner, motors, rate sensors, and associated RF components.) Similar CTS-based SOTM systems are currently under development for Ku, K/Ka, and K/Q SATCOM applications.

Figure 3.4.1-1. X-band Satellite-on-the-Move (SOTM) CTS Array

Figure 3.4.1-2. X-band Satellite-on-the-Move (SOTM) Antenna Subsystem

3.4.2 Low-Profile VICTS Antennas (X, Ku, K/Ka, K/Q) for COTM

To date, various VICTS arrays ranging in size from 10"D to 30"D and for frequency bands spanning from C-band through Q-band have been successfully demonstrated. Specific to Ground-Mobile SOTM applications, a low-profile (< 4.5"H) Ku-band COTM antenna, the "ThinSat® 300" is currently entering low-rate production. Comprised of side-by-side 20"D Receive and 30"D Transmit VICTS Antennas, this antenna subsystem is licensed by the FCC and supports two-way SATCOM data rates ranging from 1 through 8 Mbps and at unusually high "spectral efficiencies" (bits per Hz) as compared to competitive products.

Figure 3.4.2-1. ThinSat® 300 SATCOM On-the-Move Antenna Product

3.5 Aeronautical SATCOM (C, X, Ku, K/Ka, K/Q)

Both CTS and VICTS arrays are currently in development for Aeronautical applications for both Government and Commercial users.

3.5.1 Gimbaled Low-Profile CTS (X, Ku, K/Ka, K/Q) for Aeronautical SATCOM

In late 2003, ThinKom was competitively selected as the developer and manufacturer of the U.S. Air Force's FAB-T Large Aircraft Antenna based on its dual-band K/Q (20/44 GHz) CTS antenna technology. A total of 10 flight-qualified Engineering Development Models (EDM's) for this program which have been delivered to L-3 Communications for Pedestal/Positioner integration and the program is scheduled to start Low-Rate Initial Production (LRIP) in March of 2010. In 2008, the U.S. Air Force (through MIT Lincoln-Laboratories) awarded ThinKom a contract to design and fabricate a smaller version of the FAB-T Large Aircraft Antenna, the "Milstar Staring Array (MSAA)" including antenna positioner and antenna control unit (ACU).
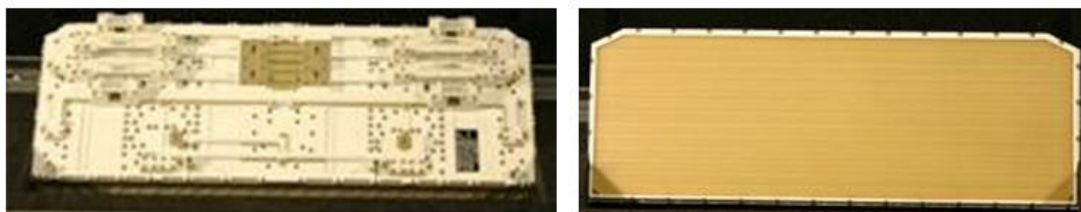

Figure 3.5.1-1. FAB-T Large Aircraft Antenna LAA (Dual-Band CTS Array)

The FAB-T LAA EDM development served to prove the repeatability and producibility of the dual-band CTS planar array. Figure 3.5.1-2 shows measured Gain (and efficiency figures-of-merit) and Axial Ratio (< 1.5 dB) metrics for 8 distinct EDM units. The absolute levels of these metrics are proof of the high-performance of this design and the strong unit-to-unit repeatability of these units is evidence of its overall robustness and manufacturability. Receive (20 GHz) and Transmit (44 GHz) total aperture efficiencies averaged 70% and 54%, respectively and with corresponding ohmic efficiencies (total ohmics losses) of 84% and 73%, respectively.
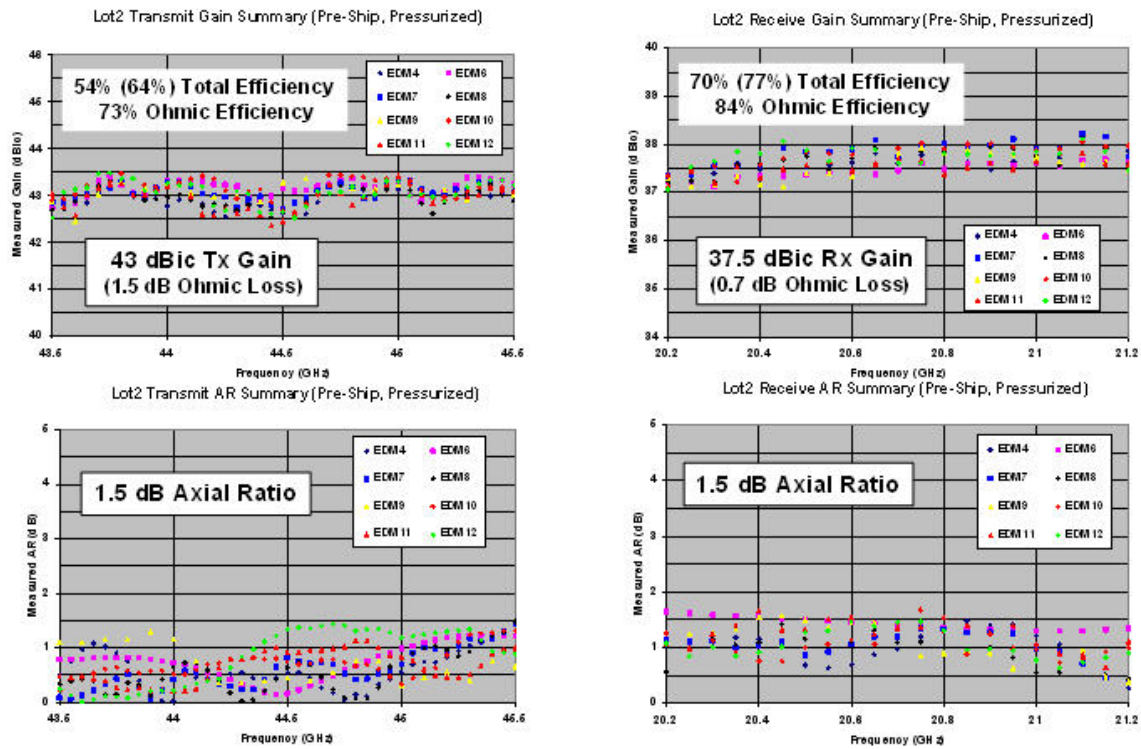
Figure 3.5.1-2. Measured Gain and AR for Dual-Band K/Q CTS EDM Antennas

3.5.2 VICTS Arrays (C, X, Ku, K/Ka, K/Q) for Aeronautical SATCOM

ThinKom's low-profile VICTS antenna technology has been demonstrated for a number of Government Aeronautical applications. In support of the US Air Force's AMCAS Program (through MIT-Lincoln Laboratories and in collaboration with Raytheon,) ThinKom is developing 20 GHz, 30 GHz, and 44 GHz VICTS antennas suitable for Aeronautical SATCOM in support of both WGS and Advanced EHF (AEHF) Satellite systems. The 20 GHz version of this antenna recently completed initial flight-tests on MIT-LL's "Paul Revere" test aircraft and demonstrated continuous 1.5 Mbps inflight data rates via the existing (MDR) EHF satellite. In addition, ThinKom has recently concluded the development of a cavity-mounted X-band prototype antenna suitable for an F/A-18 (or similar) platform for NAVAIR and has recently completed full MILSTD-810F (Uninhabited Fighter Environment) environmental testing (shock, vibration, and temperature) for this unit. In addition, this X-band unit has been link-tested on the XTAR satellite system and demonstrated 500 Kbps to 1 Mbps data rates.

Figure 3.5.2-1 illustrates the 20 GHz AMCAS VICTS antenna in aperture (test) and as a fully-integrated antenna subsystem. Figure 3.5.2-2 shows the low-profile (cavity-mountable) X-band VICTS aperture.
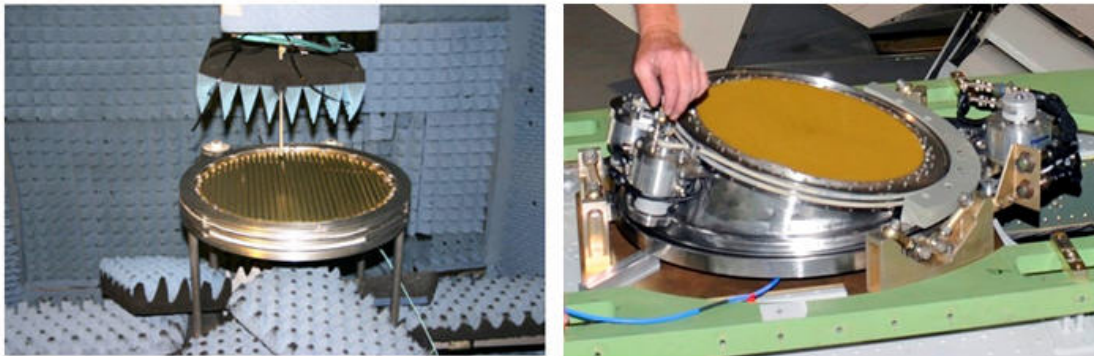

Figure 3.5.2-1. 20 GHz VICTS Antenna (and Integrated Gimbal)

Figure 3.5.2-2. X-band VICTS Antenna (Environmental Test Unit)

Conclusion

Since its original invention in the early 1990's, the "Continuous Transverse Stub (CTS)" array and its related variant, the "Variable Inclination Continuous Transverse Stub (VICTS)" array, have enjoyed increasing adoption in a broad range of Microwave and Millimeter-Wave Radar and Communication applications. These include Commercial and Government low-profile antenna products for Radar, Point-to-Point (PTP) communication, Man-Portable SATCOM, and high data rate Satellite-on-the-Move (SOTM) applications. These products embody both staring and scanning (phased-array) extensions of the original technology and exhibit a number of favorable properties in terms of footprint, profile, antenna efficiency, operating bandwidth, sidelobe control, polarization diversity, and overall tolerance insensitivity. The technology continues to be improved, refined, and adapted to a broadening range of challenging applications.

Acknowledgements

References

[1] W. W. Milroy, "Continuous Transverse Stub element devices and methods of making same," United States Patent 5,266,961.

[2] W. W. Milroy, "The Continuous Transverse Stub (CTS) Array: basic theory, experiment, and application," 1991 Antenna Applications Symposium, Allerton Park, IL, USA.

[3] W. W. Milroy, "Evolution of the Continuous Transverse Stub (CTS) Array in communication applications," (Classified Volume,) MILCOM 97 Symposium, Monterey, CA, USA.

[4] Alan Lemons, Robert Lewis, William Milroy, Ralston Robertson, Stuart Coppedge, and Todd Kastle, "W-Band CTS Planar Array," 1999 IEEE International Microwave Theory and Techniques Symposium, Los Angeles, CA, USA.

[5] W. W. Milroy "Advanced Broadband Access Applications of the Continuous Transverse Stub (CTS) Array," 2001 International Conference on Electromagnetics in Advanced Applications (ICEAA01), September 10-14, Torino, Italy.

[6] Ruey-Shi Chu, "Analysis of Continuous Transverse Stub (CTS) Array by Floquet Mode Method," 1998 IEEE International Antennas and Propagation Symposium and USNC/URSI National Radio Science Meeting, Atlanta, GA, USA.

[7] W. W. Milroy, "Planar antenna radiating structure having quasi-scan, frequency-independent driving-point impedance," United States Patent 5,995,055.

[8] W. W. Milroy, "Compact, ultrawideband matched E-plane power divider," United States Patent 5,926,077.

[9] W. W. Milroy, "Compact, ultrawideband, antenna feed architecture comprising a multistage, multilevel network of constant reflection-coefficient components," United States Patent 6,075,494.

[10] W. W. Milroy, S. B. Coppedge, A. Ekmekji, S. Hashemi-Yeganeh, S. G. Buczek, "True-Time-Delay Feed Network for CTS Array," United States Patent 7.432,871.

[11] W. W. Milroy, S. B. Coppedge, A. C. Lemons, "Variable Inclination Continuous Transverse Stub Array," United States Patent 6,919,854.